The effect of end wall profiling on secondary flow in nozzle guide vanes

Yan, Jin

The Effect of End Wall Profiling on Secondary Flow in Nozzle Guide Vanes

by

Jin Yan

A Thesis submitted in partial fulfilment of the requirements for the degree of Doctor of Philosophy

School of Engineering
University of Durham
1999

Declaration

The work contained in this thesis has not been submitted elsewhere for any other degree or qualification, and unless otherwise referenced it is the author's own work

Dedicated to my wife and daughter

Acknowledgements

I am most grateful to my supervisor Dr. David Gregory-Smith. His guidance and encouragement have been of great help throughout this project.

Dr. Li He and Dr. Robert Dominy have given me many useful hints for which I would like to thank them. I would also like to thank all the staff in the school of Engineering who have provided assistance to me during my period as a research student. In particular thanks must go to Mr. Gary Parker who has been giving his great help on manufacture and installation of the rig through this project, all the technicians in the mechanical and electrical workshop who built pieces of apparatus for me.

The help of Dr. Nadir Ince, Dr. Peter Walker and other members of the Aerodynamic group at ALSTOM Energy Ltd in Rugby is also much appreciated. In particular, their assistance in running ALSTOM software has been of great value.

Finally the financial support of ALSTOM Energy Ltd and Durham University is also greatly acknowledged.

The Effect of End Wall Profiling on Secondary Flow in Nozzle Guide Vanes

Jin Yan

Abstract

This thesis presents detailed investigations of the effect of end wall profiling on the secondary flow in a large scale, linear cascade with nozzle guide vanes. The purpose of this project is to look into the secondary flow structure in the linear cascade and the influence of the shaped end wall on the secondary flow. By applying the non-axisymmetric end wall, the secondary flow is reduced compared to the flat end wall data. The yaw angle variation at the exit of the blade passage is reduced.

The cascade was designed according to the nozzle guide vane from ALSTOM Energy Ltd. It was manufactured and connected to the low speed wind tunnel in the Thermo-Fluids Lab in Durham. The data acquisition system was designed and commissioned. Five hole probes were designed and calibrated according to the cascade test condition.

The flow field with the flat end wall in the cascade was investigated using five hole probes through different traverse slots. Flow visualisations were conducted as well. The secondary flow structure and the loss development in the cascade are understood. Transitional trips were put on the blade surfaces and their effects on the secondary flow were observed.

The CFD code was modified to fit the cascade case. It was validated against the Durham standard case and the flat end wall results. Different numerical schemes and turbulence models were evaluated. Different shaped end walls were systematically tested by the CFD code. The best end wall profile was selected and manufactured. It was then tested in the cascade. Detailed investigations by five hole probes, flow visualisation and wall static pressure measurements were conducted. The results were

compared to the flat end wall results and the CFD prediction. The secondary flow and the total pressure loss were reduced. The test data in the cascade will supply the evidence and data for the real turbine design. The chosen end wall profile will hopefully be tested in a test turbine.

Contents

List of Figures

List of Tables

Nomenclature

at	half of the maximum change of shaped endwall
st	the distance between the peak of axial direction curvature and trailing edge
b	the extension of secondary losses zone
c	chord
A	area
C_L	lift coefficient
h	blade span
H	height of the cascade
P	static pressure
P_o	total pressure
Ys	total pressure loss coefficient
C_{po}	total pressure loss coefficient
C_p	static pressure coefficient
C_{ske}	secondary kinetic energy coefficient
C_D	dissipation coefficient
Q	dynamic pressure
s	blade pitch
V	velocity
Vm	mean velocity (between upstream and downstream)
V_{free}	freestream velocity
v_n and w	secondary velocity components
X	axial direction
X_{min}	distance of the minimum suction side pressure from the leading edge plane
y	the distance from endwall
Re	Reynolds number
$\dot{m}$	mass flow rate
ν_T	kinetic viscosity
k	turbulent kinetic energy
ε	dissipation rate of the turbulent energy
α	Flow angle (Yaw angle)
β	stagger angle
δ	boundary layer thickness

δ_1 boundary layer displacement thickness

δ_2 boundary layer momentum thickness

ζ vorticity component

ρ fluid density

ϕ angle between the normal to a streamlines and the normal to the Bernoulli surfaces (in which the total pressure is a constant)

ψ secondary flow stream function

μ_T turbulence viscosity

Subscripts

1 inlet

2 outlet

ax axial

Fs free stream

ms mid-span

n normal to streamwise direction

s streamwise direction

x axial direction

y tangential direction

z spanwsie direction

l local

u upstream

Abbreviations

H_s Horseshoe vortex suction side leg

H_p Horseshoe vortex pressure side leg

SS Suction side of blade

PS Pressure side of blade

Chapter 1

Introduction

The cost of fuel is projected to continue rising at substantial rates. This makes it imperative that future steam turbines be designed to the highest possible efficiency. Typical evaluations by utilities for a recent large fossil-fired steam turbine power station (600-700 MW) currently ascribe an equivalent value of about £9 million per year for each 1% gain in cycle efficiency.

When a non-uniform flow is turned within a blade row, the flow becomes three-dimensional and there is a variation of flow angle along the span of the blade. This effect is known as secondary flow. Many important phenomena occur in gas and steam turbomachinery as a consequence of secondary flow. The secondary loss, which usually include all the losses arising on the end wall both within and outside the blade passage, probably is the most difficult loss component to understand because of its extremely complex physical nature. For low aspect ratio turbines, secondary loss typically contributes about 40% of the total loss. In compressors, the effects of the secondary loss are probably as important as in turbines. Because the current research is on a turbine blade, the compressor case will not be reviewed.

An large amount of literature on the study of the flow process near the end wall has been published. Sieverding (1984) present a comprehensive review of the flow field structure in the cascade. Detailed secondary flow investigations in a turbine cascade have been published by Walsh and Gregory-Smith (1990). The secondary flow process in the

turbine cascade has been fairly well understood. Denton (1993) gave a comprehensive loss production mechanism analysis in the turbine cascade. The secondary flow increases loss by mainly influencing the end wall boundary layer. However, as Denton (1993) concluded, the prediction on the secondary loss by correlations is far from accurate. The main hope is that loss can be quantified by three-dimensional Navier-Stokes solutions.

It is very important to control all sources of losses and so a lot of work has been directed toward the understanding and reduction of secondary loss. Profiling of the end wall(s) of the blade row holds promise for achieving improved performance through the reduction of secondary loss. Deich (1960) and Ewen (1973) both report achieving an increase in efficiency in rotating rigs attributed to axisymmetric end wall profiling. Rose (1994) used non-axisymmetric end wall profiling to improve efficiency by removing the non-uniformity of static pressure distribution after trailing edge of the nozzle guide vanes.

This project is supported by ALSTOM Energy Limited. In their high pressure (HP) and intermediate pressure (IP) blades specific volume changes due to expansion is much smaller compared to the low pressure blades (LP). Therefore the change in blade height from stage to stage is small with the streamlines approximately parallel to the turbine axis. The low aspect ratio makes the secondary losses account about 40% about the total losses.

The aim of this project is to investigate the effect of a non-axisymmetric end wall on the secondary flow in a nozzle guide vane cascade. The objectives are experiments in a linear cascade with Nozzle Guide Vanes from ASLTOM and CFD Design investigations.

All the experiments were done on a type of vane which is a main blade type of the steam turbines produced by ALSTOM. The blade is a low reaction blade. The low reaction means the velocity at the exit of the nozzle vane is much bigger than at the exit of the rotor. Because the loss contribution is the exit velocity squared time the loss coefficient, even with a smaller loss coefficient, the nozzle become more important in terms of the loss. The Nozzle Guide Vane from ALSTOM has a relatively small secondary loss compared to the others. But because it is the main working blade shape of ALSTOM, considering the future application, it is still used for the project. However, the effect of the end wall profiling on the secondary loss will not be big considering the already small secondary flow.

A linear cascade was designed and built for this type of blade. The flow field with the flat end wall was investigated. A computational fluid dynamic program was provided by ALSTOM. The code was modified and validated against the Durham cascade test case and the experimental results from the Nozzle Guide Vane cascade. The code was then used to predict the effect of different end wall profiles. The flow field in the cascade with the non-axisymmetric end wall was investigated. The effects of the non-axisymmetric end wall on the flow field were analysed and understood.

The work presented in this thesis covers the progress over the past three years. It can be divided into nine chapters.

(1). This chapter provides an introduction.

(2). The second chapter is the literature review. In this chapter the mechanism of the secondary flow inside the cascade was reviewed. Different methods of secondary flow reduction, especially end wall profiling methods were discussed.

(3). The third chapter is the instrumentation. This part includes the design of the nozzle guide vane cascade, the manufacture of the cascade, the design and calibrations of the five hole probes, the set-up of the data acquisition system and the analysis procedures.

(4). The fourth chapter describes the experiments with the flat end wall. This part provides the detailed investigations of the secondary flow structure and the loss mechanism in the nozzle guide vane cascade.

(5). The fifth chapter is the description and the validation of the CFD code. The numerical schemes and the turbulence models used in the code are briefly described. The code was validated against the Durham test case and the results of the nozzle guide vane cascade.

(6). The sixth chapter of the thesis is the end wall profile design. A series of end wall profiles were systematically tested using the CFD code. The secondary kinetic energy and the total pressure loss of different profiles were compared. The design of the final end wall profile was selected.

(7). The seventh chapter is about the experiments with the shaped end wall. The flow field in the cascade with the shaped end wall was investigated. The effect of the shaped end wall on the secondary flow and loss was analysed.

(8). The eighth chapter is the summarising discussion.

(9). The final chapter draws conclusions and proposes future work.

Chapter 2

Secondary Flow, Losses and Reduction Techniques

An overview of the physical understanding of the secondary flow is described, and the losses related to secondary flow are given. The methods of predicting secondary losses are discussed. Different secondary loss reduction techniques are reviewed and discussed. The end wall profiling methods and results done by previous researchers are also discussed.

2.1 Generation and definition

In an axial turbomachine, when flow is turned through an angle, the flow far from the end wall (hub or casing) is called primary flow which may often be considered as two-dimensional flow. Near the end wall region, the boundary layer flow at inlet contains a spanwise velocity gradient. When this is turned inside the blade passage, transverse velocity is produced. This three-dimensional effect is called the secondary flow. The basic physical reason for the appearance of secondary flow may be understood with reference to Figure 2.1. The primary flow set up a pressure gradient across the blade passage from pressure to suction surfaces. This gradient makes the fluid near the end wall flow from pressure surface to suction surface. This causes overturning of the flow. On the other hand, away from the end wall there is a back flow which causes

underturning of the flow. Though the inlet boundary layer is the product of the viscosity, the phenomenon of secondary flow is an inviscid effect. With the inlet boundary layer, the secondary flow is created by the action of the pressure gradient. The direct action of viscous forces on the secondary flow is of minor importance.

Consequences of the secondary flow in turbomachinery include:

(1). The exit angle variation which causes a change in the work output
(2). The extra losses in the blade row.
(3). The severely non-uniform flow at exit of one blade row can increase losses in a downstream row. In a high pressure turbine of low aspect ratio, up to half the loss can be attributed to secondary losses.
(4). The increased unsteadiness may affect the mechanical design of the blades.
(5). The secondary flow may enhance the heat transfer and affect the film cooling flow.

2.2 Literature review on secondary flow

Many investigations have been done to visualise and measure the structure of secondary flow. A comprehensive review of the understanding of secondary flow in turbine blade passages has been given by Sieverding (1985).

2.2.1 Development and structure of vortices in blade passages

With a non-uniform incoming flow, the vortices existing in blade passages could be classified into three types. They are horse shoe vortex, passage vortex and counter vortex.

Horse shoe vortex

The approaching boundary layer from upstream on the end wall hits the leading edge of the blade and rolls up into a horse shoe vortex around the leading edge of a blade. One leg of the horse shoe vortex curls around onto the suction surface of the blade and another leg crosses the passage to meet the suction surface of the adjacent blade. While crossing the passage the leg rolls up most of the inlet boundary layer which is thus discharged from the blade row in the form of a loss core on the suction surface a small distance from the end wall. Sieverding and Van den Bosch (1983) used a coloured smoke wire technique to visualise the evolution of entire stream surface through the cascade. They presented the flow model in Fig 2.2. It shows the shape of two stream surfaces, SS1 and SS2 with the SS1 in the end wall boundary layer and SS2 outside it. When the SS1 approaches the leading edge the lateral extremities of it start to roll up into the two counter-rotating branches of the horseshoe vortex, Hp and Hs with the main part of it keeping undisturbed. Behind the leading edge the whole stream starts to rotate. All parts of stream surface, including Hp and Hs, take part in this vertical motion and gradually develop into the so called passage vortex.

Passage vortex

The passage vortex is associated with the turning of the vorticity vector and dominates the latter half of the blade passage. It rotates in the same direction as Hp leg of the horse-shoe vortex, and the two merge together. Many researchers have studied the secondary flow in cascades showing how the passage vortex develops. Gregory–Smith and Graves (1983) described the passage vortex movement as shown in Fig 2.3. The movement is understood to be caused by the mutual convection of the vortex by its mirror image in the end wall. The passage vortex movement is believed to be linked to the strength of the vortex. In the low turning blade passages, the movement is smaller and the vortex stays closer to the end wall than in high turning blade passages.

Counter vortex

A new highly skewed boundary layer forms on the end wall downstream of the pressure side leg of the horse shoe vortex. A small vortex is formed in the corner where the strong cross flow meets the suction surface. It is formed in the same way as horse shoe vortex at the stagnation point. It reduces overturning on a line with the trailing edge and also increases losses downstream.

Vortices downstream of blades

The passage vortex is seen as the dominant feature with the effect of the counter vortex down stream of the blade exit. There is also a vortex sheet shed from the trailing edge of the blades. The vortex sheet at the trailing edge is composed of:

1. The trailing filament vortices, which arise due to the stretching of the inlet vortex filaments passing through the cascade with the different velocity between suction side and pressure side.

2. The trailing shed vorticity, which is due to the spanwise change of the blade circulation.

As the flow proceeds downstream, the vortices are slowly dissipated by viscous action. Typical spanwise exit angle and total pressure loss distributions downstream are shown in Fig 2.4 (Moore and Gregory-Smith [1996]). The characteristic under and over turning of the flow angle is seen together with the hump in loss away from the end wall. The secondary flow produced by the first blade row will considerably affect the next blade row. The non-uniform flow in the pitchwise direction at exit from one blade row produces an unsteadiness at inlet to the next row due to the relative motion. At mid-span, the variation across the pitch is small except in the wake which is relatively thin. However, in the secondary flow region there is a gross variation, and the unsteadiness is

correspondingly greater. Walraevens and Gallus (1995) have investigated the flow within a one and a half stage turbine. The flow is extremely complex and needs to be viewed at different time intervals at the exit of the second blade row. There were five different vortices being identified. The vortices change both in position and strength during the cycle. It is fair to say that the understanding of the time varying flow is far from complete.

2.2.2 Origin, growth and spatial distribution of loss.

Losses in a machine can be broken down into two groups, the cascade losses and additional stage losses. The cascade loss is measurable in the cascade, and inherent in blading design. It is often split up and the components assumed additive. The additional stage losses include gland leakage loss, rotor tip leakage loss, lacing wire loss, windage loss and loss due to partial admission. For the cascade losses, Sieverding (1985) suggested that the following loss sources can be identified:

1. Natural increases of the inlet end wall boundary layer up to the separation lines.
2. Growth of the new boundary layer behind the separation line.
3. Corner losses in both pressure side and suction side end wall corner, the latter being the most important.
4. Shear stress effects along all three dimensional separation lines
5. Losses due to the shear action of the passage vortex on the blade suction side and the mixing process between the cross flow and the blade flow along the three-dimensional separation line.
6. Dissipation of all vortices and mixing out of the non-uniform outlet flow field down stream of the cascade.

The amount of losses contributed by above loss sources varies. No.2-5 together contribute the most loss generated in the cascade. No.6 gives the biggest single loss contribution among them all, if the flow is mixed out to infinity.

Gregory-Smith and Graves (1983) found a fairly steady growth of the losses throughout their cascade. On the other hand, Langston (1977) and Marchal and Sieverding (1977) conclude that the losses remain fairly constant up to the axial position of the maximum suction side velocity and then grow rapidly to the trailing edge. The downstream spanwise loss distribution is naturally closely related to the position of the passage vortex. The loss profile does not only depend on the blade loading but also on the inlet boundary layer and the downstream distance. The end wall losses continue to rise with increasing downstream distance due to friction on the end wall and mixing out of the vortices and wake, etc (No.2 & No.6 above). Usually the downstream traversing slots are selected at the position that is about 20%-30% axial chord downstream from the trailing edge plane to measure the flow from which the mixed out loss and angle may be calculated.

Denton (1993) gave a detailed look into the loss mechanisms in turbomachinery by analysing the entropy increase which is proportional to the total pressure loss in low speed flow. He concluded that the sources of entropy generation are, in general: viscous effects in boundary layers, viscous effects in mixing processes, shock waves, and heat transfer across temperature differences. By analysing the boundary layer on the end wall, he concluded that about two thirds of the total secondary loss comes from entropy generation in the annulus wall boundary layers within, upstream of, and downstream of the blade row. As discussed by Denton (1993), the coefficient below represents the loss generated in the boundary layer.

$$Y = \frac{2 \times \rho}{\dot{m} \times V_1^2} \int V^3 \times C_D \times dA \qquad 2.1$$

Where $C_D \approx 0.002$ for a turbulent boundary layer in the range of $500 < Re_\theta < 1000$.

This loss will be used to analyse the loss caused by the boundary layer on the end wall and will be referred as $\int C_D V^3 dA$ loss. A further part comes from mixing loss of the

inlet boundary layer, which is amplified by the secondary flow. A third component is the loss associated with the secondary kinetic energy, which is of the order of one quarter of the total secondary loss. Within a multi-blade row environment, the proportion of the secondary kinetic energy lost is not predictable.

2.2.3 Secondary flow prediction and calculation methods

(1) Classical methods

The first theoretical, inviscid secondary flow calculation method was developed by Squire & Winter (1951). Neglecting the viscous effect in the blade passage, the exit streamwise vorticity was found to be equal to the inlet normal vorticity multiplied by twice the deflection of the flow through the passage. The theory was then developed by the following researchers, Hawthorne (1951), Lakshminarayana & Horlock (1963) and Came & Marsh (1974). By assuming a many bladed cascade so that the Bernoulli surfaces are not distorted, Came & Marsh applied Kelvin's circulation theorem to the secondary flow calculation. Based on the inlet streamwise and normal vorticity components, the distributed secondary flow, trailing filament and trailing shed vorticity components at the exit plane are given. The results could be reduced to the same as those of Squire & Winter for low turning. The exit secondary velocity field and angle deviations could be obtained by solving the secondary flow stream function (Hawthorne (1951)). This method can make predictions of the angle variation, but because it is inviscid, cannot make loss prediction.

Secondary loss correlations.

Much work has been done in order to develop some correlation for secondary flow which can predict the secondary loss approximately.

A total pressure loss coefficient Ys is usually defined by:

$$Ys = \frac{P_{01} - P_{02}}{Q_{2MS}} \qquad 2.2$$

Where P_{01} represents the free stream total pressure at inlet, and P_{02} represents the spanwise average of the outlet total pressure, and Q_{2MS} represents the exit isentropic dynamic pressure. This definition is usually used. But in Durham, the inlet dynamic pressure Q_{1MS} is used instead of Q_{2MS}. For the loss correlation, the Q_{2MS} is used.

The gross secondary loss is found by subtracting the profile loss from the total loss in experiments. The net secondary loss can be obtained by subtracting inlet boundary layer loss from the gross secondary loss. The profile loss is usually taken as the mid-span loss. This technique is only valid for high aspect ratio blades. The technique used for calculating the profile loss in low aspect ratio blade is to use a two-dimensional model. Dunham (1969) reviewed all the correlations predicting loss. He found the best correlation was given by an expression based on the Ainley and Mathieson (1952) blade loading parameter

$$Ys=(c/h)(\cos\alpha_2/\cos\alpha_1)(C_L/(s/c))^2(\cos^2\alpha_2/\cos^3\alpha_m)f(\delta_1/c) \qquad 2.3$$

Where $\alpha_m=\tan^{-1}(1/2(\tan\alpha_1+\tan\alpha_2))$

and $f(\delta_1/c)=0.0055+0.078(\delta_1/c)^{0.5}$

Chen and Dixon (1986) have suggest that net secondary loss is correlated by the equation

$$Ys=0.0055(c/h)(\cos\alpha_2/\cos\alpha_1)(C_L/(s/c))^2\cos^2\alpha_2/\cos^3\alpha_m$$
$$+2\delta_2/h/((3n+1)(1/2n+1/2-\delta_2/h)) \qquad 2.4$$

Where $\delta_2/h=0.379(x/h)Re_x^{-0.2}$, and x is the distance downstream from the exit plane in the flow direction and n is the index for a power law fitted to the velocity profile at inlet. There are also many other correlations such as the correlation proposed by Craig & Cox (1970) for steam turbine design. In their correlation, the secondary losses is expressed as an enthalpy loss factor (referenced by exit kinetic energy). The Reynolds number effect is included in the correlation. Although stated that the correlation was for shrouded blades, it could be adapted for unshrouded blades. These correlation show which parameters may be the most important factors that affect the magnitude of loss. But the predictions of these correlations are based on experimental data obtained either from cascade tests or from the performance of actual machines. In some cases analytical models of the loss production mechanisms were formulated, Carter (1948), but these were usually highly idealized. With the new development of experiment techniques and numerical simulations, the understanding of the flow has been greatly improved. These new measurements and calculations showed that the real flow in a turbomachine is extremely complicated due to both three-dimensional effects and unsteadiness. Although the simple models used for performance prediction were shown to be grossly oversimplified, it was not apparent how they could be extended to include the new physics. Many correlations were reviewed by Hirch and Denton (1981). As they concluded, the main factors that affect secondary loss are inlet boundary layer thickness, aspect ratio, blade loading and the geometry of the end wall. However these correlations contain little physics and often give inaccurate results. The approach of Denton (1993) in using the dissipation coefficient $\int C_D V^3 dA$ appears to offer possibilities as a loss prediction method which would have the advantage of being closer to the physics of the flow. It assumes that most of the loss is produced by shear close to the surfaces. The prediction of the surface velocities is needed for this method.

(2) CFD predictions

With the rapid development of computer power in recent years, computational fluid dynamics (CFD) has become an increasingly important tool in the design of turbomachinery components. CFD is also an important aid to understand the flow physics together with experimental investigations. Secondary flow studies and predictions have been attempted by many investigators using CFD. Gregory-Smith (1997) has compared many CFD results from different codes with the Durham test case. Generally the CFD code gives higher mid-span loss and total losses than experimental results but smaller secondary flow. It was concluded that the computational grid and the convergence level are of great importance. CFD has been widely used in the turbine design. In Singh et al (1995), the CFD method was used to investigate the complex three-dimensional flow within the blade passages. The CFD was validated against experimental results from the two and three stages test turbine in ALTOM. The prediction of the secondary flow is good. Few blade designs were investigated using the CFD code. The predicted performance gain was confirmed by the test results. Ho and Lakshminarayana (1996) used a pressure-based CFD code to simulate the flow of Durham test case. The inlet turbulence intensity and length scale was varied to investigate their effect on secondary vortices and total pressure loss. The static pressure on the blade surface was well predicted compared to the test data. The loss and yaw angle distribution predictions are poor especially at the mid-span. Different inlet turbulence intensity and length scale had great effect on the total pressure loss distribution but nearly no effect on the secondary flow prediction. With the development of the computing power and the understanding of the flow, it is believed that the three-dimensional flow structure within blade passages will be better predicted.

2.3 Secondary loss reduction

Sieverding (1975) suggested several methods to reduce the secondary loss:

2.3.1 Optimisation of aerodynamic design

The optimisation needs a careful balance between the combination of annulus area (blade height), turning angle and Mach number. If the blade height is increased, the secondary loss and its interaction with the main stream flow will become relatively less compared to the total pressure loss. The most effective way of reducing secondary losses in guide vanes with a choked throat is to choose the largest possible outlet angle (measured from axial direction) resulting in the biggest blade height, which however, in turn increases the profile losses via the increased turning. According to equation 2.4, the solidity (c/s) is of the great importance to the secondary reduction. It is expected that the smaller solidity will result in smaller secondary flow because the influence of the secondary flow on the mainstream flow will be relative smaller. For large deflection steam turbines the optimum spacing suggested by Zweifel (1945) when the tangential force coefficient C_y was equal to 0.8. This gives the optimum spacing ratio to axial chord:

$$0.8 = C_y = 2\times\frac{s}{c_{ax}}\times(\tan\alpha_2 - \tan\alpha_1)\times\cos^2\alpha_2 \qquad 2.5$$

For the nozzle guide vane from ALSTOM,

α_1=0°, α_2 =78°, c_{ax}=152 mm (see cascade design in Chapter 3)

The optimum pitch (s) from equation 2.5 should be 299 mm which is bigger than the 140 mm derived from the design data of ASLTOM.

2.3.2 2-D Optimisation of blade profile

Many research workers have attempted to minimise secondary flow effects by an appropriate profiling of the blade. Erich (1955) suggested reducing that part of the secondary flow effect which is due to the spanwise velocity component caused by an exit angle variation along the blade span. Dejc et al (1973) demonstrated that a

reduction of secondary losses could be obtained by using a decelerated and accelerated cascade flow which implies a divergent-convergent blade to blade passage in cascade, instead of a continuously convergent flow blade passage which is needed for minimum profile losses. Aft-loading is also considered as an effective method to reduce the secondary loss. By aft-loading blade, the pressure distribution around the blade surface will be changed. The diffusion on the rear part of the suction surface will be high. But more importantly, the aft-loading will reduce the pressure difference between the suction and pressure surface in the front part of the passage where the secondary flow is initiated.

2.3.3 3-D Optimisation of blade profile

(1) Straight tangential lean

The straight tangential lean was introduced to the field of turbomachinery a long time ago, Fillipov et al (1964). In an annular nozzle, swirl causes a radial pressure gradient which drives low momentum fluid towards the hub. This leads to radial secondary velocities which increase the downstream mixing loss. The accumulation of the low momentum fluid may lead to boundary layer separation in the hub-suction surface corner. If a blade is leaned so as to increase the pressure at hub, the migration of the low momentum fluid and radial secondary flow will be reduced. Hence, the loss might be reduced near the hub. But on the other hand, the straight tangential lean may increase loss near the tip. Fillipov et al (1964) found that a positive lean as shown Fig. 2.5 reduces loss at the hub but increased it at the tip. In a linear cascade, such radial flow does not exist and the tangential lean might not achieve any loss reduction and probably will increase it. Harrison (1990) investigated the straight tangential lean, as shown in Fig. 2.5, in a linear cascade. The loss generated on the end wall was evaluated by using $\int C_D V^3 dA$ method. It was found the straight lean reduced loss at one end wall with positive lean but increased it at the opposite wall. It marginally increases the total loss.

However, ALSTOM energy Ltd found a stage efficiency gain in their two-stage test turbine by applying negative lean, Haller (1997). It was found that negative lean reduced the area of loss at the tip of the fixed blade and hence provided a very uniform mass flow distribution into the next moving blade. From a careful investigation, -8 degree lean was found to give the best efficiency.

(2) Compound lean

Because the negative lean will reduce secondary flow at the tip, the positive lean will reduce the secondary flow at hub, compound lean was created. Compound lean designs as shown in Fig. 2.5 have been widely applied in gas and steam turbines. The design is normally generated by tangential displacement of the root and tip sections relative to the mid-span section such that the blade is curved in the spanwise direction. The pressure surface of the blade intersects with the hub and the tip at an acute angle. This introduces body forces on the flow which results in higher static pressure and lower velocity at the end wall. This will reduce the secondary flow generated on the end walls. But the compound lean will result in more boundary layer fluid being convected to the mid-span and hence increase the loss there. As confirmed by the experimental results from Haller (1997), it also pushes more mass flow into the root and tip region of the downstream moving blade where the secondary losses are generated. This has a negative effect on the efficiency. Harrison(1991) measured the effect of the compound lean in a linear cascade. It was found that the compound lean gave more uniform exit flow, but increased loading (exit angle) at mid-span. The compound lean also gave a more even loss distribution, with reduced losses near the end walls being offset by increased mid-span loss. Overall the loss was not reduced, but the more uniform flow into the next blade row might improve the overall efficiency in a machine environment.

(3) Controlled flow

The controlled flow design as shown in Fig. 2.5 has been developed in ALSTOM for years, Singh et al (1995). It looks similar to the compound lean. But the design

principle is very different. The controlled flow design is formed by skewing the blade sections such that the throat openings are reduced at the root and tip and increased in the mid-span. The idea is to reduce the mass flow at the root and tip where the secondary losses are generated and increase the mass flow at the efficient mid-span. The design is achieved by simply skewing the fixed blade sections about the straight radial trailing edge with a parabolic distribution of setting angle with span. The mean opening is kept the same to maintain the bulk reaction at the same level. Skewed sections of the fixed blade (nozzle) of this design near the end wall reduce the velocity levels and hence the secondary losses. From the test data and results of calculation, it was found that both the fixed blade and the moving blade were benefited because of lower mass flows were passed into the end wall region compared to the compound lean results from Haller (1997).

2.3.4 3-D Boundary layer devices, including suction or blowing, slots, fences and grooves.

Because the inlet boundary layer is the main factor that affects the secondary losses, suction seems to be the most efficient way to eliminate the boundary layer. Unfortunately suction needs more power than will be gained in the reduction in loss (Prümper [1975]).

Biesinger and Gregory-Smith (1993) found that the effect of upstream tangential boundary layer blowing is first to thicken the inlet boundary layer, leading to greater secondary losses. Then with stronger blowing, as re-energization of the inlet boundary layer takes place together with increasing counter streamwise vorticity, the passage vortex is progressively weakened, with a corresponding reduction in loss. However when the energy for inlet blowing is included, no net gain is achieved, due mainly to the mixing loss of injected air.

The use of radial slots, which connect the pressure surface to the suction surface, can achieve a successful reduction of secondary losses for compressor blades (Griepentrog [1969]). But other researchers found little success of using this method. For turbine blades the radial slots will increase the secondary losses (Prümper [1972]). This could be explained by the different blade suction side velocity distributions. In a compressor cascade the suction side flow is subject to strong adverse pressure gradients and an injection from the pressure side re-energises the low momentum boundary layer material on the suction side, thus suppressing corner stall. In the turbine the flow is accelerated over most of the blade surface and the boundary layer on the suction surface is quite thin. An injection from the pressure side will make the boundary layer on the suction surface thicker and might cause more loss.

Boundary layer fences were used by Prümper (1975) 1) on the end walls, 2) on pressure and suction surface, 3) on the suction surface only. Boundary layer fences in the form of thin metal sheets or grooves were used to correct the flow direction when, due to the influence of viscous forces and pressure gradient, the flow is unable to follow the two-dimensional flow path and prefers a more radial path. Fences are meant to reduce the interaction between two boundary layers of different flow directions and hence reduce the mixing losses. Also they limit the radial extension of the secondary flows and thereby improve the inlet conditions to the following row. The use of fences on the end walls proved to be only partially successful, and on the blade pressure surface proved to have a negative effect because of the comparatively small radial flow and rather thin boundary layer. It seems that only the third method with the fences on the suction surface is really promising. However the application of these metal sheet fences in real machines is very questionable because of their low mechanical strength. The grooves seem to have the advantage of not generating extra losses on the primary flow as do the metal sheet fences (Prümper [1975]).

2.4 Secondary loss reduction by end wall profiling.

Much work has been done to reduce the secondary loss by contoured end walls. Most of them were done with one shaped end wall and another flat end wall. Deich et al (1960) reported work investigating the effects of the end wall profiling in a linear cascade and annular cascade as shown in Fig 2.6. The selected profiles reduced the velocity in the region of highest turning and provided increased acceleration of the flow upstream of the trailing edge. He achieved 1.5 per cent increase in efficiency on blades with an aspect ratio of 0.5. Deich et al (1960) reported a very important optimum contraction ratio distribution for his tested blades as shown in Fig 2.7. Morris and Hoare (1975) described experiments with a similar profile as the optimum (shown in Fig 2.7) found by Deich (1960). Adjacent to the flat wall the maximum velocity and the amount of diffusion were reduced. Next to the profiled wall a decreasing of the velocities over the front part of blade was followed by an acceleration and then a rapid deceleration just before the trailing edge. A large reduction of the total loss was found in the half span next to the flat wall, and no change in the half span near the profiled wall. Morris and Hoare(1975) also investigated an asymmetric profile in order to move the velocity maximum nearer the leading edge and give a more rapid deceleration toward the trailing edge. But the position of the maximum velocity was hardly moved and the deceleration was increased. A large region of high total pressure loss adjacent to the profiled wall indicated that the wall boundary layer has been greatly thickened and may have separated. It was suggested that the adverse pressure gradient just upstream of the trailing edge was responsible for flow separation. It is very important to consider carefully the effects of a proposed profile on the blade and end wall pressure distribution. It was concluded that the reason for the decrease in loss near the flat wall was the more favourable pressure distribution. The sharp rise in pressure near to the trailing edge was thought to have reduced the benefits of lower loading on the profiled wall.

Atkins (1987) suggested two important points for investigations of the end wall profiling. Firstly, the investigations should not be restricted to a small number of end wall profiles because this leads to inconclusive results. Secondly, the profiles should be chosen in a systematic way, on the basis of their influence upon the pressure distribution in the cascade. Atkins used a CFD program which was a modified version of an inviscid, three dimensional, time marching program of known reliability developed by Denton (1982) to select the profiles. In his investigations, a turbine rotor blade was used. From a parametric study, it was found that the increase of the aspect ratio generally reduced the secondary loss. He also found that the boundary layer removal from the end wall contributed to the secondary loss generated within the passage and therefore it should be prevented. Seven different end wall profiles were tested in the cascade. The most advantageous profile as he found was the profile resulting in a reduction of the aerodynamic loading near the end wall. The lower cross-channel pressure gradient reduced the amount of boundary layer swept from the end wall onto the suction surface and then into the passage vortex. However, this kind of profile changes the inlet or exit area, and in a real turbine, this might be impossible.

Rose (1994) used a CFD method to design a non-axisymmetric end wall profile to reduce the non-uniformity of static pressure distribution at the platform edge downstream of the trailing edge of nozzle guide vanes. The object was to reduce the cooling air flow requirements to avoid hot gas ingestion. The profiling takes place before the leading edge and ends after trailing edge. Hartland et al(1998) used Rose's idea to design a non-axisymmetric end-wall profile for a row of rotor blades, and showed that the method worked well when tested in linear cascade. They also showed that there was a significant effect on the secondary flow. The profile had convex curvature on the end wall near the pressure surface, reducing the pressure there, and concave curvature near the suction surface, raising the pressure there. Thus the cross passage pressure gradient was reduced, reducing the secondary flow.

It is believed that the growth of the passage vortex is responsible for most of the secondary losses which are generated within the blade passage. Therefore, methods which attempt to reduce the net secondary losses should concentrate upon ways of influencing the passage vortex development by changing the end wall pressure distribution. This may be achieved by reducing the blade loading near to the end wall.

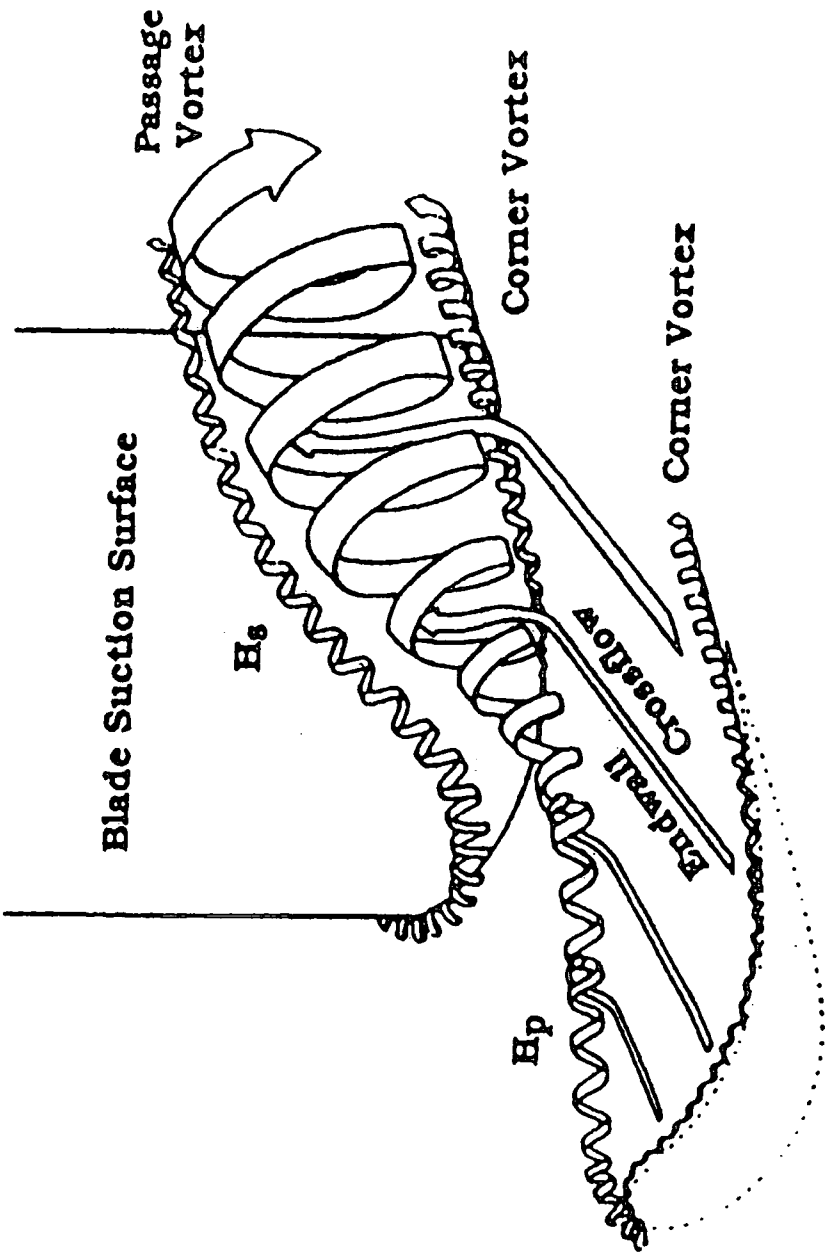

Figure 2.1—Secondary flow structure (from Kawai et al [1989]).

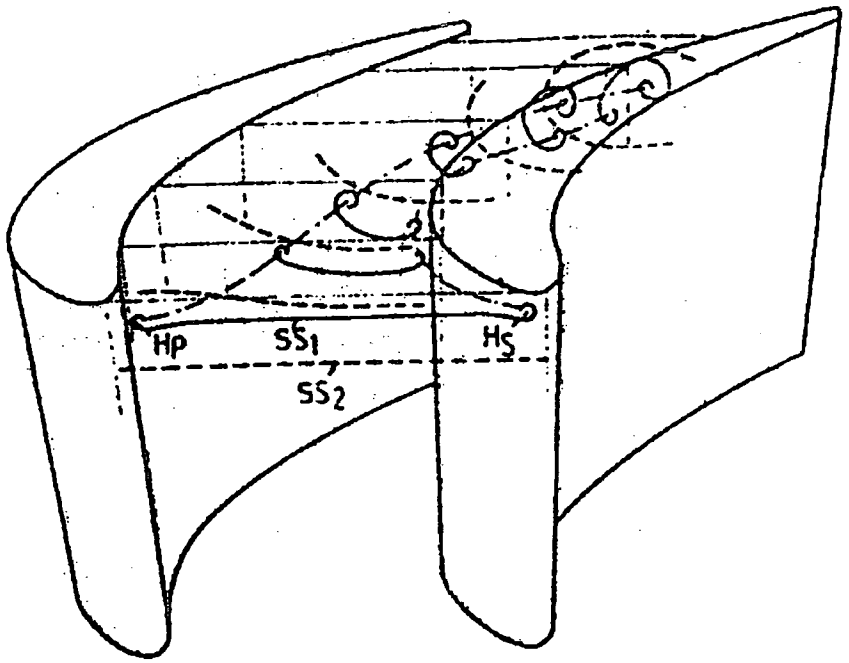

Figure 2.2— The synchronous evolution of horseshoe and passage vortices (from Sieverding [1983]).

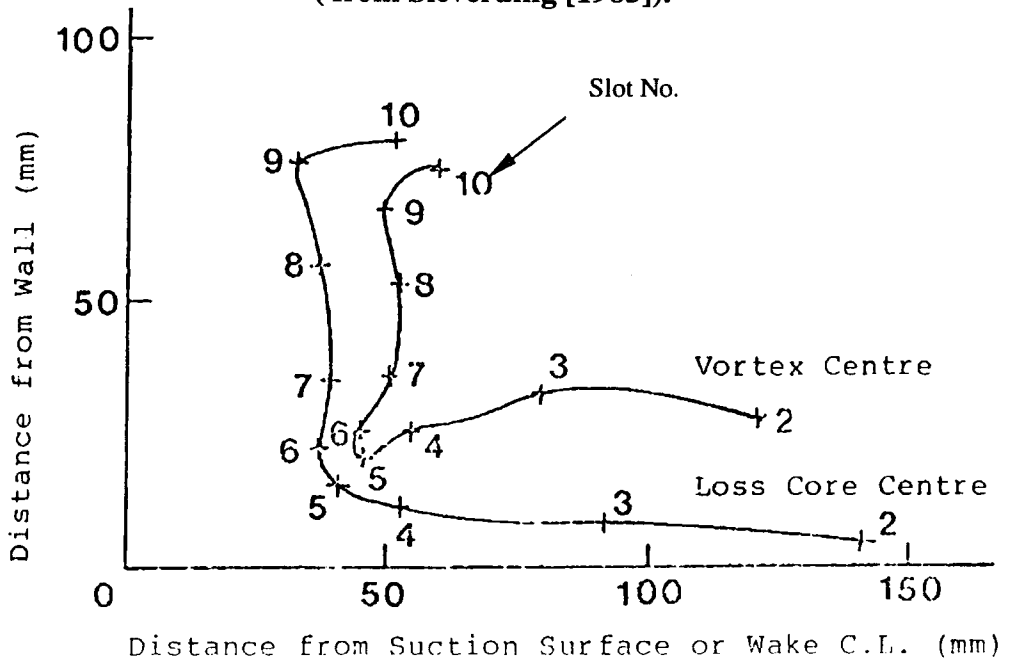

Figure 2.3— Passage vortex centre and loss core movement (Gregory-Smith and Graves)

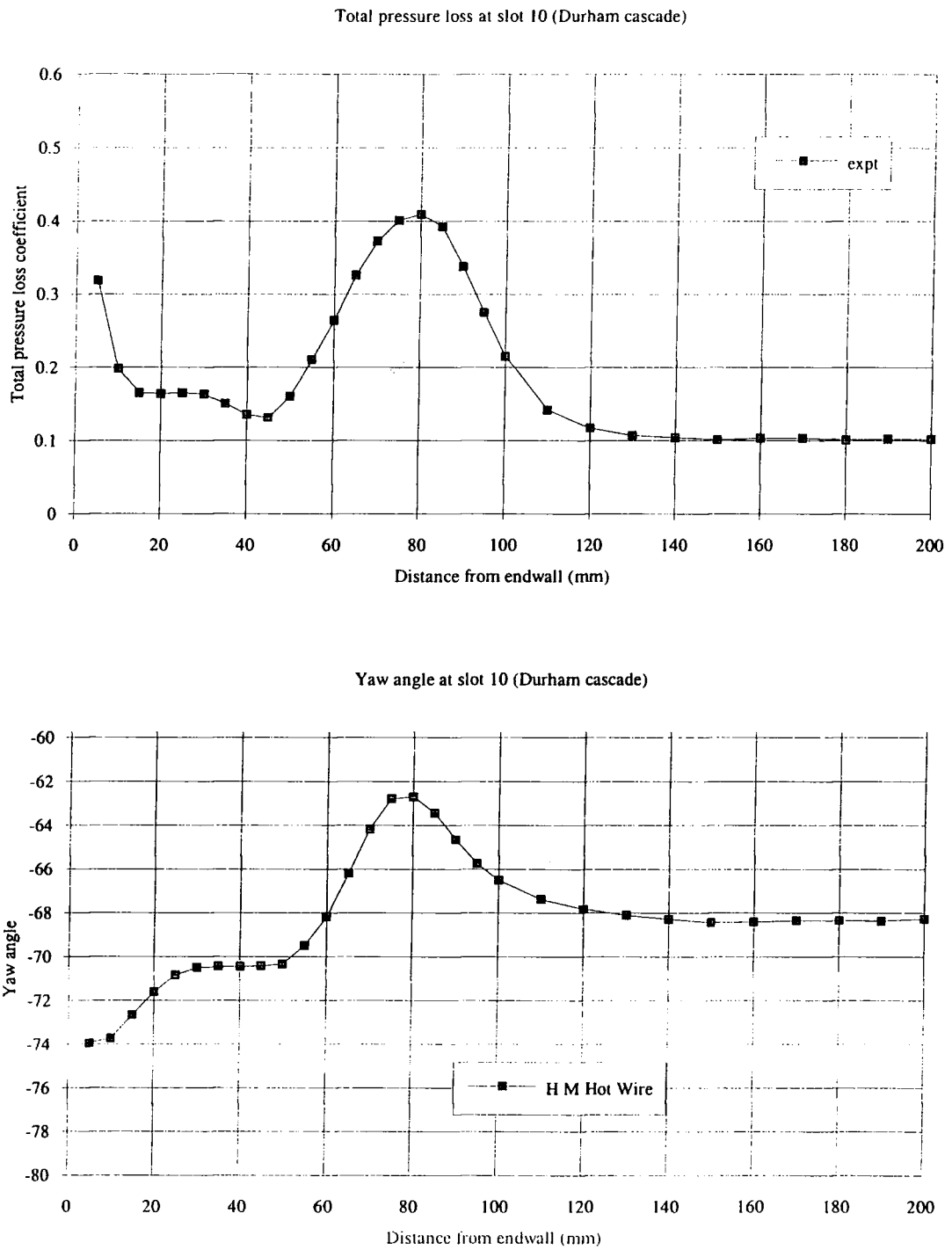

Figure 2.4— Typical spanwise exit angle and total pressure distribution (Moore and Gregory-Smith)

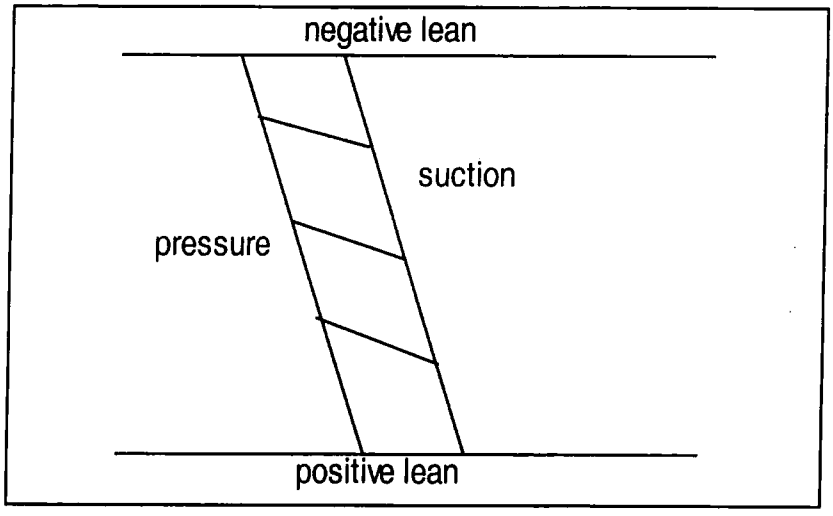

Straight tangential lean

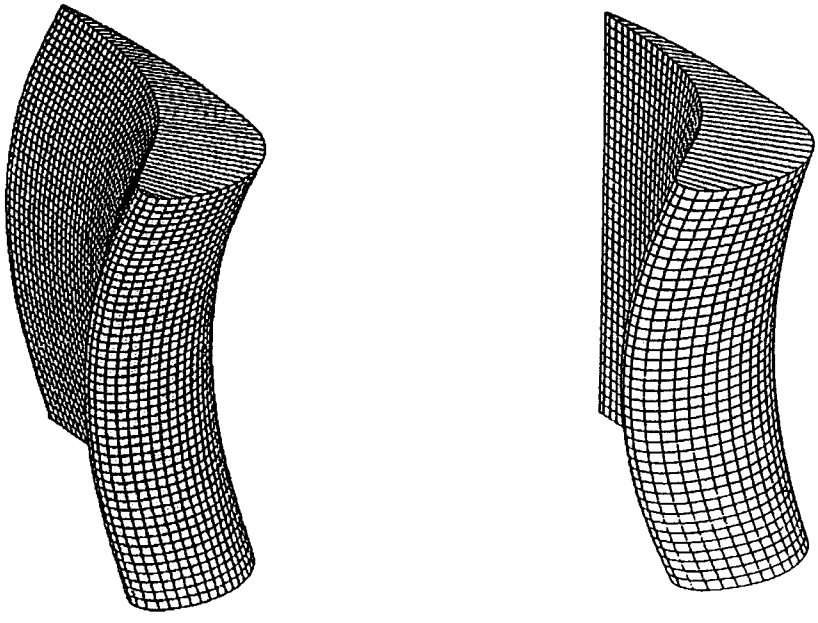

Compound lean **Controlled flow**

Figure 2.5—3-D Optimisation of blade profile

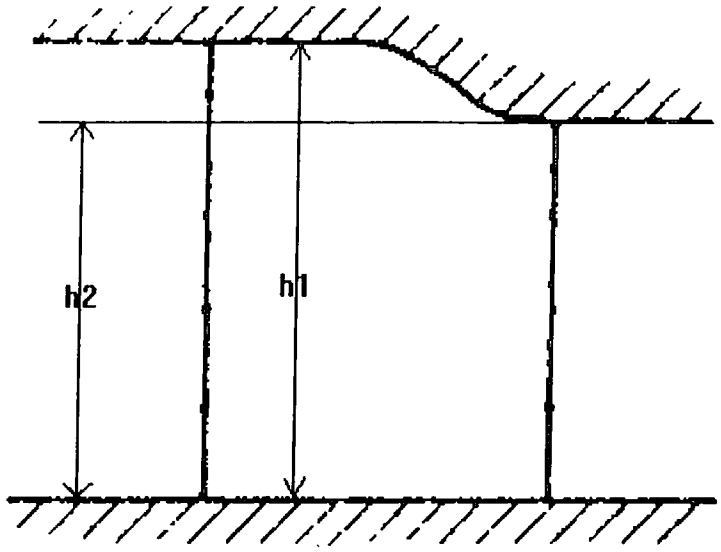

Figure 2.6— Profiled end wall contour (from Deich[1960])

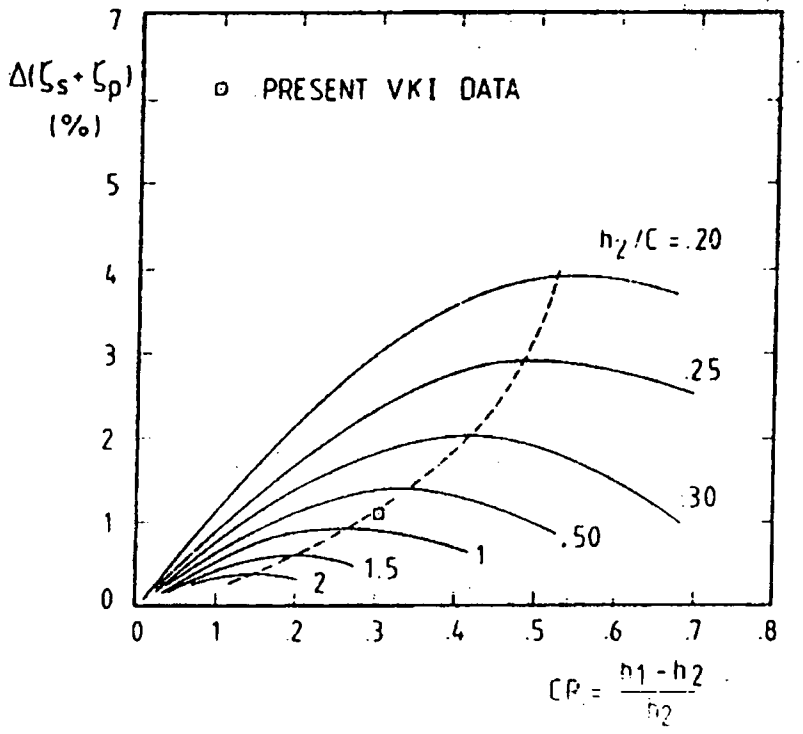

Figure 2.7—Loss reduction with tip contouring according to Deich [1960]
(CP=(h1-h2)/h2 is the constriction ratio

Chapter 3

Experimental Apparatus

Using a model of a nozzle blade from ALSTOM Energy Ltd, a cascade and connection section to the wind tunnel were designed and manufactured. In order to simulate the inlet condition of a real turbine a turbulence generating grid was installed upstream the cascade. A set of traverse gear and data acquisition system was set up. Five hole probes were designed and calibrated for the traverses. For the periodicity of the cascade, flow control units like tailboards were fitted to the cascade.

3.1 Cascade

The air supply of the new cascade is a large, low speed, blowing wind tunnel. A variable speed motor (Fuller KB25) drives a double entry centrifugal fan (Keith Blackman Series 28). Air from the fan passes through a short parallel wall section and then enters a large chamber through a diffuser. The flow is accelerated through a contraction section and a honeycomb flow straighter to the exit as a uniform high speed flow. In order to make a smooth connection, the first important thing in the design of the new cascade is to decide the number of blades.

3.1.1 Number of blades

The Nozzle Guide Vane blade from ALSTOM is shown in Fig 3.1. The details of the blade are given in Table 3.1. Its special shape accelerates the flow very rapidly through the passage.

Table 3.1—The blade configuration at the hub

Axial chord (c_{ax}),mm	Chord (c),mm	Pitch (s),mm	inlet angle	Outlet angle	throat mm	s/c	s/c_{axial}
92.55	136.54	85.09	0o	77o	20	0.623	0.919

The dimension of the wind tunnel exit is 700 mm x 460 mm. Three different plans for the cascade are given below in table 3.2.

Table 3.2—Geometry selections

Blades Number	Pitch(mm) s	Chord(mm) c	Axial Chord(mm) c_{axial}	Throat(mm)
5	175	280.82	190.35	41.18
6	140	224.65	152.28	32.94
7	116.7	187.26	126.93	27.46

From above table the best choice for the future cascade is the one with six blades. It has a large chord, which is 224.65 mm, and six blades is sufficient for the periodicity of experiments. Six blades also give a central passage which will be used predominantly for gathering the experimental data. The periodicity of the cascade means that in the different passages tested the flow field should be same. Thus the cascade design below is derived on the basis of six blades. The blade span is 400 mm except four test blades which are designed 5% longer in order to fit different end wall profiles.

3.1.2 The blades

The metal master blade was made at ALSTOM. By using this master blade, all test blades were cast in epoxy resin. The blade was cast in such a way that the blade is very slightly twisted along the span. Near the leading and trailing edges of the blade, there were cavities. There were also some bubbles on the blade suction surface. All these faults involved a lot of work to make the blade surface smooth and to get rid of the cavities. Because this work was done by hand, the blade shape repeatability is not perfect. This obviously affected the cascade periodicity slightly. It is suggested that the blades should be manufactured by a CNC machine. In order to locate the blades at the correct stagger angle in the cascade box, full scale blade profiles were plotted from the CAD and fixed to the end wall as shown in Fig. 3.2. The two blades that form the central passage were instrumented with surface static pressure tappings by casting hypodermic tubing under the surface running in the spanwise direction as shown in Fig 3.1. One blade has more tappings on the suction surface and another one has more tappings on the pressure surface. This tappings arrangement ensures that the test passage has more tappings. The tappings were drilled at appropriate spanwise distances from one end wall. When the tappings were not used, the holes on the surface of the blade were covered by thin plastic tape to preserve their integrity. The hypodermic tubing was led out through the end wall on which the blades are bolted, and could then be connected via plastic tubing to an inclined multitube manometer.

A steel spine as shown in Fig 3.2 was also cast into the blades in order to give stiffness to the blade since a cantilever mounting was being used. A stud was fitted into the internal surface of the solid end wall and another was fitted onto the top of the outer surface of the wall. This steel structure reinforces the supporting ability of the end wall.

3.1.3 The overall dimensions of the cascade.

The longer edge (H1) in Fig. 3.3 of cascade is usually decided by the last down stream traversing plane. The traversing plane is usually 20%-30% axial chord downstream from the trailing edge plane where the next blade row starts in a real turbine.

H1=4×s tangential width + 0.5×s +c×Cos (exit angle of flow)+100

=1125.27mm

H1 is then decided to be 1130 mm as shown in Fig. 3.3.

The shorter edge of the cascade is H2:

H2=5×140+tangential width+100

=976.95mm

H2 is then decided to be 990 mm as shown in Fig. 3.3.

The axial width of the cascade is affected by the axial chord of the blade, flow exit angle and the last slot position.

$$W = c_{axial} + \frac{3}{4} \times c \times \cos 77^{\circ} + 115$$

$$= 320mm$$

The cascade width then was chosen to be 320 mm. Since the blades are effectively supported by only one end wall it was constructed from 44 mm hardwood cored blockboard. The rest of the cascade box was manufactured from timber and 17 mm plywood. On the top of the cascade box, there are two steel bars which hold the cascade together and balance the extra force from the weight of the traverse gear.

3.1.4 Traversing slots and cascade axis system.

There were eleven traversing slots cut into the thick end wall of the cascade box. One of them is made horizontal so as to measure the decay of turbulence upstream. Its centre

is situated 89% axial chord upstream from the leading edge. The positions of other ten vertical slots are related to axial chord as shown in Fig. 3.4 and Table 3.3. The cascade axis system is also shown in Fig. 3.4. Positive spanwise direction was set to be away from the end wall.

The length of the slot 2 is 220 mm. The length of slot 9 and slot 10 are both 250 mm as shown in Fig. 3.4. They are designed to cover the wakes of two blades that form the passage to be measured. The horizontal slot is 202 mm long. The length of slots between the suction and pressure surface of the test passage is limited by the space at the local position. This makes slot 8 the shortest slot. Every slot not being used is covered by a T-shape wood filler which was manufactured to present a smooth end wall surface to the flow. The slot in use was sealed by two pieces of rubber door seal. In order to move a pressure probe freely between the two rubber seals, Vaseline was spread on the surface of the seals.

Table 3.3 Slot position

Slot No.	1	2	3	4	5	6	7	8	9	10
$\frac{x}{C_{ax}}(\%)$	-75	-13	3.3	25	50	70	85	97	113	126

3.1.5 Window

A window was cut on one side of cascade. The window size is 500 mm by 230 mm. It allows the perspex window to be fitted into it. The perspex window is made for the flow visualisation and to measure static pressure on the flat end wall. The window also allows the profiled end wall to be inserted there. The window position and size are shown in Fig. 3.5. The inter-blade sections of the perspex and the profiled end wall

were cut to fit closely around the four longer blades. This was achieved by using a CNC milling machine. However, there was still a gap between the blade and the perspex. This gap was then filled by silicone sealant. Holes for static pressure tappings were manufactured by CNC milling machine. Hypodermic tubing was glued into the holes in such a way that the end of hypodermic tubing was exactly at the same level of the internal surface of the perspex. The hypodermic tubing was connected via plastic tubing to a multitube manometer. The distribution of the static pressure tappings is shown in Fig. 3.5. All the dimensions are in mm.

3.1.6 Turbulence generation grid.

The level of free stream turbulence that develops naturally in most wind tunnels is far less than in a real turbine. In order to simulate the real flow conditions a turbulence grid was placed upstream of the cascade to increase turbulence intensity. The increased turbulence intensity can promote earlier transition of boundary layers and eliminate the separation bubble on the suction surface. According to later experiments, there was still a separation bubble on the suction surface. Transition trips were then fitted onto the suction surfaces of the blades. The trips eliminated the separation successfully.

The design of the grid was based upon data from the paper by Bains and Peterson (1950). A grid of 25 mm diameter bars was selected. The bars were mounted parallel to the cascade at a spacing of 100 mm in the horizontal direction. The bars in the vertical direction were designed to be adjustable in order to get the required inlet boundary layer profile across the span. The distance between the grid and cascade inlet is 1200 mm so as to obtain a uniform turbulence distribution and a 5% turbulence intensity at inlet. The design conditions at inlet to the cascade have been estimated with the method of Roach (1986) as shown in Table 3.4.

Table 3.4—Turbulence level at inlet

	Streamwise direction	Orthogonal direction
Turbulence Intensity at inlet	5%	4.5%
Macro/Integral scale	34mm	17mm
Micro/Dissipation Scale	5.2mm	3.7mm
Turbulence Intensity at Slot 1.	5.4%	4.8%

Apart from the main turbulence generating bar, a small bar (12.7 mm OD) was fitted 24 mm from the side wall in the gap between the side wall and the last bar. This small bar has proved to be essential to achieve the desired inlet boundary layer profile as shown in Fig. 3.6. Without the small extra bar, the inlet velocity profile has a bump near the end wall. This was thought to be the result of the bigger gap between bars and the end wall. After the small bar had been installed, the inlet boundary presented the desired profile.

Two slots are designed 400 mm upstream of the leading edge of the cascade on the top and bottom of the connection section. These two slots allow another grid to be installed to generate the spanwise inlet total pressure profile the same as the inlet total pressure profile which was obtained from model turbine tests at ALSTOM. However, this investigation was not carried out.

3.1.7 False side wall and other details

The inlet boundary layer thickness is decided by the Reynolds number and false wall length. The exit Reynolds number of cascade is chosen to be $5x10^5$ based on chord and $7.3x10^4$ based on throat according to the conditions produced by the Durham wind

tunnel. Therefore the inlet velocity is about 9m/s. Compared to the real steam turbine, which has a Reynolds number around 10^7, the cascade Reynolds number is quite low. The length of the false side wall is 800 mm. Therefore the inlet boundary layer thickness of cascade could be calculated.

The dimension of the inlet of the cascade is 700x400 mm. The exit of the Durham wind tunnel is 700x460 mm. Therefore there is a clearance between the false side wall and upstream wind tunnel side wall. This clearance can bleed off the upstream boundary layer. In order to obtain an equal pressure at both sides of the leading edge of the false side wall a bracket is mounted there as shown in Fig. 3.7. By adjusting the clearance between the false side wall and upstream side wall the incidence onto the leading edge of the false side wall can be made zero. This can be checked by two pressure tappings on either sides of the wall, as shown in Fig. 3.7.

3.1.8 The periodicity of the cascade.

The periodicity of the blade passages is required so that the exit flow property of every passage should be periodic. According to the design of the cascade there are six blades. The periodicity will be poor at both ends of the cascade unless some form of downstream flow control is included. There are several methods to control the flow. They are End Injection, Bleed & Feed and Tailboards.

In End Injection, air from the plenum chamber is injected into the discharge flow at the trailing edge of one end blade, as shown in Fig. 3.8. It is believed the injected flow has two effects, first, to force the cascade discharge flow to a different discharge angle, and second to feed the entrainment vortex between the discharge flow and plenum chamber top.

Bleed & Feed is developed for blades with high turning and consequently high passage contraction, shown in Fig. 3.9.

movement of the probe and another one controls the radial movement. On the end of each slide, a 400 half-steps/rev stepper motor is fitted to generate the movements. The step of the motor is 1.8° which gives a resolution of 0.005 mm. There is one rotary table mounted on the two unislides. The rotary table (Time and Precision A375TS) holds the probe and is driven by a 200 step per revolution step motor with a 90:1 gear ratio which gives an angular resolution of 0.02 °. Every motor is driven by a 4 phase bipolar driver board (RS 342-501) which is in turn controlled by a 48 channel Input/Output board (Amplicon Liveline PC14AT) installed in the computer.

3.2.2 Data acquisition system

A pitot-static probe and a five hole probe are used to collect data and transfer it to the computer.

Probes

The pitot-static probe is installed 700 mm upstream from the leading edge of the blades on the side wall of the connection section as shown in Fig. 3.3. It is used to measure the upstream dynamic pressure and total pressure. The five hole probe is mounted on the rotary table to investigate the flow field. Different shaped probes were investigated. The cobra head probe as shown in Fig. 3.13 turned out to be the best choice. However, for slot 2 which is just upstream of the leading edge of the blades, the cobra probe is too big to be used. Another small headed probe, as shown in Fig. 3.14, was made to traverse slot 2. As shown in the Fig. 3.13, the stem of the probe is 10 mm (OD). This is too big for some short slots such as slot 8. The blockage effect will be seen in the experimental results at slot 8. But due to the manufacture ability in the workshop, this is not improved.

The probe was calibrated by the same method as that of Treaster & Yocum (1979). Because the five hole probe was used in quite a big dynamic pressure range (50-800 Pa),

movement of the probe and another one controls the radial movement. On the end of each slide, a 400 half-steps/rev stepper motor is fitted to generate the movements. The step of the motor is 1.8° which gives a resolution of 0.005 mm. There is one rotary table mounted on the two unislides. The rotary table (Time and Precision A375TS) holds the probe and is driven by a 200 step per revolution step motor with a 90:1 gear ratio which gives an angular resolution of 0.02 °. Every motor is driven by a 4 phase bipolar driver board (RS 342-501) which is in turn controlled by a 48 channel Input/Output board (Amplicon Liveline PC14AT) installed in the computer.

3.2.2 Data acquisition system

A pitot-static probe and a five hole probe are used to collect data and transfer it to the computer.

Probes

The pitot-static probe is installed 700 mm upstream from the leading edge of the blades on the side wall of the connection section as shown in Fig. 3.3. It is used to measure the upstream dynamic pressure and total pressure. The five hole probe is mounted on the rotary table to investigate the flow field. Different shaped probes were investigated. The cobra head probe as shown in Fig. 3.13 turned out to be the best choice. However, for slot 2 which is just upstream of the leading edge of the blades, the cobra probe is too big to be used. Another small headed probe, as shown in Fig. 3.14, was made to traverse slot 2. As shown in the Fig. 3.13, the stem of the probe is 10 mm (OD). This is too big for some short slot such as slot 8. The blockage effect will be seen in the experimental results at slot 8. But due to the manufacture ability in the workshop, this is not improved.

The probe was calibrated by the same method as that of Treaster & Yocum (1979). Because the five hole probe was used in quite a big dynamic pressure range (50-800 Pa),

the probe was calibrated at two different dynamic pressures 100 Pa and 800 Pa. Calibration maps of those two conditions show little difference. However, the calibration map at the higher pressure turns out to be more smooth. The reason is that the background disturbance is relatively smaller than at low dynamic pressure. The Reynolds number of the probe is varying from 0.27×10^4—1.07×10^4 while the probe is moved from the inlet to the exit. According to Dominy (1992), the sensitive Reynolds number range is between 2×10^4 and 5×10^4. Apparently the Reynolds number of the probe is not within the sensitive Reynolds number range. Therefore the Reynolds number effect is negligible as confirmed by the calibration maps at high & low dynamic pressure. The calibration map is shown in Fig. 3.15. The calibration was carried out at a step of 2.5^0 angular change in pitch and yaw direction.

Transducers

The transducers (CMR CONTROLS 200-013 P-sensor) are able to measure 0-2000 Pa pressure range with 0-10 Volt linear output. Four of these are connected to the four side holes and centre hole of the probe. One transducer, with a range of ±200 Pa, is connected to the centre hole of the five hole probe and the total pressure hole of the upstream pitot-static probe. One transducer with a range of 0-500 Pa is connected to the two holes of the upstream pitot-static probe. The connection map is shown as in Fig. 3.16. All the transducers were calibrated by the manufacturer before any test was done. The calibrations were checked during the investigations. The transducers are connected to a Analog to Digital (A/D) converter. The A/D converter has 12 bit resolution and takes a ±5 V input. The standard card (PC-LabCard PCL-812PG) samples 16 channels at speeds of up to 30KHz. Only six of the channels are used, one to monitor the inlet dynamic head and others to take readings from the five hole probe.

Software

A set of C programs were written to control the movement of the traverse gear and collect the data. The detail of the program has been given by Biesinger (1993). The pitot-static probe was used for collecting data for ten seconds. Data was recorded at 3 kHz. The ten seconds data are shown in Fig. 3.17. It is seen the fluctuation of pressure is recorded and at least one period is obtained. Thus the sampling time is set to be ten seconds. The data collected in this ten seconds is time averaged by the program.

To ensure the consistency of the results, experiments were always carried out at the same Reynolds number defined by the exit velocity and blade chord. In a question and answer interface, the atmospheric condition were input into the computer. Using a standard day set of conditions, the dynamic head for setting the tunnel was calculated and shown on the screen. The controlling program and grid input file were written in such a way that the probe was always traversed away from the opposite end wall in the spanwise direction for each tangential position. For every slot, the probe was set to the approximate mid-span flow angle in order to minimise the force presented by flow on the probe head. This also ensured that the flow angle was always within the central part of the probe calibration region. The standard day condition for this cascade is shown in Table 3.5.

Table 3.5 Standard day conditions

Atmospheric temperature	Atmospheric pressure	Air viscosity
17°	776 mm. Hg	1.5×10^{-5} mPa·s

The final results of position, five pressures and dynamic head were stored onto the hard disk. After being transferred to the UNIX system, the data was analysed by a program written in FORTRAN. The yaw angle, pitch angle, local velocity, total pressure and

static pressure were all obtained for every traversing point from the calibration map. Static pressure and total pressure coefficient were calculated as shown in Appendix 1. Secondary velocity components and secondary kinetic energy for every slot were calculated. Pitch mass averaged values were obtained by integrating in the tangential direction across the pitch. An area average was obtained for the axial plane by integrating the pitch averaged values in the spanwise direction as shown in Appendix 1.

3.2.3 Experimental accuracy

It is important to make the experimental error as small as possible. Many steps were taken to ensure that the errors were minimised at each link in the chain that formed the experiments. The probes were calibrated in the small steps. The mounted traverse gear was carefully and checked by a spirit level. The position of the probes was made relative to the end wall to within 0.5 mm. For the shaped end wall, start positions were checked at every tangential position. The turret setting angle was calibrated in the far upstream and also recovered by the analysis program. The recovery method is to check the flow rate at each slot against the upstream slot. Each tubing connection was checked.

Although reasonable care has been taken to minimise errors during the experiments, it is necessary to attempt to determine the uncertainty of the results. The positional accuracy of five hole probe in the flow field was estimated to be 0.1 mm in both radial and tangential direction. The probe angle was set as the mainstream flow angle at the mid-span. This allowed most of the measured points to be located in the centre of the calibration map so as to avoid the skewed boundary cells. Because the probe has been lined up with the main stream flow, the probe deflection under the dynamic force is minimised. Though during the test at upstream slots the yaw angle varies a lot, the velocity is quite low there. Therefore the aerodynamic force on the probe is still quite

small. The deflection of the probe is too little to be observed. There are a number of other sources of error, such as the alignment accuracy between traverse gear and cascade, the turbulence and Reynolds number effects. The yaw angle was then adjusted by checking the mass flow rate in the post processing. Thus the total error applicable to angle measurements could be as great as ±0.2°. The total pressure loss error is related with the systemic and random error of the transducer, A/D converter and the calibration error. A basic error assessment was done by Biesinger (1993). Because the same Furness transducer was used, by taking the maximum error the error of the total pressure loss coefficient is estimated to be ±0.005.

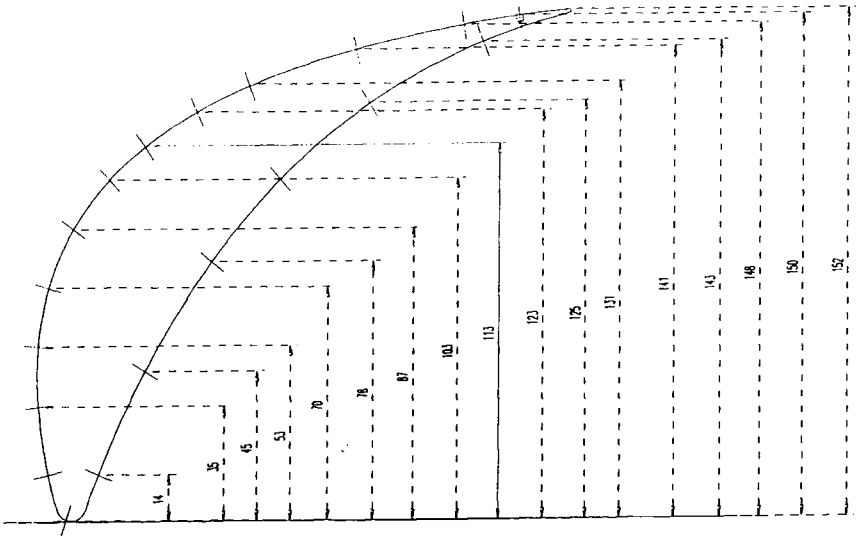

Note:The diameter of the tubes is 1.6mm

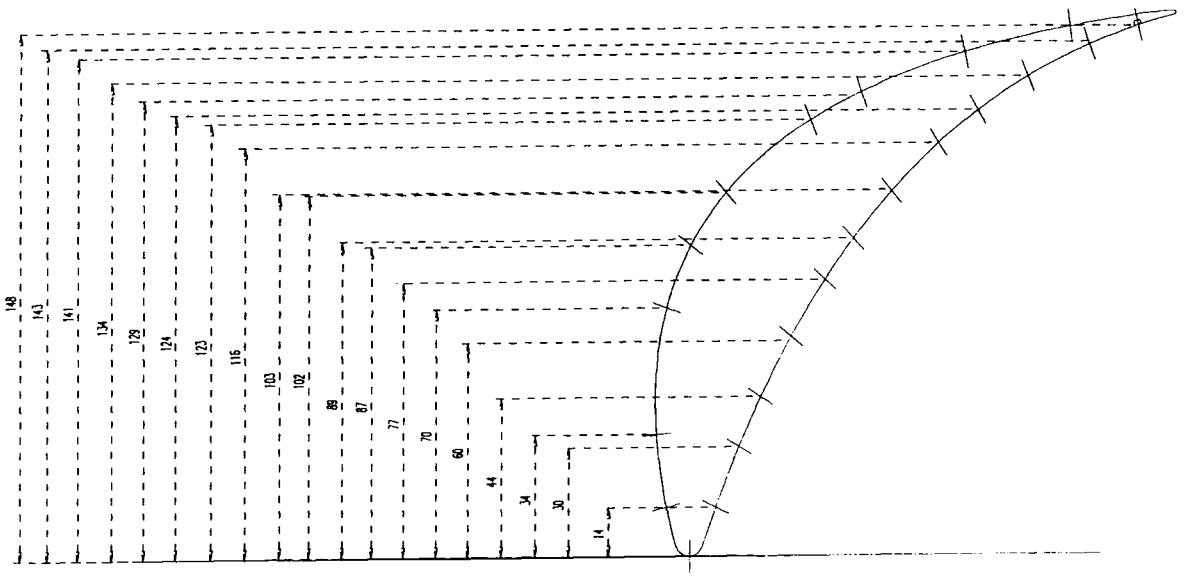

Fig 3.1 —Static pressure tappings on the blades

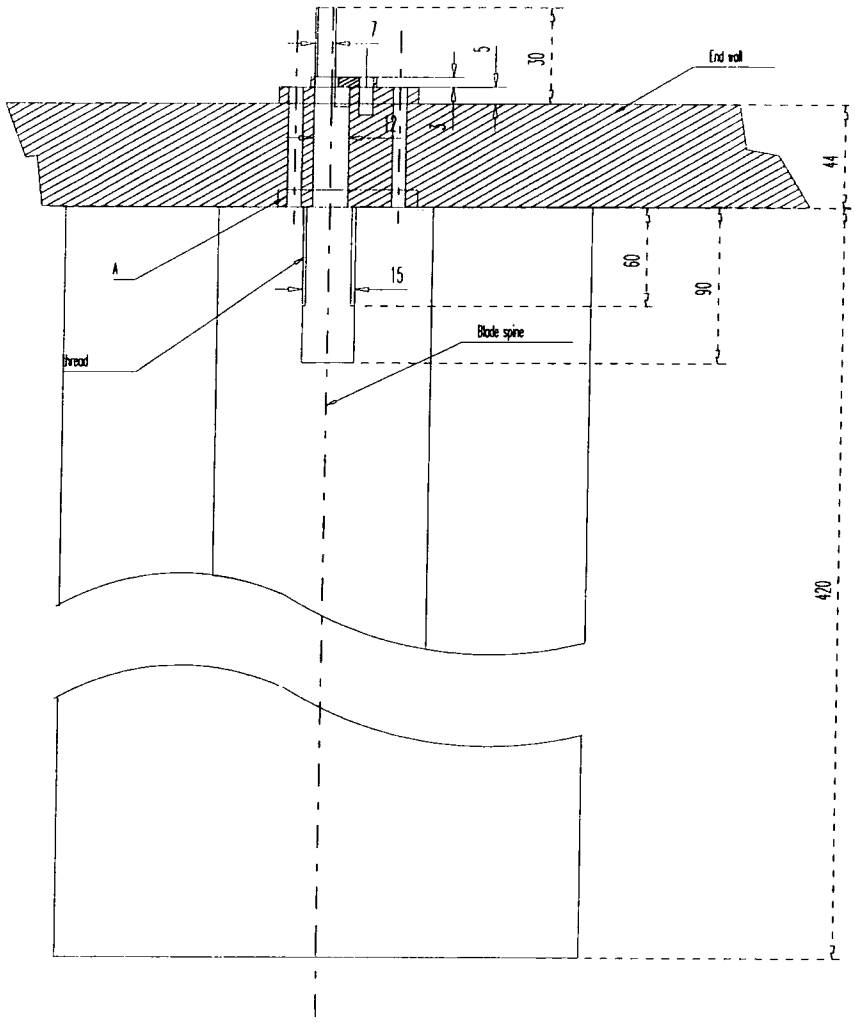

Fig 3.2 —The mounting of the blade

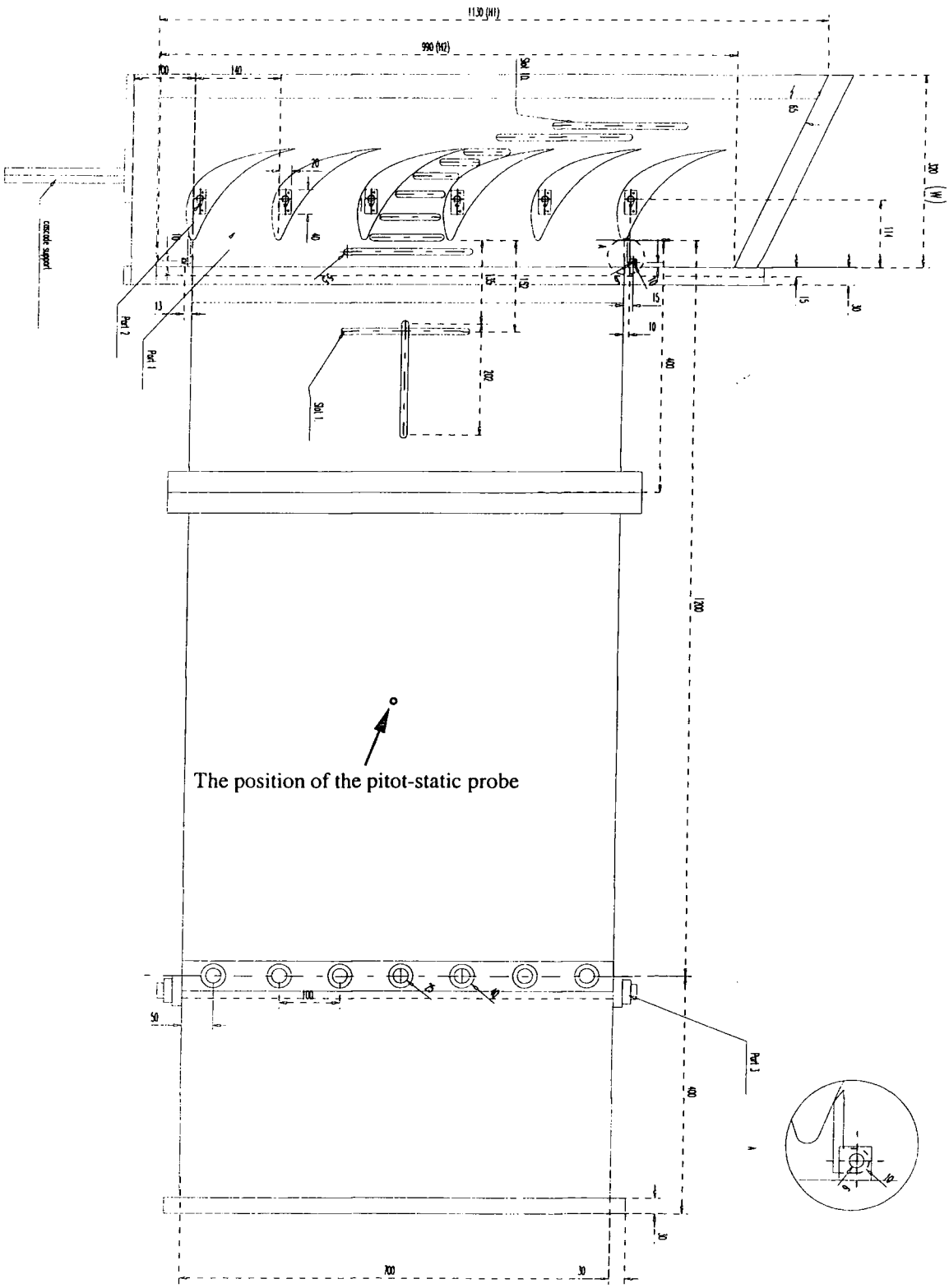

Fig 3.3 —The cascade

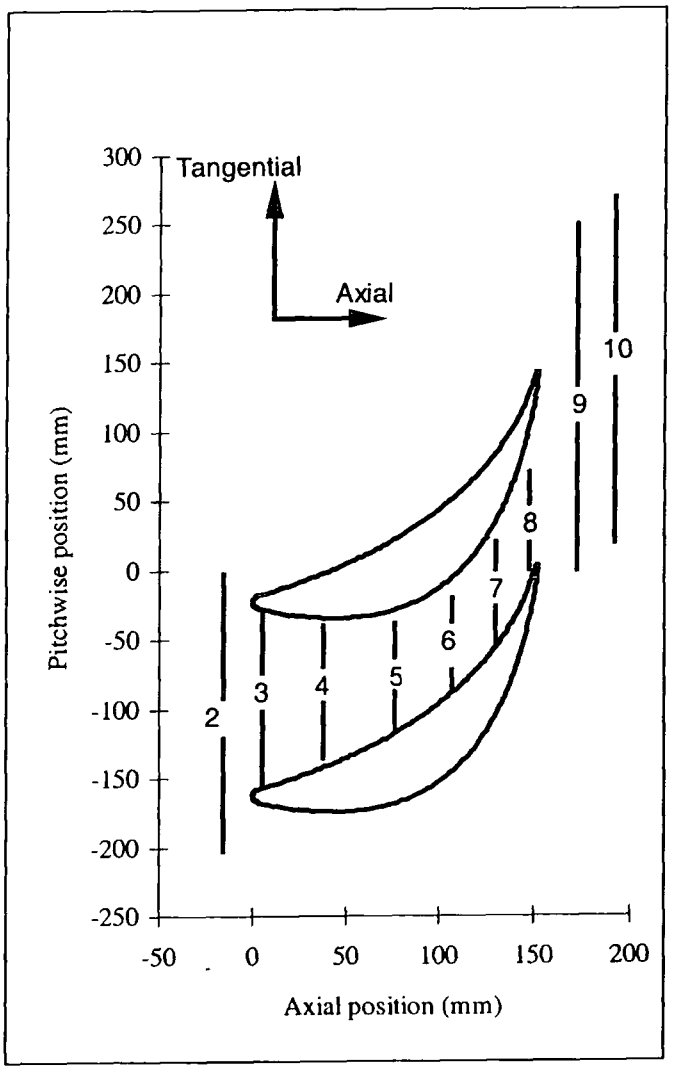

Fig 3.4—Slots distribution and cascade axis system

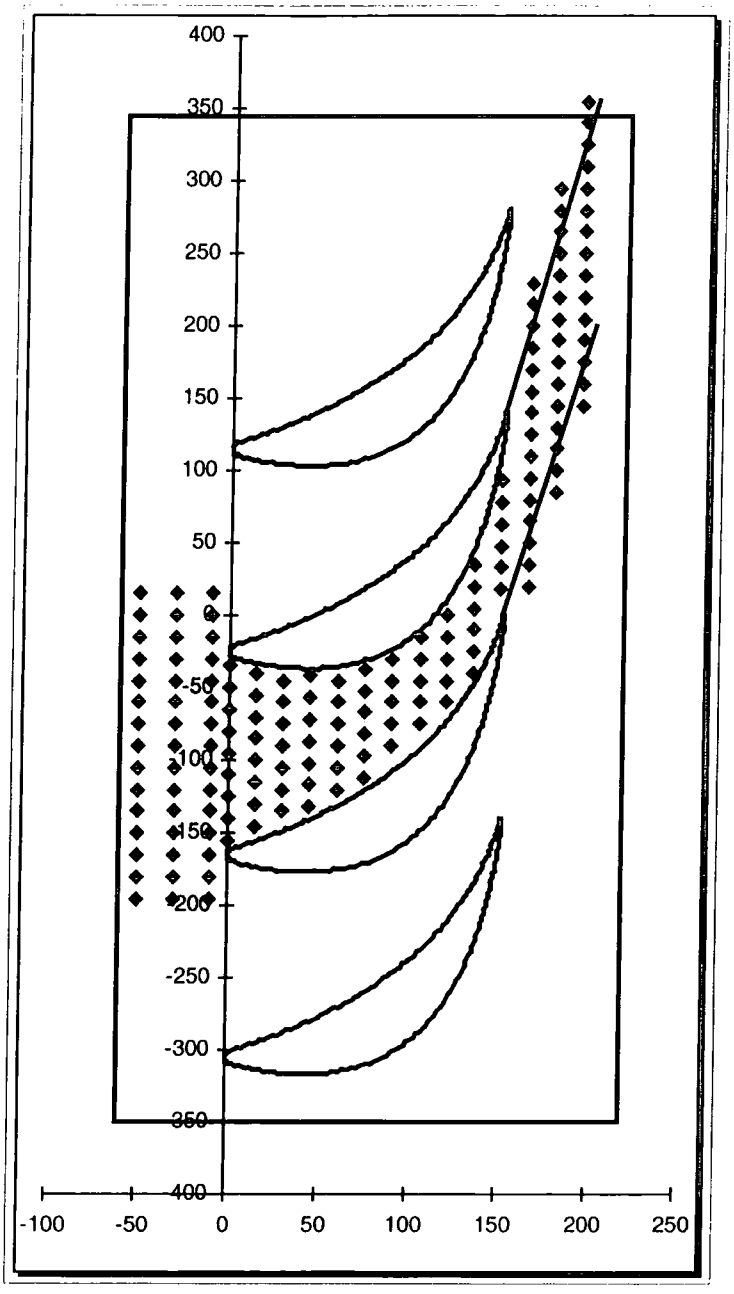

Fig 3.5—Static pressure tapping on the perspex window

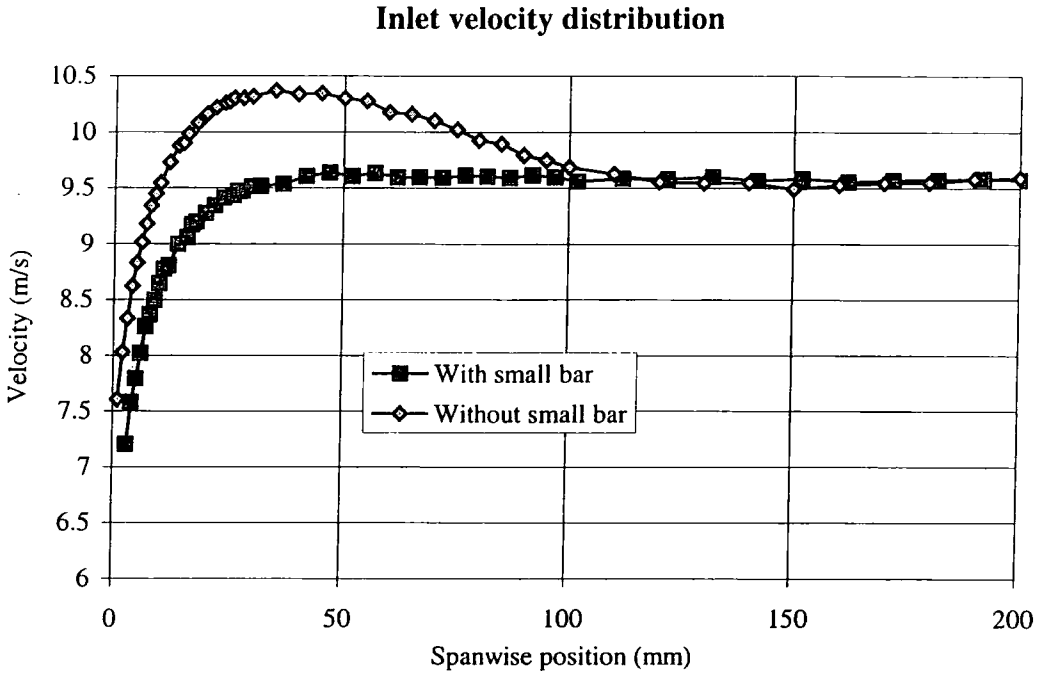

Fig 3.6 —Inlet boundary layer condition

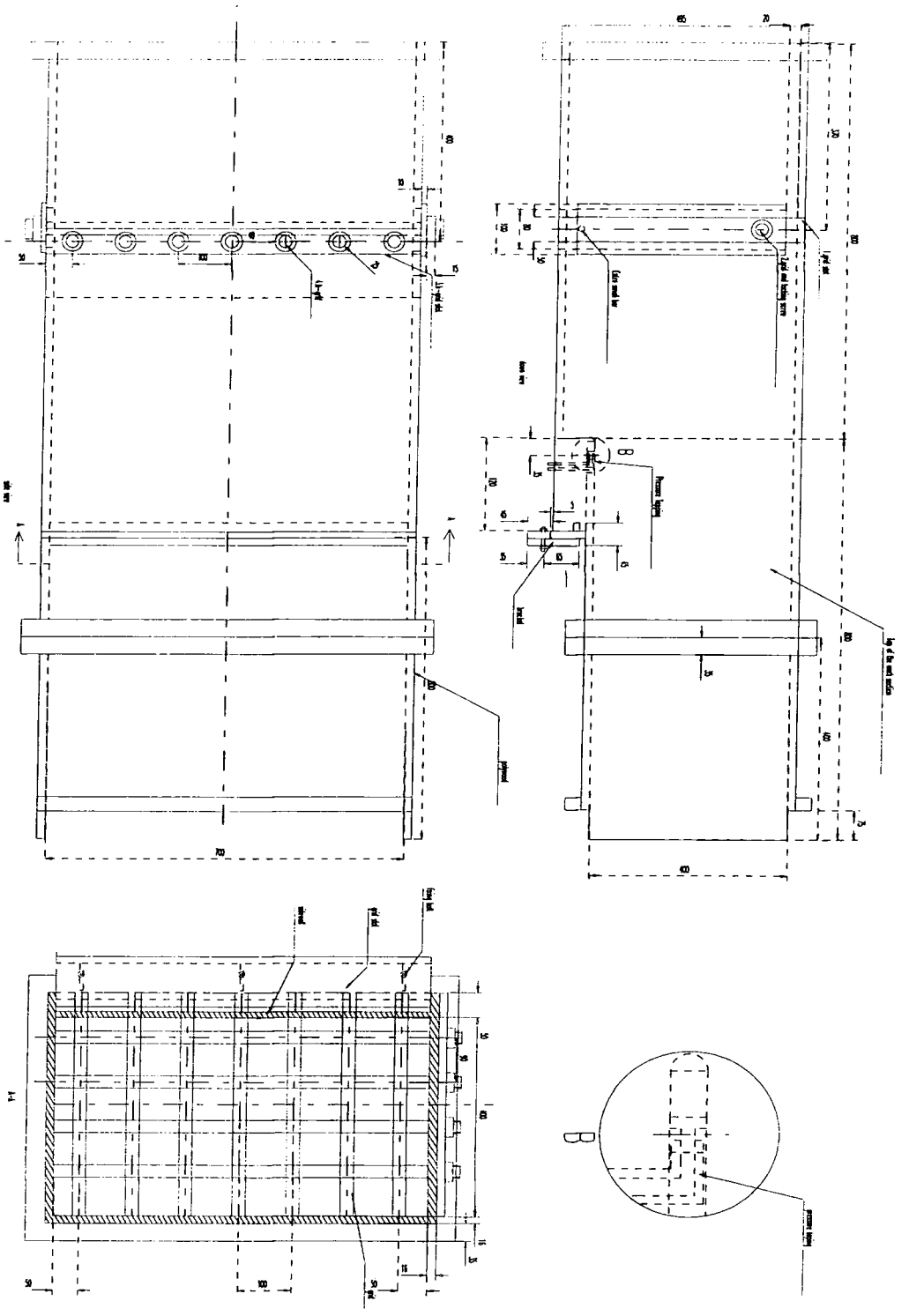

Fig 3.7—The connection to the wind tunnel

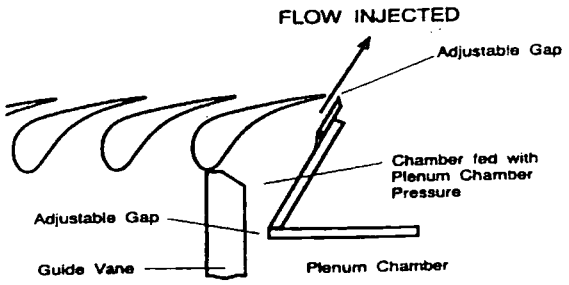

Fig 3.8—End injection

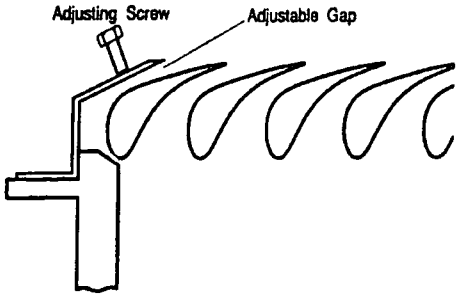

Fig 3.9—Bleed & Feed

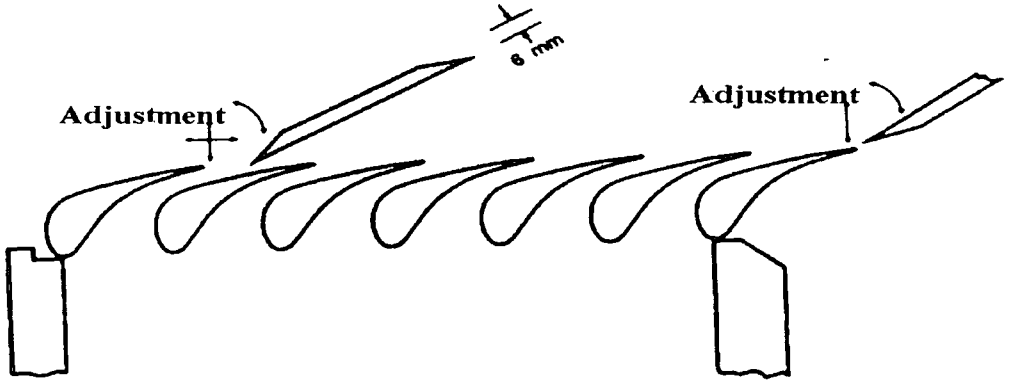

Fig 3.10—Tailboards

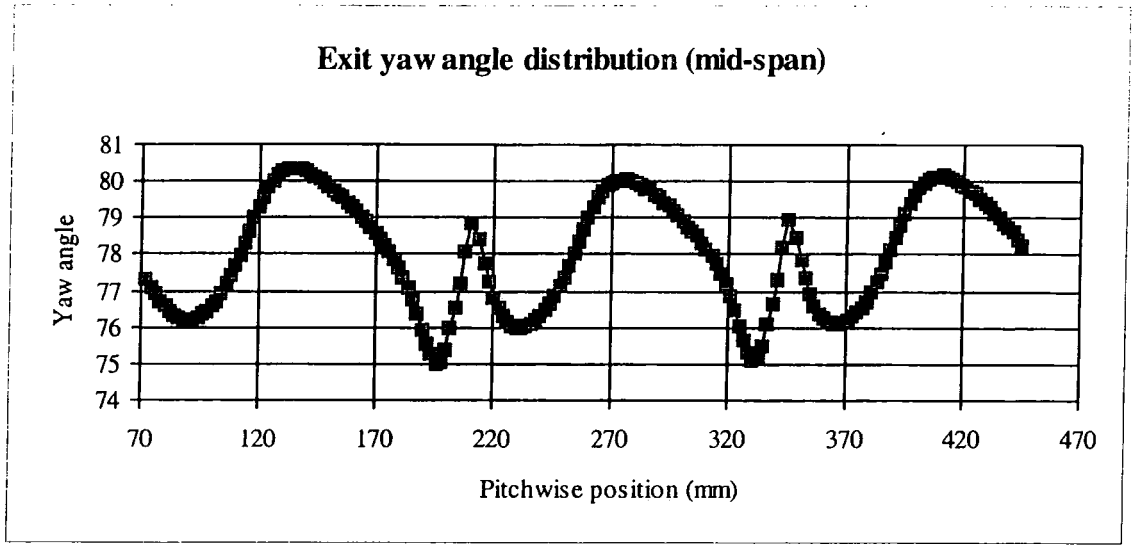

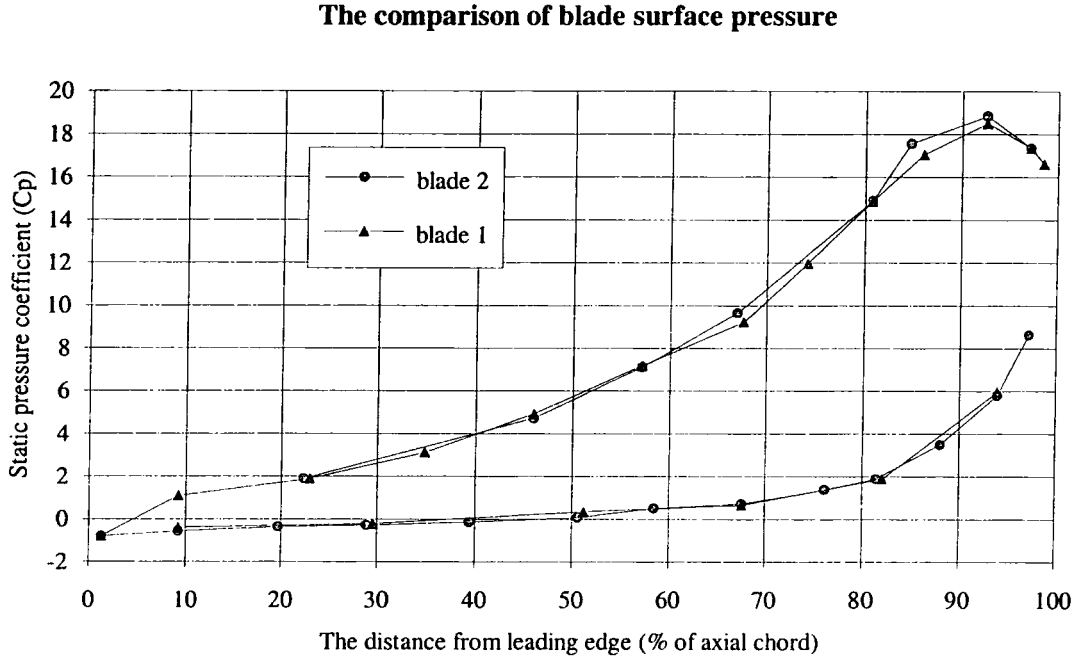

Fig 3.11—The periodicity investigations

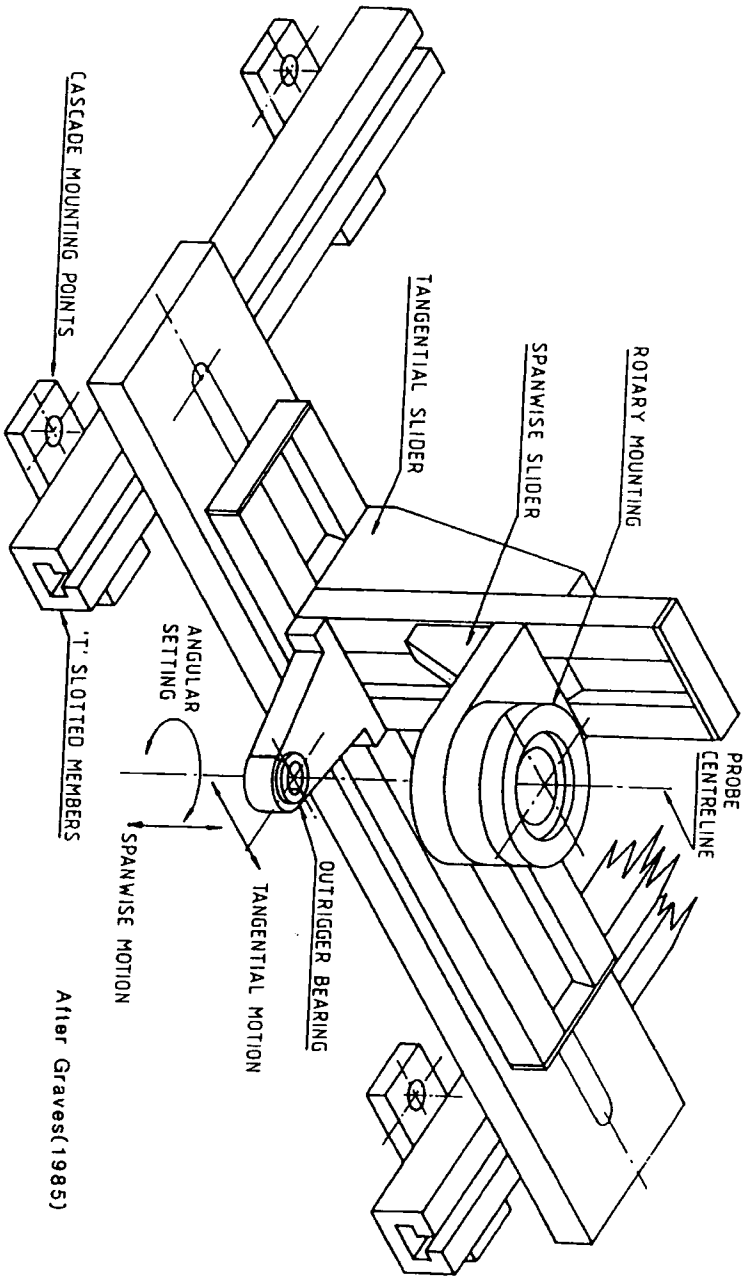

Fig 3.12—Traverse gear

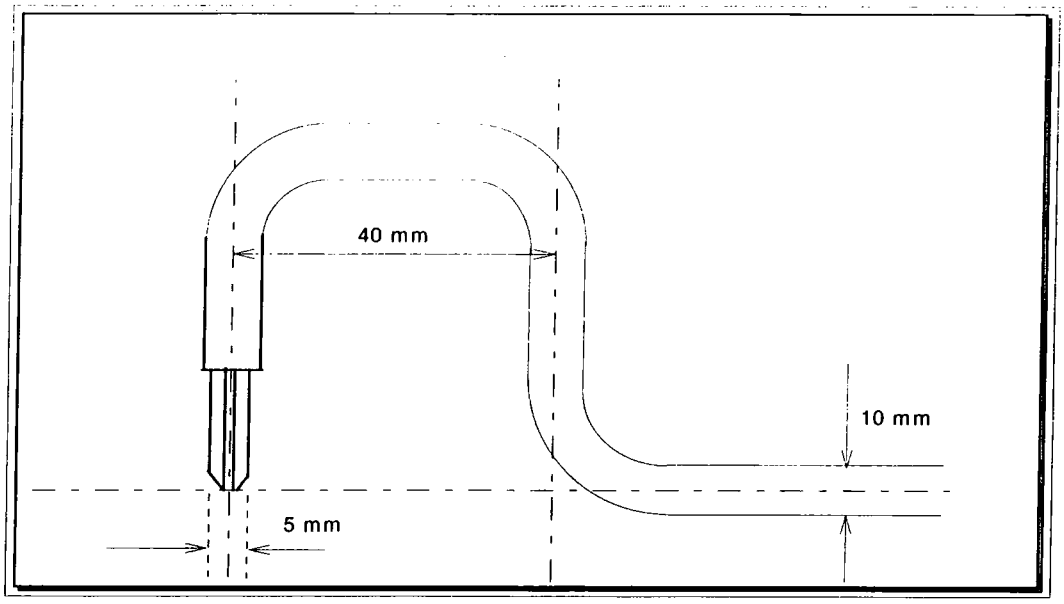

Fig 3.13—Cobra probe

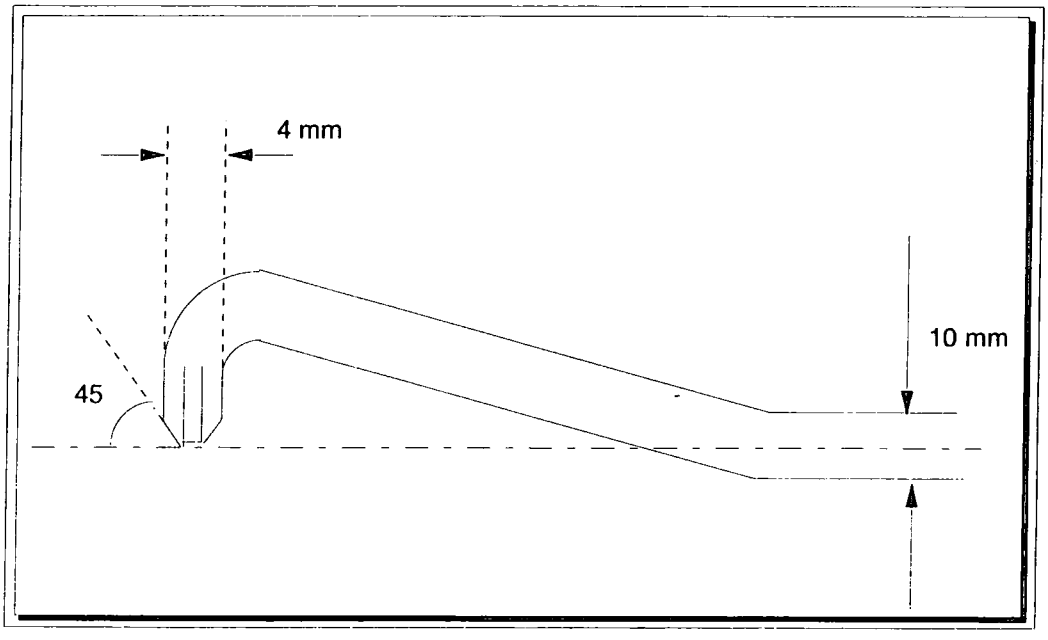

Fig 3.14—Small head probe

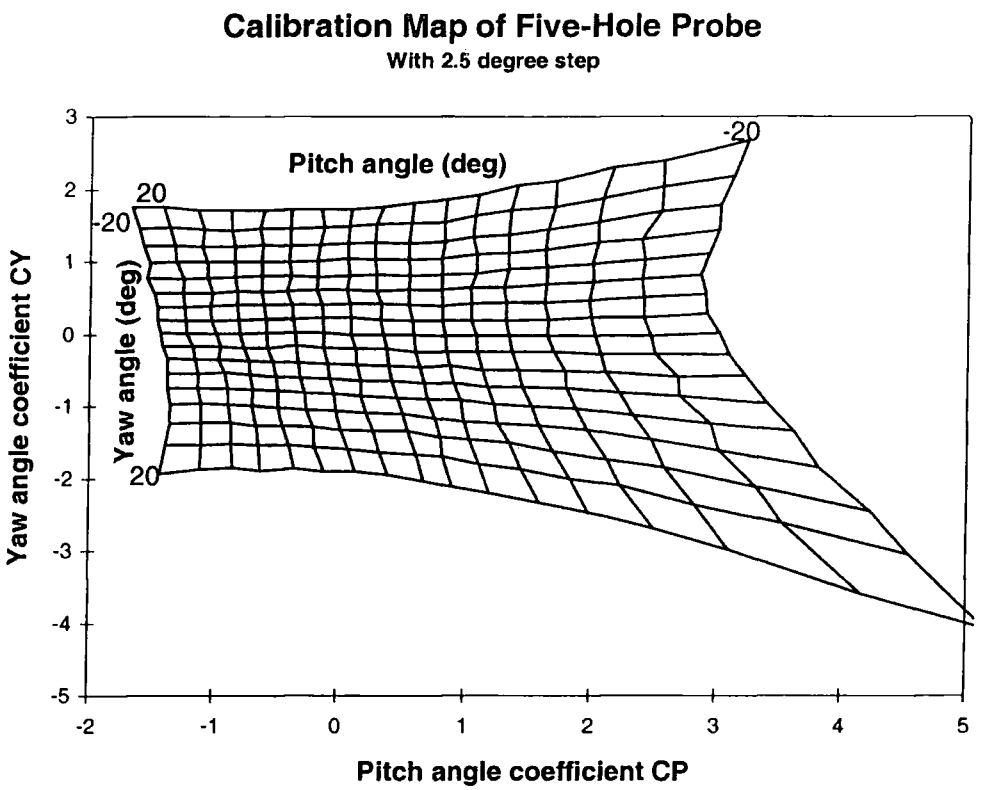

Fig 3.15—The calibration map of the cobra probe

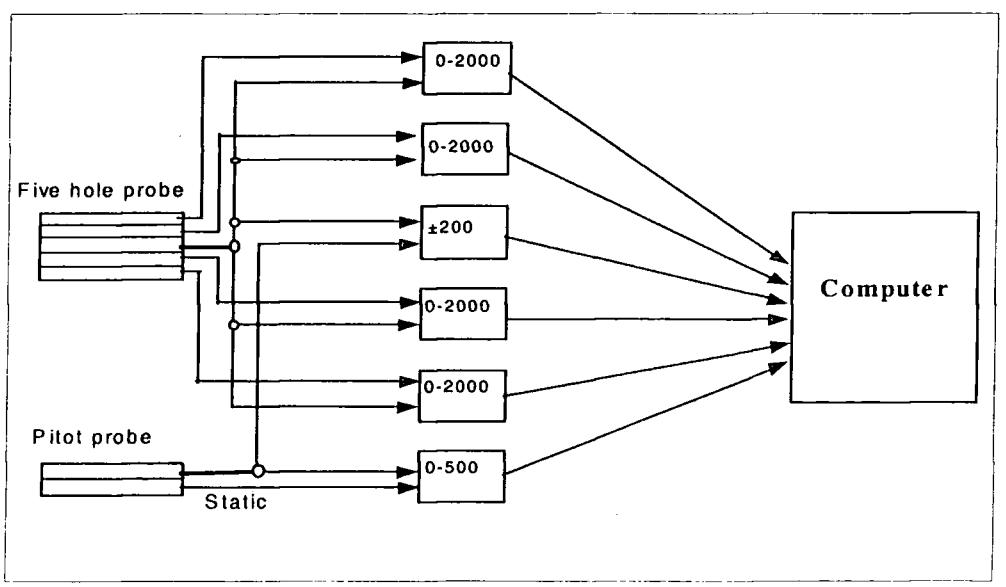

Fig 3.16 —The transducer and the probes

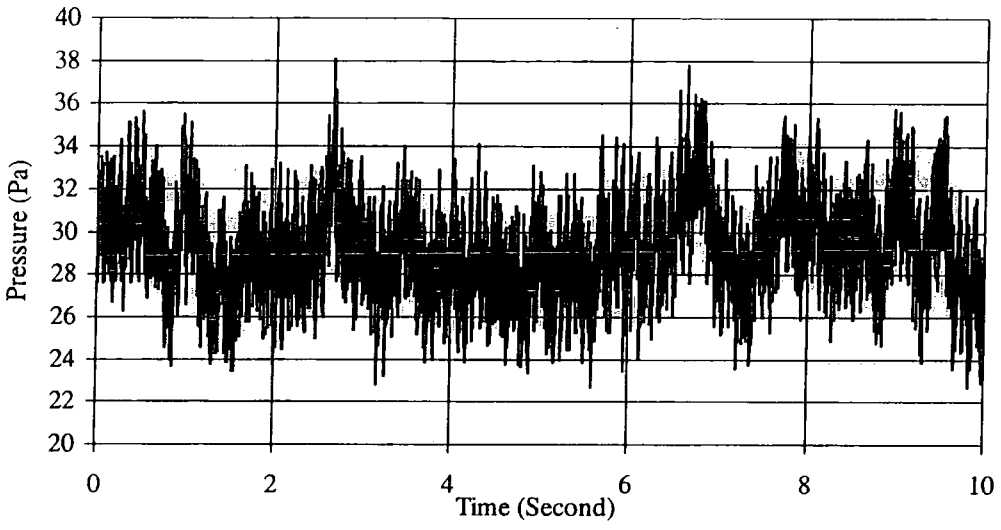

Fig 3.17 —The pressure measurements for ten seconds

Chapter 4

Experimental Results with Flat End wall

4.1 Introduction

Experiments were conducted with the flat end wall cascade. The flow field was investigated using a five hole probe, pressure tappings and flow visualisations. Every slot was traversed by a five hole probe. Transition trips were put onto the blade suction surfaces to stimulate the transition. Slot 8, 9 and 10 were traversed again with the trips in position. The raw data from five hole probe traverses was processed by a number of programs. Contours of total pressure loss, yaw angle distribution, pitch angle distribution and secondary kinetic energy are presented for every slot. A basic understanding of the total pressure losses and secondary flow development through the blade passage was obtained. The static pressures on the end wall and the blade surfaces were measured with the pressure tappings. Flow visualisations on the end wall and blade surfaces were conducted. The positions of the slots are shown in Fig. 3.4. The Cobra probe was used to investigate every slot except slot 2 which was traversed by the small head probe (see chapter 3).

The secondary velocity is defined according to the local velocity and mid-span velocity. In the linear cascade, the flow in the mid-span should be two-dimensional without secondary flow. The mid-span velocity is then treated as reference. The difference between the local velocity and the mid-span velocity is then defined as the secondary flow velocity. The plotting of the secondary vectors is slightly changed compared with the previous work by Gregory-Smith (1987). The new plot is the real projection of the secondary vector on the pitchwise direction instead of the enlarged cross flow component. The plot is shown in Fig. 4.1. This was done to make the vector plots clearer. The definition of the secondary kinetic energy is then obtained as the sum of the square of the secondary vector and the radial component of the velocity times half the density. This definition is much depended on the definition of the primary flow.

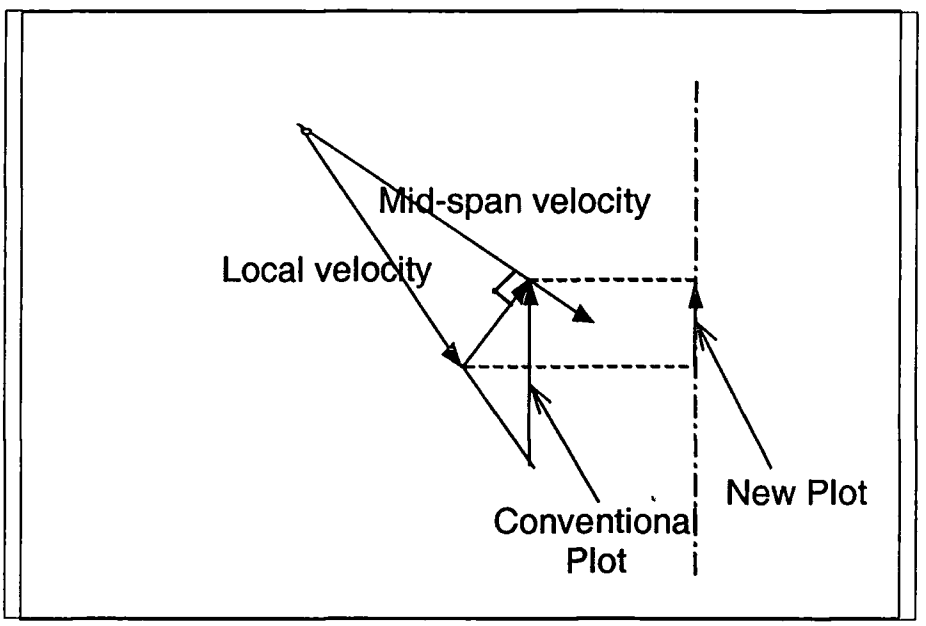

Figure 4.1—The definition of the secondary vector

4.2 Inlet boundary conditions

The inlet boundary condition is very important for the experiment and CFD. The inlet boundary layer was investigated by traversing the first vertical slot upstream the blades.

Different tangential positions were investigated. The results were compared in Fig. 4.2. The differences between them are about 0.1 m/s and are thought to be due to experimental error. This shows that the inlet flow is uniform in the tangential direction. The inlet velocity and total pressure distribution are shown in Fig. 4.2 and Fig. 4.3. By doing the log plot, the boundary layer power law exponent turned out to be 11.5. A numerical integration procedure derived the displacement and momentum thickness from inlet velocity distribution as shown in Fig 4.2. The shape factor of the inlet boundary layer is 1.20 which is about the same as the Durham test case 1.22 and smaller than the shape factor 1.37 of Harrison (1990). For the δ_1/c value, it is 0.0105 which is smaller than the Durham test case 0.0165 and bigger than the value 0.0094 from Harrison (1990). The results are contained in Table 4.1. These boundary conditions were kept the same for the rest of experiments.

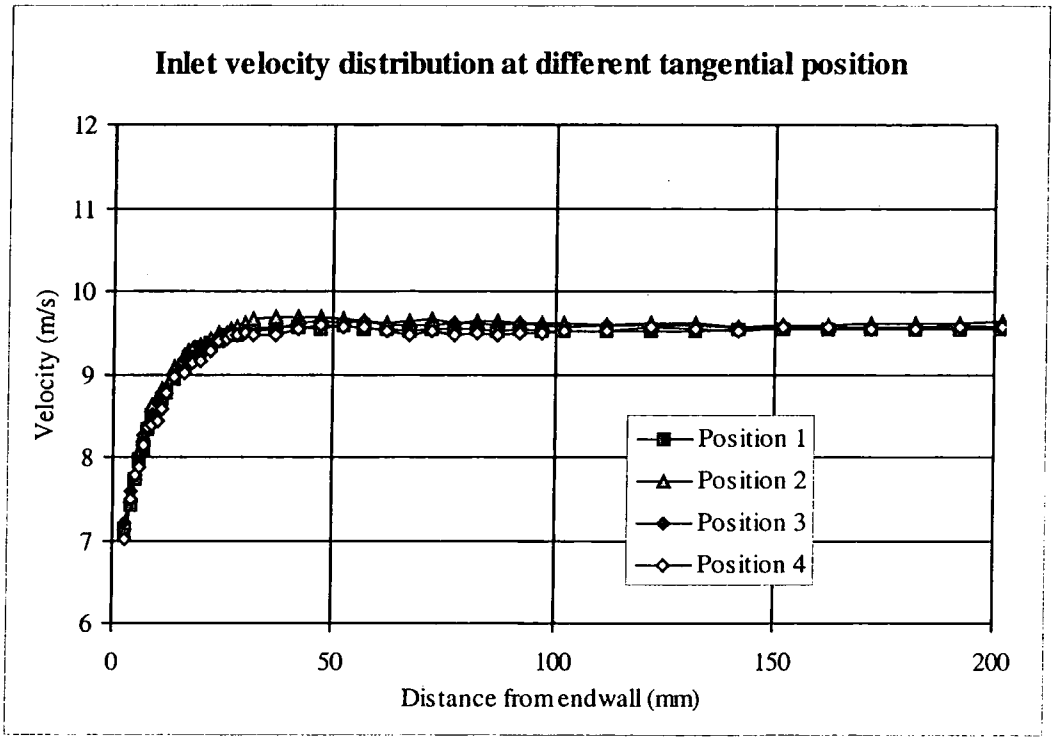

Figure 4.2—Inlet velocity at different tangential positions

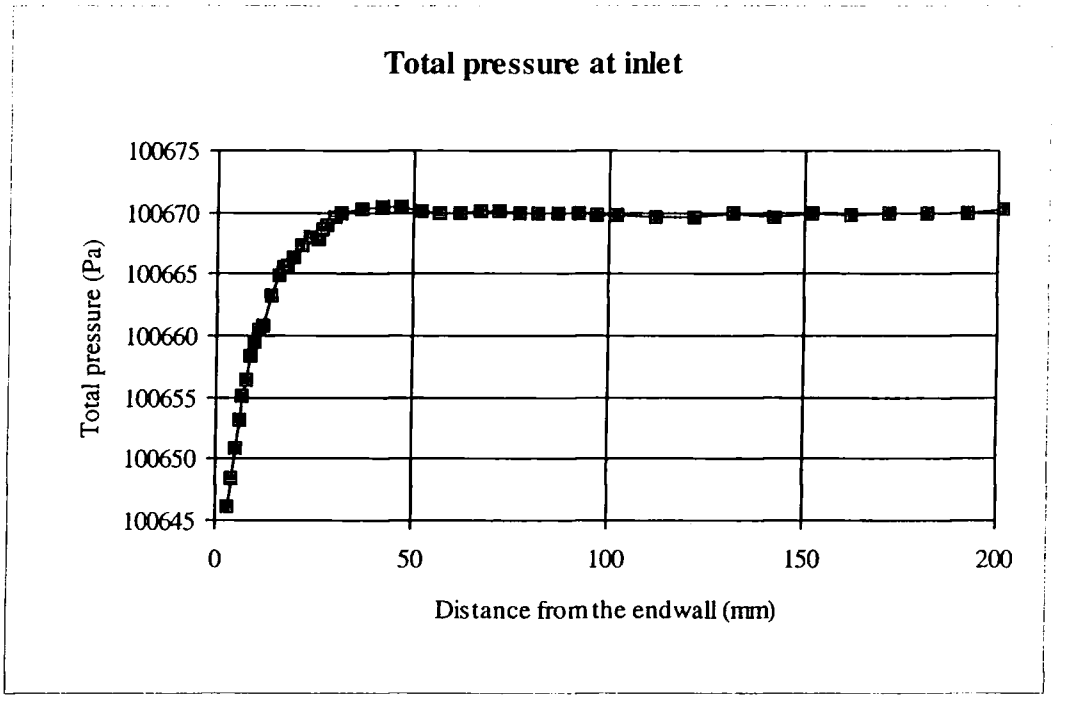

Figure 4.3—Total pressure distribution at inlet

Table 4.1—Parameters of the boundary layers at inlet and slot 2

Position	Boundary layer thickness δ	Displacement thickness δ_1	Momentum thickness δ_2	Shape factor H_{12}
Slot 1	28 mm	2.35 mm	1.95 mm	1.2
Slot 2	33.4 mm	2.43 mm	2.09 mm	1.17

4.3 Traverse gear set-up

The traverse plane is rectangular if it is looked at from the exit of the passage. It only covers the area from test end wall to the mid-span. The traverse grid distribution was controlled by the grid data file on the computer. The radial grid distribution which consists of 30 points was kept the same for every slot apart from slot 2. There are more

points concentrated in the near wall region which is 50 mm from the end wall in order to capture the rapid changes there. In the near wall region, the expanding ratio of the grid was generally set to be 1.2. There were six points in the mid-span region. In the tangential direction, the number of grid points and its distribution was different according to the length of the slot. For slots inside the passage such as slot 3, 4, 5, 6, 7 and 8, the grid was set in a such way that it expands at a ratio of 1.2 from one blade surface to the mid-pitch symmetrically For the rest of slots, mid-span pitchwise traverses were initially done to check the total pressure gradient distribution. In high total pressure gradient areas, more grid points were taken there in the pitchwise direction.

After every movement of the probe, it was stabilised for 5 seconds first, the system then took about 6,000 readings for each hole and time-averaged them. The final averaged value was written onto the hard disk for analysis. With the sampling frequency of about 3 kHz, the 30,000 readings needed ten seconds to be read. This time interval was decided as the minimum requirement to capture the low frequency fluctuation of the wind tunnel. It took about eight hours to complete a traverse for slot 9 and 10 and about six hours for the other slots

4.4 Area traverse results

Area traverse results are presented in the format of line contours or velocity vector plots. From these results, the flow development through the blade passage could be seen.

4.4.1 Traverse results for slot 2

Slot 2 is the slot just upstream of the leading edges of blades. Because of the small gap between slot 2 and blade leading edges, the cobra probe, which has a big cobra-like

head, would have hit the blade surface while traversing. The small headed probe in Fig 3.14 was employed instead. The pressure gradient and angle changes across the plane are small. Therefore, using the small head probe did not cause significant error. The length of the slot is 220 mm with a traversing grid of 29×28.

The experimental results are shown in Figs. 4.4. The total pressure loss contour shows the upstream boundary layer. The secondary vector plot and the yaw angle show that the horse shoe vortex has started to develop. There is little secondary kinetic energy at this plane.

The pitch averaged results are shown in Fig. 4.5. The total pressure loss is zero at the mid-span. Near the end wall, the loss represents a boundary layer profile. In order to compare the boundary layer with the upstream one, a table of boundary layer parameters deduced from experiments is shown in Table 4.1. Compared with the boundary layer at slot 1, the boundary layer has grown 5.4 mm thicker. The yaw angle shows zero turning in the mid-span with a small overturning near the end wall. The overturning of the flow means that the pressure side leg of the horse vortex is stronger than the suction side leg.

4.4.2 Traverse results for slot 3

Slot 3 is located just downstream of the leading edges of the blades. The actual traversing length of slot 3 is 110 mm in the tangential direction. The radial traversing length was kept same as before. The shorter slot made it possible to reduce the traversing points to 23 in the tangential direction. The probe angle was still set to zero degree.

The experimental results are shown in Fig. 4.6 which is the near wall region covering the area from 0 to 50 mm. Total pressure loss is still showing a similar shape to that of the inlet boundary layer. The yaw angle near the pressure surface is negative but

positive near the suction surface. This can be explained by the blade shape in Fig 3.4. The horse shoe vortex can be seen in Fig. 4.6 (e). The pressure side leg stays near the pressure surface corner and is still very small. The suction side leg can hardly be seen. The secondary flow is small at this stage. The secondary kinetic energy is only apparent near the pressure side corner. The pitch averaged total pressure loss in Fig. 4.7 shows a similar boundary layer to that at slot 2. The pitch averaged yaw angle shows small underturning and overturning near the end wall.

4.4.3 Traverse results for slot 4

The tangential traversing length is 90 mm with 23 traversing grid points. The off-set angle of the five hole probe was set to -10 degrees. This made sure that the probe head lined up with the mainstream and gave minimum force on the probe head.

The results are shown in Fig. 4.8. There is little change in the total pressure loss contour compared to slot 3. The yaw angle is negative and increases from the pressure surface all the way to the suction surface. The size of the passage vortex is bigger than that at slot 3, and its core is moving toward the suction surface from the pressure surface. The passage vortex starts to show a dominant role in the blade passage. On the other hand, the suction side corner vortex has become invisible. The yaw angle distribution shows that the flow is skewed toward the pressure surface. This is a result of the strength of passage vortex and secondary flow. The overturning is bigger near the pressure surface and end wall. The pitch angle distribution shows that flow near the pressure surface is flowing toward the end wall. The secondary flow is stronger than at slot 2 as shown in the secondary kinetic energy contour.

The pitch averaged results are shown in Fig. 4.9. The total pressure loss is still more or less the same as that of slot 3. There is a small underturning and overturning appearing

in the pitch averaged yaw angle distribution, this is due to the stronger passage vortex effect.

4.4.4 Traverse results for slot 5

The tangential traversing length for slot 5 is 70 mm. The traversing grid is 21×30 and the probe was set to -47 degrees.

The experimental results are shown in Fig. 4.10. The total pressure loss is bigger near the suction side. The boundary layer on the suction surface is thicker than the previous slots. This is caused by the low energy material from the end wall being driven by the passage vortex (or secondary flow) towards the suction surface.

The secondary flow is stronger than at the previous slot. The passage vortex has grown to a bigger size and has moved further away from the end wall. It can be seen that the secondary flow is stronger near the end wall, Fig. 4.10 (e). The yaw angle distribution shows a highly skewed flow on the end wall near the pressure surface. The flow is driven toward the suction surface from the pressure surface in the near end wall region. There is large overturning near the end wall and pressure surface. On the other hand, the underturning can be seen clearly at a distance of about 24 mm away from the end wall.

At this stage, the secondary flow has become a dominant effect. The secondary kinetic energy shows that the secondary is stronger. The high secondary kinetic energy centre is nearer to the suction surface.

The pitch averaged results are shown in Fig. 4.11. There is not too much change in the total pressure loss distribution. This is probably because the traversing probe could not approach the surfaces of the blades close enough to pick up the information of the

boundary layers on both surfaces. The pitch averaged yaw angle distribution shows a large overturning near the end wall and a underturning at a distance of 24 mm from the end wall.

4.4.5 Traverse results for slot 6

This slot is a very short slot with a traversing length of 60 mm. The traversing grid was set to be 21×30 with most tangential points located in the near end wall region. The probe was set to an angle of -57 degrees.

The experimental results of slot 6 are shown in Fig. 4.12. The total pressure loss is bigger and radially covers a wider area than that of the previous slots. This is due to the development of end wall boundary layer and its interaction with the boundary layers on blade surfaces.

The passage vortex has now become stronger and bigger. Near the pressure surface, the vortex movement entrains the high energy fluid outside the boundary layer into it. Near the suction surface, the end wall boundary layer is driven into the corner of the suction surface. This make the boundary layer on the suction surface thicker. The yaw angle distribution shows no obvious change from the pressure surface to the suction surface. This could be explained by the surfaces of the blade which are almost parallel at slot 6. There is a great overturning near the end wall. This indicates a highly skewed flow which is driven towards the suction surface from the pressure surface. The secondary kinetic energy contour in Fig. 4.12 b) shows stronger secondary flow. The highest secondary kinetic energy area is still near the pressure side.

The pitch averaged results are shown in Fig. 4.13. Because the probe could not approach the blades surfaces close enough, the blade profile loss was not picked up. Therefore, the total pressure loss at the mid-span is nearly zero. Compared with

previous slots, the loss covered a bigger area. The yaw angle shows an underturning at a distance of 28 mm from the end wall and a great overturning near the end wall which indicates a strong secondary flow near the end wall.

4.4.6 Traverse results for slot 7

The slot 7 is located quite near the trailing edge. The traversing length of slot 7 is 58 mm with a traversing grid of 21×30. The traverse results are shown in Fig. 4.14. The total pressure loss contour in Fig. 4.14 a) shows an increased loss. The strong secondary flow near the end wall sweeps the low energy fluid toward the suction corner. This results in the formation of the total pressure loss core

The passage vortex does not show too much difference from that in slot 6. Near the end wall the secondary vector is stronger. This is shown in the yaw angle distribution. The overturning is higher than that at the previous slot. The secondary kinetic energy contours show higher secondary loss near the end wall. The high secondary kinetic energy area is near the suction surface. This actually shows the passage vortex moving from the pressure surface towards the suction surface.

The pitch averaged results are shown in Fig. 4.15. The total pressure loss shows a peak loss away from the end wall and smaller loss near the end wall. This is can be explained as the fact that secondary flow sweeps the low energy fluid onto the suction surface and then brings the high energy fluid onto the end wall boundary layer. A new boundary layer being generated on the end wall was not picked up. The yaw angle distribution shows a larger overturning and underturning which indicates stronger secondary flow than at slot 6.

4.4.7 Traverse results for Slot 8

Slot 8 is located just before the trailing edge. The traversing length of the slot is 60 mm with a traversing grid of 21×30.

The area traverse results are shown in Fig. 4.16. It can be seen from the total pressure contours that the loss core is already on the suction surface. This is due to the migration effect caused by secondary flow. The region on the end wall near the pressure surface corner shows a low loss area. This means that the newly developed end wall boundary layer is still too thin to be picked up by the probe. The secondary vector plot shows smaller secondary flow near the end wall region than that at slot 7. This could be explained in that the pressure gradient across the passage is much smaller than that at slot 7. The small pressure gradient produces less secondary movement. On the other hand, the viscous and turbulent dissipation become more dominant which makes the secondary flow smaller. The secondary kinetic energy also shows smaller secondary flow. The high secondary kinetic area is now in the suction corner. The yaw angle contour also gives less extensive overturning near the end wall.

The pitch averaged results of yaw angle and total pressure loss are shown in Fig. 4.17. The total pressure loss shows the loss peak has moved further away from the end wall due to the convection effect from the secondary flow and the growth of the boundary layer on the end wall. At the mid-span, the total pressure loss shows a big increase. The yaw angle at mid-span shows about 10 degree increase of the flow turning from slot 7. The general distribution profile is more or less the same as at slot 7. This implies that the secondary flow has not changed much from slot 7 to slot 8. Another data set in the figure is the pitch averaged results with transition trips on the blade suction surfaces. This will be discussed later in section 4.6.1.

4.4.8 Traverse results of Slot 9

Slot 9 is the first slot downstream of the trailing edge of the blade. The traversing length of the slot is 250 mm with a grid of 36×30. The traversing plane nearly covers two passages. The cobra five hole probe was used with a setting angle of -67 degrees.

The area traverse results are shown in Fig. 4.18 and Fig. 4.19. Because slot 9 is a very important slot in terms of total pressure loss and secondary flow measurements, both half span and near end wall results, which covers the area of from the end wall to 50 mm, are shown here.

The half span total pressure loss contour shows that the change is still concentrated in an area of 50 mm from the end wall. From there till mid-span, the wake is shown to be almost constant, being about 55 mm in width. In the near end wall plot, the detail of flow near the end wall can be seen. The loss cores are located about 30 mm from the end wall. There is a loss peak existing very near the end wall that indicates a counter vortex. A rather thin boundary layer has also developed. From the secondary vector plot, it can be seen that from the 50 mm to the mid-span region, there is little secondary flow. In the detailed plot shown in Fig. 4.19, the passage vortex generates a strong upward secondary flow. The counter vortex is hardly seen near the end wall. At this stage, the passage vortex is suffering the viscous and turbulent diffusion effect so that the secondary kinetic energy peak near the end wall is smaller compared with that at slot 8. There is a massive increase of the secondary kinetic energy at about 30mm away from the end wall in Fig. 4.19b). The two concentrations of the secondary kinetic energy represent the shed vorticities in the wakes from two blades. From the area contours, the secondary kinetic energy generated in the wake is almost the half of the total secondary kinetic energy at slot 9. The yaw angle distribution shows the interaction between flows from the suction surface and the pressure surface in the wake region. Because of the diffusion, the yaw angle distribution is showing much smaller

pitchwise gradient. The detailed contours, Fig. 4.19e), near the end wall show the overturning and underturning effect clearly. The counter vortex effect on the yaw angle distribution is also observed in Fig. 4.19c). The pitch angle distribution shows a large amount of secondary flow near the end wall. Comparing the two wakes, there is a slight difference between them. The difference is possibly due to the slight difference between the blades.

Pitch averaged results are shown in Fig. 4.20. The total pressure loss shows almost a constant value from 50 mm to the mid-span. The loss peak is located at about 30 mm from the end wall. The newly developed boundary layer can be noticed near the end wall. Between the loss peak and the boundary layer, there is a low loss region which is quite thin. This could be explained by the secondary flow effect. The secondary flow movement drives the low energy fluid away from the wall and also brings in high energy fluid from the outside. With the diffusion effect, it can be seen that low loss region will become smaller. The yaw angle distribution shows the underturning and overturning effect near the end wall. There is another data set in Fig. 4.20 which indicates the results with transition trips will be described in section 4.6.2.

4.4.9 Traverse results of Slot 10

Slot 10 is the last slot down stream from the trailing edge. The position of slot 10 is shown in Fig. 3.4. The traversing length of slot 10 is 250 mm with a traversing grid of 36×30. The probe is set at an angle of -76 degrees. The purpose of the research is to investigate the shaped end wall effect on the loss. For turbine design, slot 10 is typical of where a next blade row starts. It is the reference position for comparing the effect of end wall profiling. Therefore, slot 10 is an important slot for the loss investigation.

The experimental results of slot 10 are shown in Fig. 4.21 with the detailed description in Fig. 4.22. The total pressure contours of half span shows almost the same pressure distribution from about 50 mm to the mid-span position. The wake has become much

wider than that in slot 9, which is due to the strong mixing out effect. The loss core is located about 34 mm away from the end wall. The loss core migration is caused by the secondary flow and the growth of the boundary layer. The detailed flow near the end wall shows a much thicker boundary layer on the end wall.

The secondary vector plot shows a smaller secondary flow compared to that of the slot 9. There is little secondary flow outside the 50 mm region. In the detailed picture, the secondary flow is more evenly distributed with the strongest secondary vectors in relatively the same position as that in slot 9. The vortex centre is still located in the same position of that in slot 9 relative to the end wall. Downstream from the trailing edge, the driving force for secondary flow generation is nearly zero. On the other hand, the mixing out effect, which is dissipating the secondary flow, is dominating the flow field. The secondary kinetic energy contours also show a smaller secondary flow. There is still a strong secondary kinetic energy concentration at about 30 mm away from the end wall. This also indicates the vortex reduction after the trailing edge. The yaw angle distribution contour shows less change across the pitch near the mid-span. The flow is becoming more uniform by the mixing effect. The yaw angle near the end wall shows an underturning at a distance of 30 mm from the end wall and an overturning near the end wall. The pitch angle contours show the secondary flow movement.

The pitch averaged results of total pressure loss and yaw angle are shown in Fig. 4.23. In the mid-span region, both yaw angle and loss have almost constant values. The loss peak is located about 34 mm from the end wall. A thicker boundary layer than before is also seen near the end wall. The yaw angle distribution near the end wall shows the underturning and overturning of the flow. The angle difference between the underturning and overturning, which is about 7 degrees, is smaller than that of slot 9 which is about 9 degrees.

From all these slot investigations, the flow movement is fairly well understood. At slot 2 and slot 3, the horse shoe vortex around the leading edge was indicated. The difference between two legs of horse shoe vortex can be seen. From slot 4 to slot 8, the secondary flow is progressively increasing and the passage vortex is moving from the suction surface to the pressure surface. From somewhere between slot 7 and slot 6, the end wall boundary layer began to move away from the end wall. High energy fluid has been brought in by the movement of the secondary flow. A new end wall boundary layer has started to develop on the end wall. After the trailing edge, the mixing out effect becomes dominant and so the secondary flow starts to decline. The flow is becoming more uniform with higher total pressure loss.

4.5 Static pressure measurements on the blade and end wall surfaces

The static pressure was measured by the pressure tappings on the blade surfaces and end wall surface. The static pressure on the end wall was shown in Fig. 4.24. There is a big pressure gradient across the blade passage and also high acceleration through the blade passage. The static pressure distribution along the blade surfaces was also taken. Two adjacent blade surfaces bounding the main testing passage were investigated. Different spanwise positions were measured as shown in Fig. 4.25. The static pressure along the suction surface decreased rapidly towards the trailing edge of the blade. The static pressure along the pressure surface shows very little change until 80 % of axial chord downstream from the trailing edge. It then decreases rapidly towards the trailing edge. The readings near the end wall show very small difference from the mid-span reading.

4.6 Flow visualisation

The flow visualisation was done on the end wall and blade surfaces. Red dye was mixed with diesel oil which is easy to vaporise. For the end wall, because of the gravity effect, the dye tended to flow downward, and so the injection method was used. After

the wind tunnel was turned on, the dye mixture was injected onto the end wall through the pressure tappings on the wall. U-V light was used to stimulate the dye and pictures were taken. The results are shown in Fig. 4.26. Because the flow was accelerated greatly through the passage, the exit speed was 40 m/s, with a inlet speed as low as 9 m/s. This makes the flow visualisation very difficult. Even with the injection method, the gravity effect was still obvious. The inlet horse shoe vortex structure can not be seen. In the later half of the passage, the flow runs from the pressure surface straight towards the suction surface. This indicates the high pressure gradient between the pressure and suction surface giving strong secondary flow on the end wall.

For the blade surfaces, the dye mixture was brushed onto the surfaces. Then the wind tunnel was switched on. The results are shown in Fig. 4.27 and Fig. 4.28. The suction flow visualisation in Fig. 4.27 shows a large separation bubble near the trailing edge. This indicates that the boundary layer on the blade surface is still laminar. This is thought to be caused by the low Reynolds number compared with real turbines and insufficient turbulence intensity at the inlet. Near the end wall, because of the vortex movement, the boundary layer is clearly different from the rest. There is no separation because of the high turbulent intensity there. On the pressure surface, because of the low velocity of the flow the gravity is the dominant effect. So the flow visualisation does not show much information about the flow, see Fig. 4.28.

In a real machine, the Reynolds number is about three times higher than in the cascade, and the boundary layer on the blade surface is turbulent. In order to simulate the real machine, it was decided to use turbulent transition trips on the blades suction surfaces. The trip position, height, additional loss caused by the trip were calculated according to a ALSTOM method using a blade-to-blade inviscid calculation (FINEL), followed by an integral boundary layer method (BLINC). Aluminium tape was used for the trip. The size and position of the trips are shown in the following table 4.2:

Table 4.2—Transition trip design data

Distance from LE	Height	Width	Additional loss
96 mm	0.24 mm	12 mm	0.73%

The transition trips were put on three blade suction surfaces for periodicity. The surface of the tape was grooved by a special tool to increase its transition effect. With these trips on, the flow visualisation was repeated on the blade surfaces. The results are shown in Fig. 4.29. The aluminium belt near the leading edge in Fig. 4.29 is the trip. The separation bubble has been eliminated completely from the suction surface. It has proved that the transition trip has successfully initiated the turbulent boundary layer on the blade surface.

4.7 Experimental results with the transition trip

With the boundary layer transition trips, the flow field was changed. In order to check the effect of these trips, slot 8, 9, and 10 and also the static pressure on the blade surfaces were investigated again. The trip effect on upstream slots was thought to be little considering the fact that the traversing probe could not pick up the flow detail near the blade surface.

4.7.1 Traverse results of Slot 8

Slot 8 is traversed by the cobra five hole probe with the same grid as before. The area contours and vector plot are shown in Fig. 4.30. Compared with the results without the trip in Fig. 4.16, the total pressure loss contour shows a small increase of total pressure loss. The separation bubble on the blade surface is very thin. All these reasons make the traversing results nearly the same as before, Fig. 4.16.

The pitch averaged results are shown in Fig. 4.17. The total pressure loss was increased slightly from the mid-span to the end wall. The loss peak with the trips is higher and located slightly nearer to the end wall than those without the trips. From the loss peak

position, it indicates that the convection effect from secondary flow is smaller than without the trips. This is due to the smaller secondary flow which will be seen in the yaw angle distribution as well. The yaw angle distribution shows lower underturning and higher overturning which means smaller secondary flow. From the experiment results, the transition trips have slightly reduced the secondary flow at slot 8.

4.7.2 Traverse results of slot 9

Slot 9 was traversed with the same grid. The area contours and vector plot are shown in Fig. 4.32 and Fig. 4.33 which is the detailed flow near the end wall. The total pressure loss contours show no obvious change near the mid-span. From the theoretical prediction, the trip may only increase total pressure loss by 0.9% in the mid-span which is too small to be seen. The flow near the end wall has a big change. The boundary layer is obviously thicker than that without the trip see Fig. 4.18 and 4.19. As shown in Fig. 4.32b), the secondary kinetic energy shows a great reduction from that without the trip. This indicates that without the trip the separation bubbles on the suction surface generate a great deal of secondary flow. With the trip, the fully turbulent flow has a greater dissipation effect on the secondary flow. Combining these two factors together, the secondary flow difference between the flow with and without trip might be explained. The secondary vector plot also show generally smaller secondary vector than without the trip in Fig. 4.19e). The yaw angle shows less underturning and overturning which indicates smaller secondary flow as well.

The pitch averaged total pressure loss and yaw angle are shown in Fig. 4.20. For the total pressure loss, there is not a noticeable change near the mid-span. Near the end wall, there is a bigger high loss area than that without the trip. The weaker secondary flow produces less convection effect so that more low energy fluid stays near the end wall. The yaw angle distribution shows far less underturning and overturning than without the trip. This is the result of the much smaller secondary because of the trip.

4.7.3 Traverse results of slot 10

Slot 10 traverse was repeated with the trip. The results are shown in Fig. 4.33 and Fig. 4.34 with detail flow near the end wall. The total pressure loss is about the same as the case without trip. Near the end wall, the boundary layer is thicker than before. There is less secondary kinetic energy in the shed vorticities area than without the trip. But the difference between with and without the trip is much less than at slot 9. The secondary vector plot also shows smaller secondary vectors compared to Fig. 4.22. But the difference is quite small.

The pitch averaged results are shown in Fig. 4.23. Near the end wall, the total pressure loss is increased. The boundary layer thickness on the end wall is increased with the trip. This is also due to the less convection caused by the weakness of the secondary flow. The yaw angle shows less underturning and overturning than without the trip. This confirms the information that with the trips the secondary flow is reduced. At slot 9, the yaw angle distributions show more difference with and without the trip. The reason for the less difference is suggested to be the mixing out process.

4.7.4 The development of the total pressure loss and the secondary flow

The mass flow rate was calculated from the traverse results for every slot, shown in Table 4.4. The mass flow rate from slot 3 to slot 8 is obtained by linearly extrapolating from the last two data points nearest the blade surface to the blade surface. This may not be accurate but the results are very good in terms of the continuity through the passage.

Table 4.3—Mass flow rate for every slot

Slot No.	Slot2	Slot3	Slot4	Slot5	Slot6	Slot7	Slot8	Slot9	Slot10	CFD
Mass flow rate (kg/s)	0.232	0.232	0.232	0.230	0.232	0.233	0.232	0.231	0.232	0.243

The mass averaged loss for every slot is shown in Fig. 4.35. For the experimental results without the trip, the loss remains quite low until slot 8. The loss from slot 3 to slot 8 which is plotted in dotted line does not include the boundary layer on the blade surface due to the access problem. This means the loss from the boundary layer on the blade surface is not measured. The loss rises sharply to the slot 9 because of the loss from the wake. Another reason for the big loss increase is that the results of slot 3-8 do not include the blade boundary layer as mentioned earlier. From slot 9 to slot 10, the loss increase is rather slow. The data representing the case with the transitional trips are also shown in Fig. 4.35. With the trips, the loss is always slightly higher than without the trip from slot 8 to 10.

The mass averaged secondary kinetic energy for slot 2 to 10 is shown in Fig. 4.36. With the trip, the secondary kinetic energy goes through a steady increase till slot 6. After slot 6, the secondary kinetic energy increased dramatically till slot 9. The big secondary kinetic energy jump between slot 6 and slot 7 is due to the big turning angle increase between these two slots. Slot 9 is downstream of the trailing edge, the shed vortex after the trailing edge gives a huge increase of the secondary flow. This is the reason for the difference between slot 8 and 9. From slot 9 to 10, the secondary kinetic energy shows a sharp drop. The dissipation and diffusion are obviously the main physical process and they decrease the secondary flow. With the trip, the secondary kinetic energy at slot 8 remained more or less the same as that without the trip. But after the trailing edge, the increase of the secondary kinetic energy is far less than that without the trip. This is the most obvious difference between with and without the trip in terms of the secondary flow. This might imply that the separation bubbles have dramatically increased the secondary flow.

Table 4.4—Area averaged results for the nozzle cascade at slot 10

	Total pressure loss	Mid-span loss	Gross secondary loss	Net secondary loss	Secondary Kinetic Energy
Experiment without trip	0.86	0.75	0.11	0.09	0.0063
Experiment with trip	0.94	0.75	0.19	0.17	0.0042

The area averaged results with and without transitional trips are shown in Table 4.4. The results with the trip shows more total pressure loss and less secondary kinetic energy compared with those without the trip.

4.7.5 Static pressure on the blade surfaces

The static pressure measurement on the blade surfaces was repeated. The results show no difference from the case without the trip. This confirms the supposition that the separation bubble is very thin on the suction surface.

From the investigations, the boundary layer transition trip has not changed the main flow field. The change was concentrated in the near wall region.

4.8 Conclusion

The flow field of the cascade was investigated by the five hole probes. The secondary flow movement was understood. The flow hit the leading edge of the blade. The horseshoe vortex appeared after the leading edge. The pressure side leg of the horse shoe vortex merged with the passage vortex. The passage vortex was moved from the pressure surface toward the suction surface while going downstream. The end wall

boundary layer separated from the end wall in the position between slot 7 and slot 8 because of the secondary flow movement and a new boundary layer developed. The passage vortex was weakened by the diffusion effect after the trailing edge. The boundary layer transition trips were applied onto the blade suction surfaces to eliminate the separation bubble. The trips did not change the main flow field but affected the flow near the end wall and reduced the secondary flow, particularly reducing the secondary flow in the shed vorticity region. The flat end wall data has been established for the validation of the computational codes and the comparison with the shaped end wall results. The experimental results of the flat end wall with transition trips were treated as the datum from slot 8 to 10.

a) Total pressure loss contours

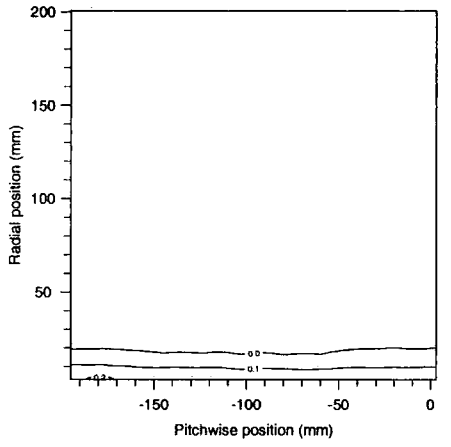

b) Secondary kinetic energy contour (%)

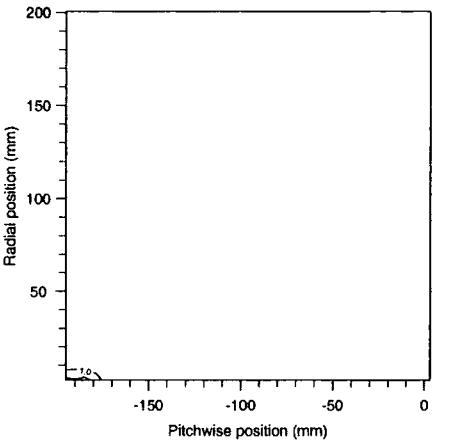

c) Yaw angle contour

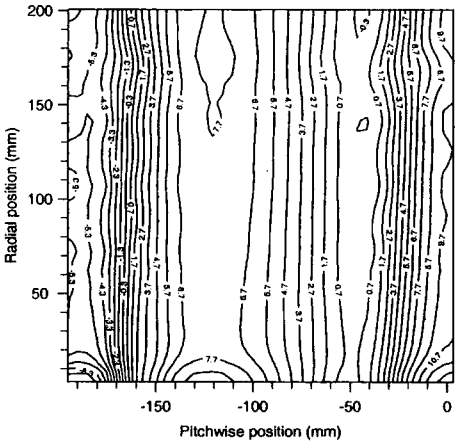

d) Pitch angle contour

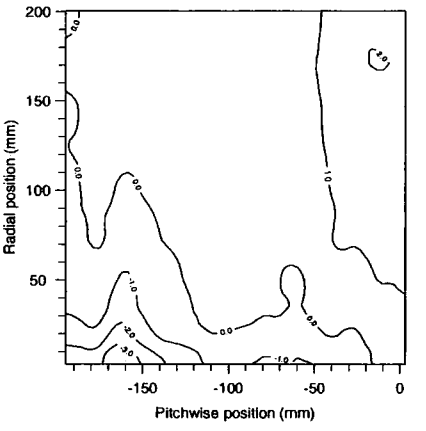

e) Secondary vector plot

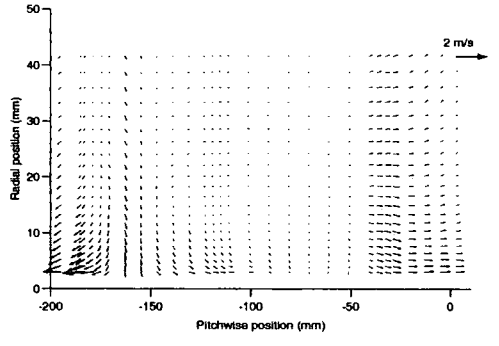

Figure 4.4—Area traverse of Slot 2

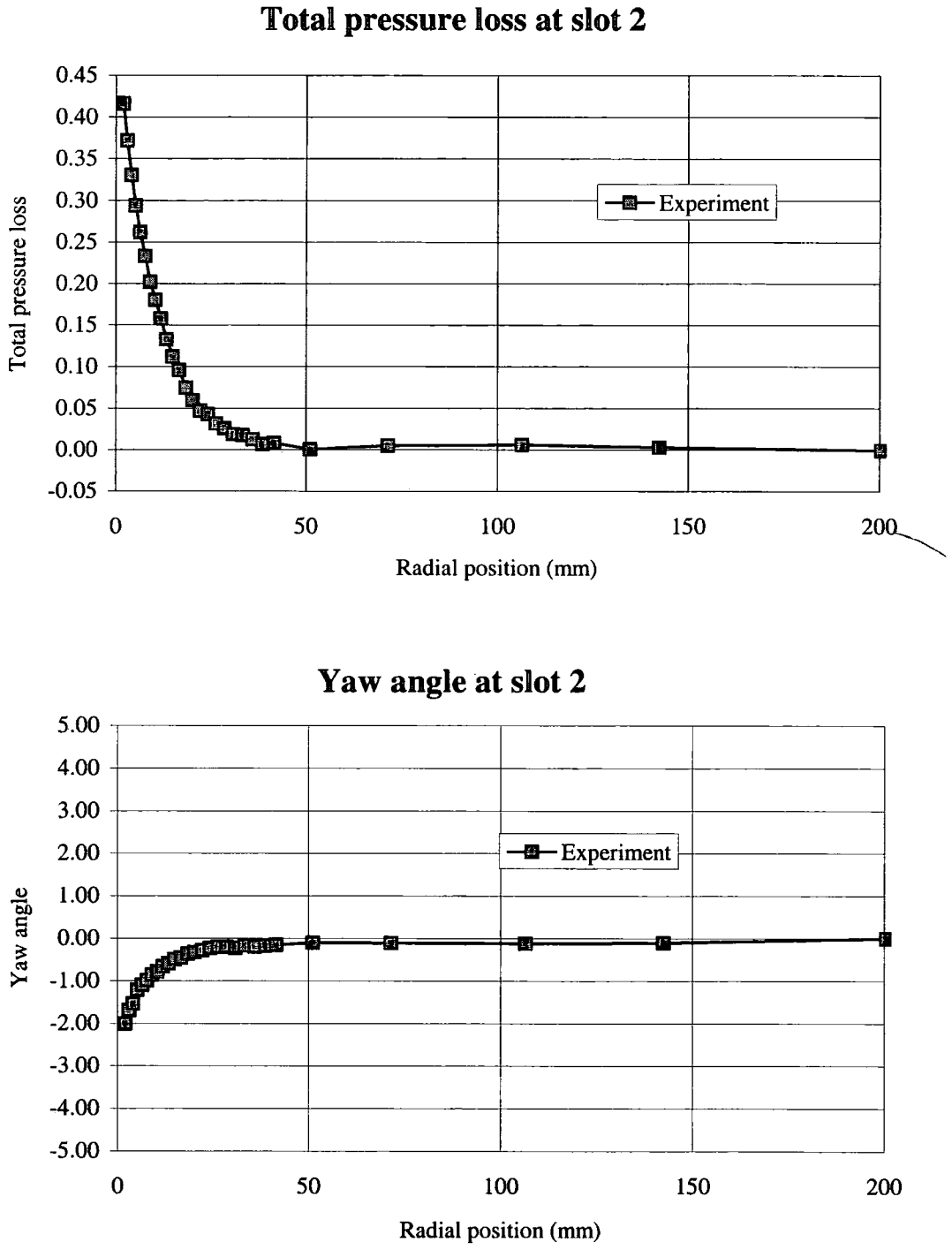

Figure 4.5—Pitch averaged results for Slot 2

a) Total pressure loss contours

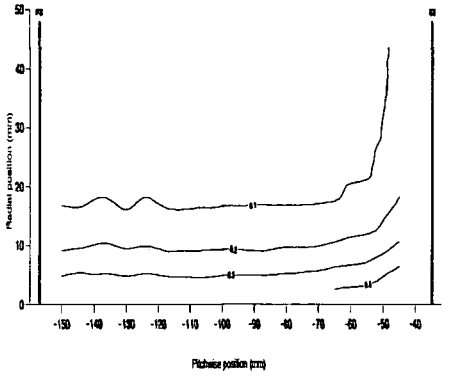

b) Secondary kinetic energy contour (%)

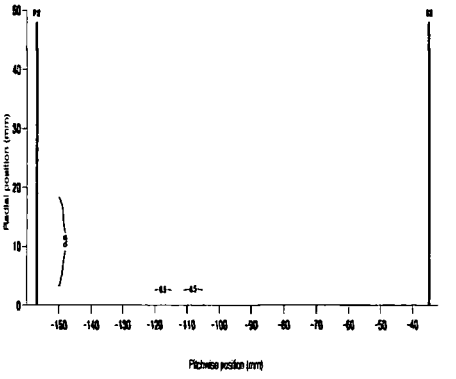

c) Yaw angle contour

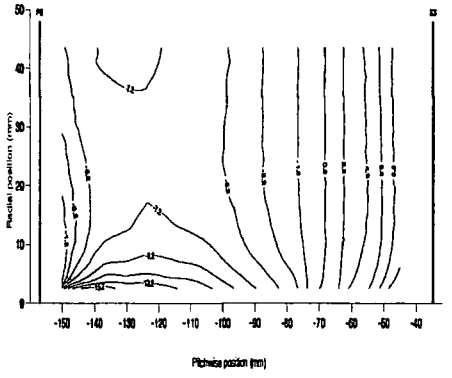

d) Pitch angle contour

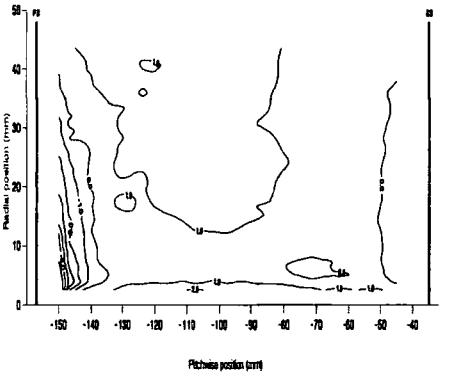

e) Secondary vector plot

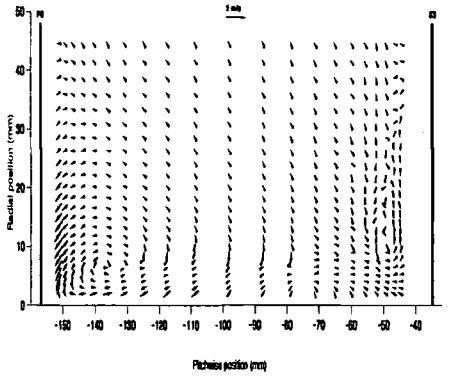

Figure 4.6—Area traverse of Slot 3

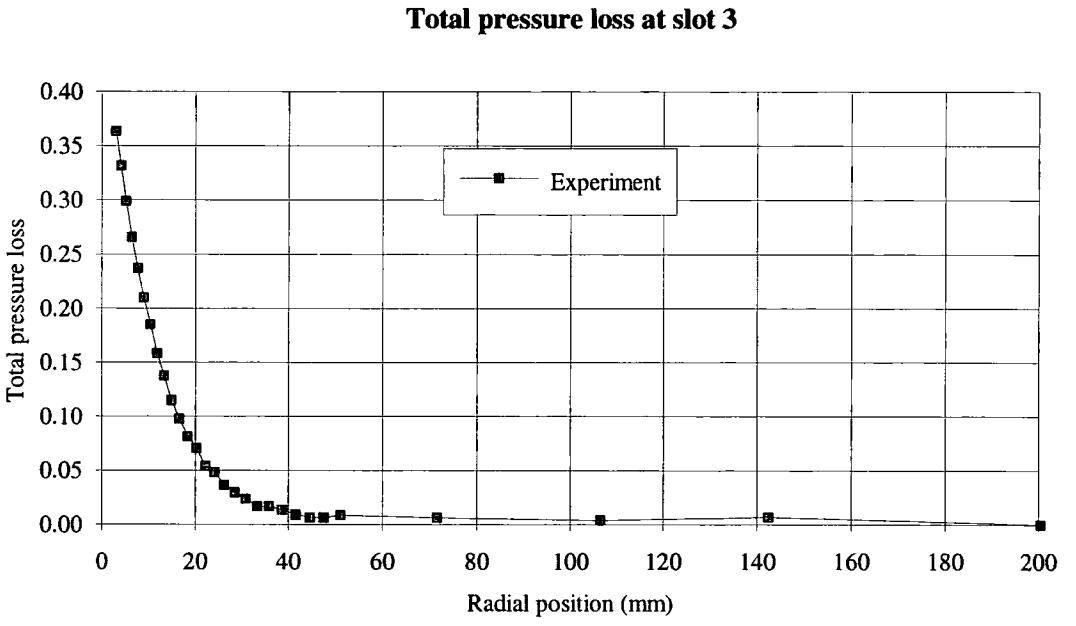

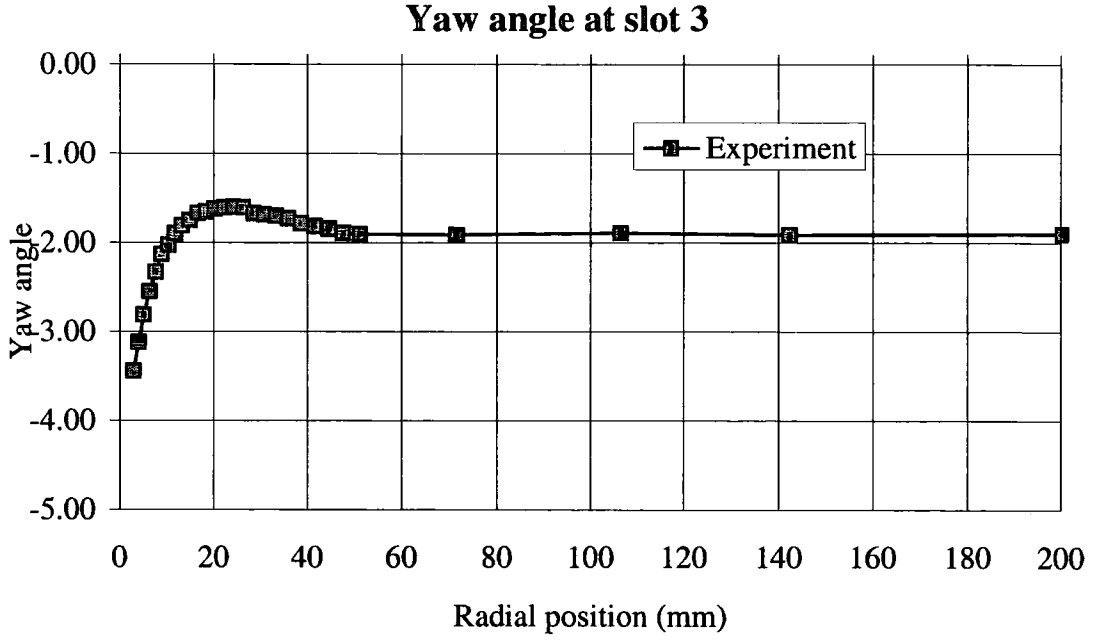

Figure 4.7—Pitch averaged results for Slot 3

a) Total pressure loss contours

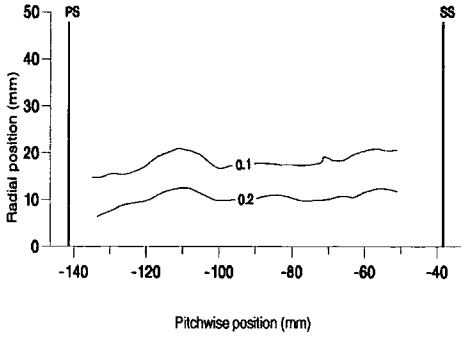

b) Secondary kinetic energy contour (%)

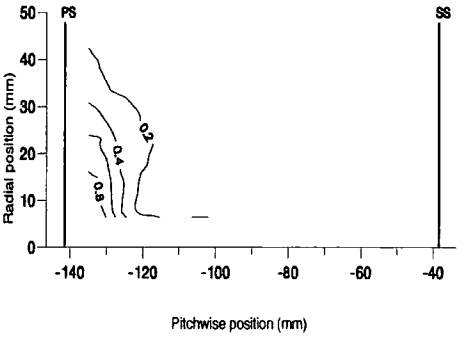

c) Yaw angle contour

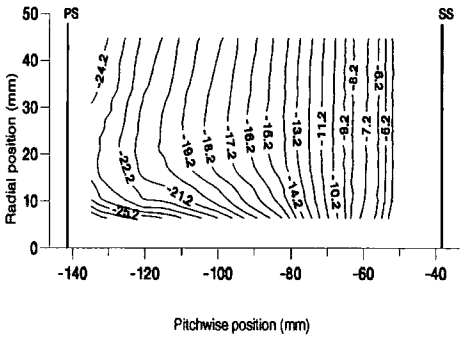

d) Pitch angle contour

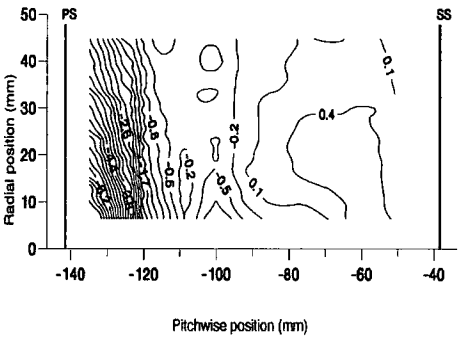

e) Secondary vector plot

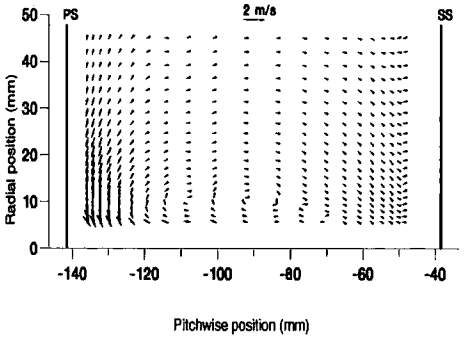

Figure 4.8—Area traverse of Slot 4

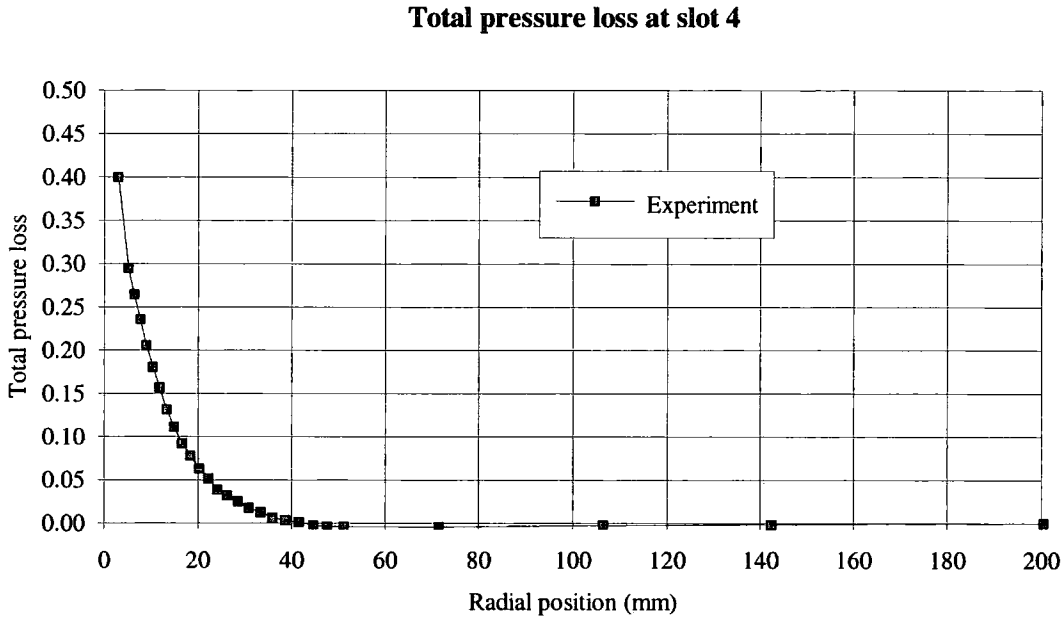

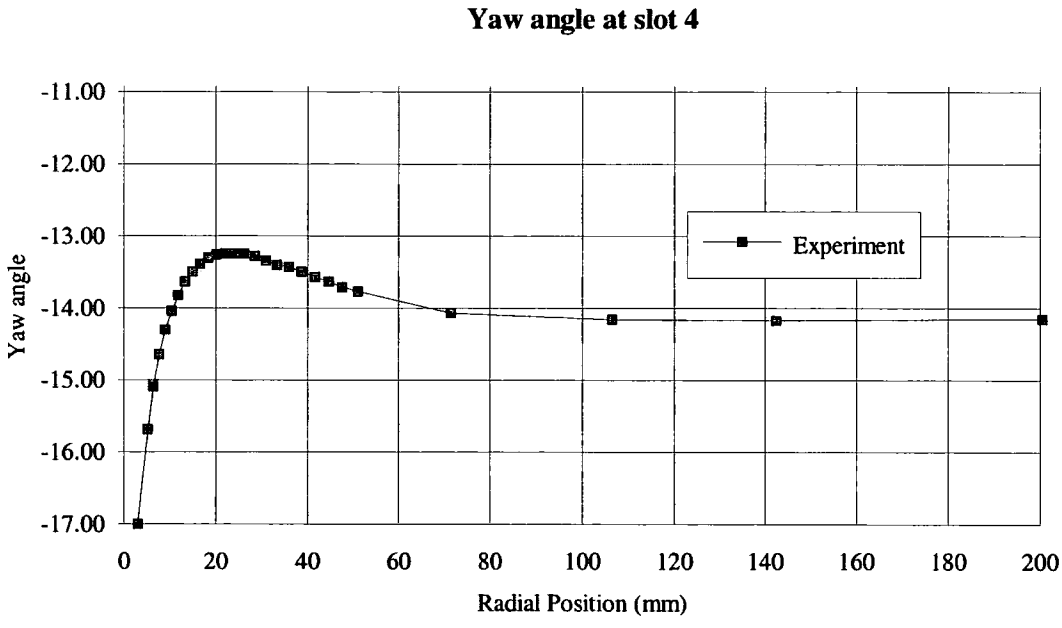

Figure 4.9—Pitch averaged results for Slot 4

a) Total pressure loss contours

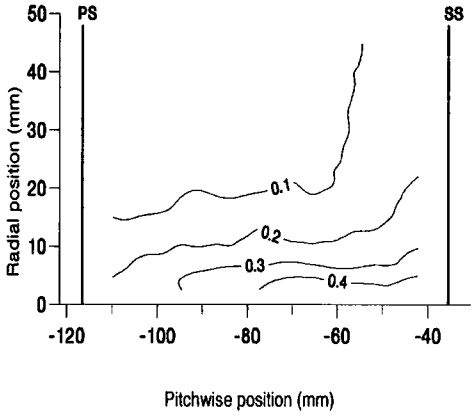

b) Secondary kinetic energy contour (%)

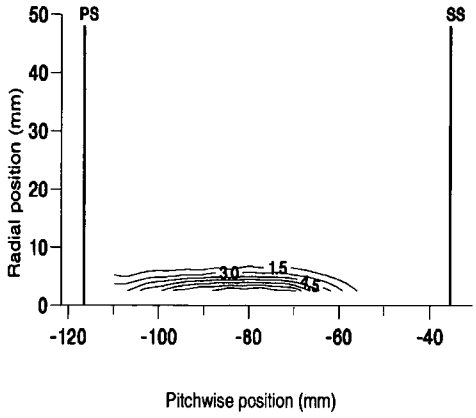

c) Yaw angle contour

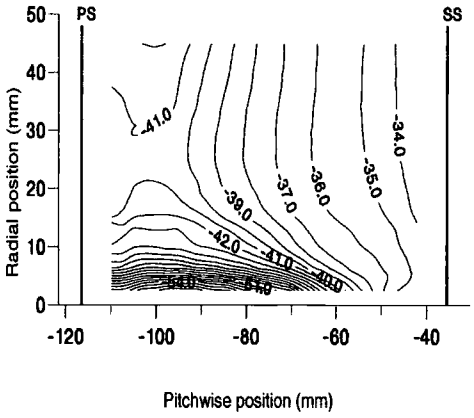

d) Pitch angle contour

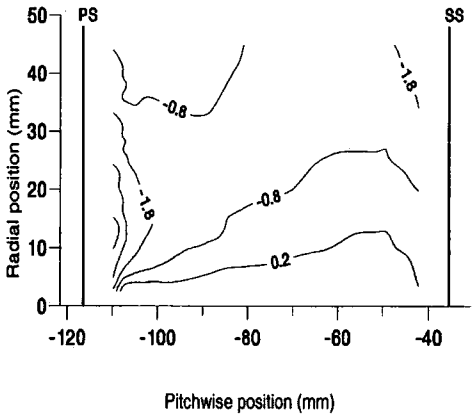

e) Secondary vector plot

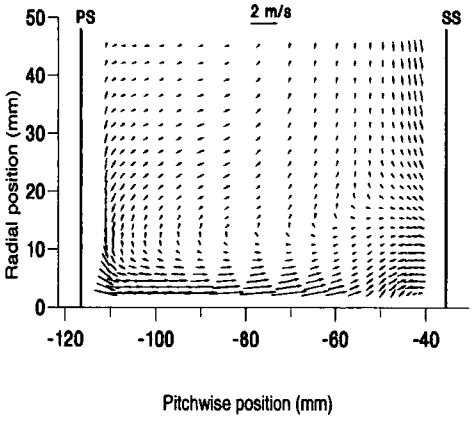

Figure 4.10—Area traverse of Slot 5

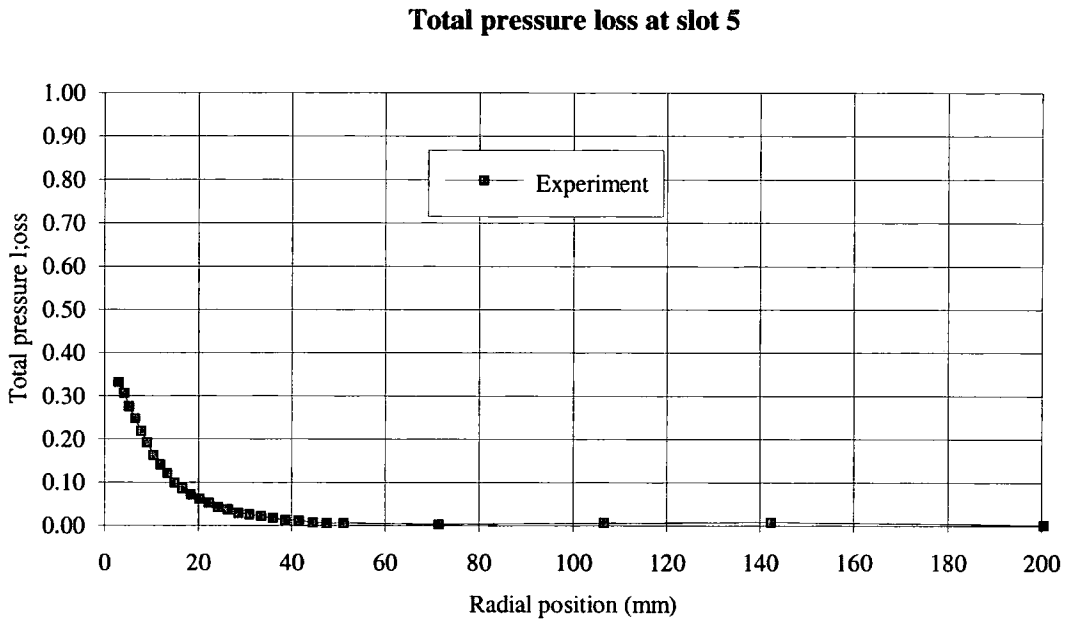

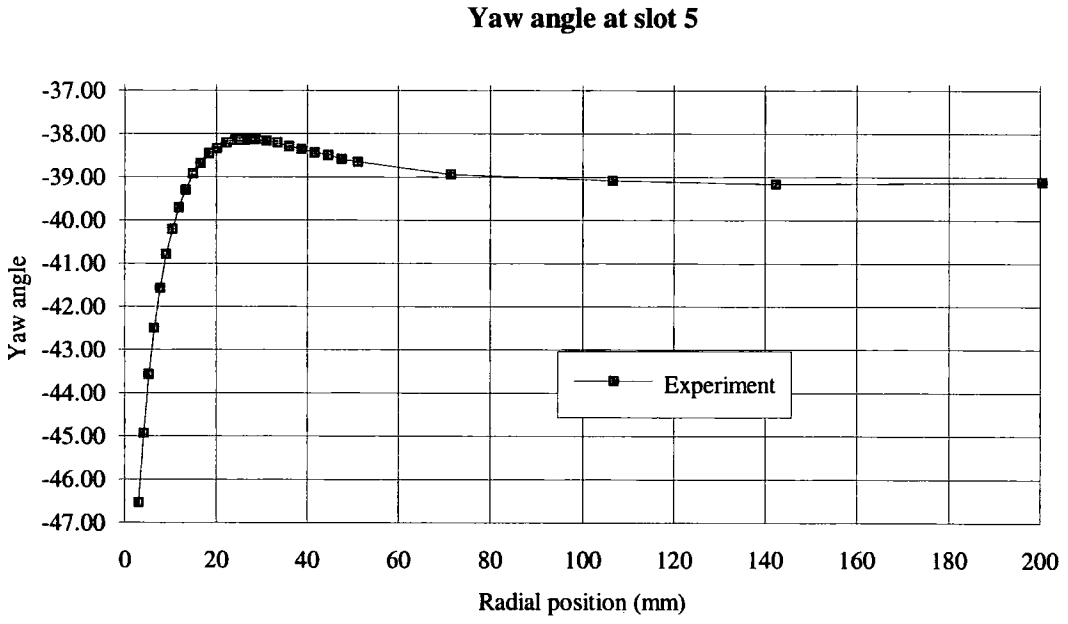

Figure 4.11—Pitch averaged results for Slot 5

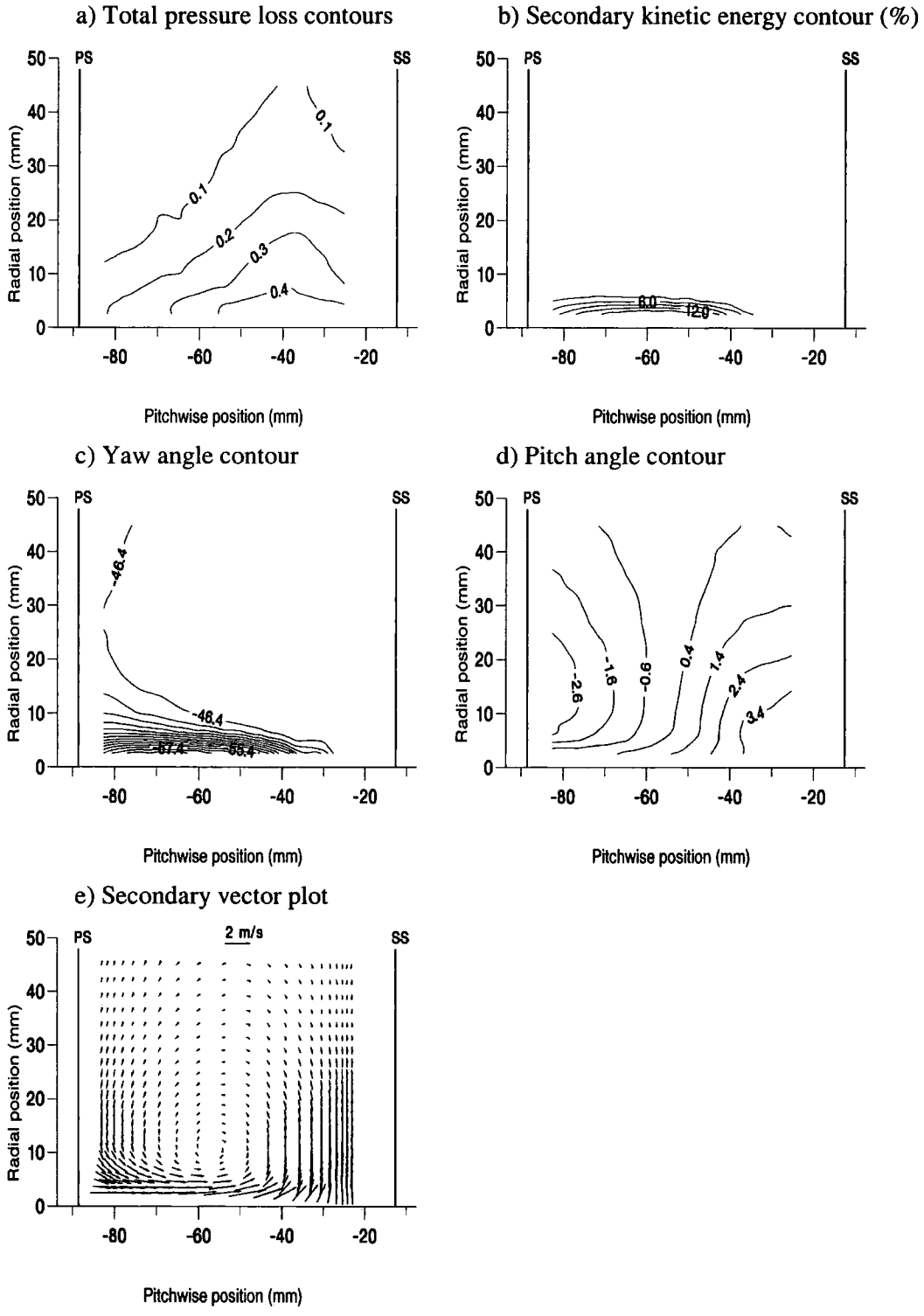

Figure 4.12—Area traverse of Slot 6

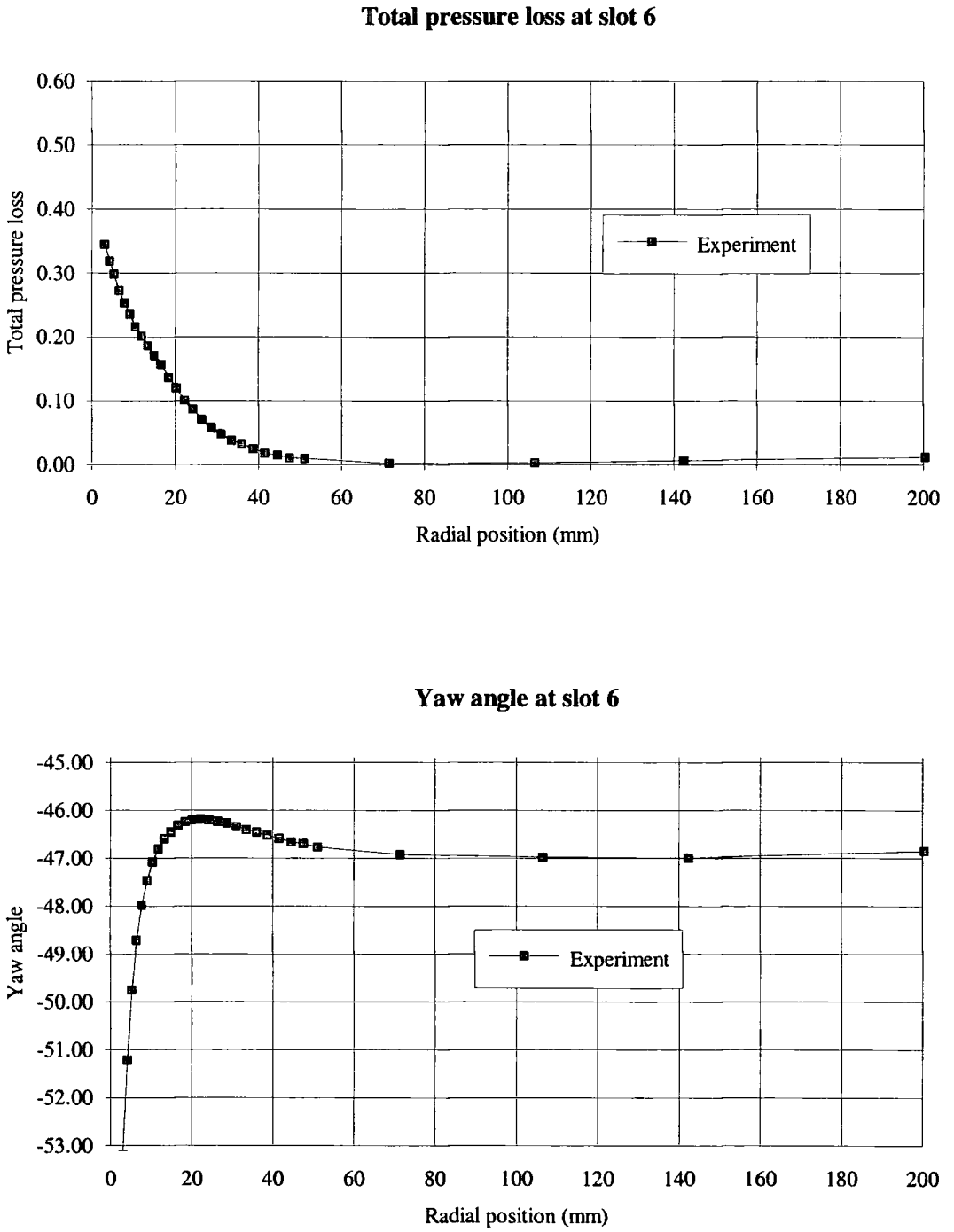

Figure 4.13—Pitch averaged results for Slot 6

a) Total pressure loss contours

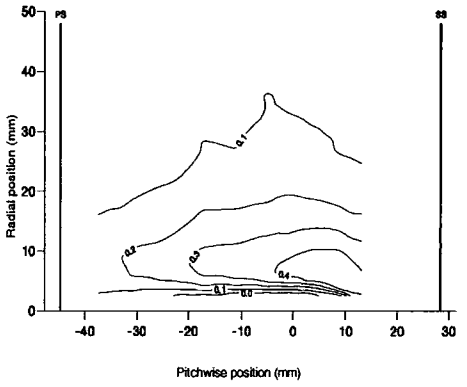

b) Secondary kinetic energy contour (%)

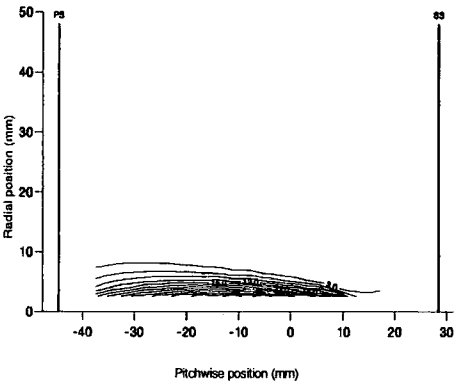

c) Yaw angle contour

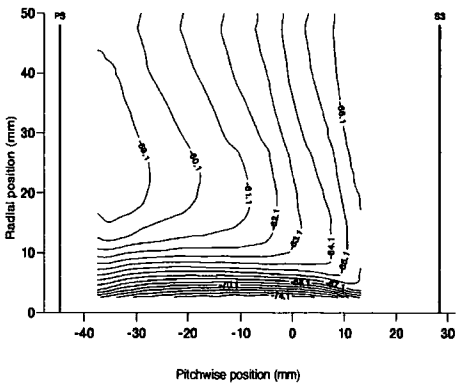

d) Pitch angle contour

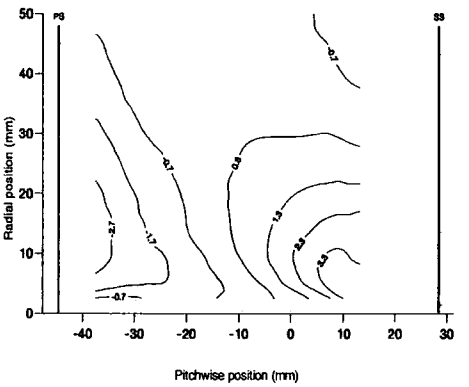

e) Secondary vector plot

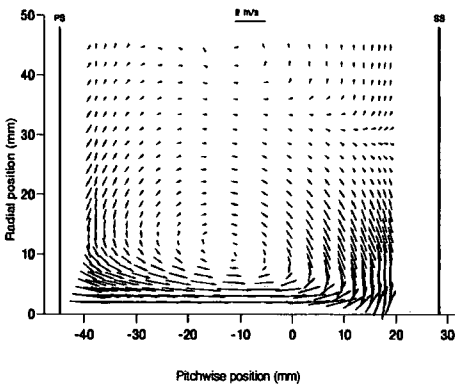

Figure 4.14—Area traverse of Slot 7

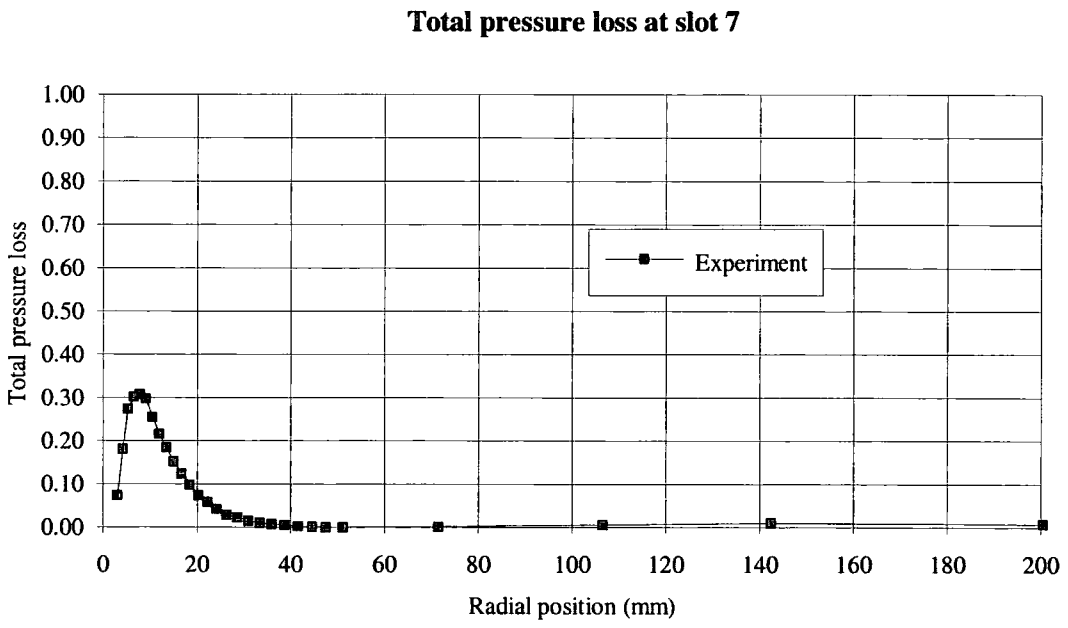

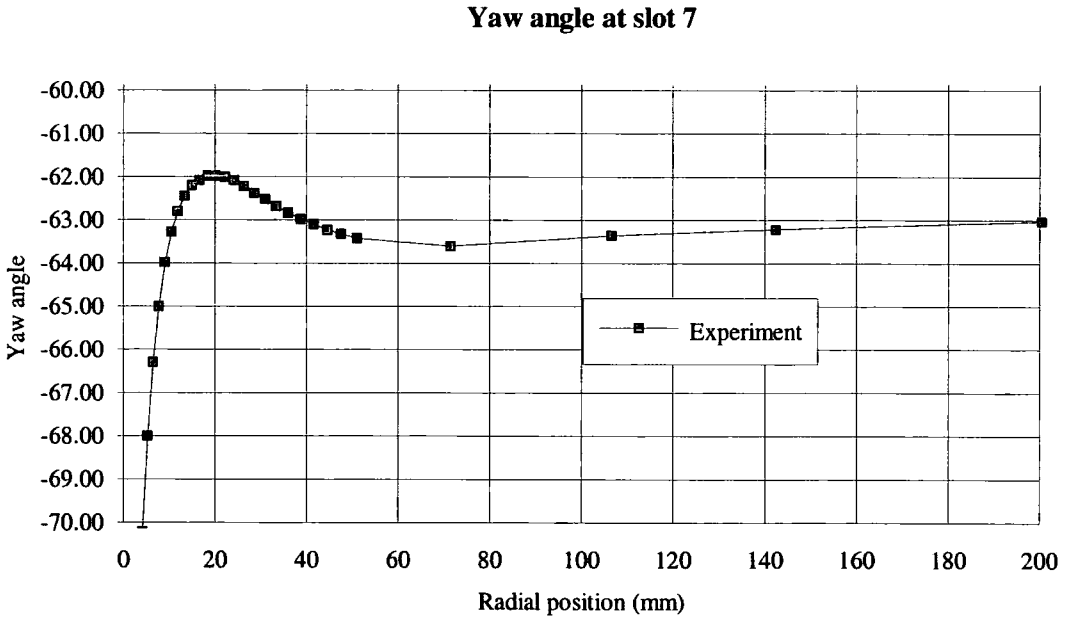

Figure 4.15—Pitch averaged results for Slot 7

a) Total pressure loss contours

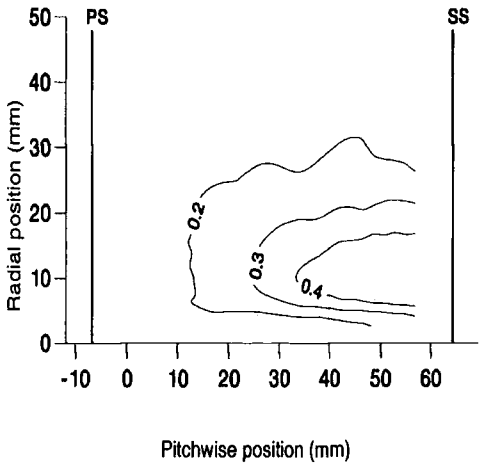

b) Secondary kinetic energy contour (%)

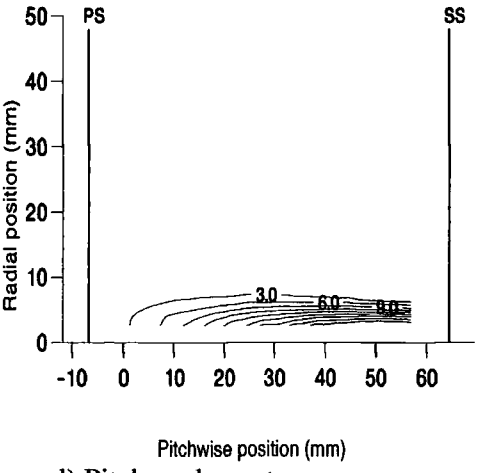

c) Yaw angle contour

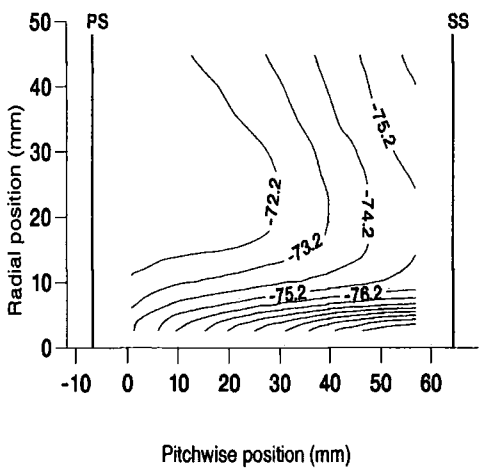

d) Pitch angle contour

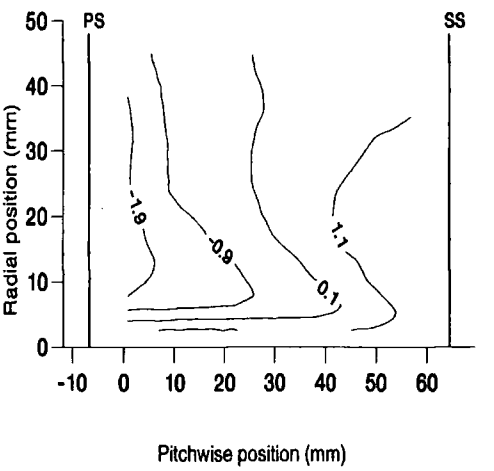

e) Secondary vector plot

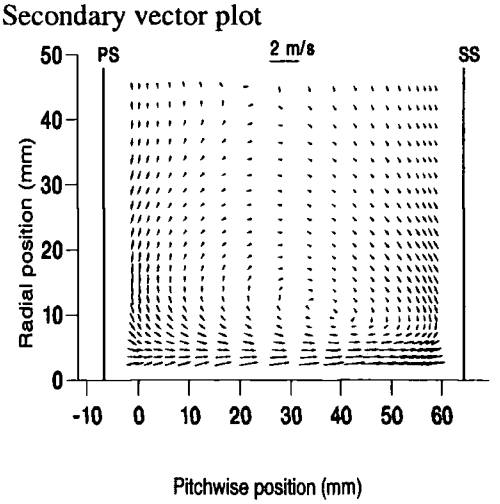

Figure 4.16—Area traverse of Slot 8

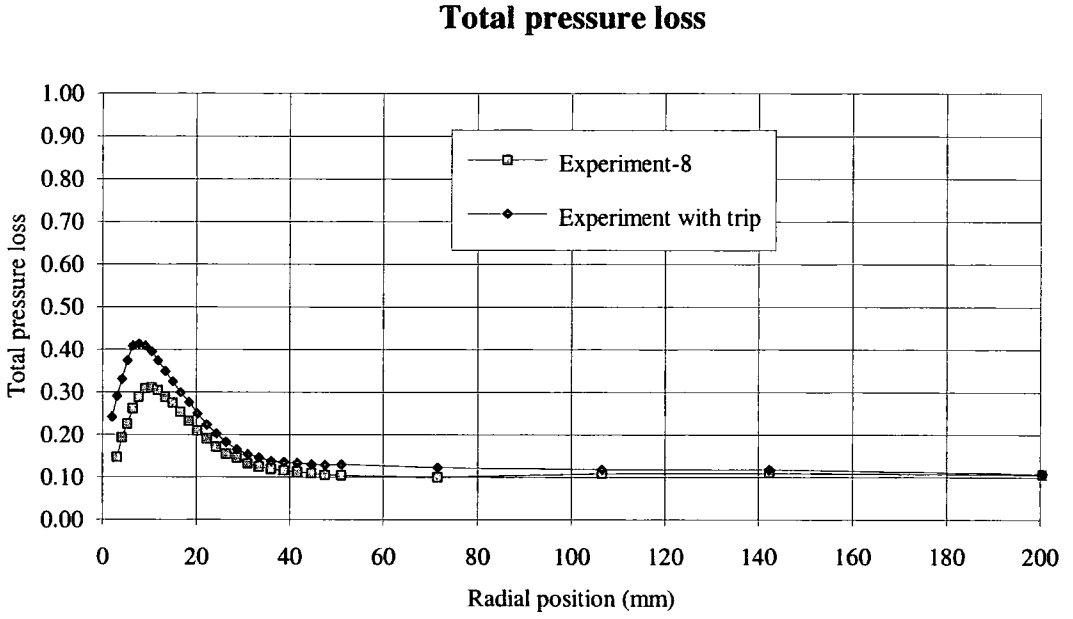

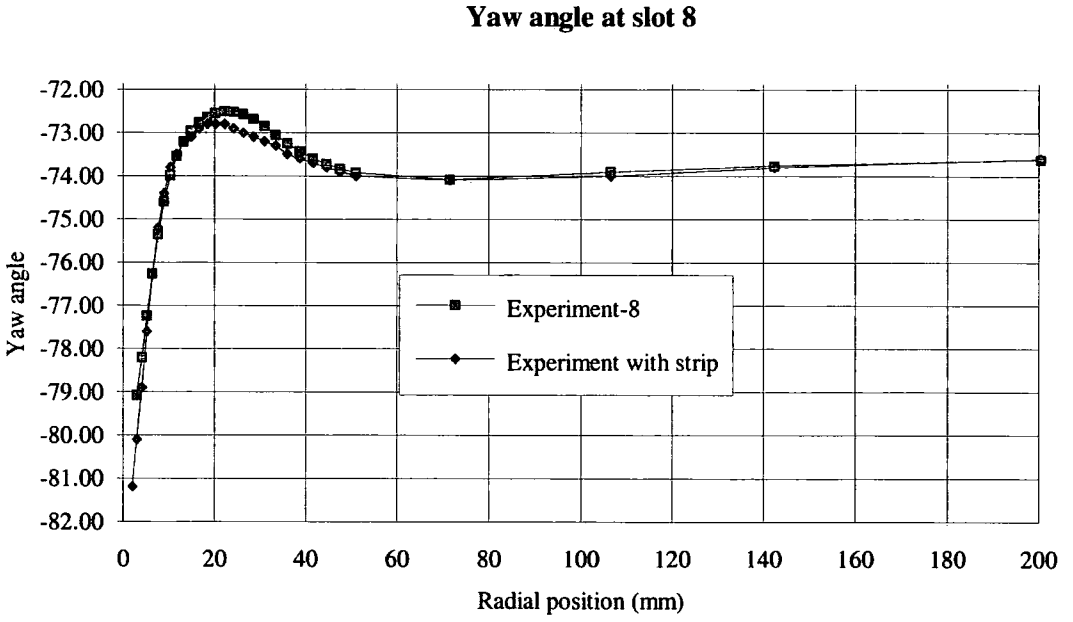

Figure 4.17—Pitch averaged results for Slot 8

a) Total pressure loss contours

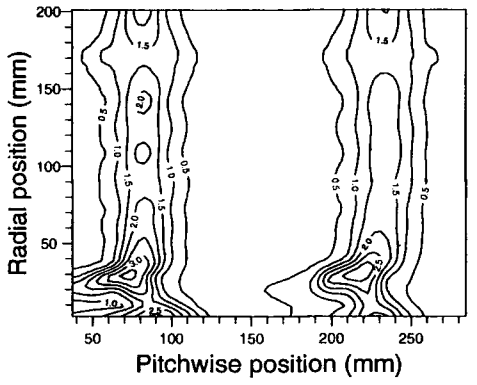

b) Secondary kinetic energy contour (%)

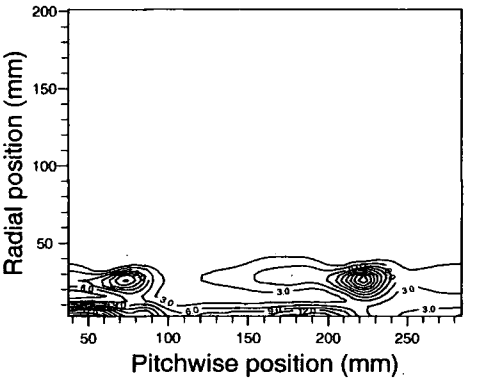

c) Yaw angle contour

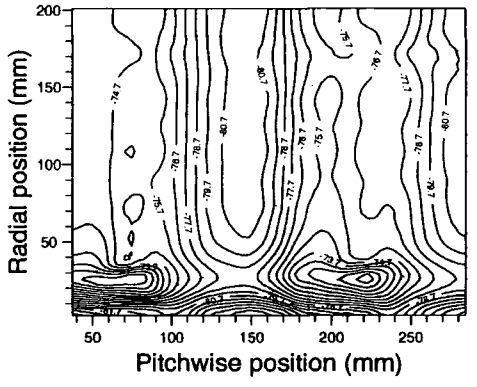

d) Pitch angle contour

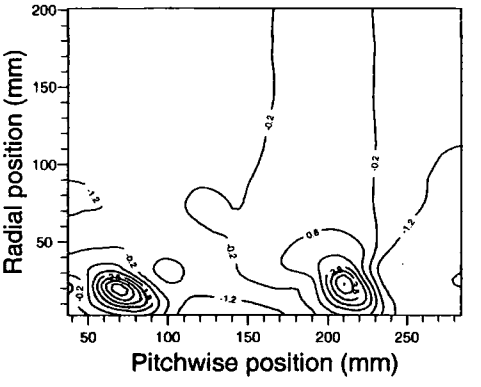

e) Secondary vector plot

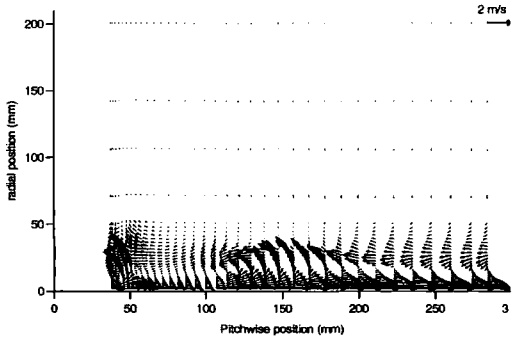

Figure 4.18—Half span area traverse of Slot 9

a) Total pressure loss contours

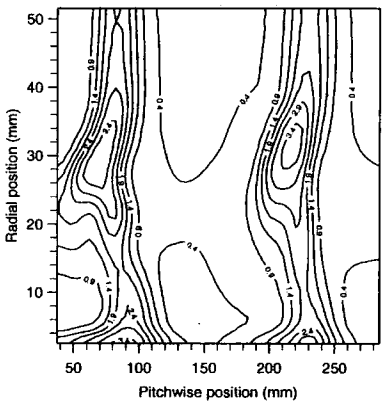

b) Secondary kinetic energy contour (%)

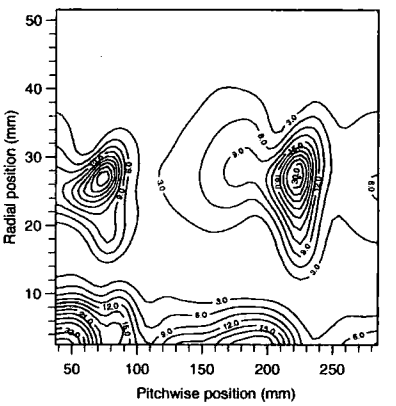

c) Yaw angle contour

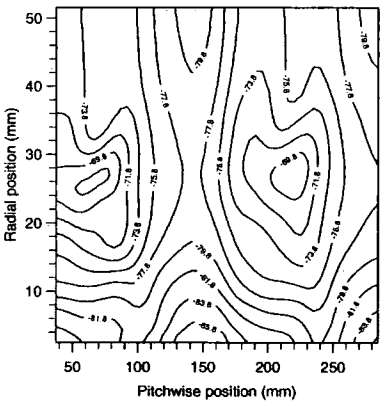

d) Pitch angle contour

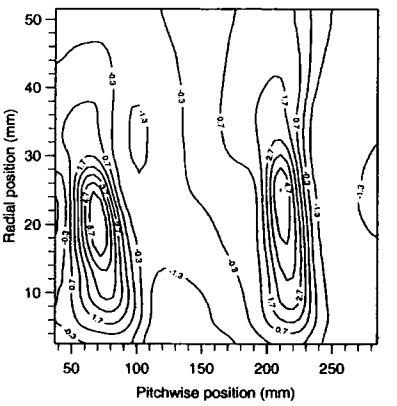

e) Secondary vector plot

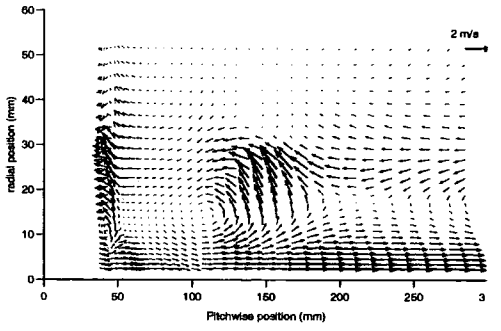

Figure 4.19—Near wall area traverse of Slot 9

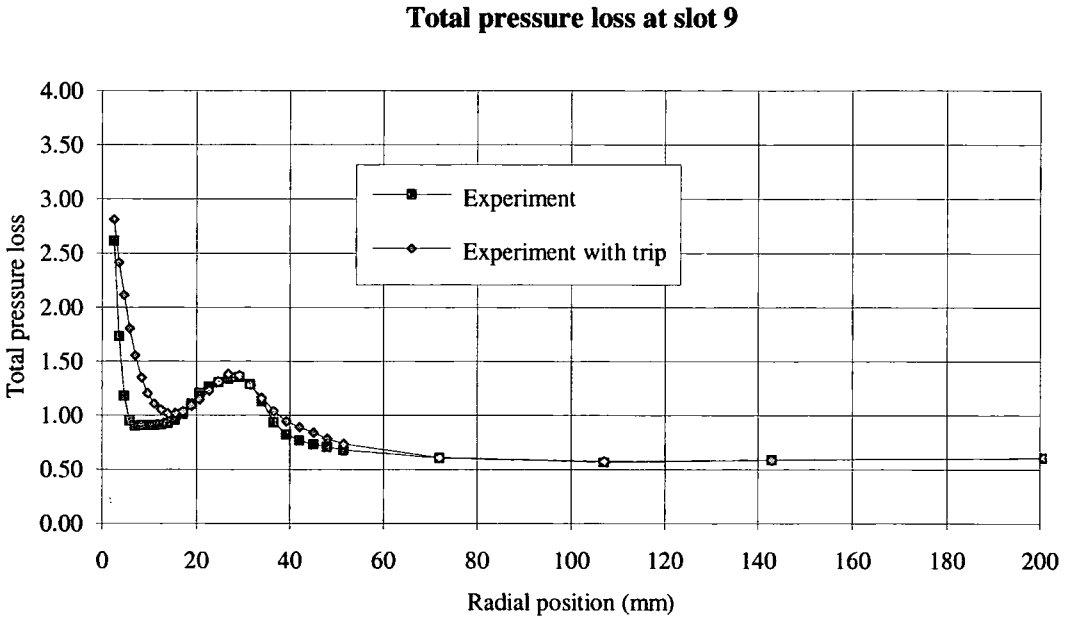

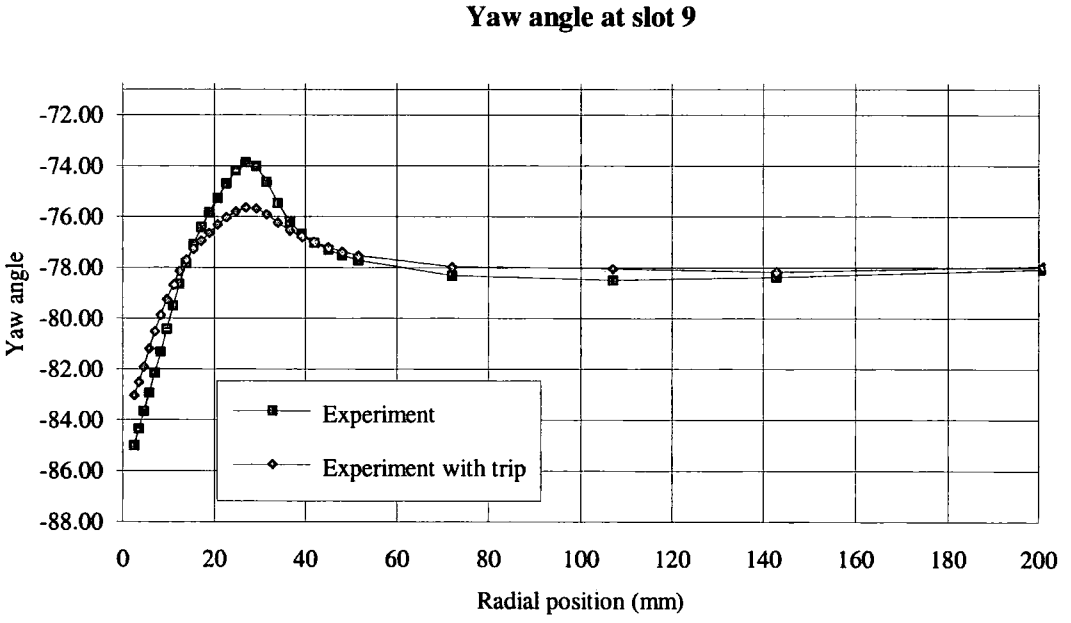

Figure 4.20—Pitch averaged results for Slot 9

a) Total pressure loss contours

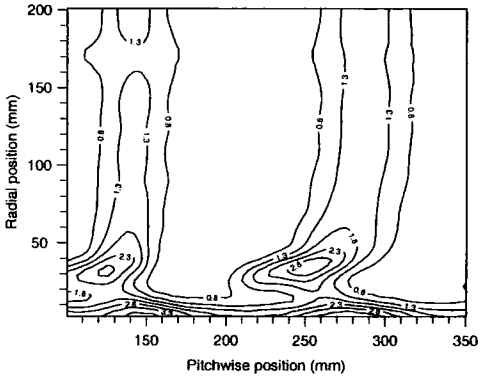

b) Secondary kinetic energy contour (%)

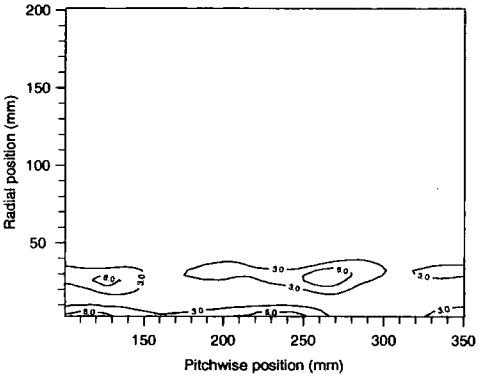

c) Yaw angle contour

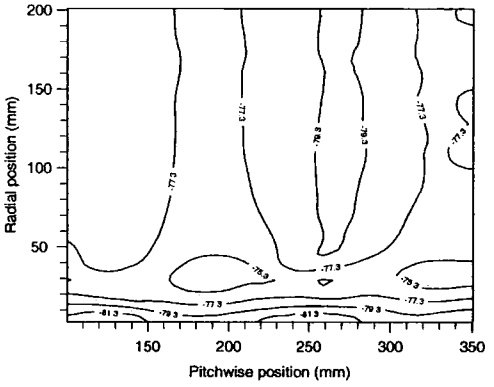

d) Pitch angle contour

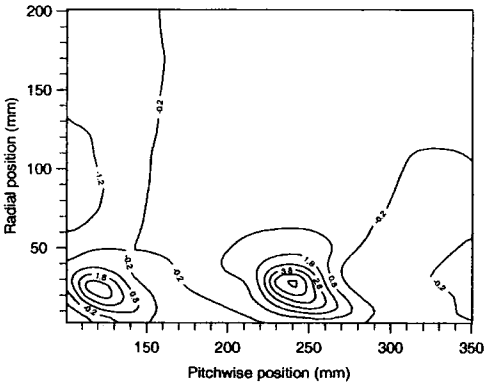

e) Secondary vector plot

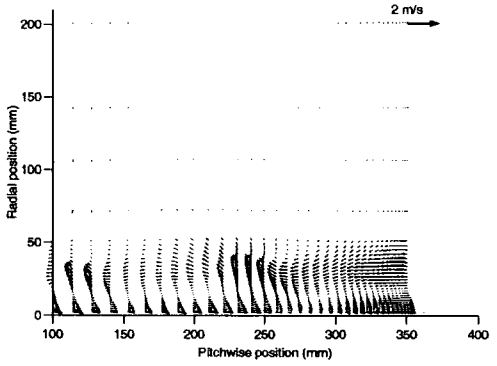

Figure 4.21—Half span area traverse of Slot 10

a) Total pressure loss contours

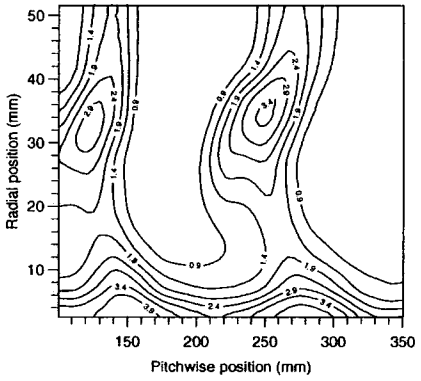

b) Secondary kinetic energy contour (%)

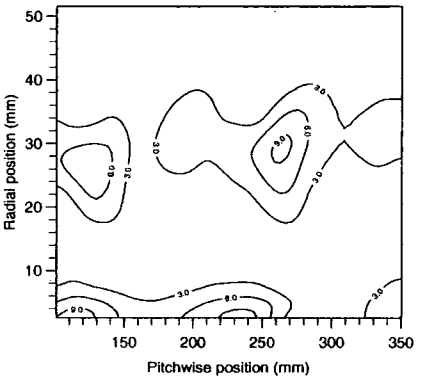

c) Yaw angle contour

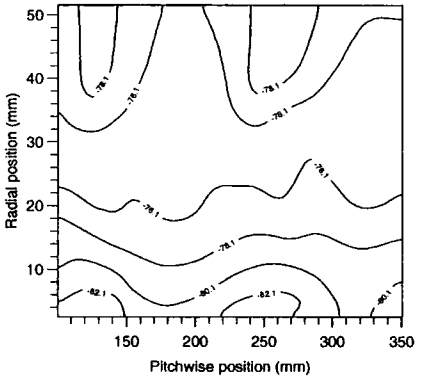

d) Pitch angle contour

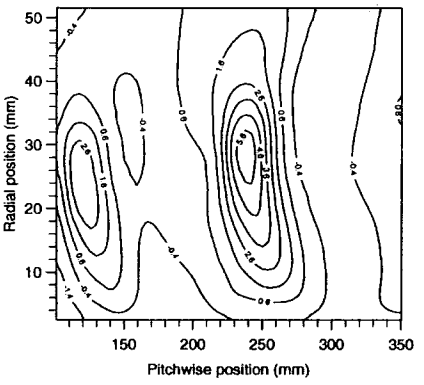

e) Secondary vector plot

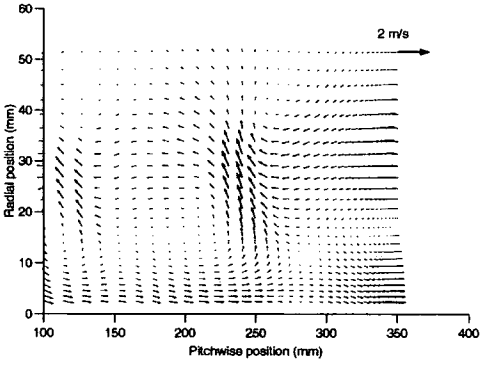

Figure 4.22—Near wall area traverse of Slot 10

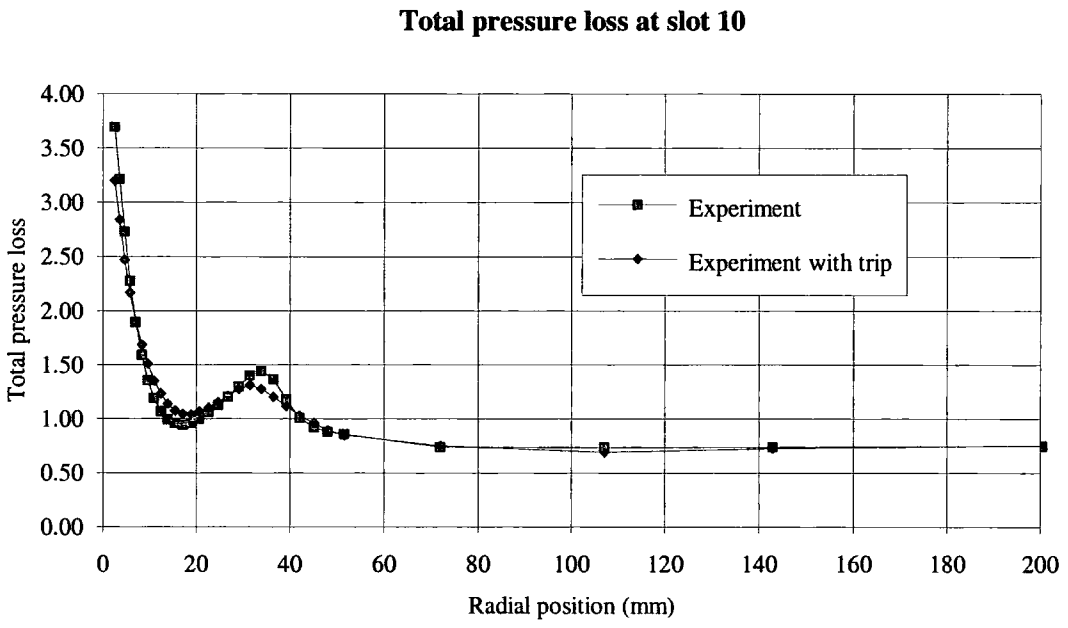

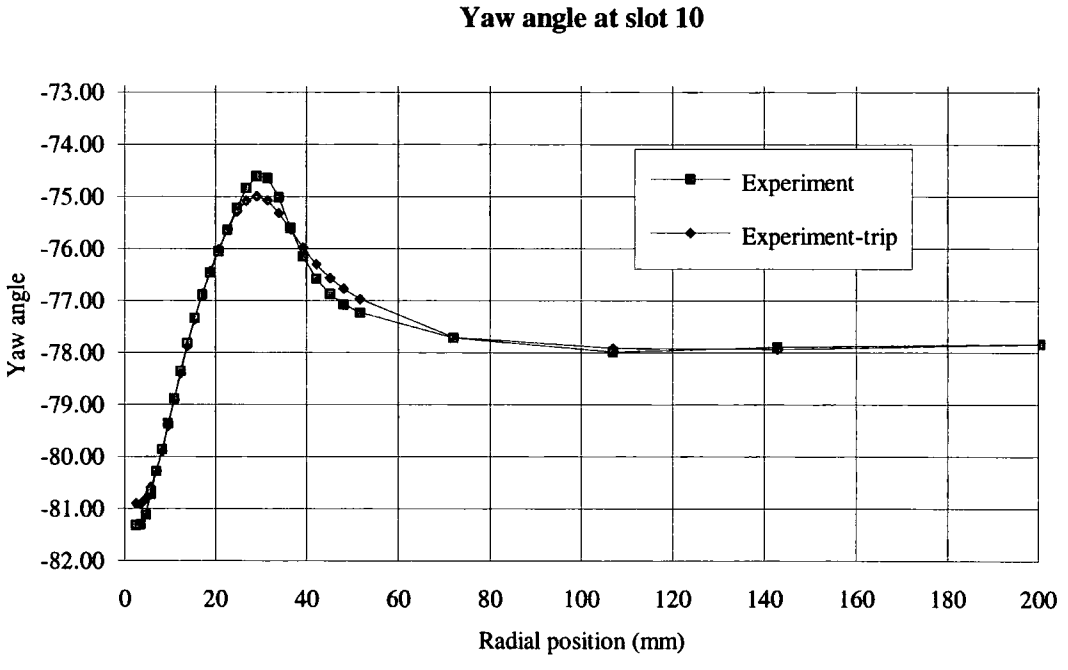

Figure 4.23—Pitch averaged results for Slot 10

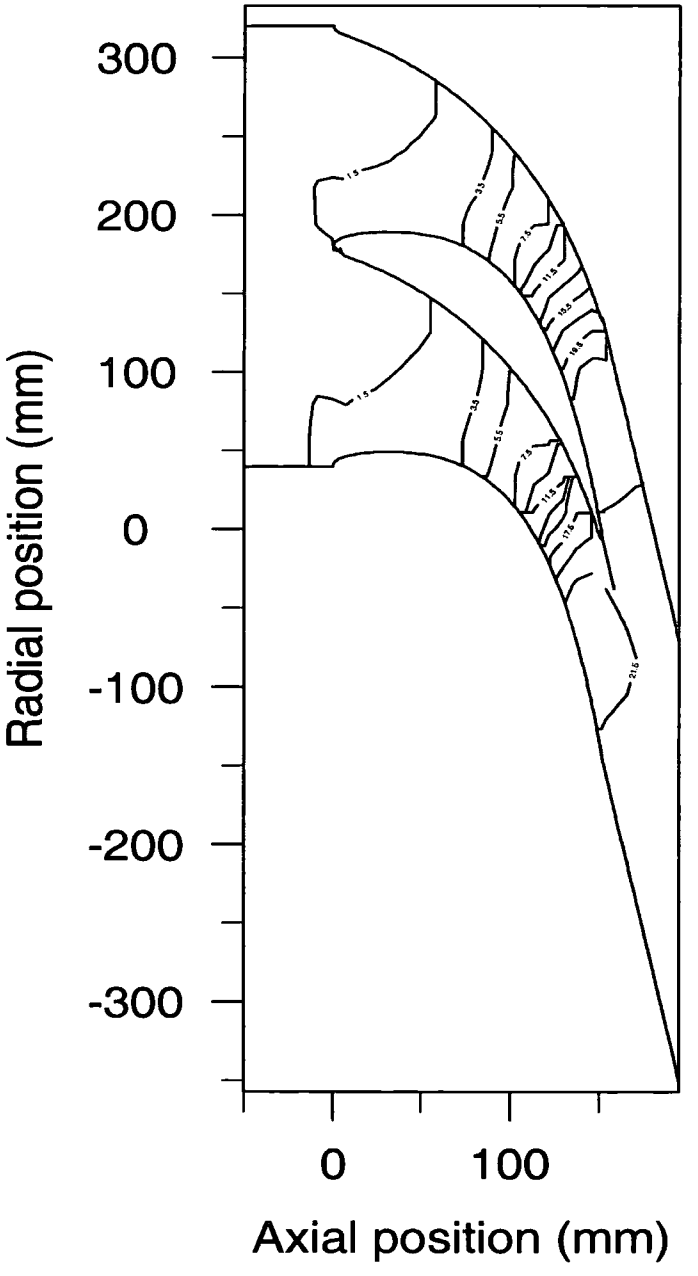

Figure 4.24—Static pressure on the flat end wall

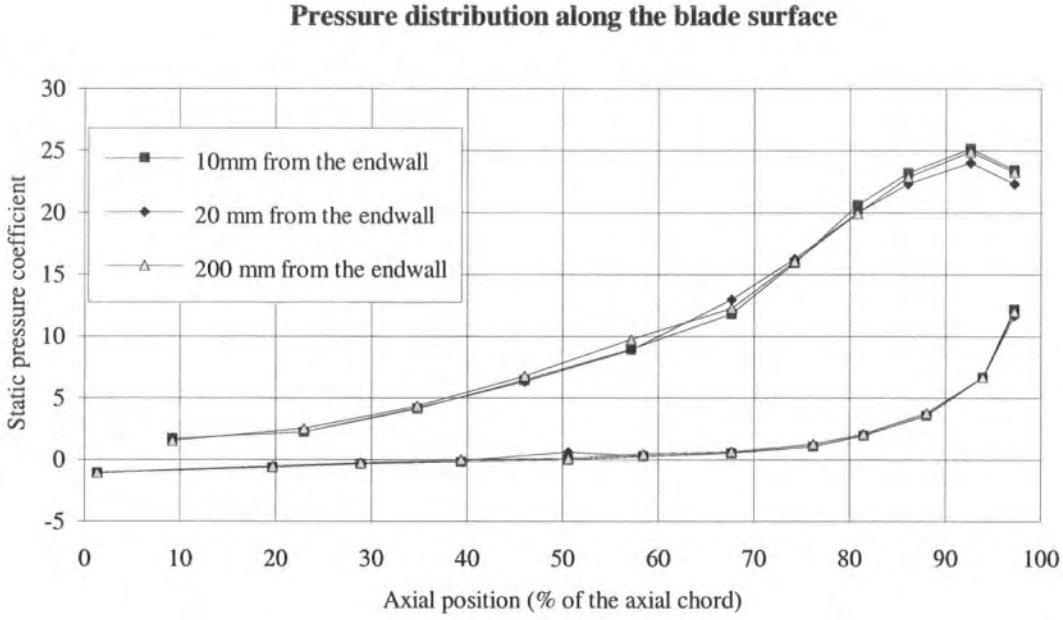

Figure 4.25—Static pressure around the blade surfaces

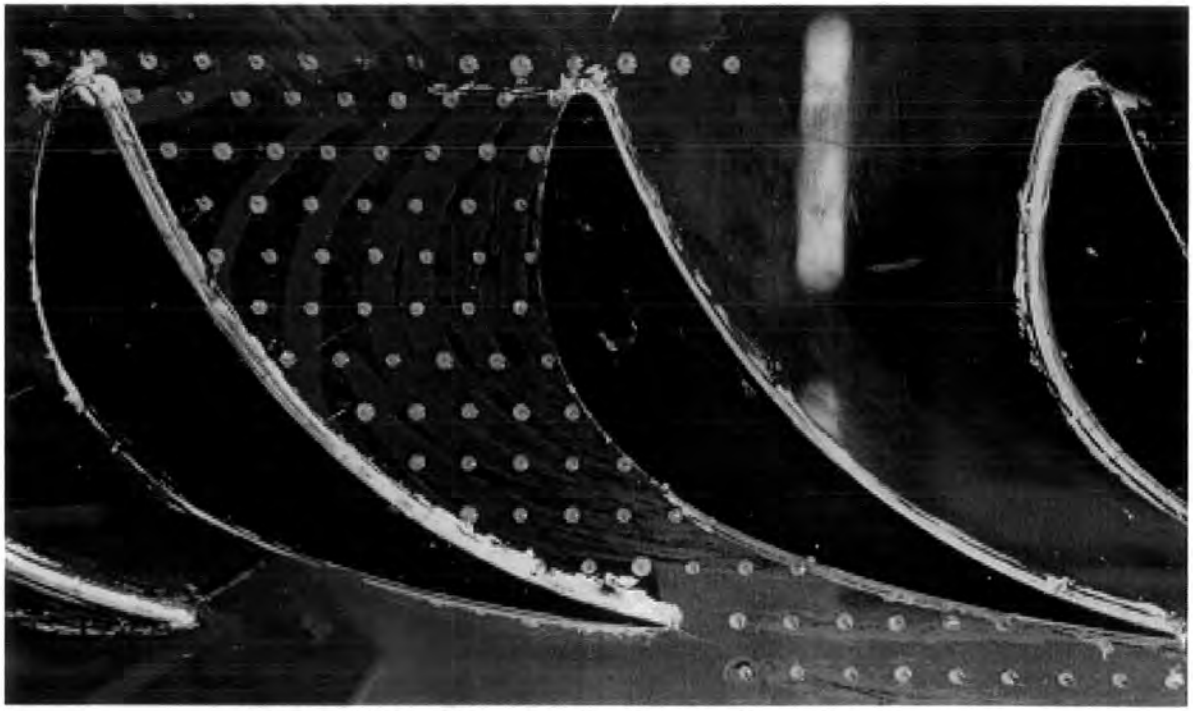

Figure 4.26—Flow visualisation on the end wall

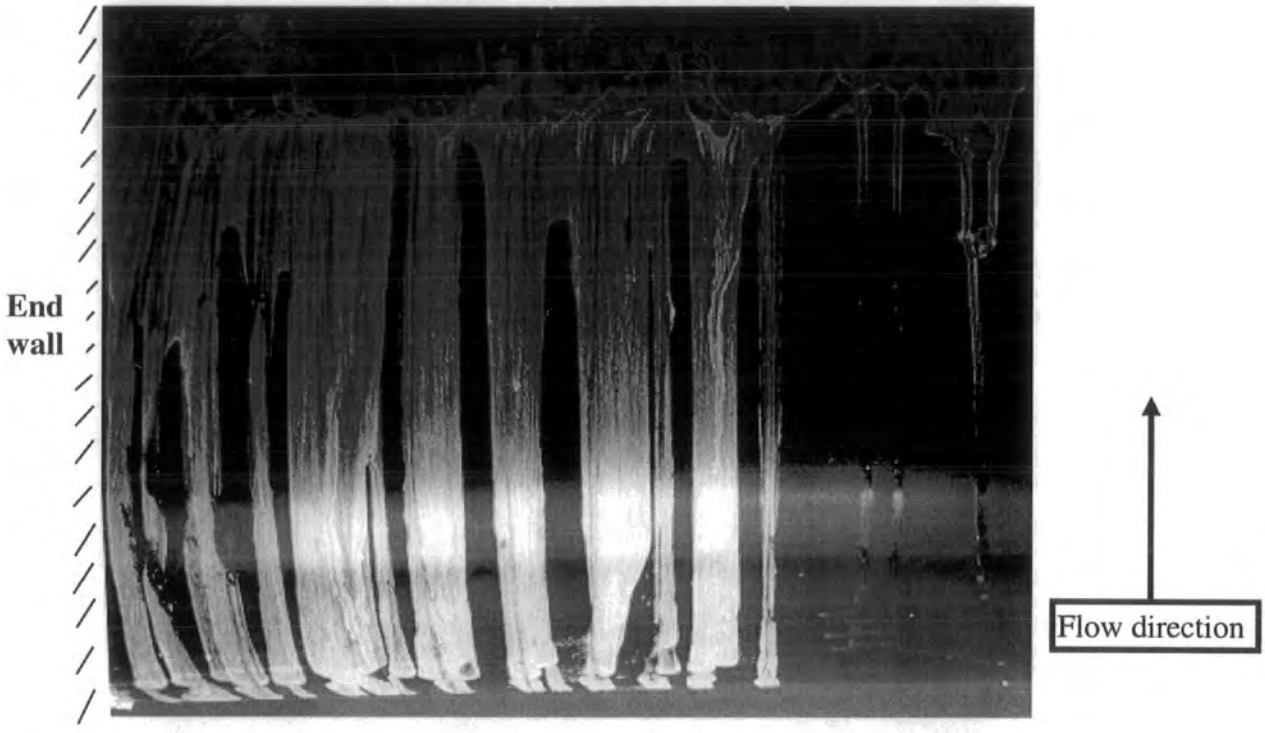

Figure 4.27—Flow visualisation on the blade suction surface

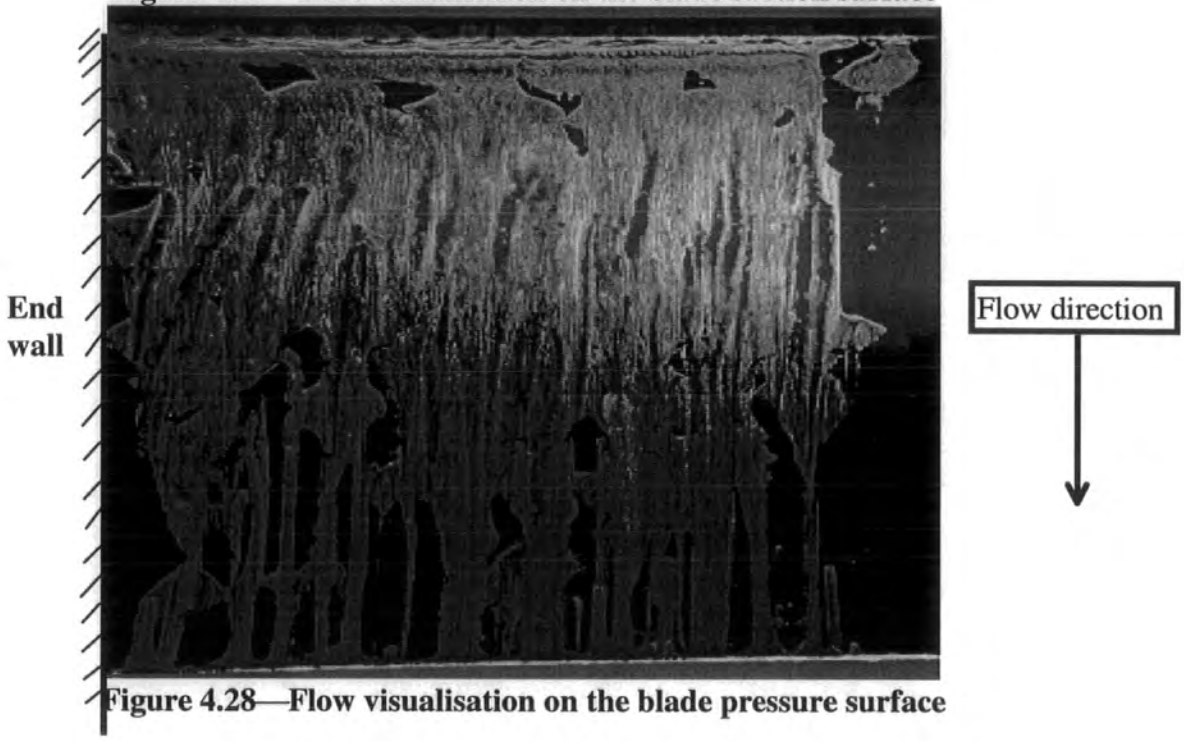

Figure 4.28—Flow visualisation on the blade pressure surface

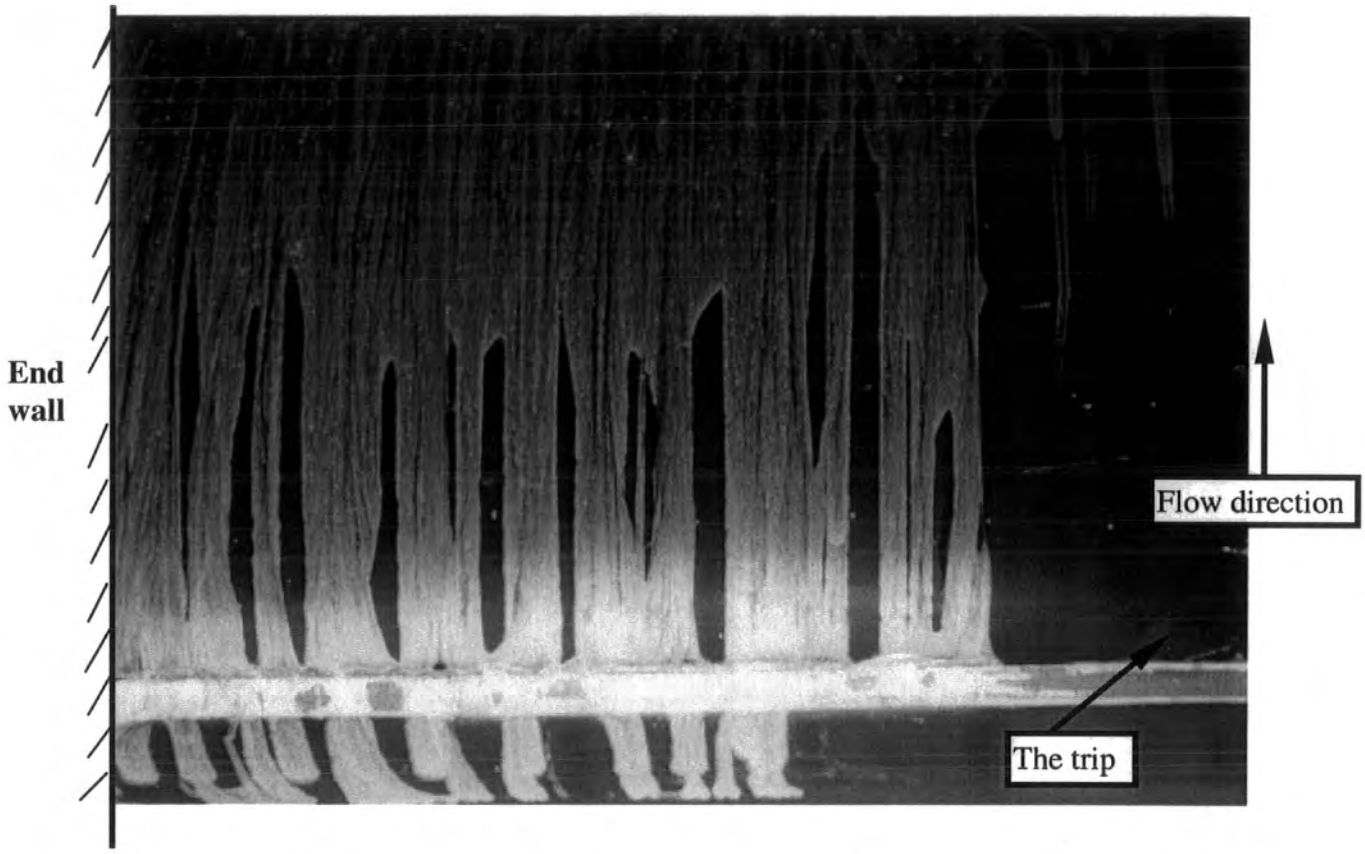

Figure 4.29—Flow visualisation on the suction surface with transition trip

a) Total pressure loss contours

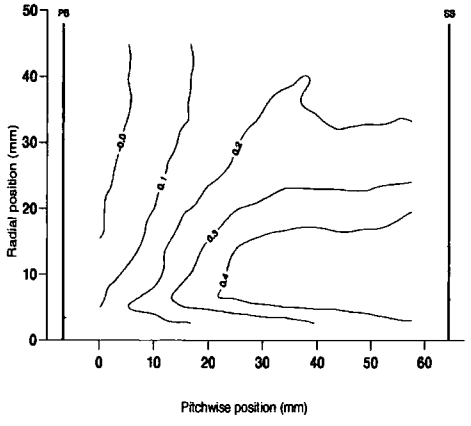

b) Secondary kinetic energy contour (%)

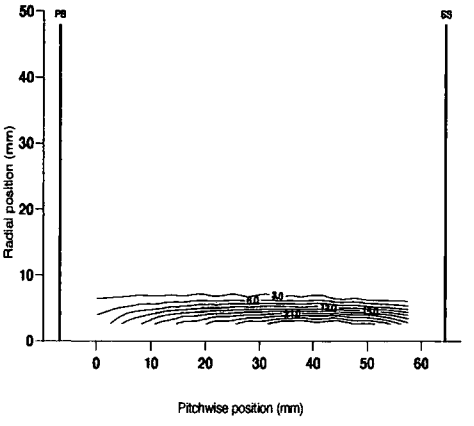

c) Yaw angle contour

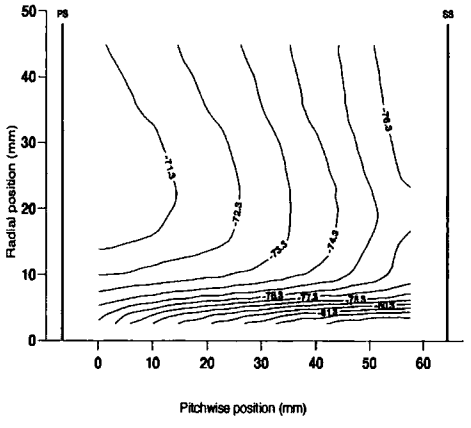

d) Pitch angle contour

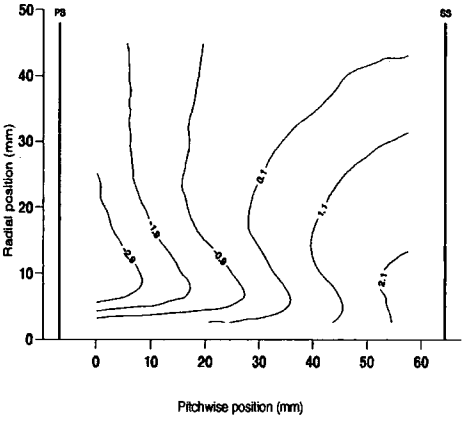

e) Secondary vector plot

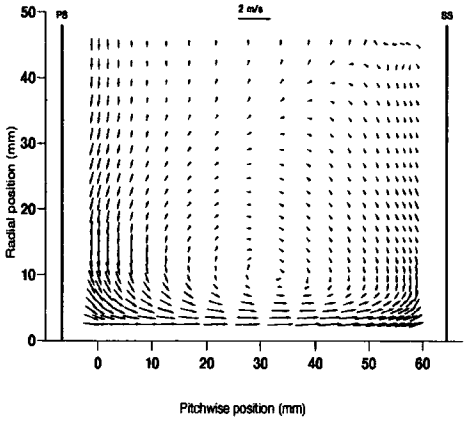

Figure 4.30—Area traverse of Slot 8 with trip

a) Total pressure loss contours

b) Secondary kinetic energy contour (%)

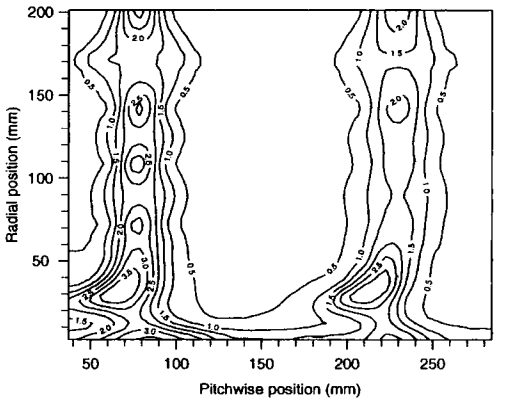

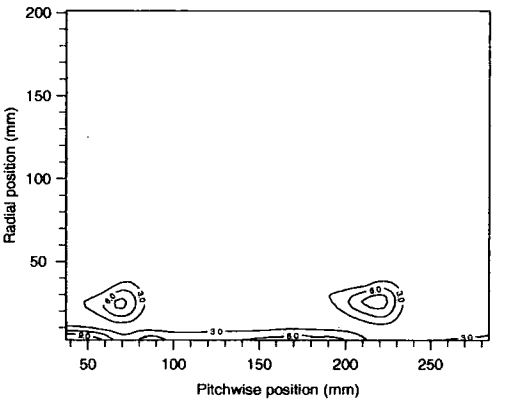

c) Yaw angle contour

d) Pitch angle contour

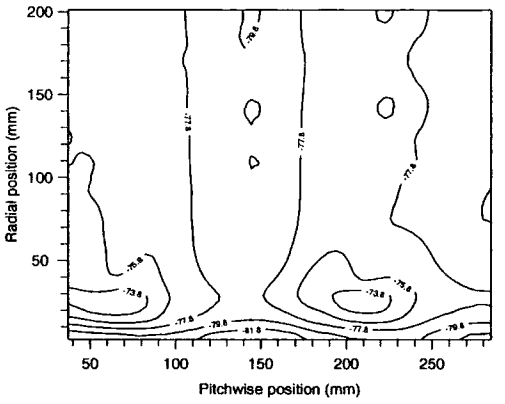

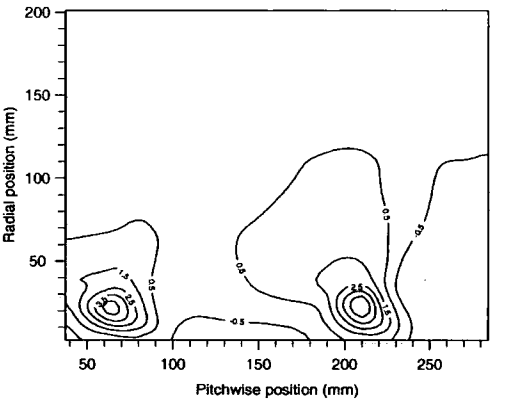

e) Secondary vector plot

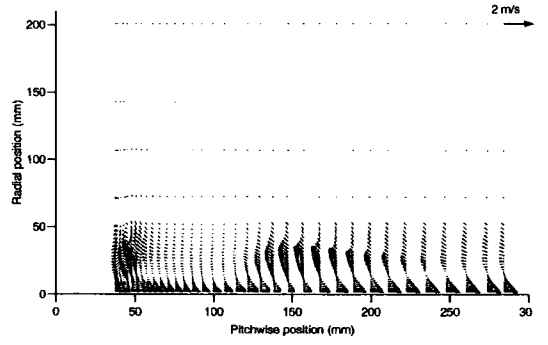

Figure 4.31—Half span Area traverse of Slot 9 with trip

a) Total pressure loss contours

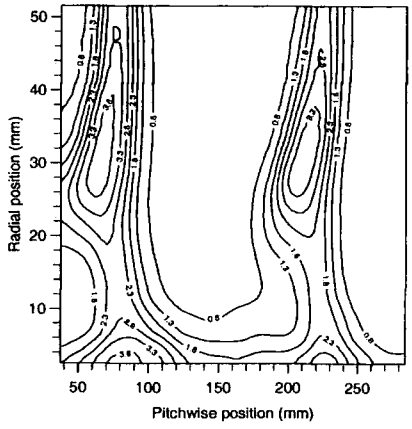

b) Secondary kinetic energy contour (%)

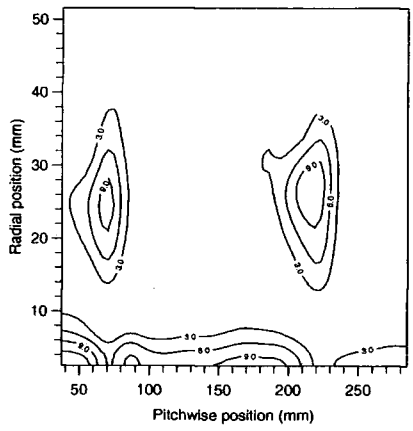

c) Yaw angle contour

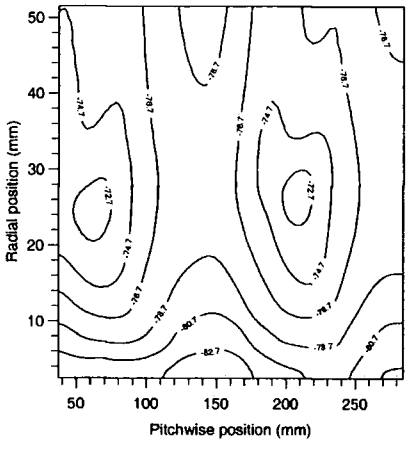

d) Pitch angle contour

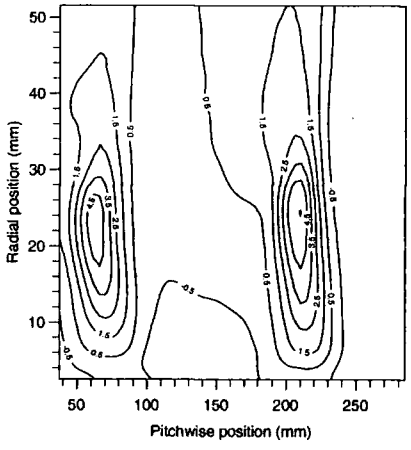

e) Secondary vector plot

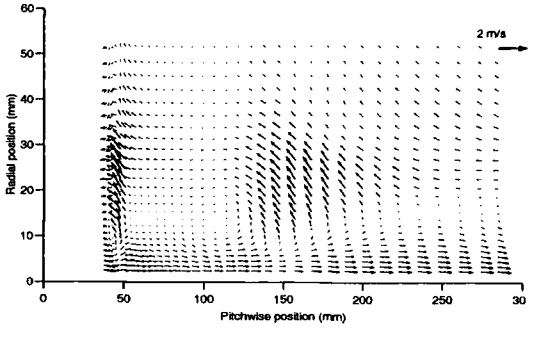

Figure 4.32—Near wall Area traverse of Slot 9 with trip

a) Total pressure loss contours

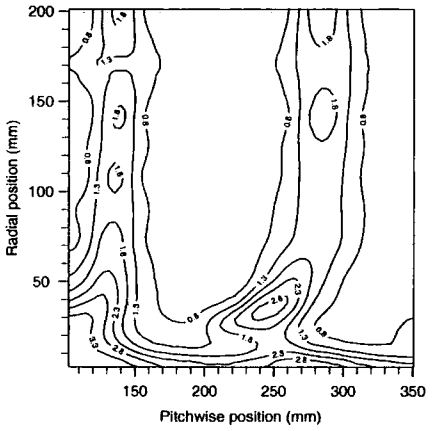

b) Secondary kinetic energy contour (%)

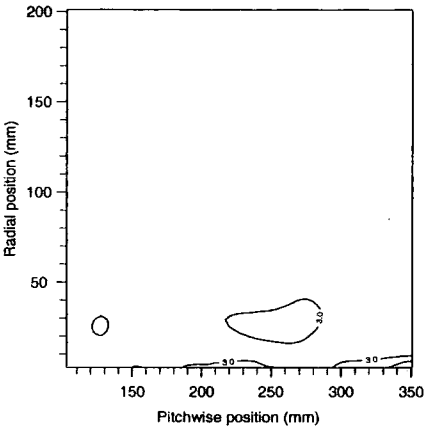

c) Yaw angle contour

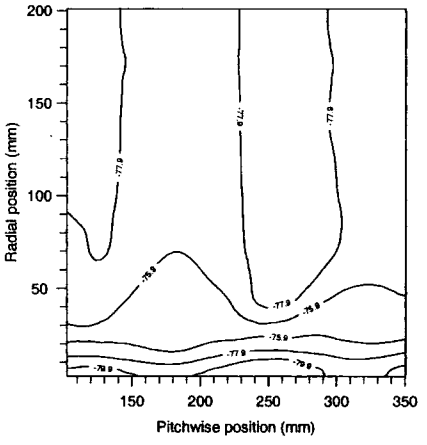

d) Pitch angle contour

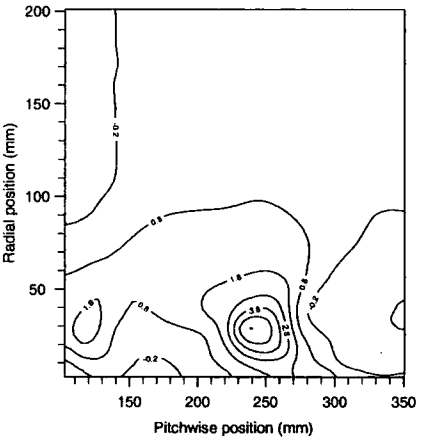

e)Secondary vector plot

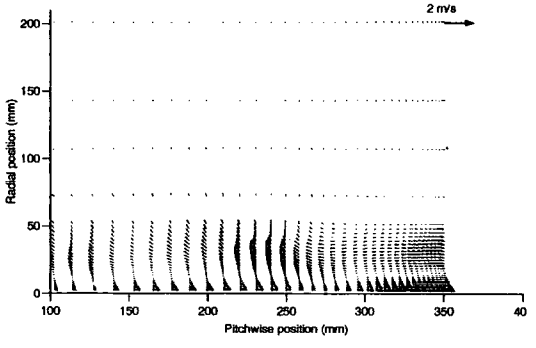

Figure 4.33—Half span Area traverse of Slot 10 with trip

a) Total pressure loss contours

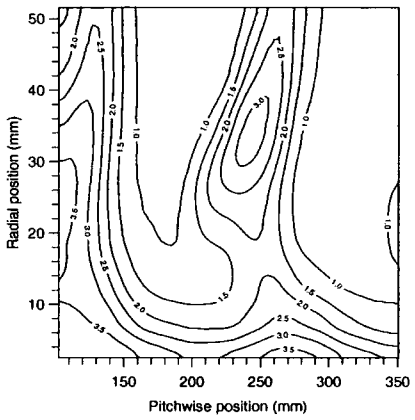

b) Secondary kinetic energy contour (%)

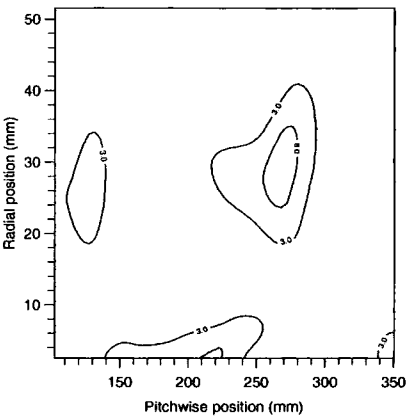

c) Yaw angle contour

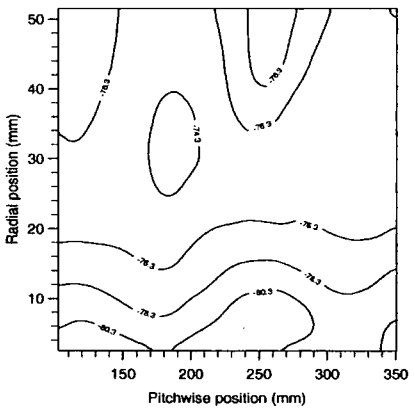

d) Pitch angle contour

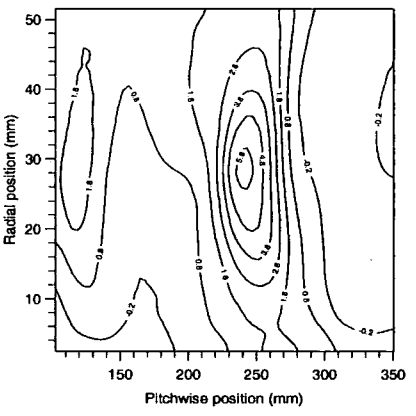

e) Secondary vector plot

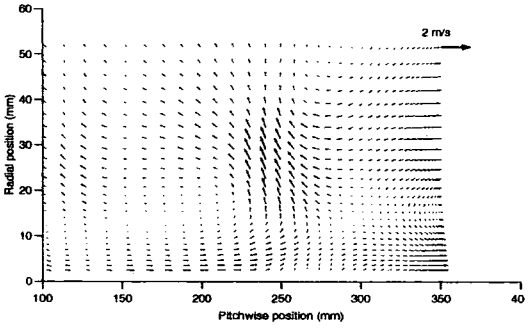

Figure 4.34—Near wall Area traverse of Slot 10 with trip

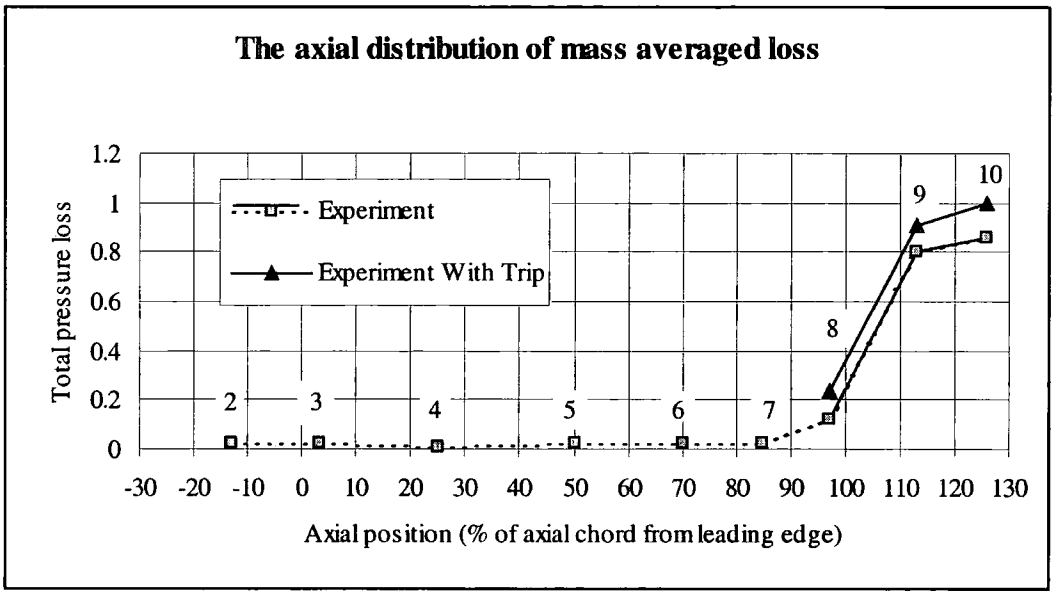

Figure 4.35—The development of mass averaged total pressure loss across the blade passage

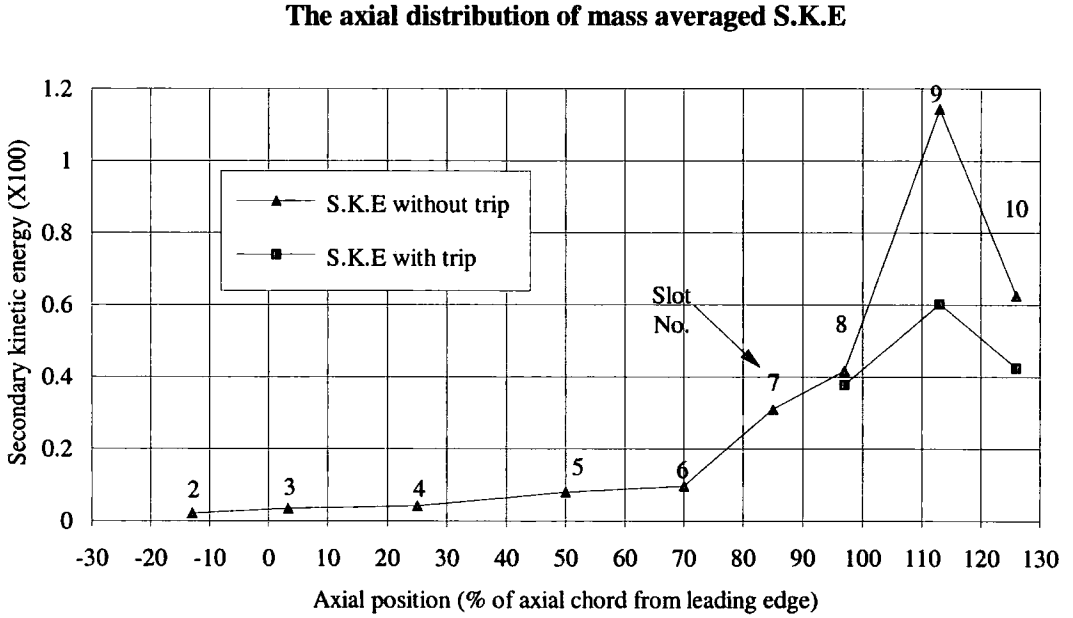

Figure 4.36—The development of mass averaged secondary kinetic energy across the blade passage

Chapter 5

Description and Validation of Computational Codes

5.1 Introduction

The CFD codes are described in this chapter. The turbulence models, the numerical schemes, input format and output format are discussed. Different numerical schemes and turbulence models were tested against Durham cascade test case in a 2-D calculation. A 3-D calculation of Durham cascade test case was then carried out. The results were compared with those from experiments. A 2-D calculation of the Nozzle blade was compared with the experimental results from ALSTOM. A 3-D calculation of the nozzle cascade with a flat end wall were completed and the results were compared with those of the experiments.

5.2 A brief description of the code.

The program that is being used is a 3-D viscous pressure correction code from **ALSTOM**. The program needs substantial memory and high computing speed and was performed on a Silicon Graphics work station. Because only the executable program of the main part was received, the details of methods used in this program are not given.

Together with the main program there is an input program which accepts data from the user and transfers it to the main program. The source code of this part was made available. This input program was modified according to the actual conditions of the cascade to be tested. The input program was initially written only for a cylindrical end wall. It was rewritten to fit the shaped end wall which is actually 3-D. Beside this, an input file including all the information required by the main program was created. A number of programs have been written to post-process the solution file. Because the program was-still in the process of development, a great deal of time had been spent on making it work on the 3-D end wall case.

5.2.1 The scheme of the CFD program.

The program was written using a fully implicit scheme. In general, there are three different schemes which are the explicit scheme, the Crank-Nicolson scheme and the fully implicit scheme.

The explicit scheme is convenient but has a serious limitation. In order to get a physically realistic result a stability condition must be satisfied which leads to a large number of iterations.

The Crank-Nicolson scheme is usually described as unconditionally stable. However, it does not mean that a physically realistic solution will result no matter how large the iteration step. It does not guarantee physically accurate solutions.

It seems the fully implicit scheme could achieve a solution which is closer to reality than the Crank-Nicolson scheme over a comparatively larger interval. This method can satisfy requirements of simplicity and physical reality. This is the reason why the fully implicit scheme was chosen here.

In the iterative solution of the algebraic equations or in the overall iterative scheme employed for handling non-linearity, it is often desirable to speed up or slow down the changes in the values of the dependent variables from iteration to iteration. This process is called over-relaxation or under-relaxation, depending on whether the variable changes are accelerated or slowed down. In this program under-relaxation is used to slow down the changes. In order to avoid divergence and keep a high speed there are two groups of under-relaxation factors in this program. One of them gives smaller values to make the initial iteration convergent. When the error has become smaller than a certain value the program uses another group of under-relaxation factors which are larger to make the iteration faster. Both of the two groups of under-relaxation factors are decided by users in the input data file.

5.2.2 The calculation method.

In this main program the pressure correction scheme SIMPLE is used. A brief introduction to the pressure correction method is given here following the description by Patankar (1980).

For a real flow field, the difficulty in calculation of the velocity lies in the unknown pressure field. The pressure gradient forms part of the source term for a momentum equation. Yet, there is no obvious equation for obtaining pressure. The difficulty associated with the determination of pressure has led to methods that eliminate pressure from the governing equations such as vorticity-based methods. There are, however, some major disadvantages to these methods. The value of vorticity at a wall is difficult to specify and is often the cause of trouble in getting a converged solution. The major shortcoming of the method is that it can not easily be extended to three dimensional situations. Thus the pressure correction method was developed. This method is

physically meaningful and uses the so-called primitive variables, namely the velocity components and pressure. The pressure correction procedure is briefly described below:

1. Guess the pressure field p*.

2. Solve the momentum equation to obtain u*, v*, w*.

3. Solve the p' equation. (The p' is a pressure correction derived from continuity equation.)

4. Calculate the corrected pressure p : p=p*+p' (at this stage, the under-relaxation is probably used in this form: p=p*+αp' where α refers to the under-relaxation coefficient.).

5. Calculate u, v, w from their starred values using the velocity-correction formulas. (The under-relaxation is used here as well.)

6. Solve the discretization equations for other variables such as temperature, concentration, and turbulence quantities if they influence the flow field through fluid properties, source terms, etc. (If a particular quantity does not influence the flow field, it is better to calculate it after a converged solution for the flow field has been obtained.)

7. Treat the corrected pressure as a new guessed pressure p*, return to step 2, and repeat the whole procedure until a converged solution is obtained.

5.2.3 Numerical schemes

The numerical schemes in the codes are UPWIND, QUICKS, MINMOD and UMIST. In the input file, there are two options for different numerical schemes. The first one is

for the momentum equation. The second one is the numerical scheme for the scalar variables. The accuracy of the computational codes is determined by the numerical scheme being used. High order schemes lead to better accuracy but higher instability.

1 The UPWIND scheme

The simplest scheme available in this program is the first order UPWIND scheme. The scheme offers a high level of robustness. It also creates an unacceptable high level of numerical errors if the flow field is not aligned with the grid lines. It is known that in 3-D calculations the numerical errors increase when the flow-grid skewness is increased. Furthermore, if the skewness is too high, the numerical errors may swamp the real physical process.

2 The QUICKS scheme

The QUICKS scheme developed by Leonard (1979) is a combination of a central difference scheme, which can offer high order of accuracy and easy implementation, and an UPWIND which can offer high stability. Being investigated by several researchers, this scheme seems to hold a good compromise of accuracy and stability though it tends to create oscillation around discontinuities due to its unboundness.

3 The MINMOD scheme and the UMIST scheme

The MINMOD scheme is a modern approach of TVD (Total Variation Diminishing) to obtain stability. This scheme avoids the overshoot around the sharp gradient or discontinuities by limiting the gradients in the formulation of the high-order schemes. The UMIST scheme is a similar high order scheme with limiter to the MINMOD. It is always used for scalar variables in the computation codes.

5.2.4 The turbulence models

The turbulence models used in this program are the standard k-ε model and its modified version which is called S-Ω modification proposed by Launder and Kato (1993).

1 The k-ε turbulence model from White (1991)

For turbulent flow, the mean motion is of primary interest. The Reynolds-averaged governing equations for the incompressible turbulent flow are shown in tensor notation below:

$$\frac{\partial \overline{u_i}}{\partial x_i} = 0 \tag{5.1}$$

$$\overline{u_j}\frac{\partial \overline{u_i}}{\partial x_j} = -\frac{1}{\rho}\frac{\partial \overline{p}}{\partial x_i} + \frac{1}{\rho}\frac{\partial}{\partial x_j}\left(\mu\frac{\partial \overline{u_i}}{\partial x_j}\right) - \frac{\partial}{\partial x_j}\overline{u_i' u_j'} \tag{5.2}$$

Where $\overline{u_i}$ are mean values and u_i' are turbulent fluctuations. The $\overline{u_i' u_j'}$ terms are the Reynolds stresses which appear as a result of the time averaging. The Reynolds averaged equation is not closed unless a model is provided that ties the Reynolds stress to the global history of the mean velocity in a physically consistent fashion. This model is the turbulence model.

In the k-ε turbulence model, differential equations are introduced for the turbulent kinetic energy k and the rate of dissipation of turbulent energy ε , where

$$k = 0.5(\overline{u'u'} + \overline{v'v'} + \overline{w'w'}) = 0.5(\overline{u_i'u_i'}) \tag{5.3}$$

and

$$\varepsilon = \nu_l \overline{(\frac{\partial u_i'}{\partial x_j})(\frac{\partial u_i'}{\partial x_j})} \tag{5.4}$$

The governing equations for k and ε proposed by Jones and Launder (1972) are

$$\rho\frac{Dk}{Dt} = \frac{\partial}{\partial x_j}(\frac{\mu_T}{\sigma_k}\frac{\partial k}{\partial x_k}) + \mu_T(\frac{\partial u_i}{\partial x_j} + \frac{\partial u_j}{\partial x_i}) - \rho\varepsilon \tag{5.5}$$

and

$$\rho\frac{D\varepsilon}{Dt} = \frac{\partial}{\partial x_j}(\frac{\mu_T}{\sigma_k}\frac{\partial \varepsilon}{\partial x_j}) + \frac{C_{\varepsilon 1}\mu_T\varepsilon}{k}(\frac{\partial u_i}{\partial x_j} + \frac{\partial u_j}{\partial x_i})\frac{\partial u_i}{\partial x_j} - \frac{\rho C_{\varepsilon 2}\varepsilon^2}{k} \tag{5.6}$$

The left-hand side of equation 5.5 and 5.6 represent transport of k and ε, respectively. The three terms on the right-hand side represent diffusion, production and dissipation, respectively.

From the local values of k and ε, a local (turbulent) eddy viscosity μ_T can be evaluated as:

$$\mu_T = \frac{C_\mu \rho k^2}{\varepsilon} \tag{5.7}$$

And the eddy viscosity is used to relate the Reynolds stress, in equation 5.2 and 5.3, to the mean quantities by:

$$-\rho\overline{u_i u_j} + \frac{2}{3}\rho k\delta_{ij} = \mu_T(\frac{\partial u_i}{\partial x_j} + \frac{\partial u_j}{\partial x_i}) \tag{5.8}$$

Where, $\delta_{ij} = 1$ for i=j.

$\delta_{ij} = 0$ for i≠j.

In above equations the following values are used for the recommended empirical constants for attached boundary layer calculations by White (1991):

$$C_\mu = 0.09, \quad C_{\varepsilon 1} = 1.45, \quad C_{\varepsilon 2} = 1.90, \quad \sigma_k = 1.0, \quad \sigma_\varepsilon = 1.3$$

These values are not universal but have to be modified for other problems such as jets and wakes and recirculating flows.

The above k-ε model, which is a high Reynolds number form of the k-ε turbulence model, is used in combination with a wall function by Launder and Spalding (1974) to describe the turbulent flows in this program. Away from the walls the turbulent viscosity is obtained from equation 5.8. The equation 5.8 is only valid where the direct influence of molecular viscosity is negligible. Therefore, within boundary layers the wall function is used. Because the wall function used here does not accommodate the buffer region or the viscous sub-layer, it is very important that the near wall grid points are within the logarithmic region($12 \leq R_y \leq 200$) for acceptable results to be obtained. Here, R_y is a function of the wall shear-stress, τ_w, the normal distance to the wall, y, and the laminar kinematic viscosity, υ_l as follows:

$$R_y = y\sqrt{\tau_w / \rho} / \nu_l \qquad (5.9)$$

2 S-Ω modification

One weakness of the standard k-ε models is that they can predict excessive levels of turbulence due to the fact that irrotational strain terms (they are the second right hand side term of equation 5.5 in the turbulence energy equation) act to generate turbulence irrespective of their sign. The S-Ω modification proposed by Launder and Kato (1993)

provides a method of alleviating this problem by replacing the strain, S^2, in the production term with $S\Omega$. The S and Ω are shown as below:

$$S = \frac{k}{\varepsilon}\sqrt{\frac{1}{2}\left(\frac{\partial u_i}{\partial x_j} + \frac{\partial u_j}{\partial x_i}\right)^2} \tag{5.10}$$

$$\Omega = \frac{k}{\varepsilon}\sqrt{\frac{1}{2}\left(\frac{\partial u_i}{\partial x_j} - \frac{\partial u_j}{\partial x_i}\right)^2} \tag{5.11}$$

In a simple shear S and Ω are equal, but not otherwise. It is verified that when Equation 5.8 is adopted for the stress field the energy production rate is given by:

$$P_k = C_\mu \varepsilon S^2 \tag{5.12}$$

The very high levels of S in a stagnating flow are what produce the excessive levels of κ. However, the deformation near a stagnation point is very nearly irrotational, which means $\Omega=0$. Thus the replacement:

$$P_k = C_\mu \varepsilon S\Omega \tag{5.13}$$

leads to a marked reduction in energy generation near the stagnation point while having no effect in a simple shear flow. This modification can give more realistic predictions than the standard k-ε model. However, this modification will cause spurious production in rotating or swirling flow; also, it is not physically correct to suppose that turbulence is not amplified by irrotational strains.

5.2.5 The computational grid

A H type grid is used in this program. The calculation domain is divided into three parts. The first part is from about a half axial chord upstream to leading edge of the blades. The second part is from the leading edge to the trailing edge of the blade. The third part is from the trailing edge to about a half axial chord downstream. The grid of each part is developed and meets at the leading edge and trailing edge. It is important to make the grid cells near the leading edge or the trailing edge equivalent in the axial chord direction both sides of the join. The grid cells become smaller and smaller approaching the leading edge or trailing edge in the axial direction. In the pitchwise direction the grid cells are allocated in such a way that near the suction surface and pressure surface the cells are smaller and have a higher density. Thus the boundary layers could be obtained in detail. Two programs were written to produce grid cell distribution files for grid generation.

In the spanwise direction a similar method to the pitchwise direction is used to generate the grid. Thus a computational grid in the blades' passage is achieved, this is the first part of input file.

An investigation of grid dependence and effect of using half the span with a symmetric boundary condition were carried out both for the Durham test case and the nozzle cascade which will be shown in section 6.5.1.

5.2.6 The boundary conditions

1 Static pressure at the downstream boundary of the passage. Because the pressure at the exit of the cascade is atmosphere, the static pressure at the downstream boundary was set to be atmospheric pressure.

2 Total pressure distribution at the upstream boundary. This will be obtained from experiments or assumed conditions. In order to obtain the total pressure distribution near the end wall a careful investigation of the upstream end wall boundary layer needed to be carried out. For a certain computation grid, the boundary values at each grid point were calculated by interpolation.

3 Total temperature distribution at the upstream boundary. The total temperature values were set to a constant value across the span.

4 Absolute inlet swirl angle. The nozzle blade from ALSTOM has an inlet angle of zero degrees. The absolute inlet swirl velocity values across the span for the case were set to zero. The Durham test case has an inlet angle of 43.5°.

5 Turbulence intensity at inlet. For the nozzle blade cascade, the turbulence intensity at inlet is 4.5%. For the Durham test case, the turbulence intensity at inlet is 4.95%. The CFD code also assumes fully turbulent boundary layer in the caculation because there is no facility in the code to switch from turbulent boundary layer to laminar boundary layer.

5.2.7 The output file

As the program runs, it generates a history file which contains the mass flow rate to check the convergence. It also produces an output file which has the result of every iteration at the monitoring point which is chosen by the user. A solution file which includes the final result of all the information at every grid node is generated as well. A set of programs were written to extract required data from the solution file to calculate the static pressure coefficient C_p, total pressure loss coefficients C_{po} and secondary velocity vectors, etc. Results were presented in the format of contour and vector plots for each slot. Pitch and area mass averaging were done by using the same program as the one that deals with the experimental data.

5.3 Validation of the code

2-D flow cases of the Durham cascade test case were computed so that different numerical schemes and turbulence models could be assessed. Several 3-D flow computations with different grids for the Durham cascade test case were made and computational and experimental results were compared. 2-D and 3-D cases of the nozzle cascade with flat end wall were computed by the code. The results were compared with the experimental results.

5.3.1 2-D case results.

In order to verify the program, a data input file including the 2-D geometry of the Durham standard cascade was generated.

1. Geometry of the Durham standard cascade.

The geometry of the Durham standard cascade is described by Table 5.1. According to its geometry an H type computational grid was generated as shown in Fig 5.1. The grid size is 25×99. An FORTRAN program was written to produce the data input file in the format that the CFD program requires. For the 2-D flow calculation, only one spanwise cell is needed for every end wall position. The grid size is 25×99×2. The calculation results should represent the mid-span condition for the 3-D flow with high aspect ratio.

Table 5.1 Geometry of the Durham standard cascade

Blades Number	Pitch(mm) s	Chord(mm) c	Axial Chord(mm) C_{axial}	span(mm)
6	191	224	191	400

2. Boundary conditions.

According to the Durham standard test case (Gregory-Smith(1995)), the boundary conditions at inlet are shown as following table 5.2.

Table 5.2 Boundary condition of Durham standard test case

Inlet Flow Angle	Dynamic Head	Free Stream Velocity	Air Density	Dynamic Viscosity	Free stream Turbulence length scale
42.75°	215Pa	19.1m/s	1.179kg/m^3	1.814*10^{-5} Ns/m^2	9.36mm

The Reynolds number of the cascade exit is 4.3x10^5 (C_{ax} and U_{exit}). From all these data, the boundary conditions in the format required by this program are shown in table 5.3.

Table 5.3 Boundary conditions of Durham standard test case for CFD calculation

Exit Static Pressure	Inlet Total pressure	Total Temperature	Absolute Inlet Swirl angle	Turbulence intensity
101278Pa	102174Pa	301.4K	43.5°	4.95%

A number of cases were tried to compare the results of the different turbulence models, which are k-ε model and S-Ω modification, and the results of different numerical schemes available in this program with the experimental results at mid-span of the Durham cascade test case. Results with the same boundary conditions are shown in table 5.4,

Table 5.4 Comparisons of CFD results at slot 10

CALCULATION METHOD		MIXED OUT FLOW ANGLE (DEGREE)	MIXED OUT LOSS COEFFICIENT
EXPERIMENTAL DATA		-68.1	0.098
NUMERICAL SCHEME (S-Ω MODEL)	UPWIND&UPWIND	-67.32	0.619
	QUICKS&UMIST	-67.17	0.173
	MINMOD&MINMOD	-67.35	0.211
TURBULENCE MODEL(QUICKS &UMIST)	S-Ω	-67.17	0.173
	k-ε	-67.24	0.179

The UPWIND & UPWIND scheme is a very stable first order scheme and usually leads to a convergent result. However, it does cause very high numerical errors. The QUICKS & UMIST scheme is a higher order scheme. It gives more accurate results, but it is not very stable. In this program, because the inlet velocities are guessed values, the UPWIND & UPWIND scheme is firstly used for few hundred iterations to make the computation converge. Then it switches to the QUICKS & UMIST scheme to get accurate results. From the table 5.4, it can be seen that all schemes gave much more loss than the experiments. The QUICKS & UMIST scheme gives the least loss which is the best approach to the experimental results, but the mixed out flow angle is not very good. This is due to the H type grid as shown in Fig 5.1 for the Durham blades. Computational cells near the trailing edge of the blade are highly skewed. This shortcoming of the computational grid affects the CFD results and makes the flow angle too small and loss too big. For this reason a new kind of grid, which is multi-block grid, is being developed now at ALSTOM. It is believed that it will overcome the shortcomings of the H type grid. Another high order scheme MINMOD & MINMOD was also tried, but this was not as good as QUICKS & UMIST, although it was better

than UPWIND & UPWIND. From present results, the QUICKS & UMIST numerical scheme seems to be the best choice.

For the turbulence model, the standard k-ε and its S-Ω modification were compared. From table 5.4, the S-Ω modification gives less loss than the k-ε model. The explanation of this was shown in section 5.2.4. However, the S-Ω turbulence model still gave excessive losses. It was expected that the CFD codes will give better prediction of losses if transition points on the blade surfaces could be obtained by experiment and put in the codes. Other reasons for the excessive loss prediction are perhaps due to the incorrect base pressure and the highly skewed computational cell near the trailing edge as mentioned above.

5.3.2 3-D Durham standard cascade case.

The CFD codes was run for the 3-D Durham standard cascade case. The computational grid size is 25×99×50 as shown in Fig. 5.1. The spanwise computational grid was generated from the wall to mid-span position at an expanding ratio of 1.2. The inlet boundary layer was set exactly the same as experimental results as shown in table 5.5. The velocity values of the grid points which are nearer to the end wall than 1.5mm were linearly extrapolated from the velocity values at point 1.5mm and 2.0mm.

The blade static pressure distribution is compared in Fig 5.2 and 5.3. There are six comparison pictures in Fig 5.2 and 5.3 which represent the static pressure distribution at different spanwise location. Compared with experimental results, the CFD gives good static pressure predictions before the 60% position at the suction surface and before 90% position at the pressure surface. Near the trailing edge on the suction surface the CFD gives a lower static pressure coefficient. It means that the CFD gives a higher static pressure near the trailing edge on the suction surface. Near the trailing edge on

pressure surface the CFD gives a sudden jump. This indicates that the incorrect base pressure was predicted. This might have caused the poor loss prediction by affecting the wake from the trailing edge. The vortex shedding after the trailing edge makes the base pressure prediction a quite difficult problem. The highly skewed cell near the trailing edge and the turbulence model used are expected to affect the pressure distribution near the trailing edge. However, as mentioned earlier, a new multi-block grid is being developed now in ALSTOM. Hopefully the multi-block grid will improve the results.

Table 5.5 Inlet boundary layer of Durham cascade

Span (mm)	V/V_{free}	Span (mm)	V/V_{free}
1.5	0.782	24.0	0.969
2.0	0.796	27.0	0.976
3.0	0.828	30.0	0.978
4.0	0.852	33.0	0.983
5.0	0.866	36.0	0.986
7.0	0.885	39.0	0.989
9.0	0.893	42.0	0.993
11.0	0.910	45.0	0.994
13.0	0.923	48.0	0.997
15.0	0.937	51.0	0.998
18.0	0.944	54.0	0.999
21.0	0.966	57.0	1.000

The total pressure loss of the CFD and the experiments are shown in Fig. 5.4. The CFD gives fairly similar loss distribution to the experiments. Higher loss is given by the CFD results at the mid-span. The loss core predicted by CFD is closer to the end wall and covers a relatively smaller region. The experiments show a loss increase at a distance of 110 mm away from the end wall while the CFD results show a loss increase at 90 mm

from the end wall. The predicted boundary layer on the end wall is thicker than that of experimental results. The counter vortex near the end wall from the experimental results is located at a different position from that of the CFD prediction. The reasons that the CFD gives more loss are probably the same as mentioned in the 2-D case.

The secondary vector plot from the CFD results shows a good agreement with that of the experimental results. The vortex centre is located closer to the end wall and the CFD gives more secondary flow near the end wall and less secondary flow near the mid-span. The yaw and pitch angle distributions are also well predicted.

For the pitch average of total pressure loss coefficients in Fig. 5.5, the CFD gives a qualitatively good result. The basic shape of the loss distribution seems to agree quite well. The loss core predicted by CFD is nearer to the end wall and covers a larger area than that of the experiments. The loss at the mid-span is too high compared with the experimental result at slot 10 as shown in Fig 5.5. The CFD loss at mid-span is about 0.17, but the experimental result is about 0.1, and this agrees with the 2-D results in Table 5.4. The pitch averaged yaw angle at slot 10 is described in Fig 5.6. Compared with the experimental results, the CFD gives poor prediction at the mid-span. The reason for this was explained in the 2-D calculation. The yaw angle distribution from CFD has a similar profile to that of the experiments. The CFD gives lower underturning near the mid-span and higher overturning near the end wall. The loss and the yaw angle distribution indicate that the secondary flow is under-predicted by the CFD.

The area averaged results are shown in Table 5.6. The total pressure loss predicted by the CFD method is about 40% higher than the experimental result. The CFD gives almost 100% more mid-span loss than the experimental result. The secondary loss and secondary kinetic energy from CFD are all smaller than the experimental results. In this case, the CFD predicts less secondary flow than the experiments.

Table 5.6—Area averaged coefficient for Durham cascade

	Total pressure loss	Mid-span loss	Secondary loss	secondary kinetic energy
CFD	0.250	0.173	0.065	0.012
Experiment	0.179	0.095	0.084	0.025

5.4 The code validation against the nozzle cascade with flat end wall

A 2-D case with ALSTOM blade was carried out. The results were compared with the results from ALSTOM. A 3-D calculation for the nozzle cascade was completed and the CFD results were compared with the experimental results.

5.4.1 Geometry of the cascade.

The geometry of the cascade is described by Table 3.1. According to the geometry of the cascade, an H type grid is generated as shown in Fig 5.7. The grid size is 35×99. The grid distribution structure is the same as that for Durham cascade test case described in section 5.2.5. The expanding ratio in the pitch wise direction is 1.1.

5.4.2 2-D calculation.

The 2-D case was first tried with the CFD calculation. In order to compare with the experimental results from ALSTOM, the Reynolds number was set to 1.47×10^6, and the Mach number was set to 0.45. Then the exit temperature was assumed to be 298K. From these conditions the boundary conditions for this case were obtained and shown in table 5.7.

Table 5.7—Boundary conditions at Re=1.47×10^6

Exit Static Pressure	Inlet Total Pressure	Total Temperature	Absolute Inlet Swirl angle	Inlet Turbulence Intensity
88711.7Pa	102522.9Pa	298K	0°	4.5%

Table 5.8—2-D calculations results

Reynolds Number		CFD (QUICKS& UMIST)	CFD (UPWIND & UPWIND)	Experiment
$1.47x10^6$	Flow exit angle (degree)	77.26	77.11	77.20
	Mixed out loss (defined by exit isentropic velocity)	0.033	0.096	0.030
$4.3x10^5$	Flow exit angle (degree)	77.15	none	77.85
	Mixed out loss (defined by exit isentropic velocity)	0.046	none	0.039

The CFD results are compared with experimental results ALSTOM (1992) in Table 5.8. The CFD with the QUICKS & UMIST scheme gives a very good prediction in flow exit angle for the ALSTOM blade at high Reynolds number. The loss prediction is good as well compared with the experimental results. The UPWIND & UPWIND scheme is not as good as the QUICKS & UMIST scheme since it gives higher loss. All the cases were run with the S-Ω turbulence model. This indicates that the CFD program is good at high Reynolds number for this blade.

Using the QUICKS & UMIST scheme and S-Ω turbulence model, another 2-D calculation was carried out with the same boundary conditions as shown in Table 5.9 with the cascade Reynolds number of 4.3×10^5. The flow exit angle from the calculation is 77.15^o. The total pressure loss coefficient based on inlet velocity at slot 10 is predicted as 0.833. The mixed out loss coefficient as defined by exit isentropic velocity at slot 10 is 0.046 compared with 0.033 at high Reynolds number. As shown in Table 5.8, the lower Reynolds number has little effect on the exit angle, but increases the loss.

5.4.3 3-D calculation

The effect of the grid change was investigated. Half span option and different grids were tested and compared to investigate the grid dependence of the code. The CFD results are compared with the test data.

5.4.3.1 The comparison of half and full span calculation

There are two options in the CFD codes, namely full-span and half-span calculations. In order to reduce computing time, the half-span option was expected to be used. A full-span calculation with km = 43 and a half-span calculation with the same grid distribution in the spanwise direction were investigated. The results at slot 10 are shown in Fig. 5.7 and Fig. 5.8. From the comparison, the half span version gives exactly the same loss distribution and yaw angle distribution along the span as the full span version. Because the half span calculation gives the same result and only needs less than half of the running time that the full span version needs, the following CFD tests were all done with the half span version.

5.4.3.2 The investigation of the effect of coarse and finer grid.

Because the CFD code may be grid dependent, an investigation of the grid effect needs to be done. The grid dimensions in axial direction and pitchwise direction, which are decided by im = 25 and jm = 99, are kept the same as before. The spanwise grid was

increased from km = 22 to km = 51. The result comparisons are shown in Fig. 5.9 and Fig. 5.10. The finer grid (with im = 25 and km = 51) shows a higher loss peak than the coarse grid (with im = 25, km = 22) near the end wall. The loss peak of the finer grid result also is further away from the end wall than the coarse grid result. The finer grid also gives higher under turning near the end wall. This means that the finer grid gives more secondary flow which is reasonable, because the grid near the end wall needs to be fine enough to catch the dramatic flow change there. However, the finer grid needs much more computing time to get the result. Considering the time and accuracy, the grid with im = 35 and km = 28 was created. This grid has the same grid distribution near the end wall (within 40 mm from end wall) as the finer grid, with the grid number near the mid-span being reduced. Eventually, the grid for further testing was decided as the grid with im = 35, jm = 99 and km = 28, the test results are shown in Fig. 5.9 and 5.10. It gives almost the same results as for the finer grid. The reason that im is increased from 25 to 35 is that the grid with im = 35 gives better resolution. The final grid only needs 70% of the time of the finer grid and gives nearly the same accuracy. The used computational grid is shown in Fig 5.11. Because the Reynolds number of the cascade exit is decided to be $5x10^5$, the inlet velocity could be calculated as 9.11m/s. According to the data from ALSTOM the boundary condition is shown in the following table 5.9.

Table 5.9—Boundary conditions for the nozzle cascade

Exit Static Pressure	Inlet Total pressure	Total Temperature	Absolute Inlet Swirl angle	Inlet Turbulence intensity
101325Pa	102475Pa	296K	0°	4.5%

The inlet boundary layer was set the same as that for experiments as shown in Fig. 4.3. The velocity at every grid points at inlet was interpolated from the experimental results. The exit static pressure was set to the same as shown in Table 5.9.

The experimental results have been shown in Chapter 4. The computational results from the CFD simulation are presented in the same format as that for the experimental results. The pitch averaged computational results of total pressure loss and yaw angle distribution are plotted for every traversing slot. Only the computational results at slot 7 and 10 are presented in plots of total pressure loss, yaw angle, pitch angle, secondary kinetic energy and secondary vector.

The pitch averaged total pressure loss and yaw angle distribution are shown in Figs. 5.12-5.16 for slots 2-6. Slots 2-7 were investigated without transitional trips and slots 8-10 were investigated with and without transitional trips. At slot 2 shown in Fig. 5.12, the total pressure loss show excellent agreements with the measurements. The yaw angle shows an almost straight line compared with the small overturning near the end wall of the experimental results. This indicates a small error in the input file with the swirl angle. At slot 3, the total pressure loss remains almost the same as the measurements. The yaw angle shows a very small overturning near the end wall compared with the underturning and overturning in the experiments. At slot 4, the CFD gives a higher loss at mid-span. The experimental results certainly have not picked up the profile loss because of the limited access to the blade surfaces. In the near wall region, the loss distribution profile is the same as the experimental results. The yaw angle shows very good prediction apart from smaller underturning. At slot 5, the CFD gives a sudden rise of the total pressure loss in the mid-span which is unrealistic. The reason for this is probably that there is not enough grid points at slot 5 referring to Fig. 5.11. The yaw angle shows an excellent agreement with the experimental results. At slot 6, the total pressure loss predicted by the CFD is higher in the mid-span and exhibits a sharper increase near the end wall region than the experimental results. In the mid-span, the loss is smaller than the mid-span value at slot 5. It is hard to understand the reason of this. The yaw angle from the CFD calculation is slightly higher than the experimental results with a similar distribution profile.

The area plot results from CFD are shown for slot 7 in Fig. 5.17 and slot 10 in Fig. 5.21. At slot 7, the CFD shows that total pressure loss is concentrated in the suction corner. There is a very thick boundary layer on the suction surface. The loss area is smaller than the experiments as shown in Fig. 4.14 in the spanwise direction. The secondary kinetic energy contour, the CFD gives much more detailed description near the suction surface. The secondary flow near the end wall is smaller than in the experimental results. The convection effect which brings the low energy fluid out of the suction corner is smaller because of the smaller secondary flow. This can explain why the loss from the CFD covers a smaller area in the spanwise direction than the experiments. The yaw angle distribution predicted by the CFD gives smaller overturning near the end wall. The pitch angle shows almost the same distribution as the experimental results. The secondary vector plot gives less secondary flow near the end wall. The vortex centre is much closer to the suction surface corner than in the Fig. 4.14e).

At slot 7, the total pressure loss shows the new boundary layer's appearance and the old boundary layer moving away from the end wall. This indicates that the CFD is giving fairly good prediction of the secondary flow development. However, in Fig. 5.18 the total pressure loss predicted by the CFD is much higher than the experimental results. Fig. 5.17 shows this is due to the suction surface boundary layer which is not picked up by the experiments. The yaw angle distribution is almost the same as the experimental results. At slot 8 in Fig. 5.19, the CFD gives a loss peak moving away from the end wall and a new growing boundary layer on the end wall. The loss is generally much higher than the experimental results. The yaw angle predicted by the CFD shows a much closer underturning peak to the end wall than the experimental results. At slot 9 in Fig. 5.20, the first downstream traversing slot after trailing edge, the CFD gives excessive loss in the mid-span and a much higher loss peak. The CFD predicted loss peak is located closer to the end wall than those of the experimental results. At mid-span, the yaw angle shows higher turning than the experimental results. This could be explained by the highly skewed the cells near the trailing edge and the difficult base

pressure problem as discussed for the 2-D results. In the near wall region, the yaw angle from the CFD shows a similar distribution profile with less underturning and less overturning than the experimental results without trip, but more underturning than the experimental results with the trip. These indicate that the secondary flow predicted by the CFD is bigger than the experimental results with trip.

The total pressure loss contours for slot 10 in Fig. 5.21 show a overall similar shape as that in Fig 4.21. At the mid-span, the loss values in the wake are higher than those of the experiments. The loss peak near the end wall also shows much higher value than that of experiments. The positions of the loss peak and corner counter vortex are well predicted by the CFD. The secondary vector plot shows a much stronger secondary flow than the experimental results. The CFD gives slightly larger vortex than experiments. The secondary kinetic energy predicted by the CFD is higher than the experimental results. The yaw angle distribution shows similar underturning and overturning near the end wall. The pitch angle contours show very similar distribution to the experimental results.

The pitch averaged total pressure loss and yaw angle at slot 10 was compared with the experimental results in Fig. 5.22. The total pressure loss in the mid-span is still much higher than the experimental results. Near the end wall, the CFD gives a thinner boundary layer and a higher loss peak compared with the experimental results. The loss peak stays closer to the end wall. The yaw angle shows lower turning at the mid-span as at slot 9. Near the end wall, the yaw angle stays similar to the experimental results except the CFD gives a closer underturning peak to the end wall. The area averaged results are shown in table 5.10. The CFD gives higher total pressure loss compared with the experimental results. Apart from the reasons mentioned before in Durham cascade calculation, the uncertain inlet turbulence intensity is another reason which might make the loss prediction higher. However, the CFD code gives better prediction on the blade pressure distribution as shown in Fig. 5.23 than for the Durham cascade. The transition

trips' effect could be noticed from the mid-span loss in the table 5.10. The CFD gives a higher secondary kinetic energy which means stronger secondary flow. The stronger secondary flow sweeps more low energy material away from the end wall and results in a higher loss peak in Fig. 5.22.

Table 5.10—Area averaged coefficients for the nozzle cascade at slot 10

	Total pressure loss	Mid-span loss	Secondary loss	Secondary Kinetic Energy
CFD	1.14	0.99	0.16	0.0088
Experiment without trip	0.86	0.75	0.11	0.0063
Experiment with trip	0.94	0.75	0.19	0.0042

The static pressure on the blade surface from the CFD and the experiments are shown in Fig. 5.23. The experimental data was measured without the trips. The CFD results is only shown around the blade surface at the position of 10 mm away from the end wall because the static pressure on the blade surface does not vary too much for different spanwise positions. The CFD gives lower static pressure on the pressure surface and higher on the suction surface. This is consistent with the lower turning angle predicted by the CFD. The static pressure on the end wall predicted by the CFD is shown in Fig 5.24. Compared with Fig. 4.24, the static pressure distribution predicted by the CFD is good compared to the experimental results.

5.5 Conclusion

The CFD code and the computational grid, numerical schemes, turbulence models have been described. The validation of the codes has been carried out against the Durham Test Case and the nozzle blade cascade experimental results. The code gives higher total pressure loss compared with the experimental results. The yaw angle distribution

and the secondary flow are fairly well predicted by the code. However, the code gives too little secondary flow for the Durham cascade, but too much for the nozzle cascade. One possible reason for this is the Durham test case has a much bigger turning angle 110^{o} than the nozzle cascade 77^{o}. For the nozzle cascade, although the secondary flow is predicted too much, the loss peak is not far enough from the end wall. The errors in the yaw angle distribution at the downstream slot (9 and 10) are related to the highly skewed computation cell near the trailing edge and the incorrect base pressure prediction. From the validation results, it may be concluded that the CFD code gives results sufficiently accurate to predict trends in the design study, even if absolute values are not precise.

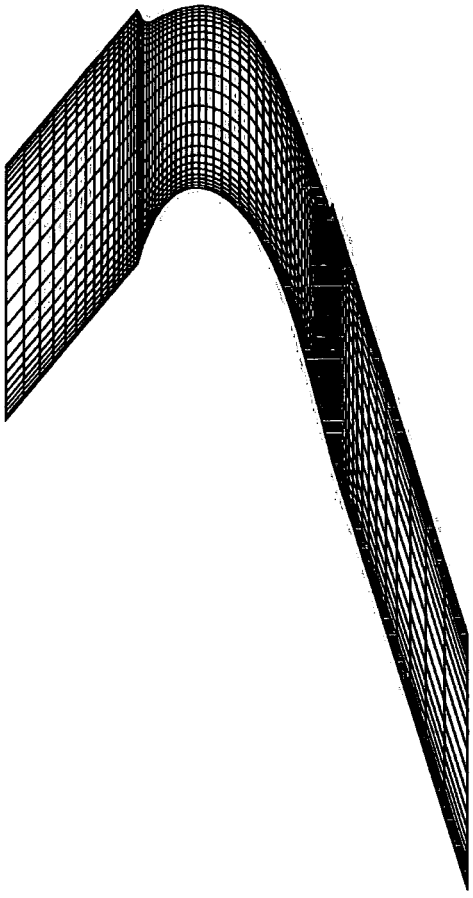

The computational grid at axial-pitch direction

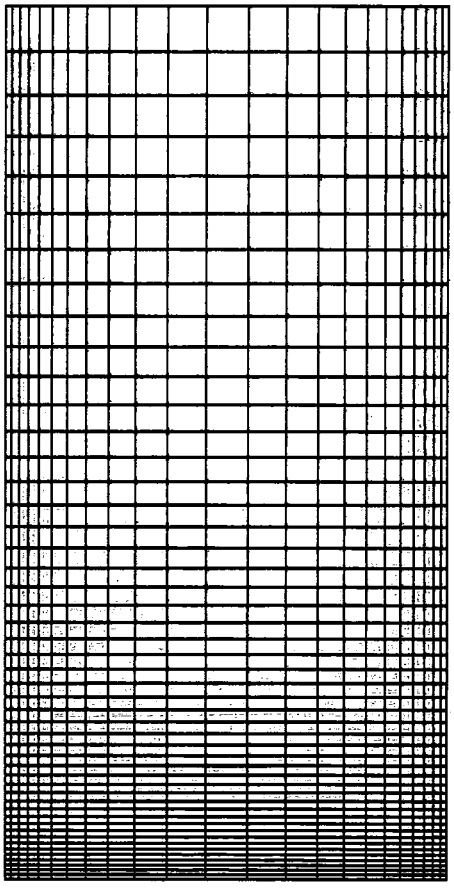

The computational grid at pitch -span direction

Figure 5.1— The computational grid for the Durham standard cascade

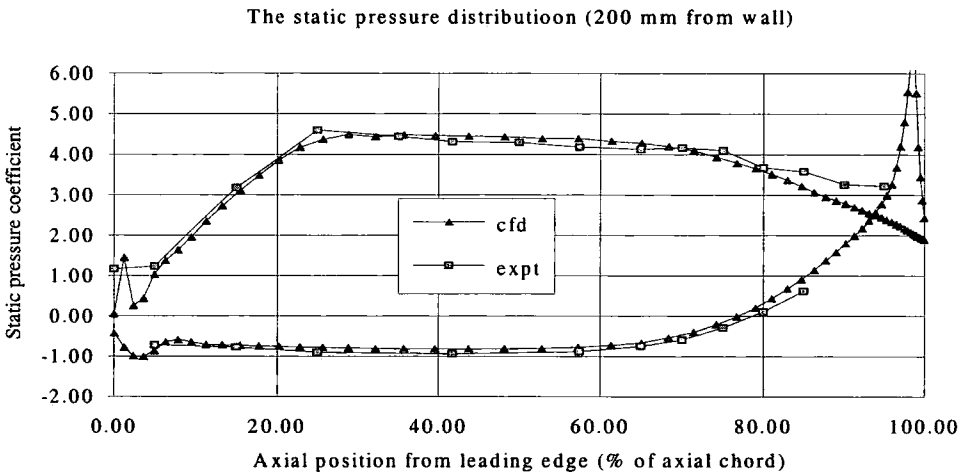

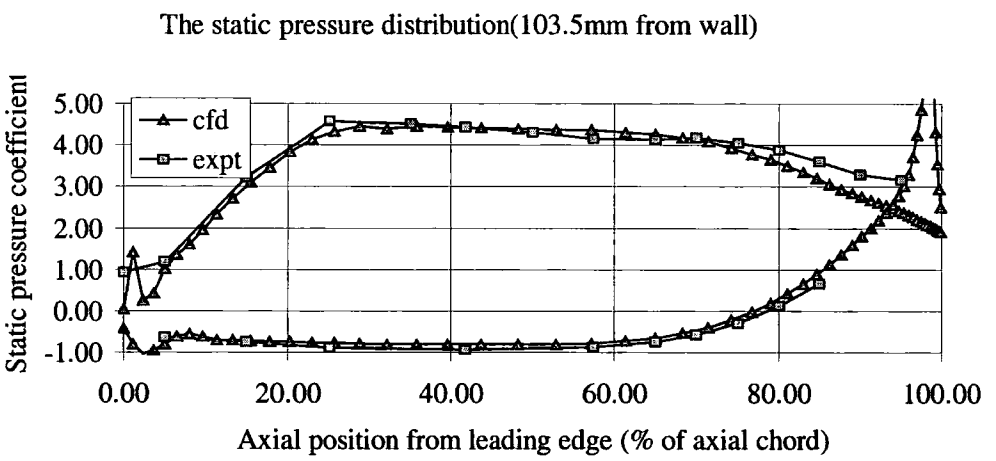

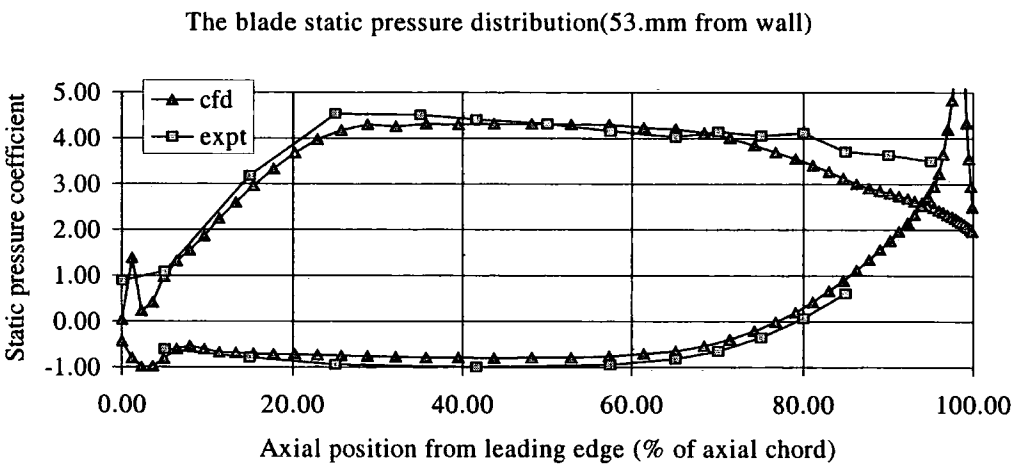

Figure 5.2— The static pressure on the blade surface

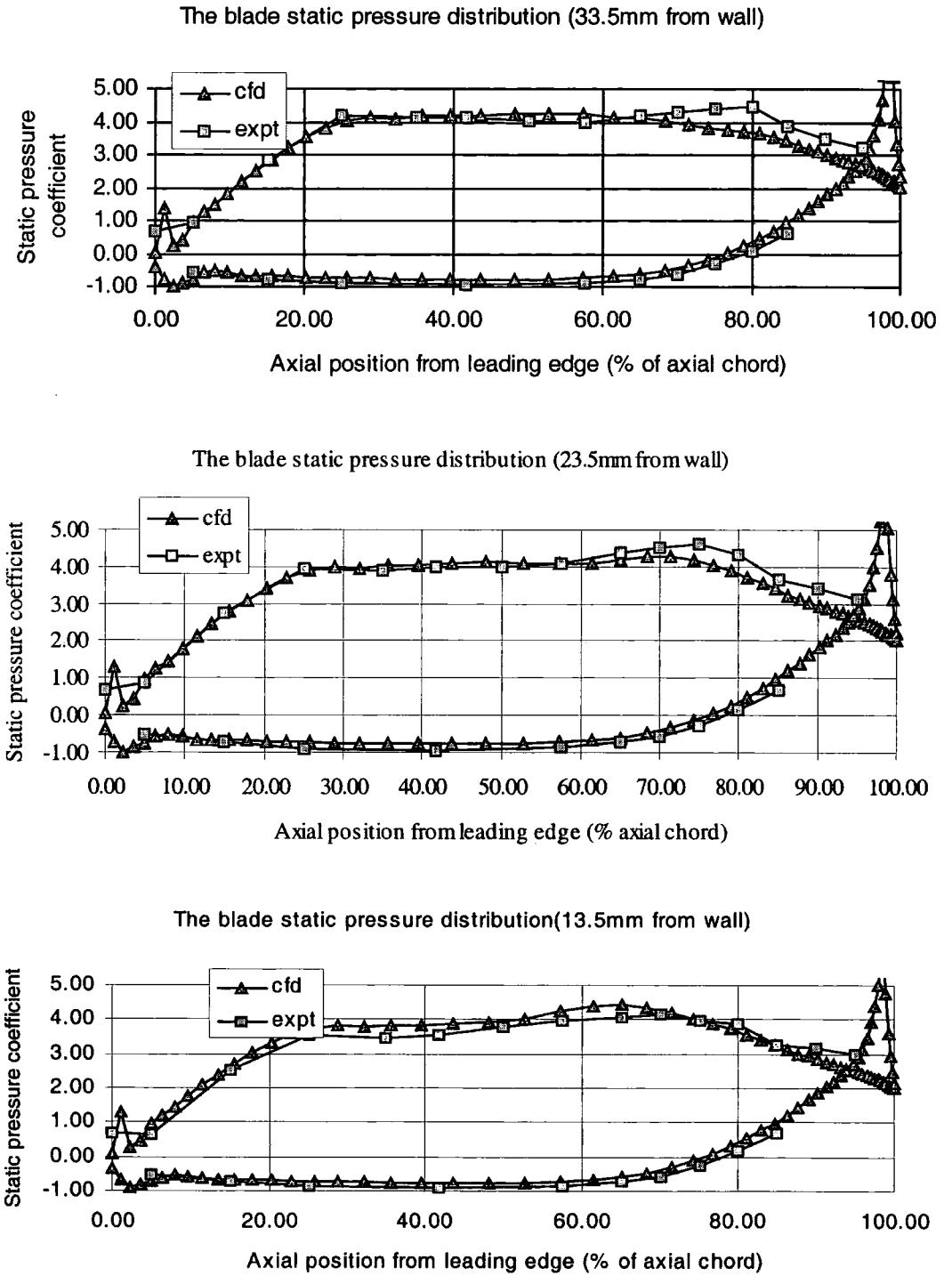

Figure 5.3— The static pressure on the blade surface

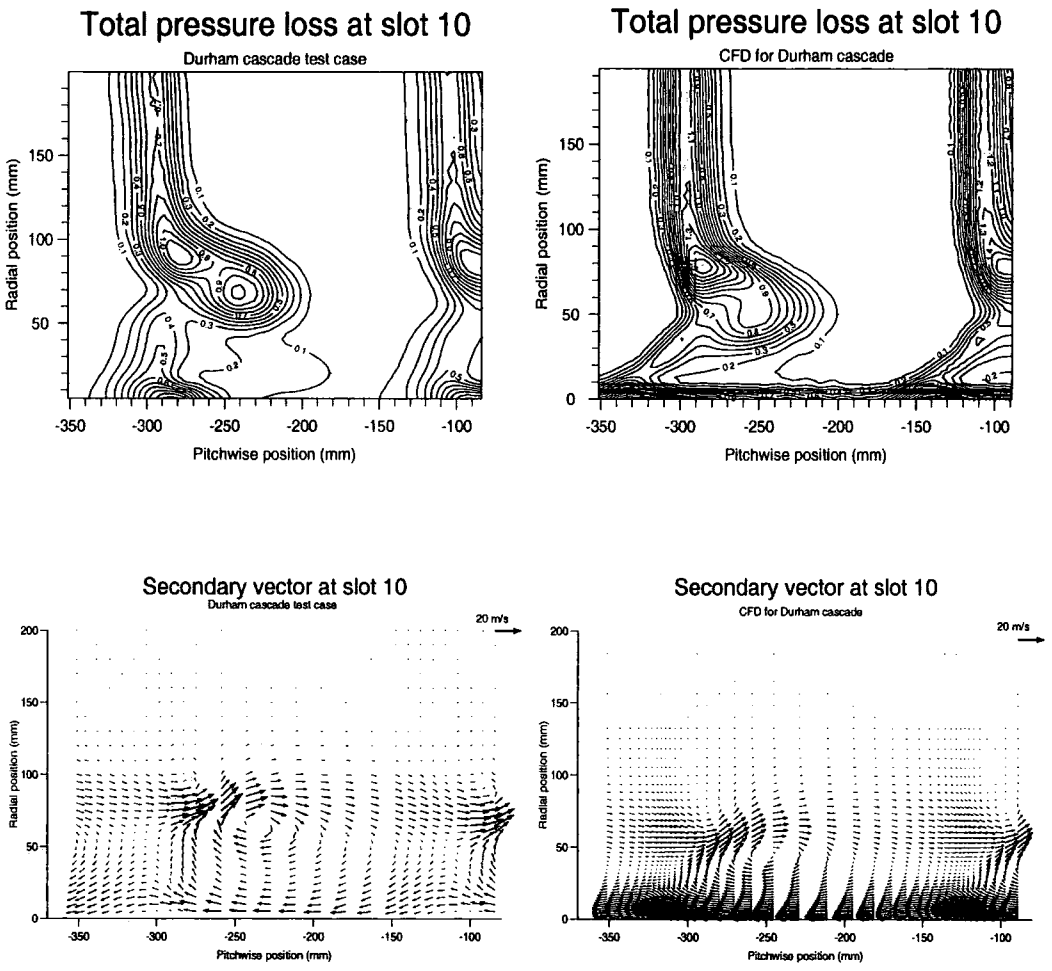

Figure 5.4a— The area plot at slot 10 for Durham test case

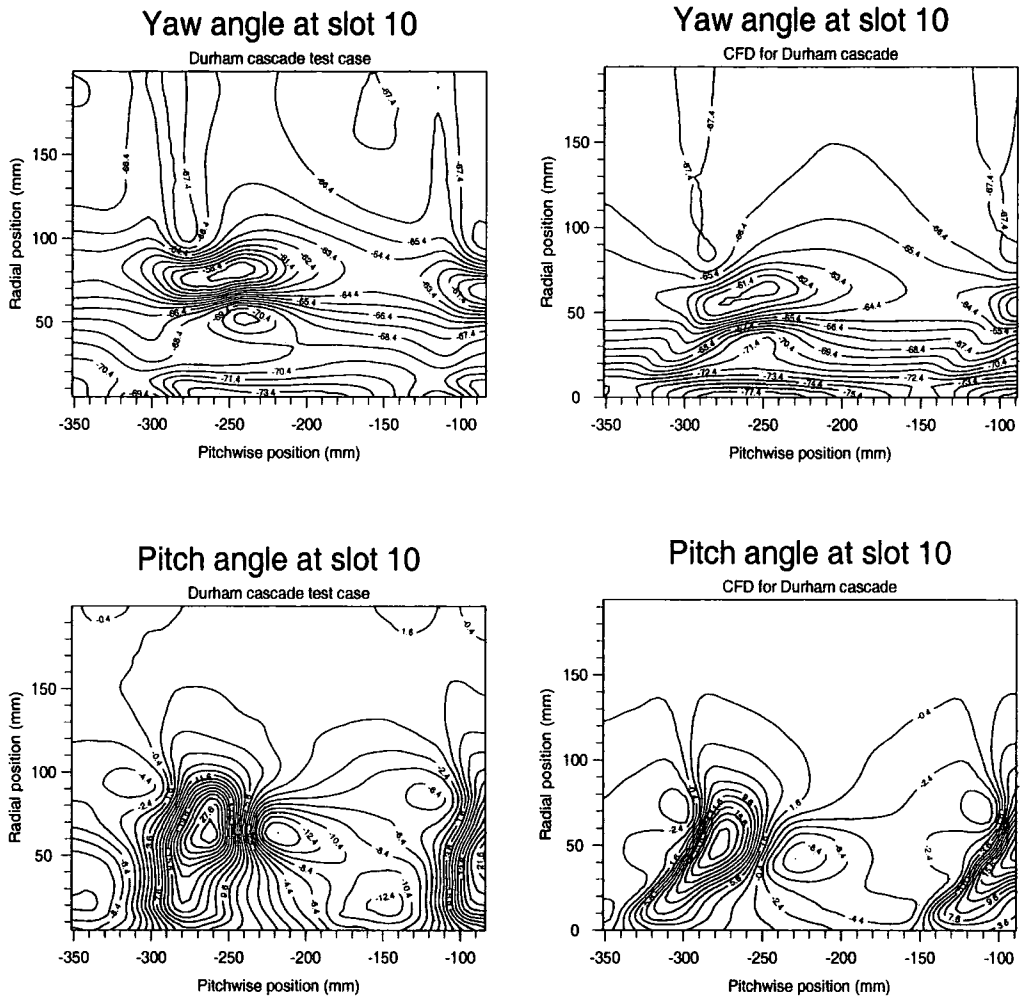

Figure 5.4b— The area plot at slot 10 for Durham test case

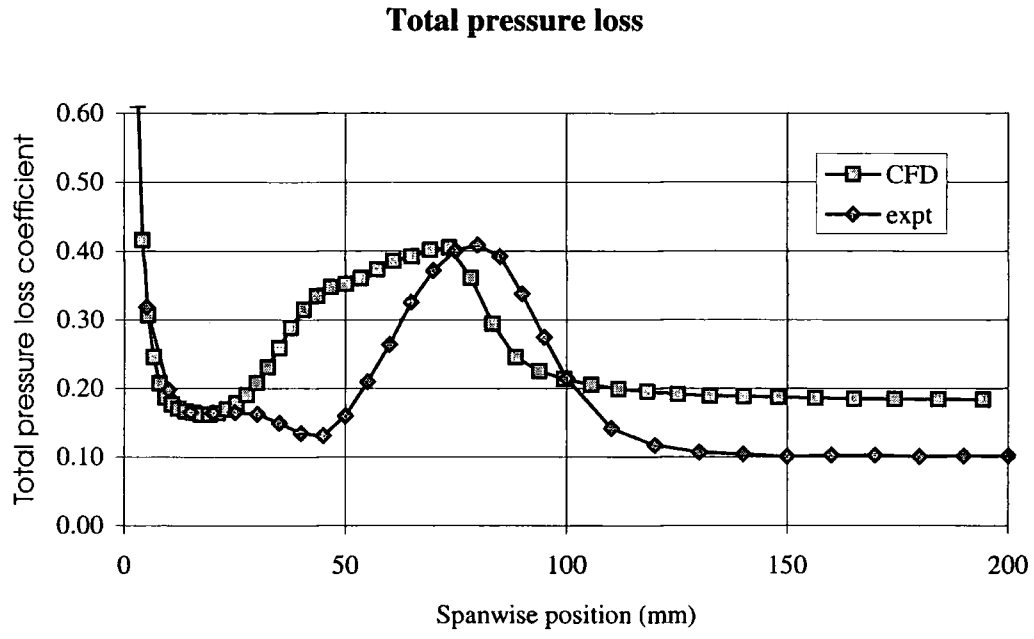

Figure 5.5— The comparison of pitch averaged total pressure loss at slot 10

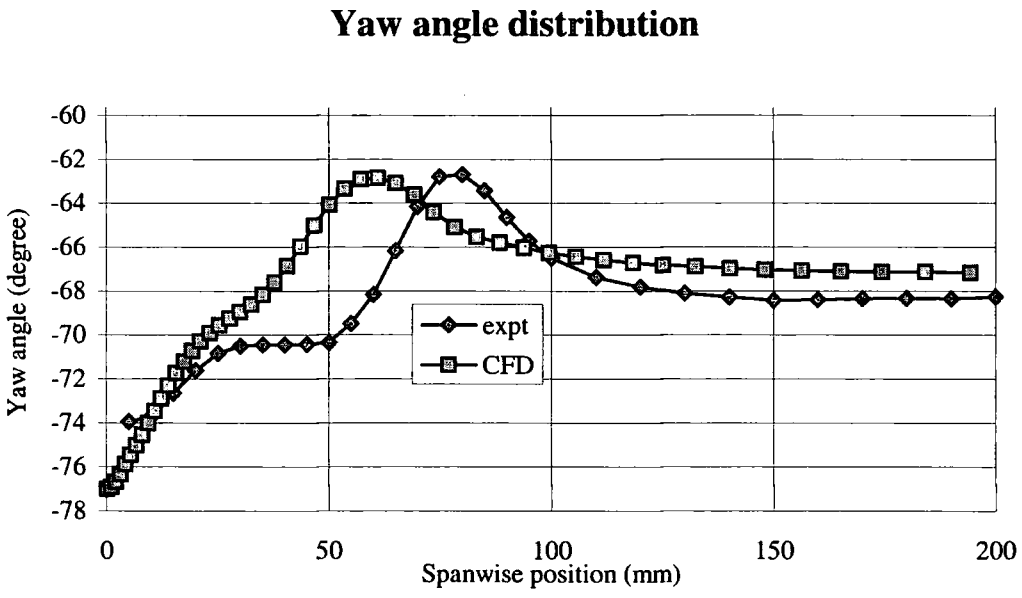

Figure 5.6—The comparison of pitch averaged Yaw angle at slot 10

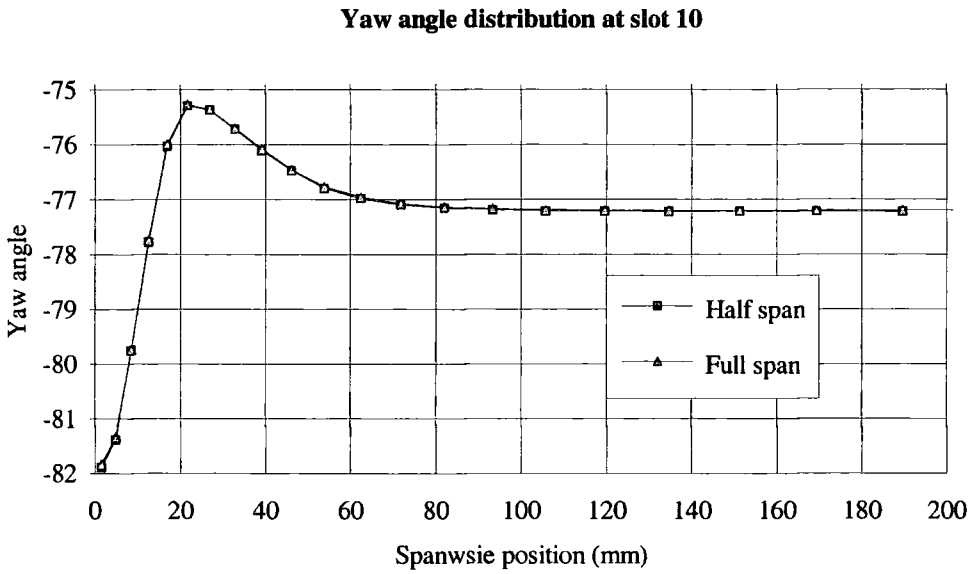

Figure 5.7—The yaw angle comparison between the full span and half span computation

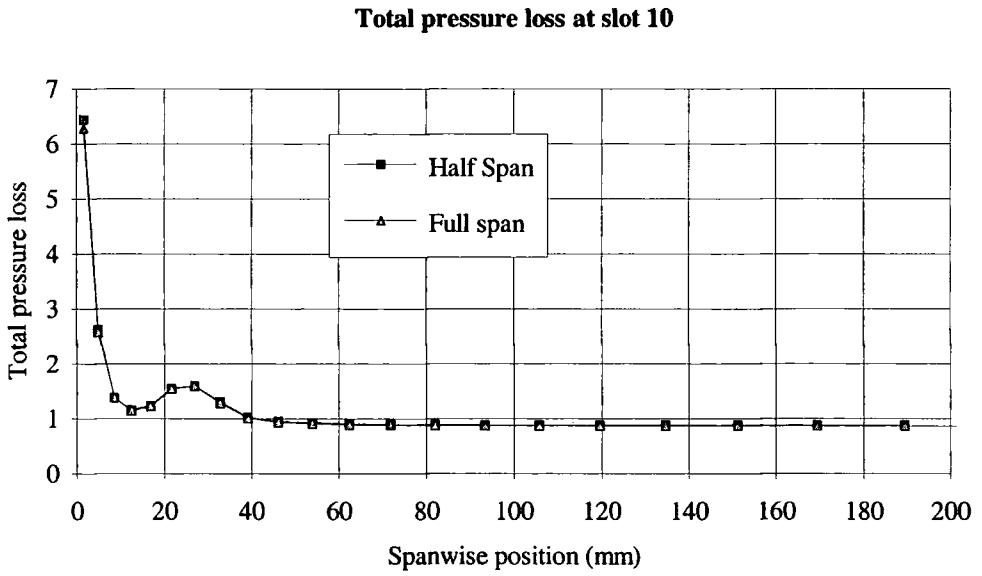

Figure 5.8—The total pressure loss comparison between the full span and half span computation

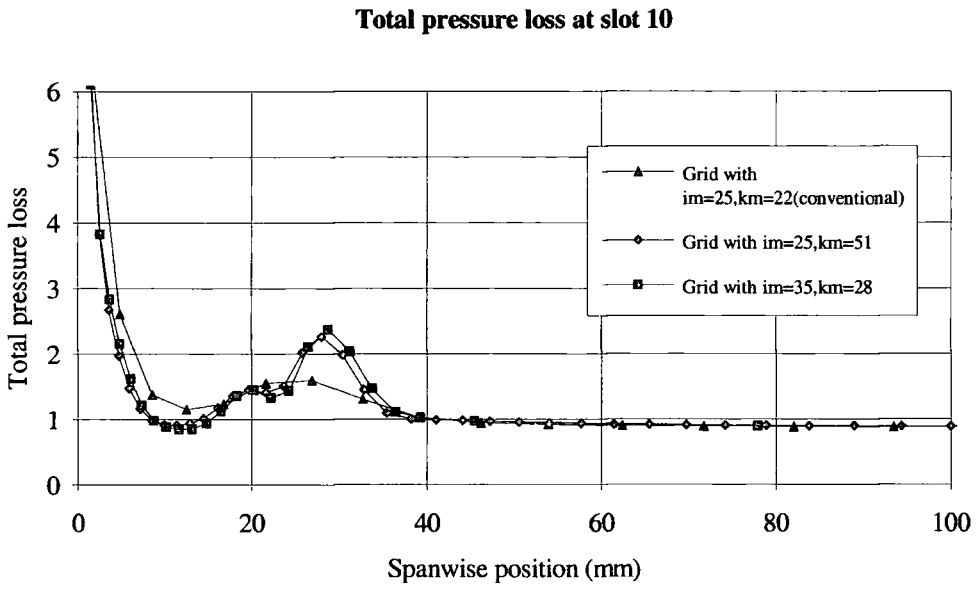

Figure 5.9—The grid effect on the total pressure loss

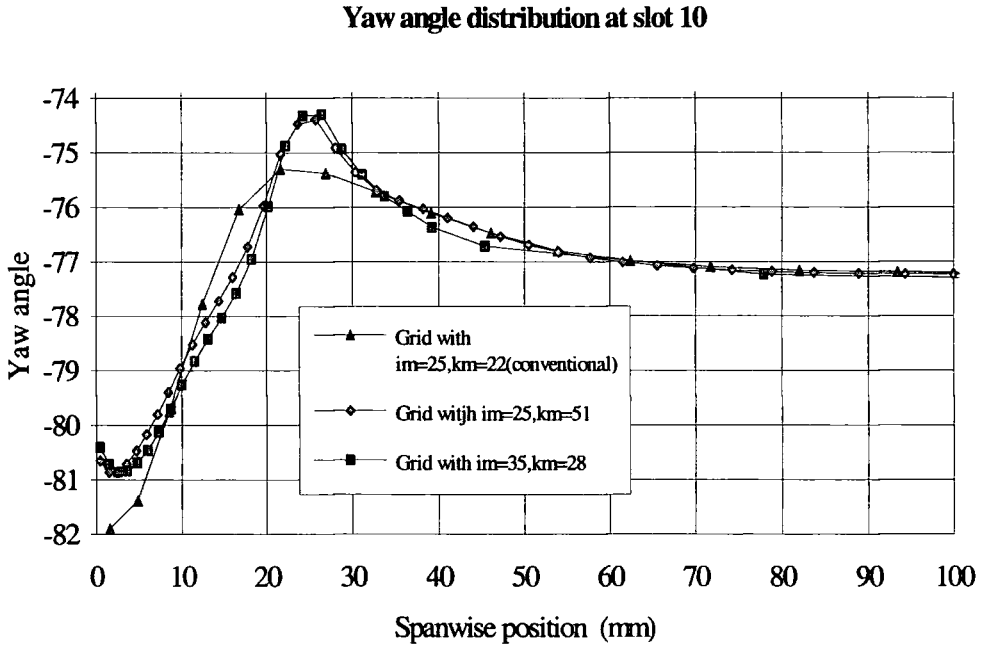

Figure 5.10—The grid effect on the yaw angle distribution

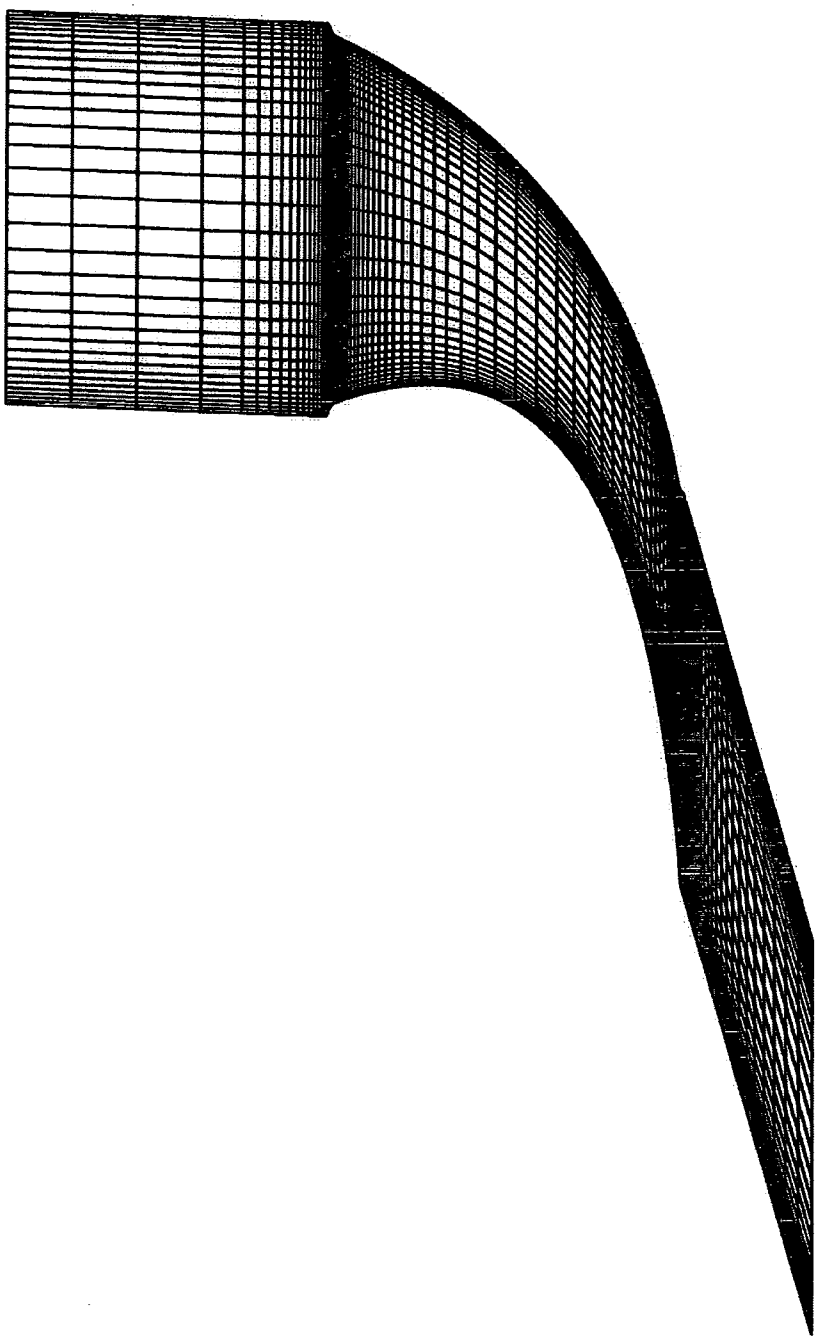

Figure 5.11— The computational grid for the ALSTOM blade

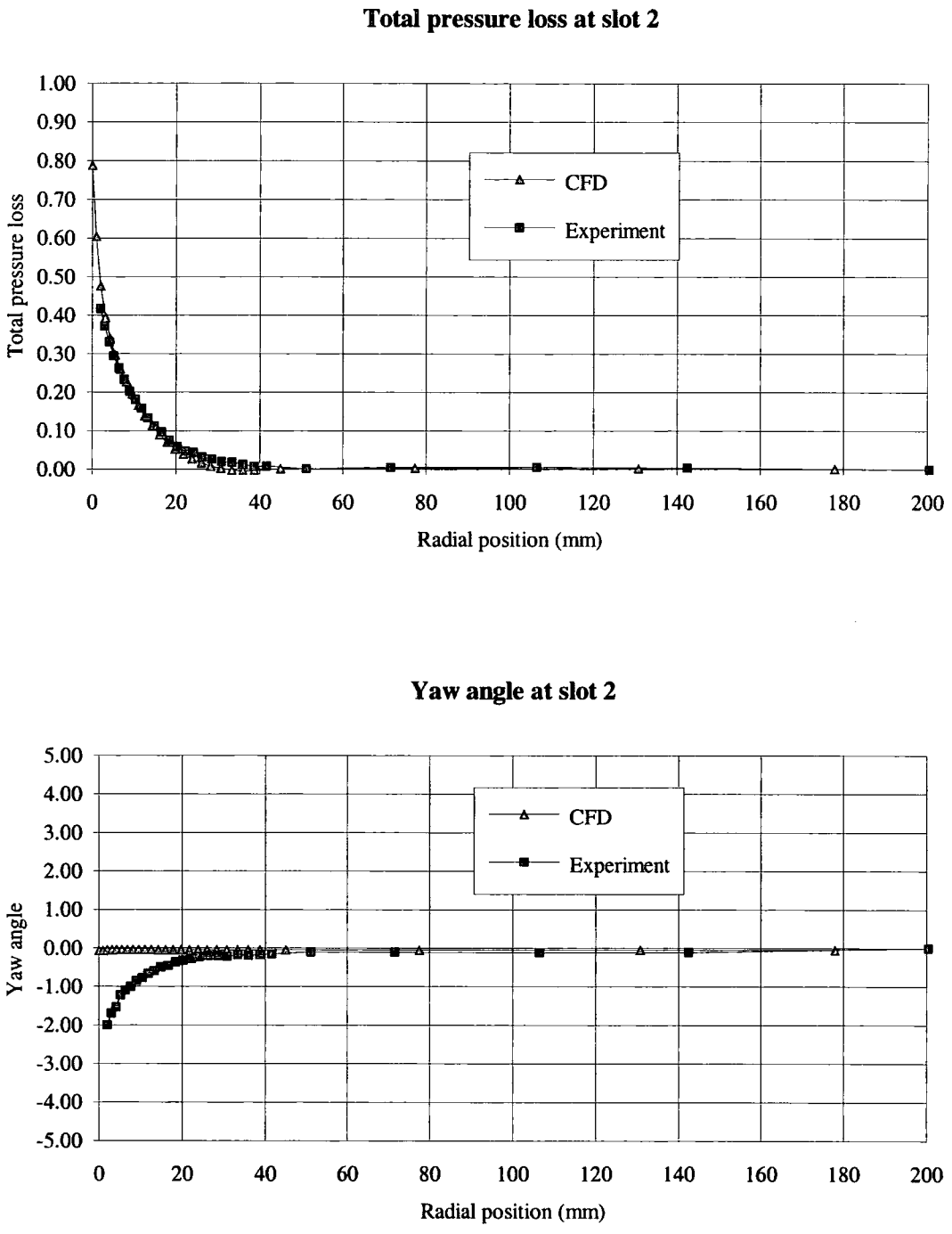

Figure 5.12— The pitch averaged results at slot 2

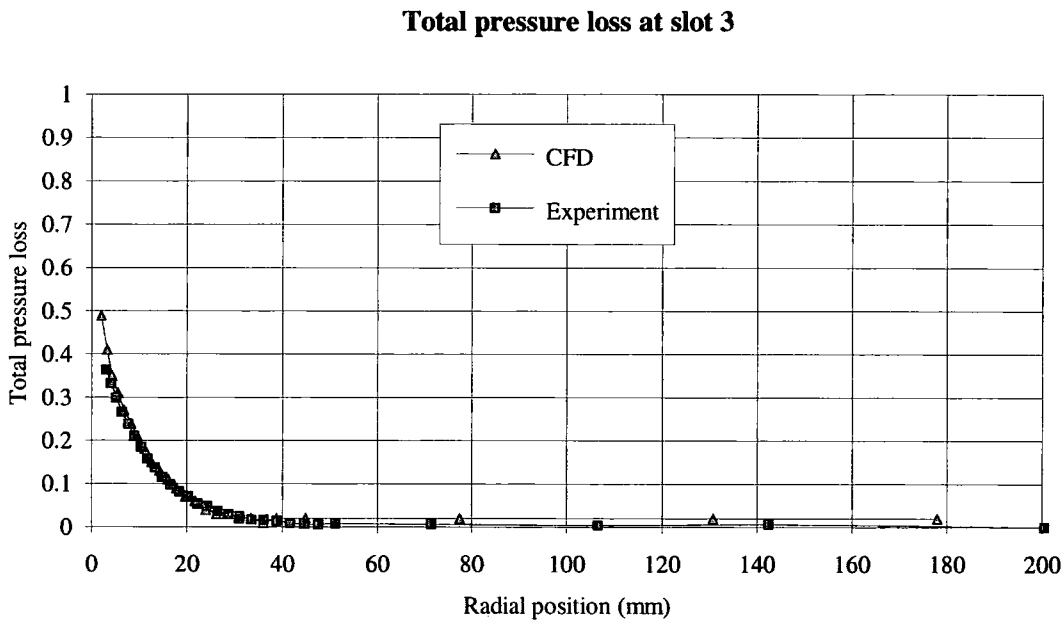

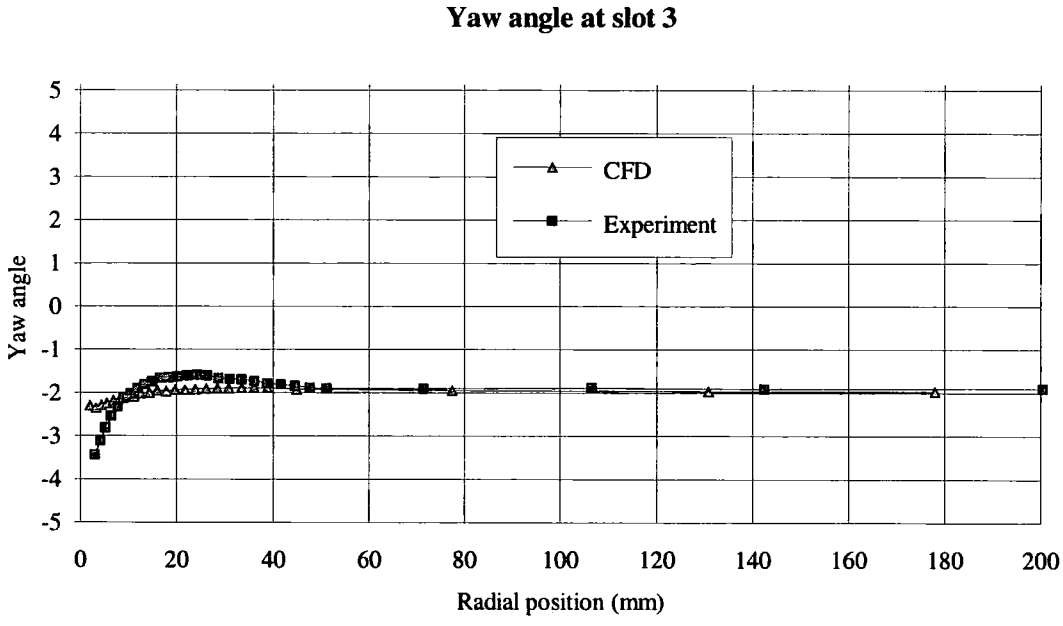

Figure 5.13— The pitch averaged results at slot 3

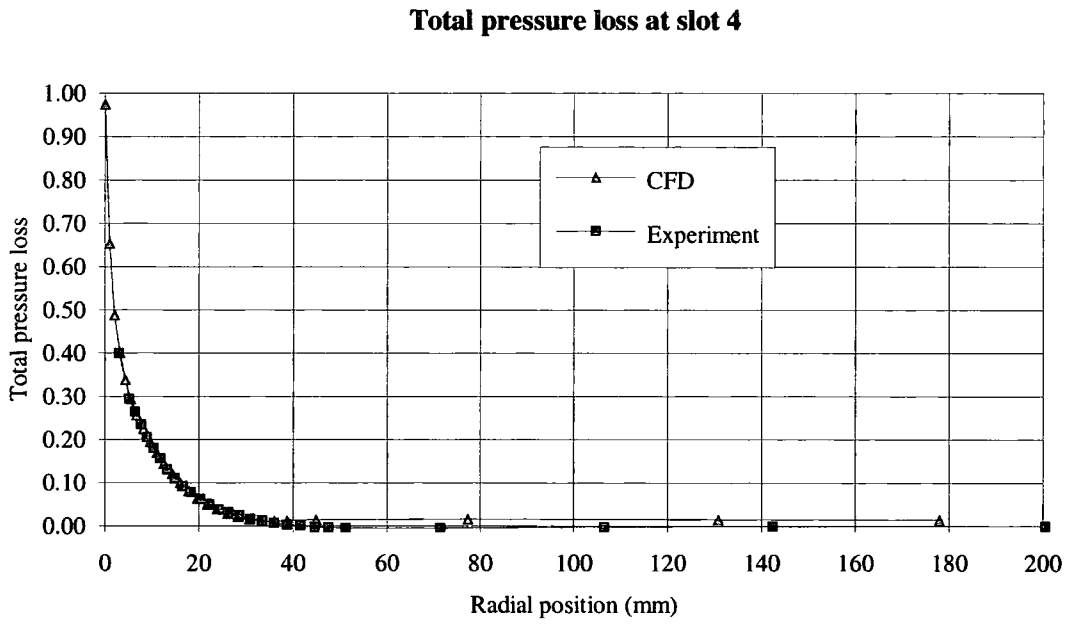

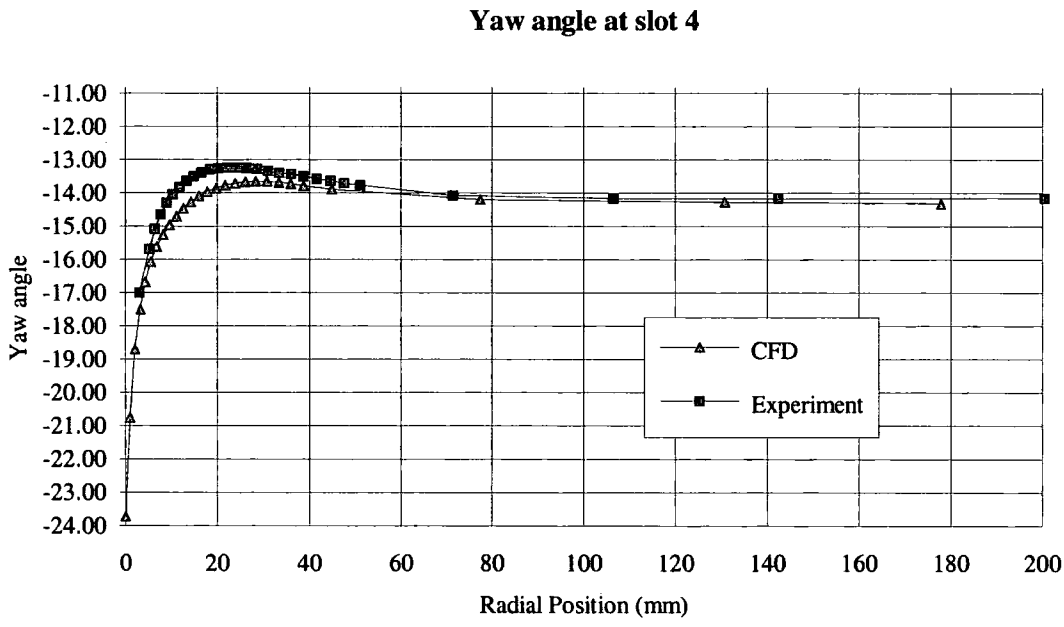

Figure 5.14— The pitch averaged results at slot 4

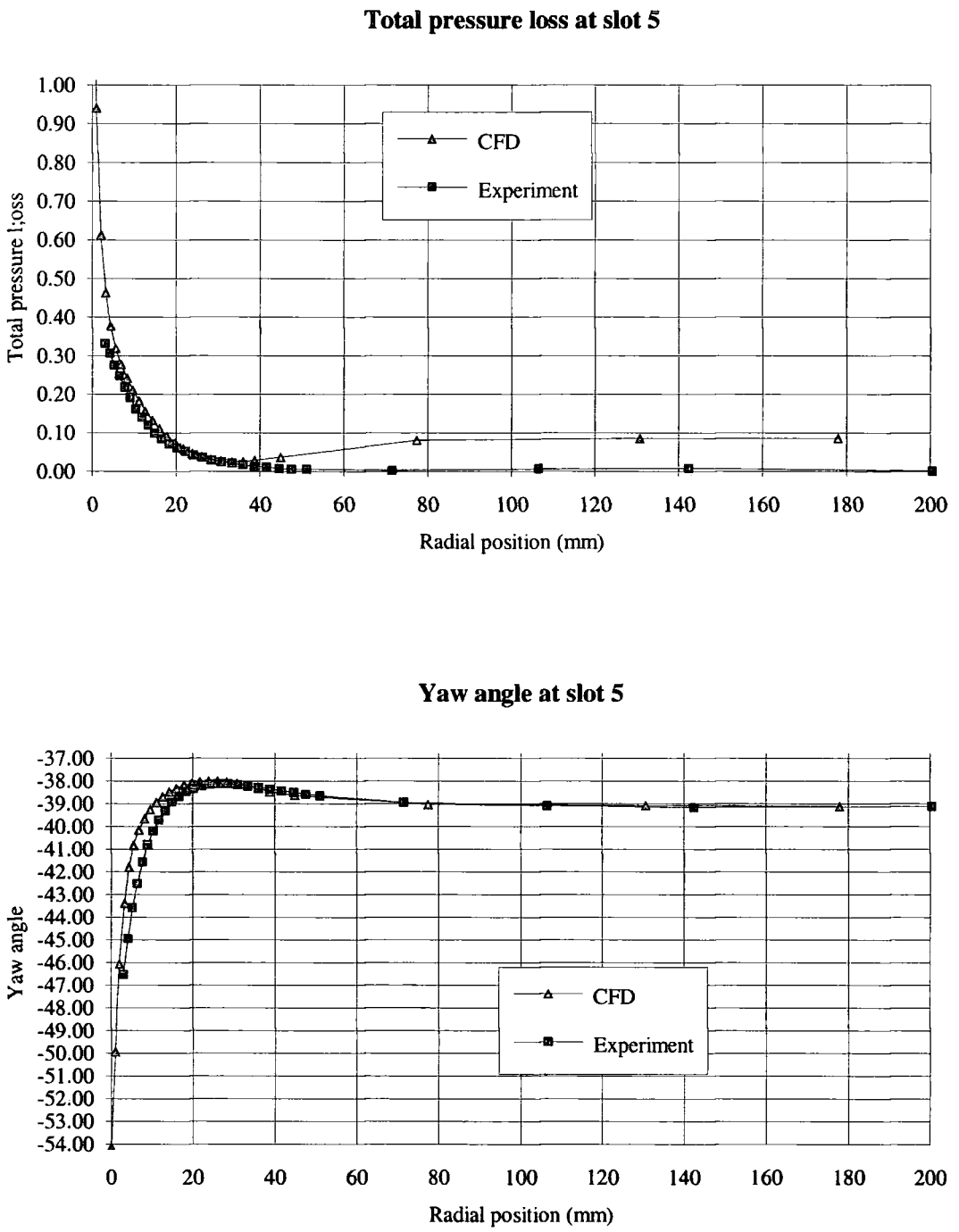

Figure 5.15— The pitch averaged results at slot 5

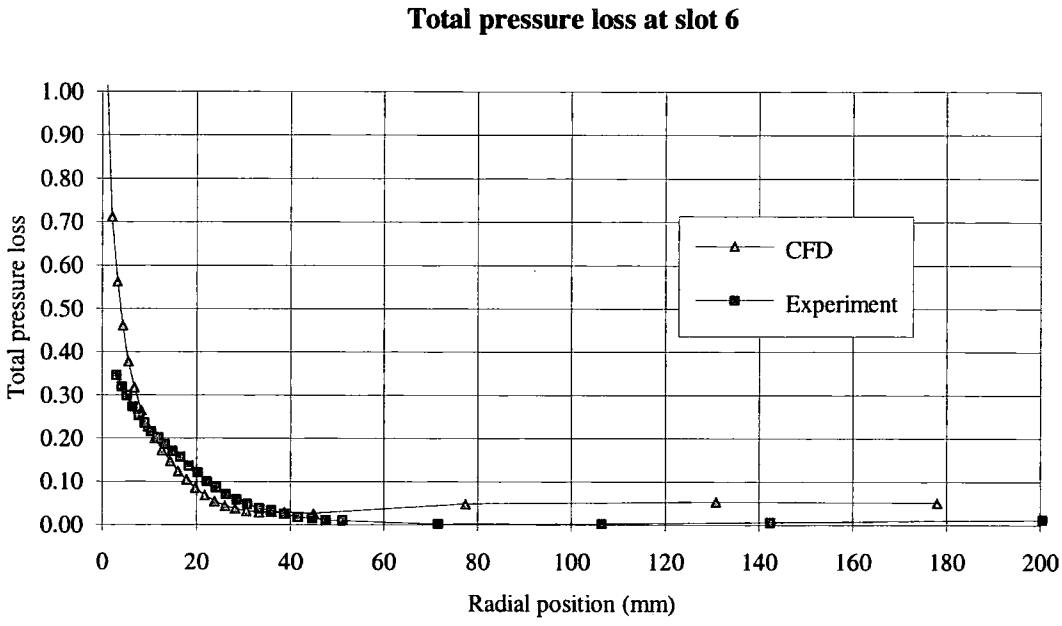

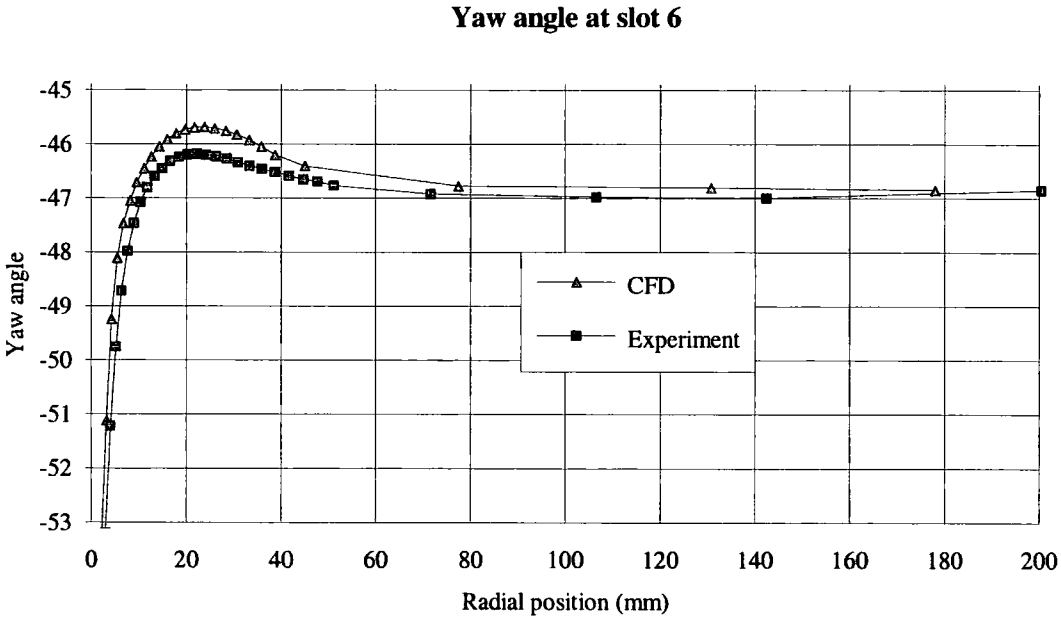

Figure 5.16— The pitch averaged results at slot 6

a) Total pressure loss contours

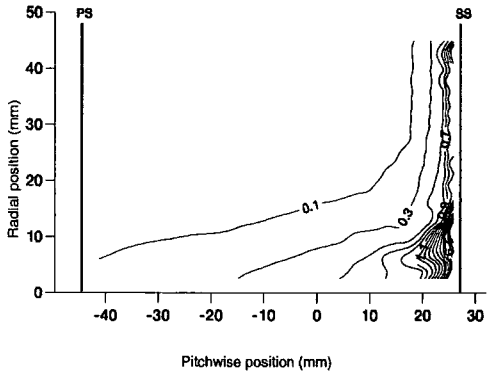

b) Secondary kinetic energy contour (%)

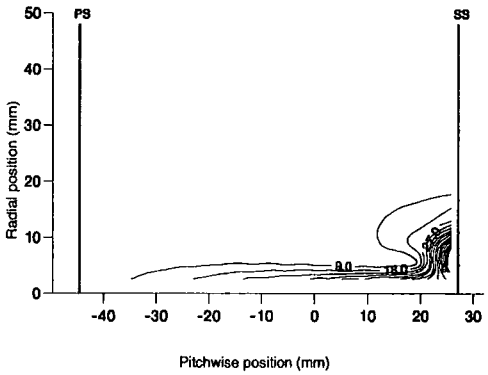

c) Yaw angle contour

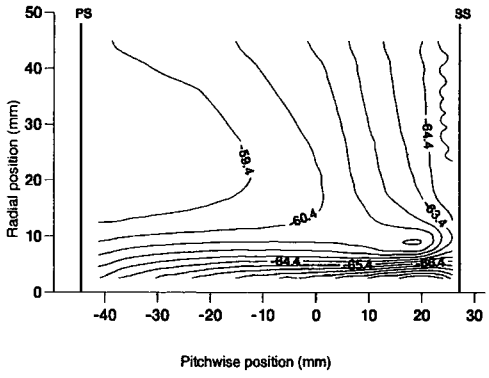

d) Pitch angle contour

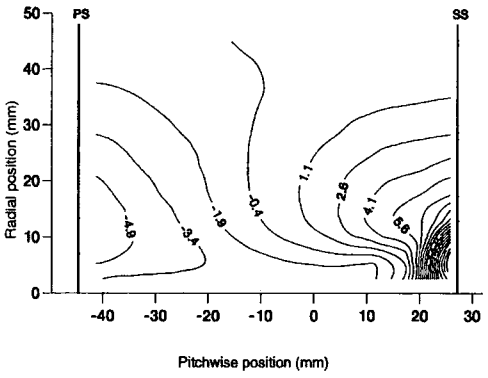

e) Secondary vector plot

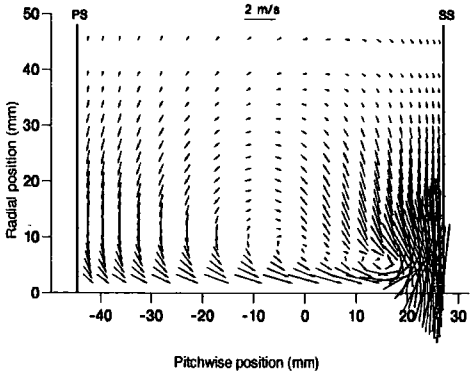

Figure 5.17—Area plots of Slot 7

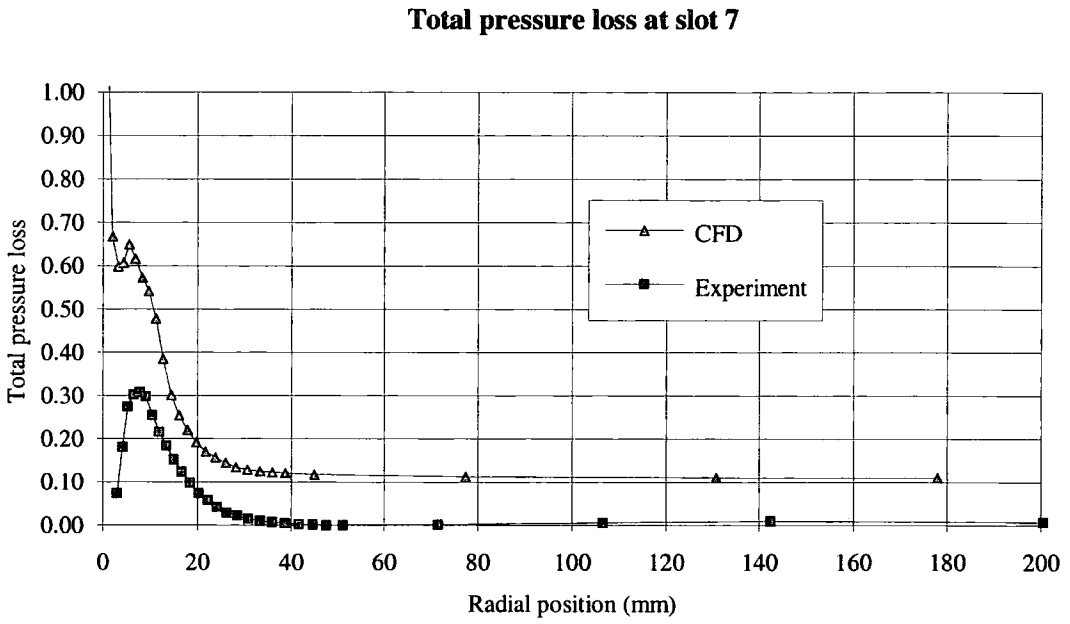

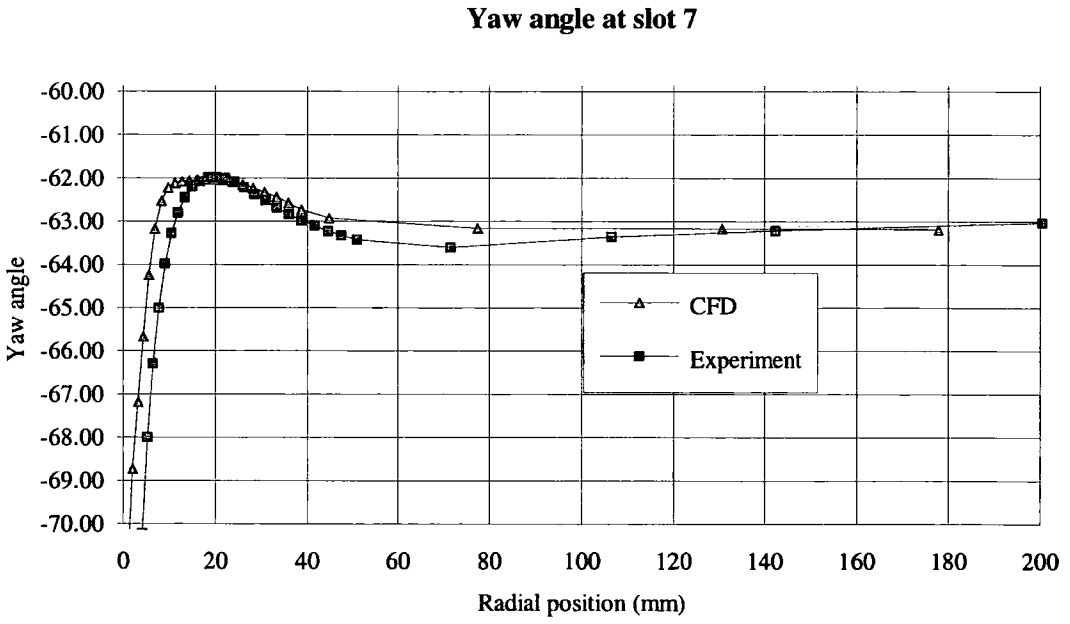

Figure 5.18— The pitch averaged results at slot 7

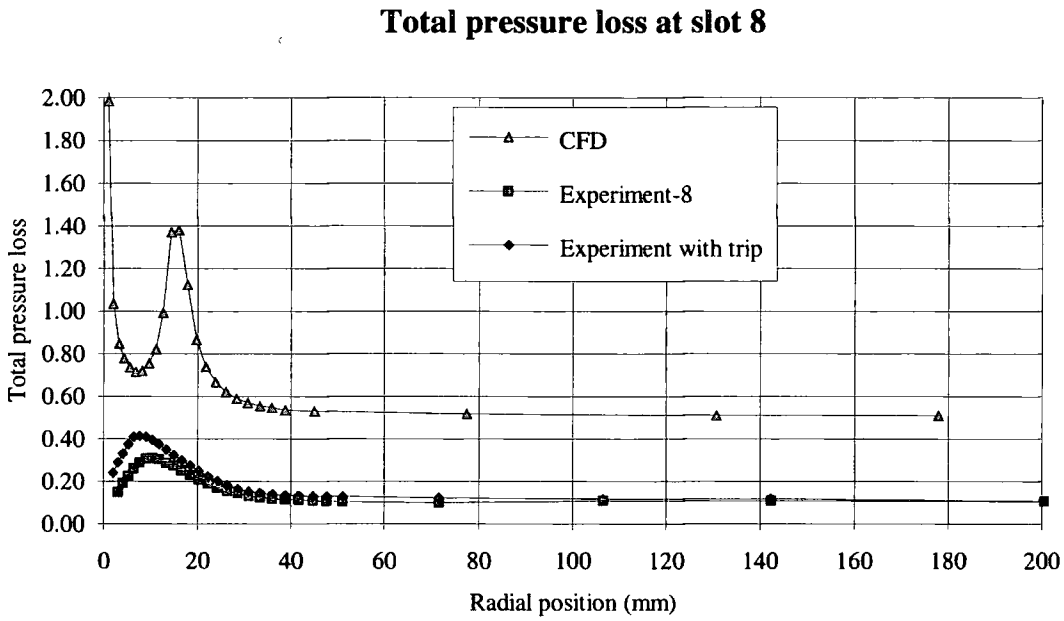

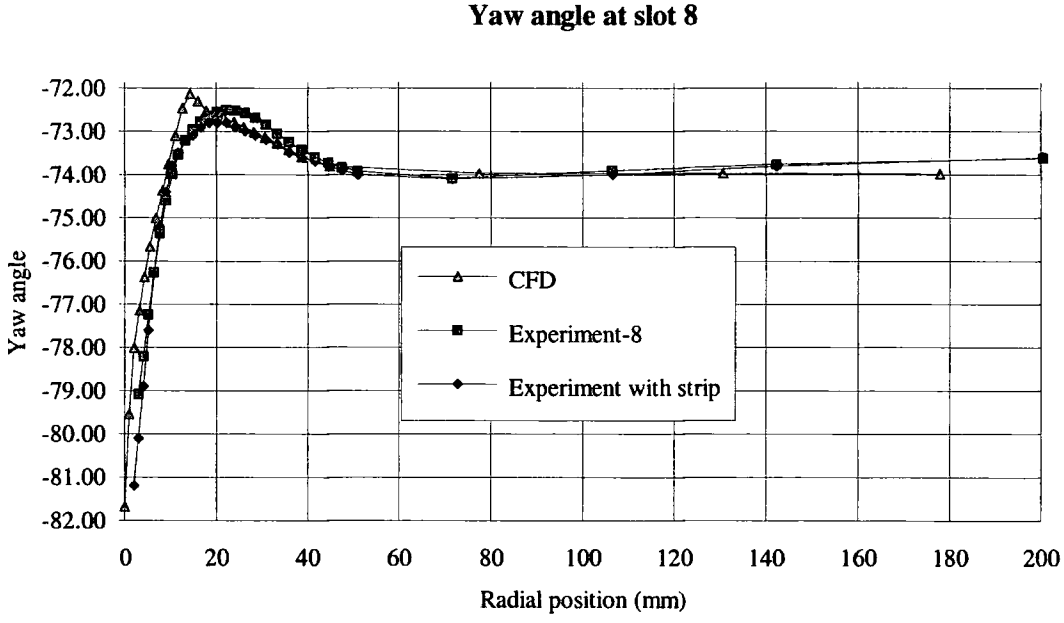

Figure 5.19— The pitch averaged results at slot 8

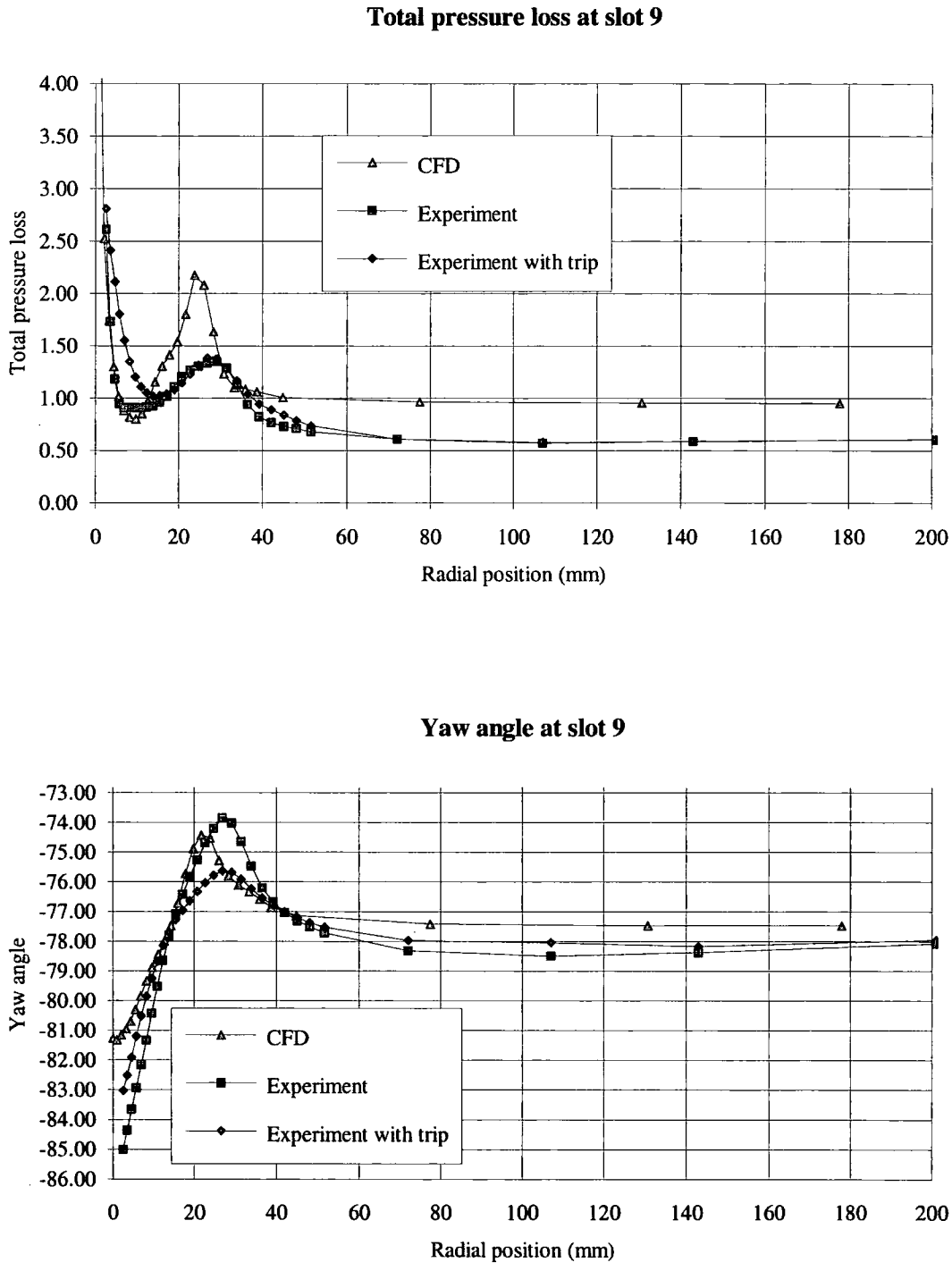

Figure 5.20— The pitch averaged results at slot 9

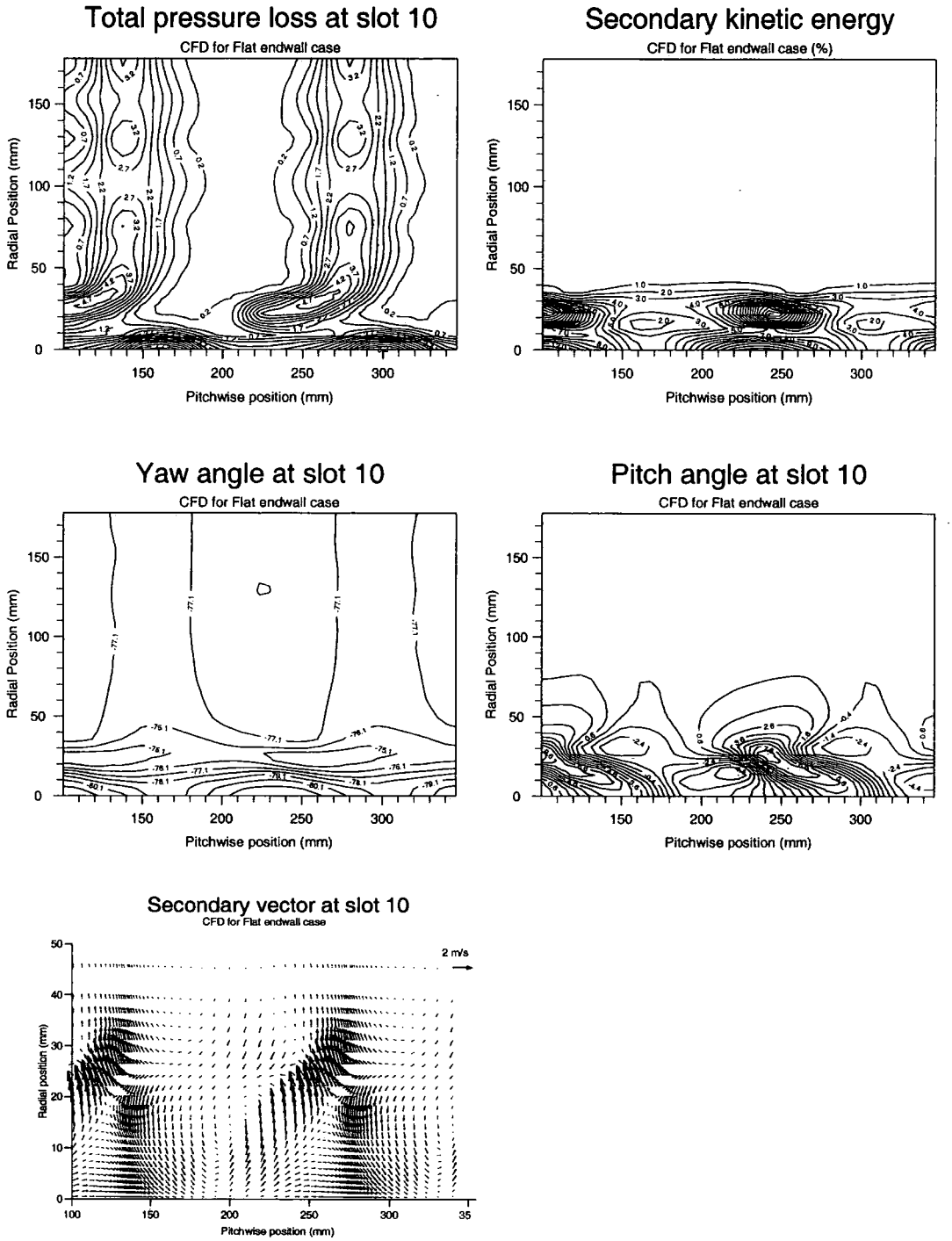

Figure 5.21—Area plots of Slot 10

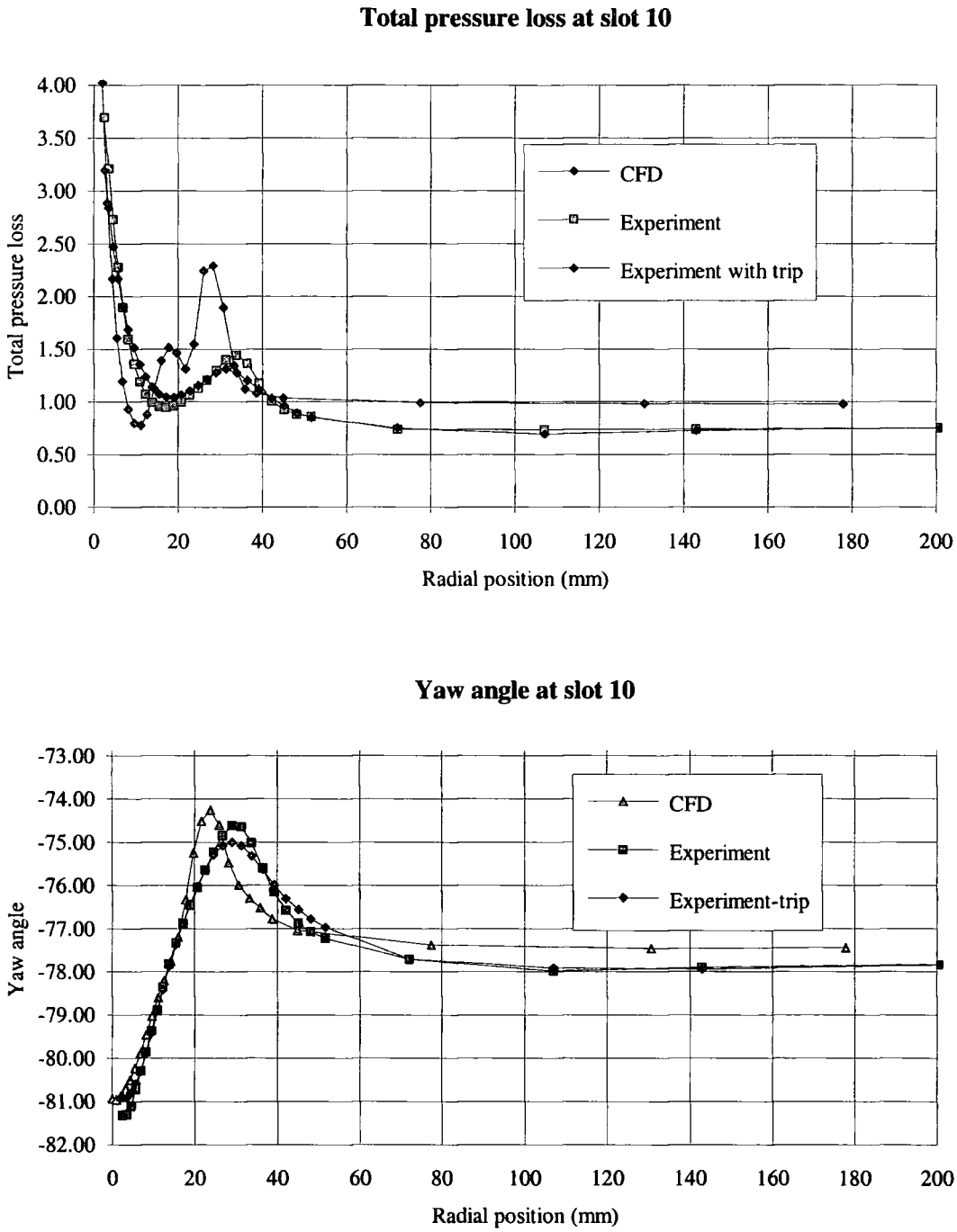

Figure 5.22— The pitch averaged results at slot 10

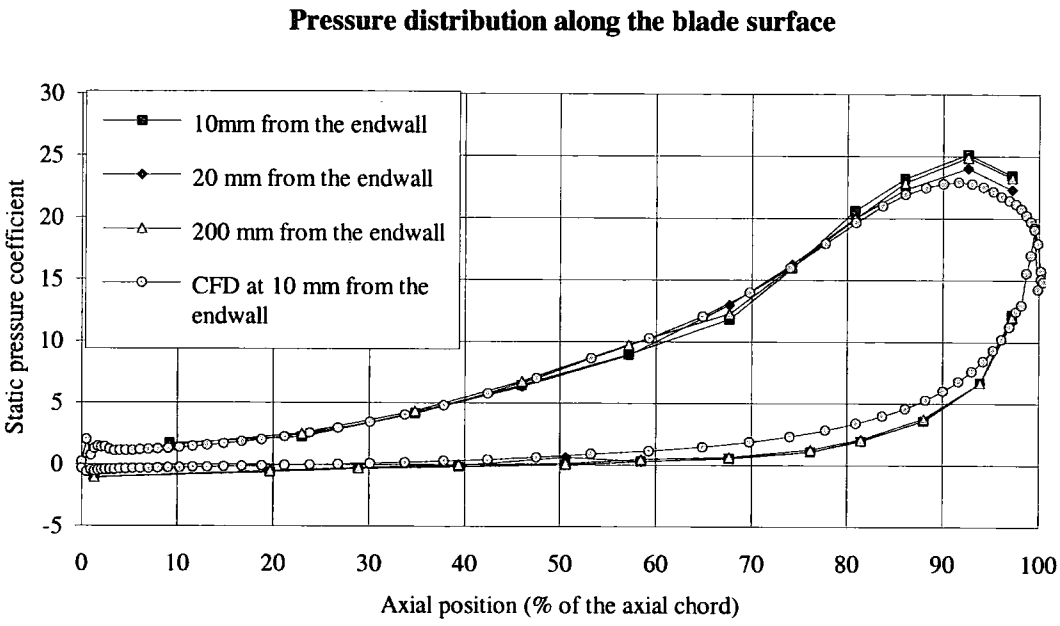

Figure 5.23— The static pressure distribution on the ALSTOM blade (The experimental results were collected without trip)

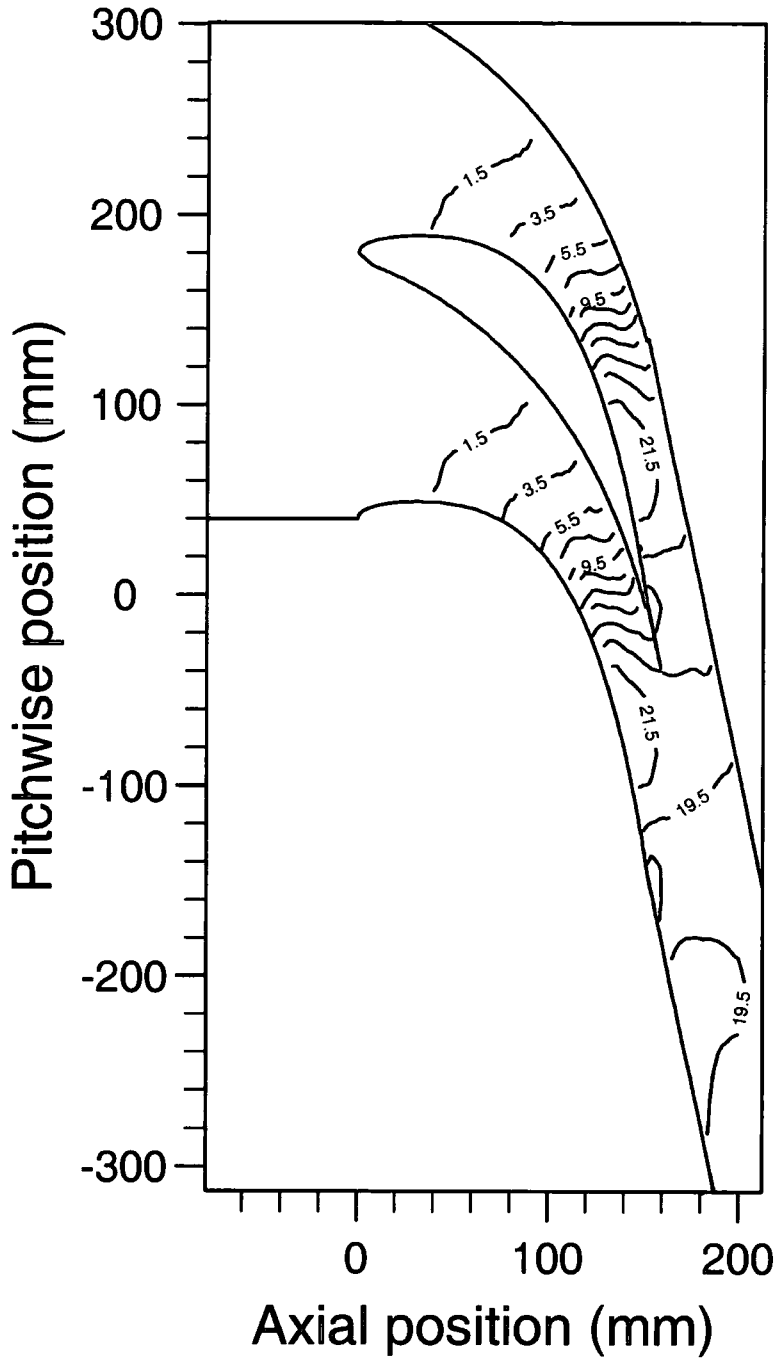

Figure 5.24—Static pressure on the flat end wall (CFD results)

Chapter 6

End wall Profile

Design

6.1 Introduction

The idea of the non-axisymmetric end wall profile design was to influence the local pressure field. Different end wall profile data files were generated. Four groups of end wall profiles were tested by the CFD method. A detailed investigation of how the end wall profile affects the secondary flow and total pressure loss have been completed. Comparisons were made between individual profiles and between the different groups. The best profile was chosen to be tested in the cascade.

6.2 The design philosophy of end wall profiles

The streamwise profile was designed based on the assumption that the end wall static pressure could be locally raised by applying a concave curvature to the end wall. Likewise, the static pressure could be lowered by convex curvature. According to previous work from Deich (1960), those profiles which he selected reduced the velocity in the region of highest turning and provided increased acceleration of the flow upstream of the trailing edge. It was thought that a similar profile should be applied to

the axial profile of the shaped end wall. Therefore, a profile designed with curvature towards the trailing edge of the blade was decided to be the shape in the axial direction as shown in Fig. 6.1. The change starts 15% upstream from the leading edge and finishes at the trailing edge. The upstream and outlet shapes of the blade passage are the same as for the flat end wall. This makes it possible to apply the shape to a real turbine. The profile is divided into three parts in the axial direction. The first part is an arc that makes the change smooth with the flat upstream end wall and the linear second part. The third part is a sinusoid that connects the second part and the trailing edge platform as shown in Fig. 6.1. The static pressure distribution along the pitch in the blade passage is shown in Fig. 6.3 (CFD results). The static pressure distribution in the passage and after the trailing edge both look like a sine wave. A pitchwise profile to vary the tangential magnitude of the curvature to match the pressure non-uniformity is shown in Fig. 6.2. The profile is basically two sine waves which have a smooth connection between them. The final non-axisymmetric profile shown in Fig. 6.6 is the combination of the axial and the pitchwise variation.

6.3 The end wall shape generation

In order to generate the non-axisymmetric end wall profile, a program has been written. The important parameters to decide the end wall shape are shown in Fig. 6.1 and Fig. 6.2. ct is the distance between the trailing edge and the peak of axial profile and at is the amplitude of the peak. sp and ss define the peaks of the pitchwise sine waves near the pressure and suction surfaces. They are expressed as fraction of the local pitch (distance between the blade surfaces), with the mid-pitch end wall height being fixed at zero. The program makes it very easy to change the end wall design. The program also generates a file which includes the information of the geometry and the computational grid of the cascade for input into the CFD codes.

6.4 The definition of end wall profiles

The names of end wall profiles are defined in a simple way. Every profile name which begins with n indicates that it is a non-axisymmetric end wall. On the other hand, the profile which begins with ax indicates that it is a axisymmetric end wall. For example, the name of n4042 profile is explained as following:

(1) n**40**42: The first two digital **40** means the distance from trailing edge **ct = 40 mm**.

(2) n404**2**: The third digital **4** means the maximum change is 2×**at** = 2×**4** mm. The at and ct are shown in Fig. 6.1.

(3) n4042: The last digital refers to the type of change along the pitchwise direction. The **2** refers to the shape as shown in the pattern "2" in Fig. 6.4.

(4) n4043: The **3** means the pitchwise shape is the pattern "3" in Fig. 6.4.

(5) n4044: The **4** refers to the pattern "4" in Fig. 6.5.

(6) n404**t**: The **t** refers to the pattern "t" in Fig. 6.5.

All of these four pattern are shown in Fig. 6.4 and 6.5, the values of parameter sp and ss are shown in Table 6.1. All these end wall profiles were tested using the CFD code. The results and comparisons are presented.

Table 6.1—Different patterns of end wall profiles

Pattern	pattern "2"	pattern "3"	pattern "4"	pattern "t"
sp (Divided by the local pitch)	0.25	-0.05	-0.05	0.25
ss (Divided by the local pitch)	0.225	0.225	-0.05	0.225

6.5 The CFD investigations of different profiles

After their definition, the different profiles were tested systematically by running the CFD codes. The total pressure loss and secondary kinetic energy were compared as a basis for the design choice.

A series of end wall profiles have been tested by the CFD method. The mass averaged total pressure loss at slot 10, the pitch averaged total pressure loss at slot 10, the pitch averaged yaw angle distribution at slot 10 and the static pressure distribution along the blade surfaces near the end wall were calculated and recorded. The total pressure loss, the static pressure and the secondary kinetic energy coefficients based on the inlet means they were divided by the inlet dynamic pressure. Those based on the exit means they were divided by the exit isentropic dynamic pressure.

After some preliminary tests, the pattern "2" was selected to be tested systematically. The profiles with at = 4 mm, 5 mm and 6 mm were tested with different ct. In order to see the effect of different ct's, the comparison are made for a fixed at.

The mass averaged values of total pressure loss, yaw angle and secondary kinetic energy were calculated and shown in Table 6.2. Compared with the flat end wall, the yaw angle is not changed very much which indicates an almost constant mass flow rate. The CFD results for type "2" and type "t" are also shown in Fig. 6.7. It can be seen that the secondary flow is reduced as ct increases, with a minimum point around ct=50mm. The loss is reduced compared to the flat end wall, without a very clear trend, but some indication of a minimum around ct=40-55mm.

However, the mass averaged values only show the overall results of the shaped end walls. Pitch averaged results can give a further explanation of what is happening. Area plots for the chosen end wall shape gives a detailed description of the effect of the shaped end wall. In order to understand the effect of the shaped end walls, the pitch

averaged results and area plots for the chosen profile are discussed in the following sections.

Table 6.2—The results of different end wall profiles

Profile	ct (mm)	2*at (mm)	YAW (degree)	SKE Based on inlet	SKE Based on exit	CPO Based on inlet	CPO based on exit	Secondary kinetic energy on inlet	Secondary kinetic energy on exit
flat	none	none	77.35	0.0098	0.461×10^{-3}	1.161	0.0546	0.210	9.87×10^{-3}
n3042	30	8	77.23	0.0095	0.441×10^{-3}	1.096	0.0509	0.194	9.02×10^{-3}
n4042	40	8	77.26	0.0089	0.416×10^{-3}	1.098	0.0513	0.191	8.92×10^{-3}
n5042	50	8	77.29	0.0088	0.413×10^{-3}	1.092	0.0512	0.181	8.49×10^{-3}
n3052	30	10	77.27	0.0094	0.437×10^{-3}	1.126	0.0523	0.183	8.51×10^{-3}
n3252	32	10	77.21	0.0097	0.450×10^{-3}	1.089	0.0505	0.193	8.96×10^{-3}
n4052	40	10	77.24	0.0089	0.416×10^{-3}	1.089	0.0509	0.190	8.87×10^{-3}
n4552	45	10	77.26	0.0087	0.408×10^{-3}	1.088	0.0510	0.186	8.71×10^{-3}
n5252	52	10	77.28	0.0086	0.404×10^{-3}	1.087	0.0511	0.181	8.51×10^{-3}
n525t	52	10	77.26	0.0087	0.408×10^{-3}	1.088	0.0510	0.186	8.71×10^{-3}
n565t	56	10	77.29	0.0089	0.419×10^{-3}	1.095	0.0515	0.178	8.28×10^{-3}
n605t	60	10	77.30	0.0089	0.419×10^{-3}	1.096	0.0516	0.176	8.28×10^{-3}
n3262	32	12	77.18	0.0101	0.468×10^{-3}	1.087	0.0504	0.196	9.08×10^{-3}
n4062	40	12	77.22	0.0090	0.423×10^{-3}	1.089	0.0509	0.194	9.06×10^{-3}
n5262	52	12	77.27	0.0086	0.404×10^{-3}	1.084	0.0509	0.182	8.55×10^{-3}
n6062	60	12	77.30	0.0090	0.425×10^{-3}	1.083	0.0511	0.175	8.26×10^{-3}
n4043	40	8	77.31	0.0091	0.426×10^{-3}	1.129	0.0528	0.186	8.70×10^{-3}
n404t	40	8	77.26	0.0090	0.422×10^{-3}	1.105	0.0518	0.169	7.93×10^{-3}
n4044	40	8	77.27	0.0100	0.470×10^{-3}	1.145	0.0538	0.166	7.80×10^{-3}
n405t	40	10	77.24	0.0086	0.402×10^{-3}	1.100	0.0514	0.192	8.97×10^{-3}
n506t	50	12	77.24	0.0086	0.404×10^{-3}	1.095	0.0515	0.185	8.71×10^{-3}
ax5062	50	12	77.24	0.0182	0.908×10^{-3}	1.117	0.0557	0.157	7.82×10^{-3}

6.5.1 The comparison of at = 4 mm series

Three profiles with ct = 30 mm, 40 mm and 50 mm were tested. The results of the CFD are shown in Figs. 6.7, 6.8 and 6.9. Fig. 6.9 shows that the effect of the end wall shape is to reduce the pressure difference in the region of the maximum turning, which is at about 66% axial chord. So the cross passage pressure gradient is reduced in the region of the maximum turning. The loading is compensated again around 80-90% axial chord, so that the overall loading is not changed, giving very nearly the same exit angle from the row as shown in table 6.1. The static pressure distribution as shown in Fig. 6.9 shows that n5042 gives smallest pressure change near the trailing edge and largest change at the mid-axial chord. The change of the static pressure is not much. When ct is too small, the profile changes too quickly from the maximum point to the zero height platform. This could cause flow separation in that region. The possible separation is shown by the static pressure distribution which gives a rapid change near the trailing edge. The low value of ct also give a higher diffusion on the suction surface. The mass averaged total pressure loss and secondary kinetic energy (which has been enlarged 100 times) are shown in Fig. 6.7. The total pressure loss and the secondary kinetic energy become smaller while the ct is increased. The profile n5042 gives the lowest secondary kinetic energy and total pressure loss. The reason can be found in Fig. 6.8. In the near end wall region, the n5042 gives the lowest loss as shown in Fig. 6.8. The n5042 shows the smallest overall secondary flow by the comparisons of the mass averaged values in Table 6.1. The lower secondary flow is also shown by the total loss distribution which gives higher loss in the near end wall region because of the smaller convection effect.

6.5.2 The comparison of at = 5 mm series

The profiles with ct = 30 mm, 40 mm and 50 mm were tested. The results are shown in the following Figs. 6.10 and 6.11. The static pressure on the blade surface is changed slightly by the end wall profiling. From Fig. 6.7, the profile n5252 gives the lowest loss

and secondary kinetic energy. When 'ct' is small, there is a large region upstream of the peak, which is desirable, but the rapid change between the peak and the exit may cause separation due to higher diffusion on the suction surface. When 'ct' is big, the profile can not change the pressure distribution much as shown in the Fig. 6.11. The n5252 gives the lowest total pressure loss in the near wall region as shown in Fig. 6.10.

6.5.3 The comparison of at = 6 mm series

The profiles with ct = 32 mm, 40 mm and 62 mm were tested. The comparisons are shown in Figs. 6.12 and 6.13. The static pressure shows that the n5262 has the smallest change near the trailing edge but the biggest change near the mid-axial position. From Fig. 6.7, the n5262 shows the smallest secondary kinetic energy. There is little difference in total pressure loss among them. The pitch averaged total pressure loss shows that the n5262 gives the lowest loss near the end wall. The other two profiles show a loss increase near the end wall compared with the flat end wall.

6.5.4 Other kinds of profiles

The other types of profiles like pattern "3", pattern "4" and pattern "t" were tested as well. Patterns "3" and "4" do not give good results because they have less effect on the pressure distribution. The pattern "t" is almost the same as pattern "2" except pattern "t" has a flat surface near the pressure surface which is easier to manufacture. It is not very clear from CFD results whether this flat surface will benefit the efficiency. The comparisons are shown in Fig. 6.14 and 6.15. The lowest loss and secondary kinetic energy point seems to locate at the ct = 52 mm position seen Fig. 6.7. The profile n525t does not give too much difference from the n5252. The pressure changes these two profiles have made along the blade surface are nearly the same as shown in Fig. 6.15.

An axisymetric end wall ax5062 was also tested. The meaning of the name is the same as defined before except that this is an axisymmetric shape. The ax5062 gives higher

loss and increases the secondary kinetic energy as shown in Table 6.1. In Fig. 6.14, the loss peak is shifted away from the end wall. This means that the high loss area is increased.

6.6 The chosen design

Overall, the n5252 and n5262 seem to give the best results. They give the lowest total pressure loss and secondary kinetic energy. A value of 5mm rather than 6mm was chosen for at as there seems to be no advantage with the higher value, and it would be more difficult to manufacture. The n525t gives the very similar result as n5252 gives. Since the type "t" is easier to manufacture and it would reduce the 'wetted area' of the end wall and pressure surface, the n525t profile with at=5mm and ct=52mm was made the final choice.

A detailed study was made of the flow with the chosen profile. The CFD results of Slot 4, 5, 6, 7 and 10 are shown in Figs. 6.16—6.21. The total pressure loss, secondary kinetic energy, yaw angle distribution, pitch angle distribution and secondary vector plot are presented for every slot. The pitch averaged results for some slots will be presented in chapter 7 along with the experimental results for comparisons.

At slot 4 in Fig. 6.16, the total pressure loss is concentrated on the blade suction surface and the suction corner. The secondary kinetic energy stays nearer to the pressure surface with its highest value at the mid-pitch. The yaw angle contour shows small underturning at about 35 mm away from the wall and large overturning near the end wall. The flow turning angle is decreasing from the pressure surface to the suction surface. The pitch angle shows that the flow is going towards the end wall because of the end wall shape. The secondary vector plot shows strong secondary flow near the end wall which is due to the inviscid effect. The vortex can hardly be seen. This is due to the inviscid blockage effect of the convex part of the end wall profile.

At slot 5 in Fig. 6.17, the total pressure loss is similar to that at slot 4. The highest value of the secondary kinetic energy has moved to nearer to the suction surface. The yaw angle contour shows stronger overturning which indicates the movement to lower region by the inviscid effect. The secondary flow has become stronger and the passage vortex is clearly noticed near the suction surface. The strong secondary flow very near the end wall is another indication of the strong inviscid blockage effect of the convex part of the end wall profile.

At slot 6 in Fig. 6.18, the shaped end wall has the biggest change. The total pressure loss has not changed too much from slot 5. The secondary kinetic energy centre has moved to the suction corner. The yaw angle shows a uniform yaw angle from the pressure surface to the suction surface because the two blade surfaces are nearly parallel at this slot position. The pitch angle and the secondary vector both show a quite dominant passage vortex. There is substantial amount of the secondary flow existing in the suction surface corner.

At slot 7 in Fig. 6.19, the profile of the shaped end wall is becoming smaller. The total pressure loss has spread towards the mid-span a little bit with the highest loss still on the suction surface and the suction corner. The peak of the secondary kinetic energy has moved onto the suction surface. There is an increase of the secondary kinetic energy in the pressure surface corner as well. The turning angle of the flow is increasing from the pressure surface to the suction surface shown in the yaw angle contour. The secondary vector shows that the passage vortex centre is still at the mid-pitch position. This implies the pressure gradient between the pressure surface and the suction surface which drives the vortex centre towards the suction surface has been reduced. Compared with the flat end wall results shown in Fig. 5.9, the secondary kinetic energy with the profiled end wall is less concentrated and covers larger area. The secondary vector plot shows much smaller secondary flow near the end wall. The vortex centre is located nearly the

centre of the pitch but the vortex is located in the suction corner with the flat end wall. From the secondary vector plot, the secondary flow with the shaped end wall is generally smaller than with the flat end wall.

There are not only the half span plots but also the plots near the end wall region at slot 10 as shown in Figs. 6.20 and 6.21. The total pressure loss shows reductions near the end wall. Compared to Fig. 5.17 for the flat end wall CFD results, the thickness of the low energy layer on the end wall has been reduced. The secondary kinetic energy is also reduced. The secondary vector plot shows smaller secondary flow. Both the underturning and the overturning are smaller than those of the flat end wall. The secondary vector plot shows a big reduction by the shaped end wall.

The static pressure on the end wall was plotted in Fig. 6.22. Compared with the CFD results with flat end wall in Fig. 5.24, there seems to be a increase of the pressure on the suction surface of the blade. To aid the comparison, the change which shaped end wall has made on the static pressure was obtained by using the shaped end wall results minus the flat end wall results. The difference is shown in Fig. 6.23. The negative value in the contour means an increase of the local pressure, positive means a pressure reduction. It can be seen that there is a pressure decrease area near the pressure surface and a pressure increase area on the suction surface in the region of 50-70% axial chord. These changes corresponds to the end wall profile in Fig. 6.6. The cross passage pressure gradient is reduced here.

6.7 Conclusion

From the CFD investigation, the n525t profile was chosen to be tested in the cascade. The shaped end wall reduces the predicted total pressure loss and secondary flow at slot 10. The reason of the reduction is the smaller cross passage pressure gradient achieved by the shaped end wall. The smaller secondary flow has smaller convection effect which drives the low energy fluid away from the end wall. From the pitch averaged

comparisons as shown in Fig. 6.18, it can be seen that the loss peak is nearer to the end wall than that for the flat end wall.

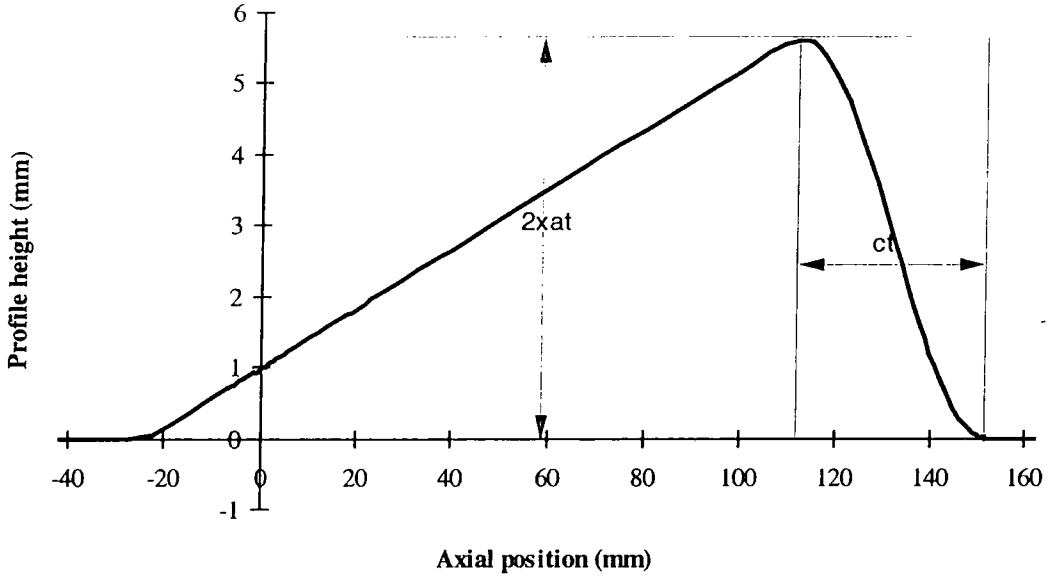

Figure 6.1—The end wall shape at the axial direction

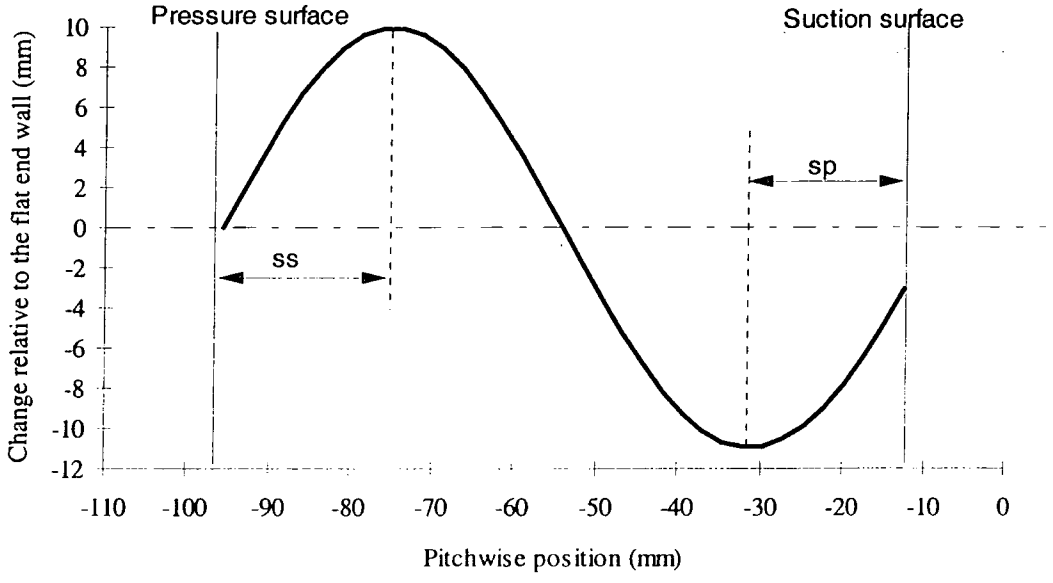

Figure 6.2—The end wall shape at the pitchwise direction

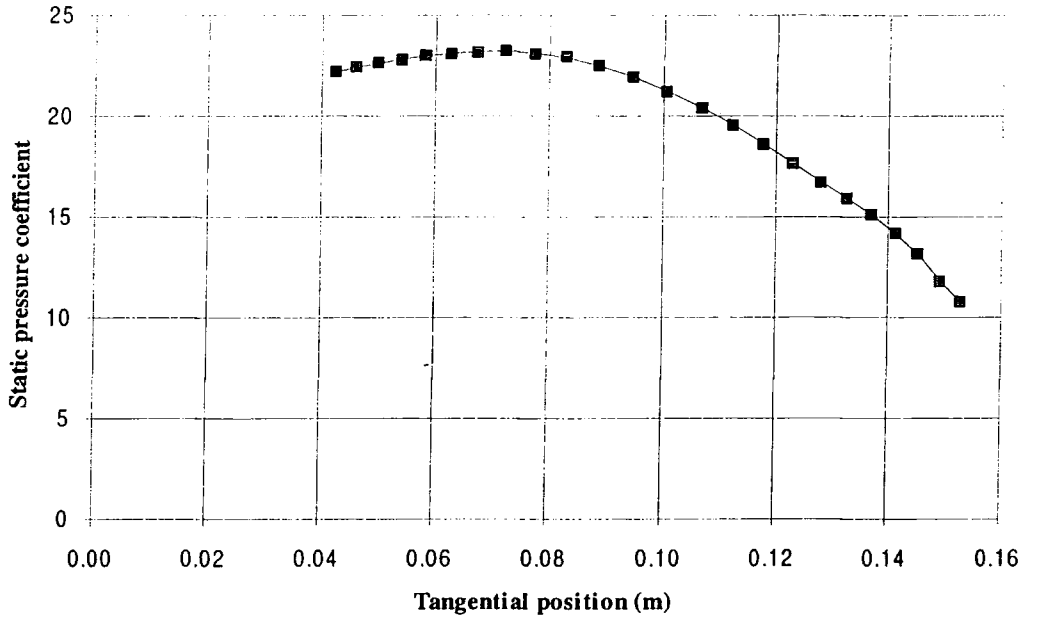

a. Static pressure distribution across the pitch near the end wall at slot 8 (ALSTOM blade).

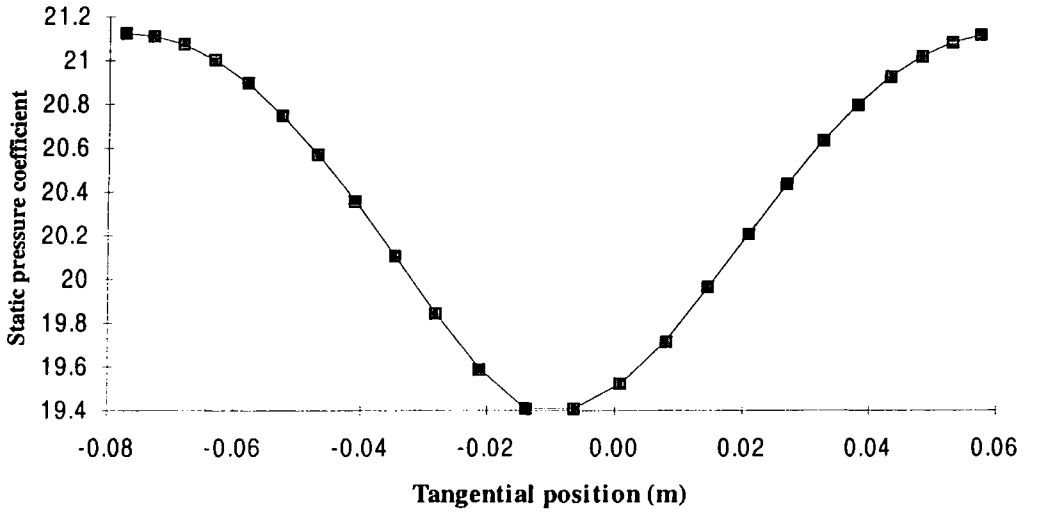

b. The static pressure distribution across the pitch at slot 10(ALSTOM blade)

Figure 6.3—The static pressure distribution across the pitch (CFD)

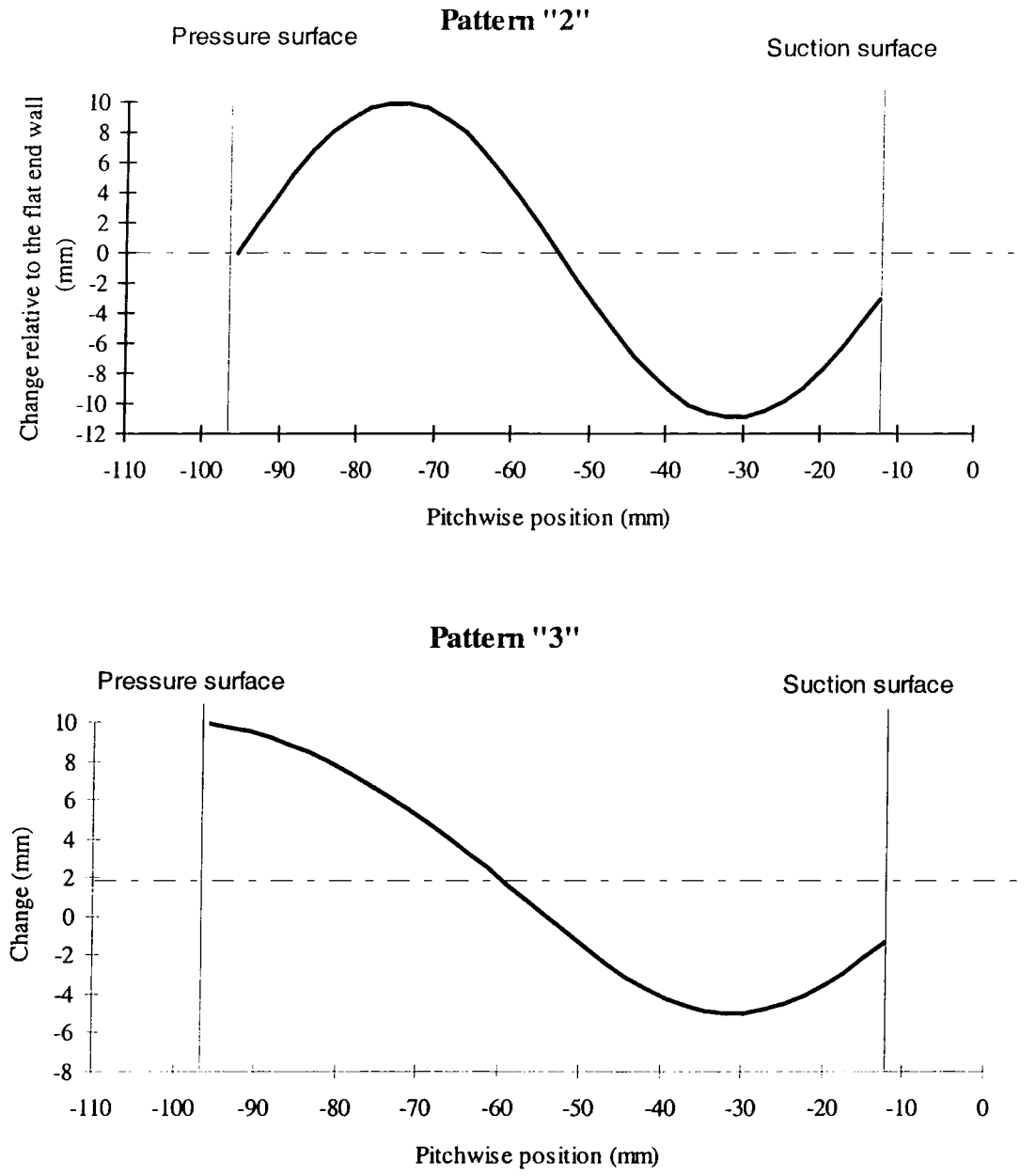

Figure 6.4—The description of different pitchwise end wall shape

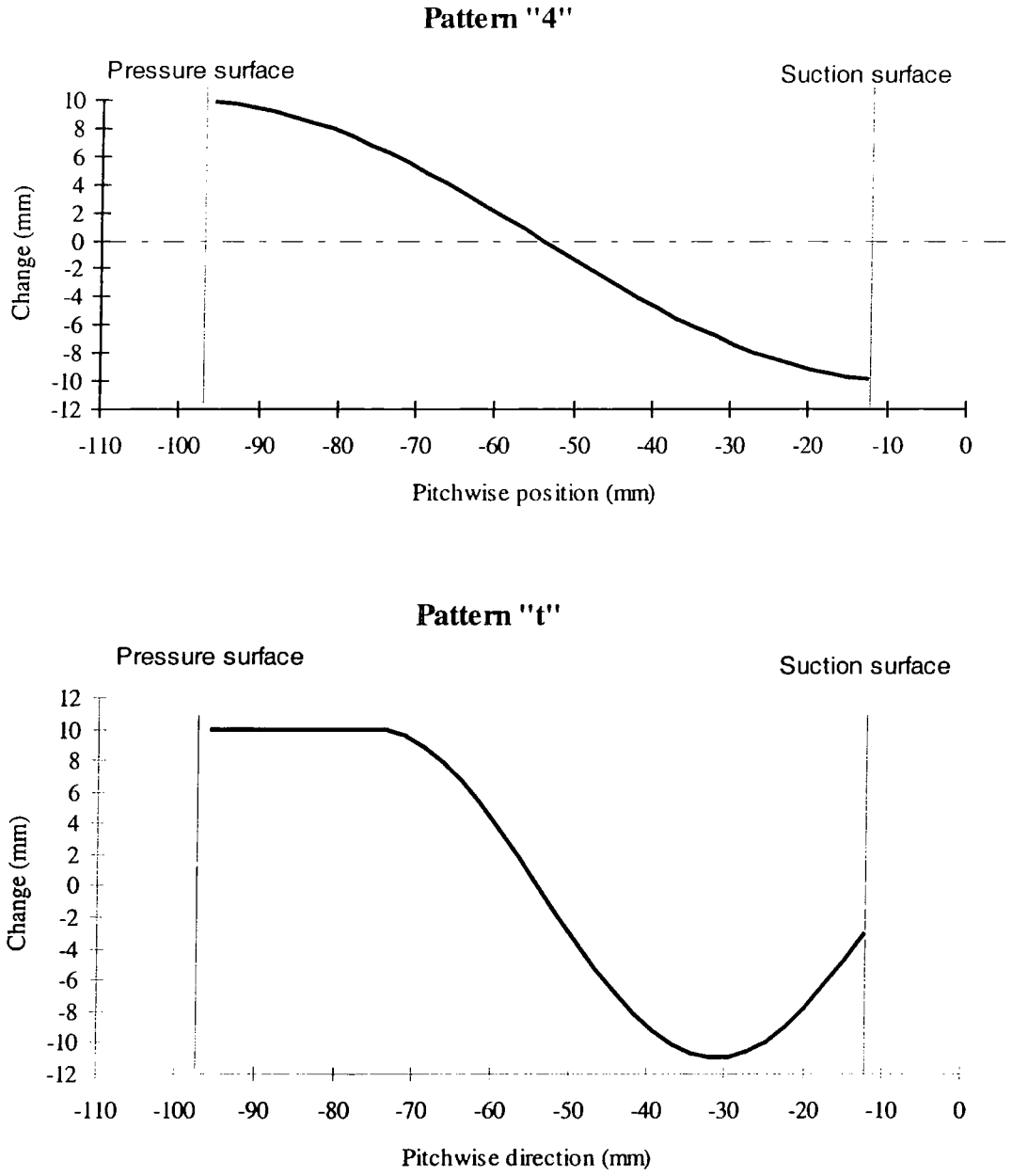

Figure 6.5—The description of different pitchwise end wall shape

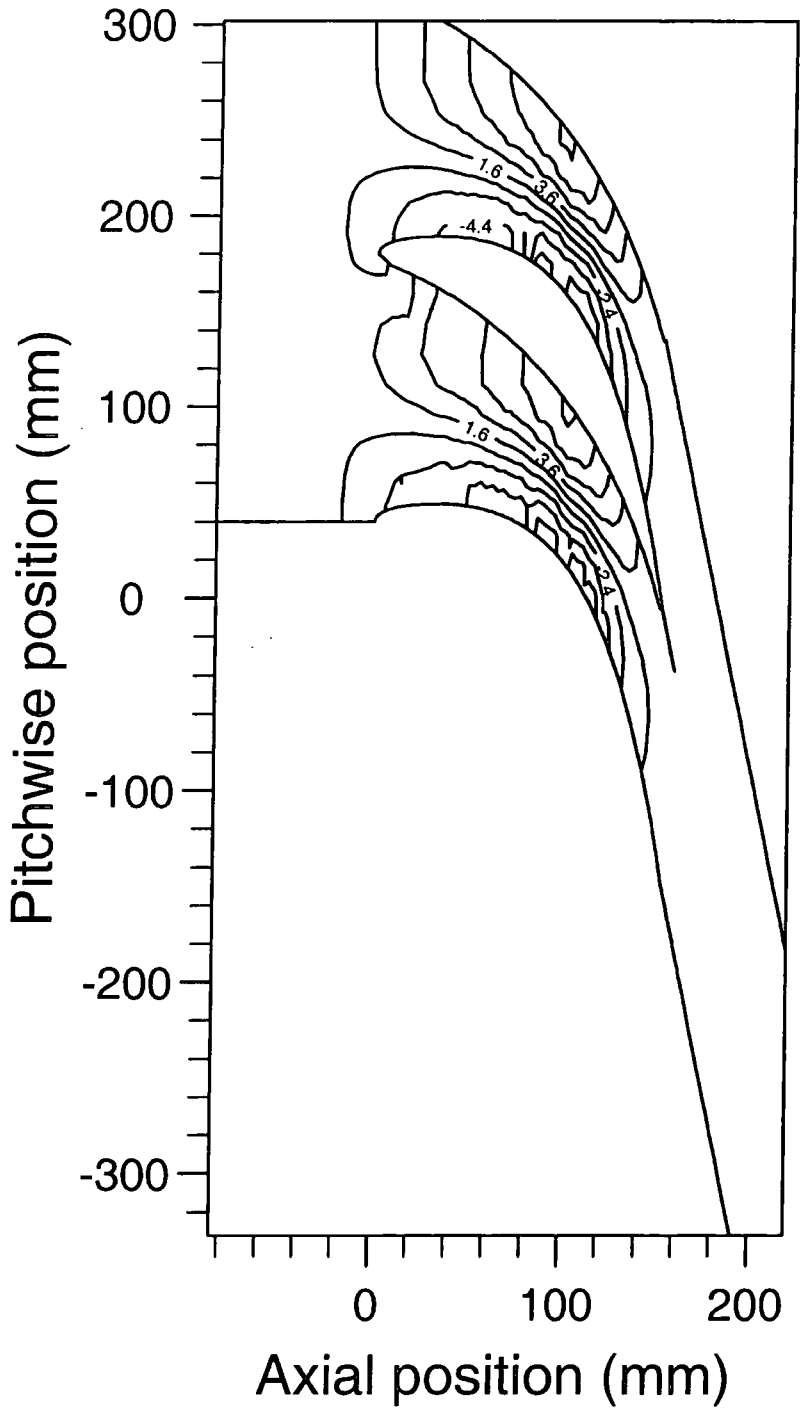

Figure 6.6—The non-axisymmetric end wall profile (n525t)

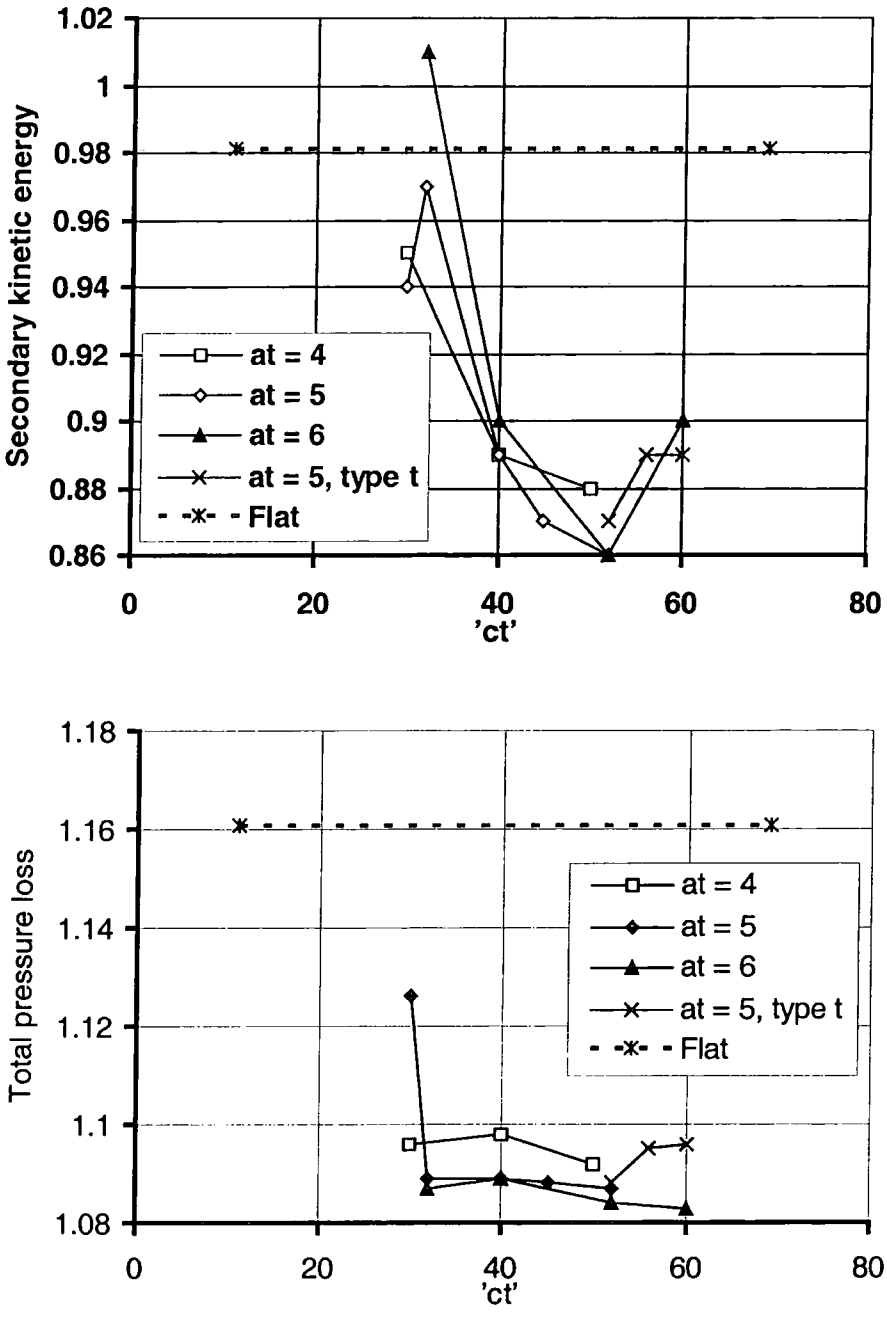

Figure 6.7—The comparisons of different series

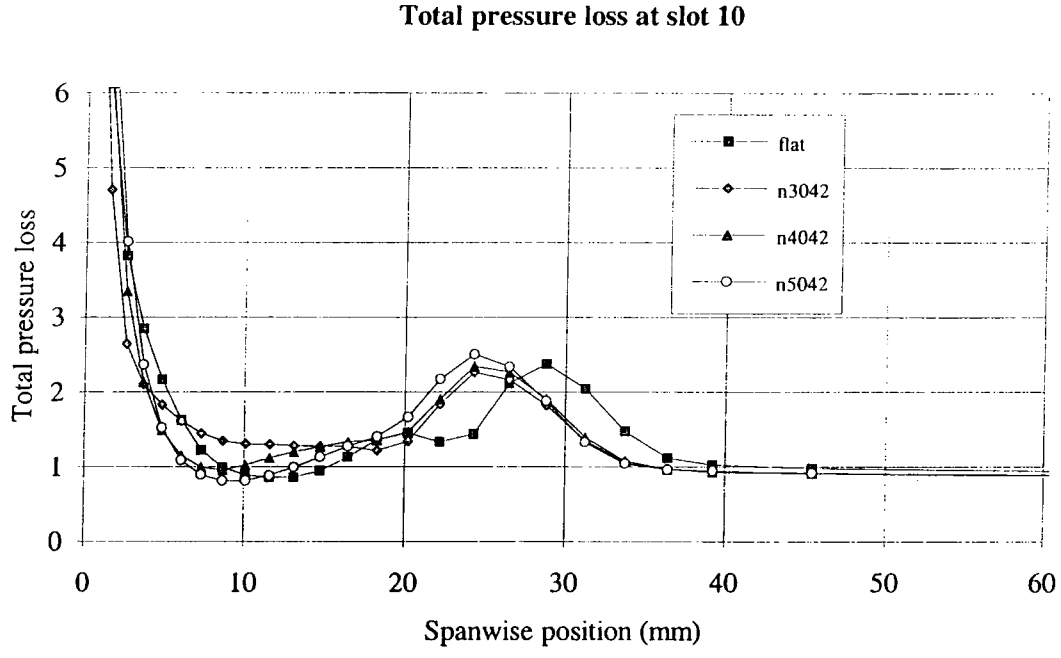

Figure 6.8—The total pressure loss comparisons for the at = 4 mm series

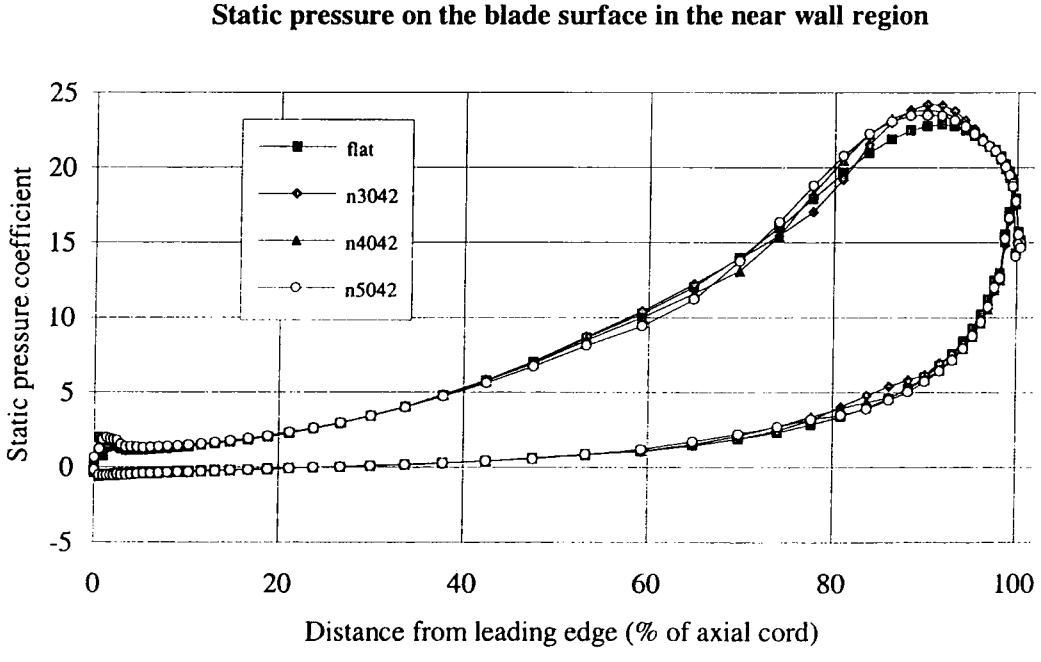

Figure 6.9—The static pressure on the blade surface

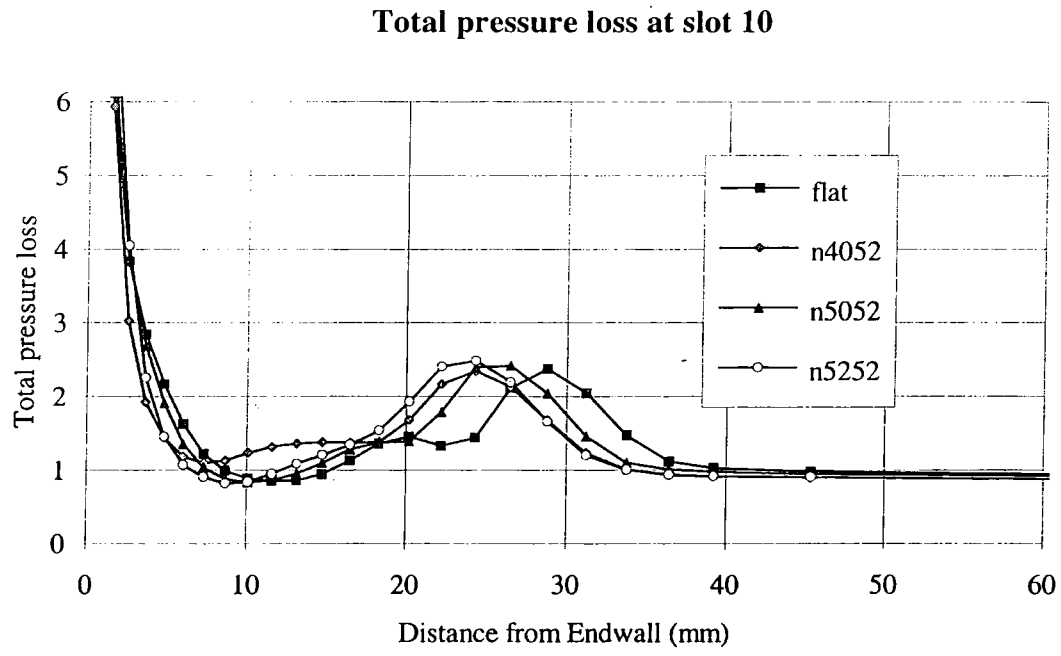

Figure 6.10—The total pressure loss comparisons for the at = 5 mm series

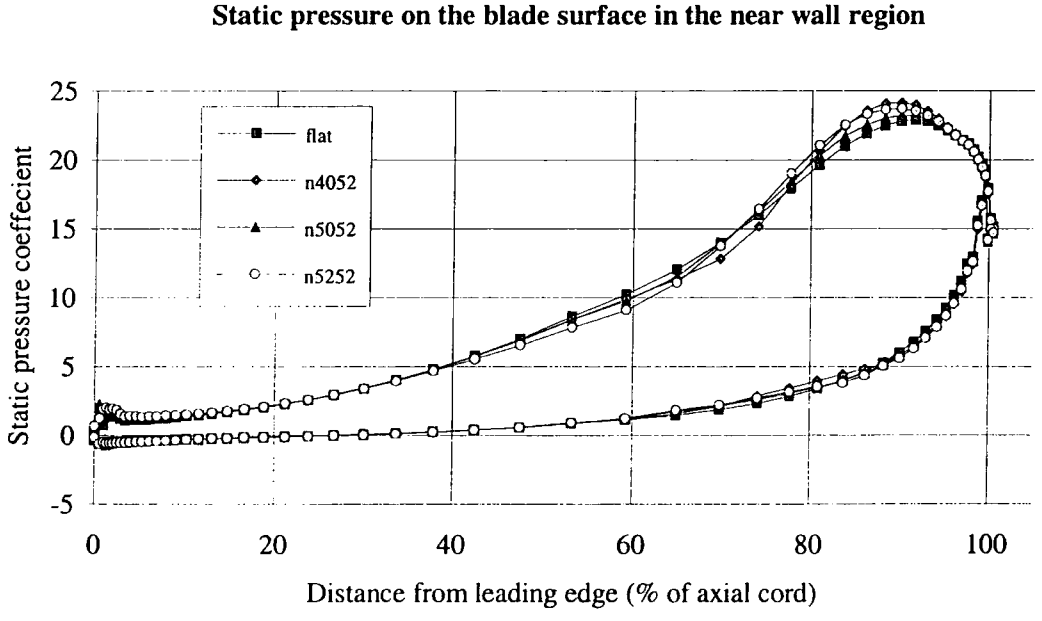

Figure 6.11—The static pressure on the blade surface

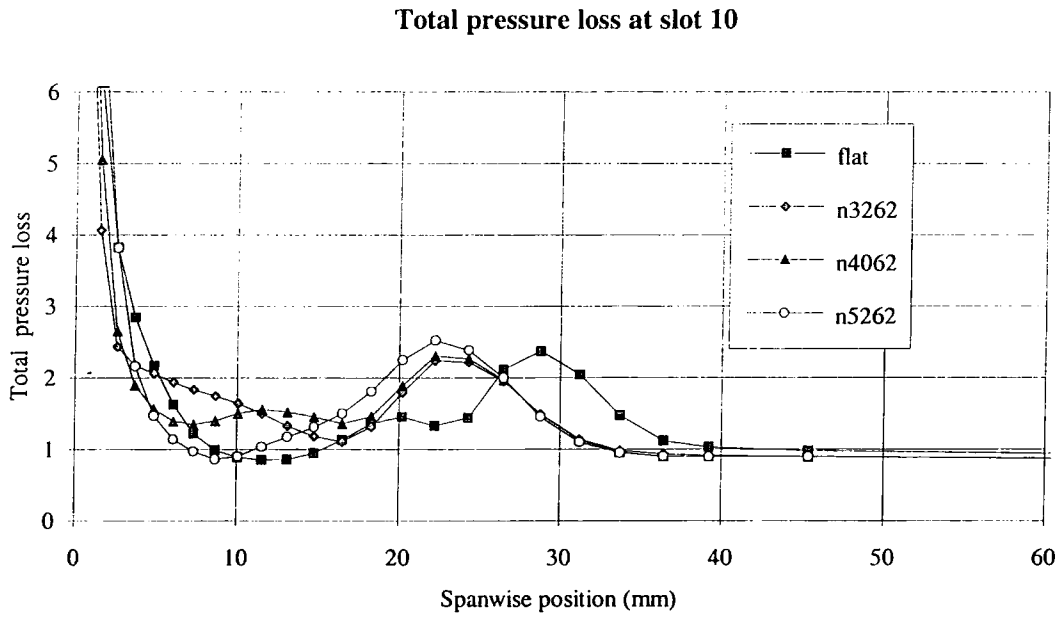

Figure 6.12—The total pressure loss comparisons for the at = 6 mm series

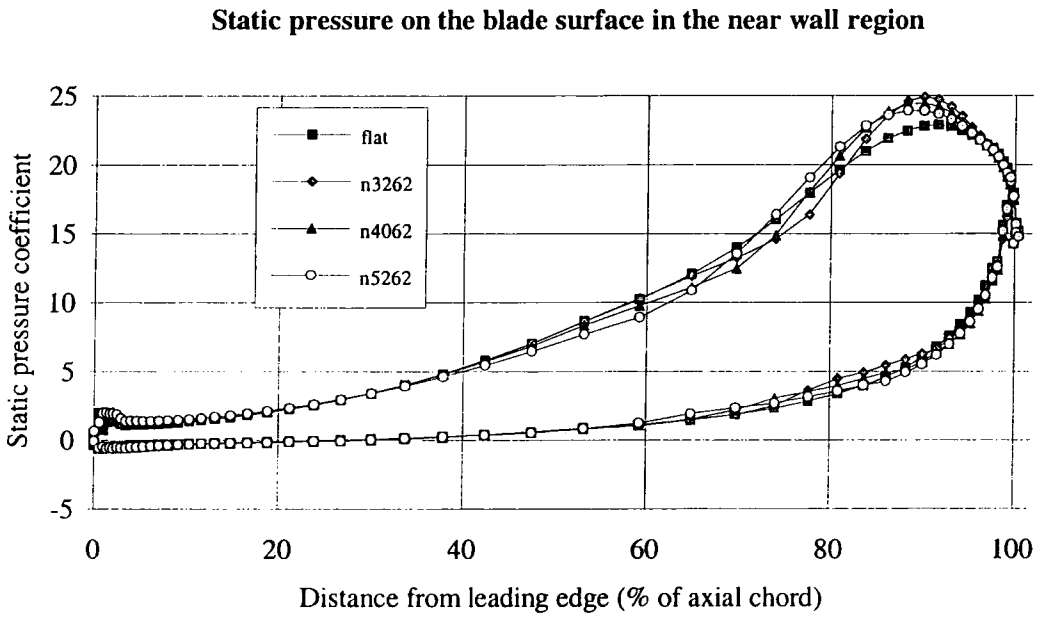

Figure 6.13—The static pressure on the blade surface

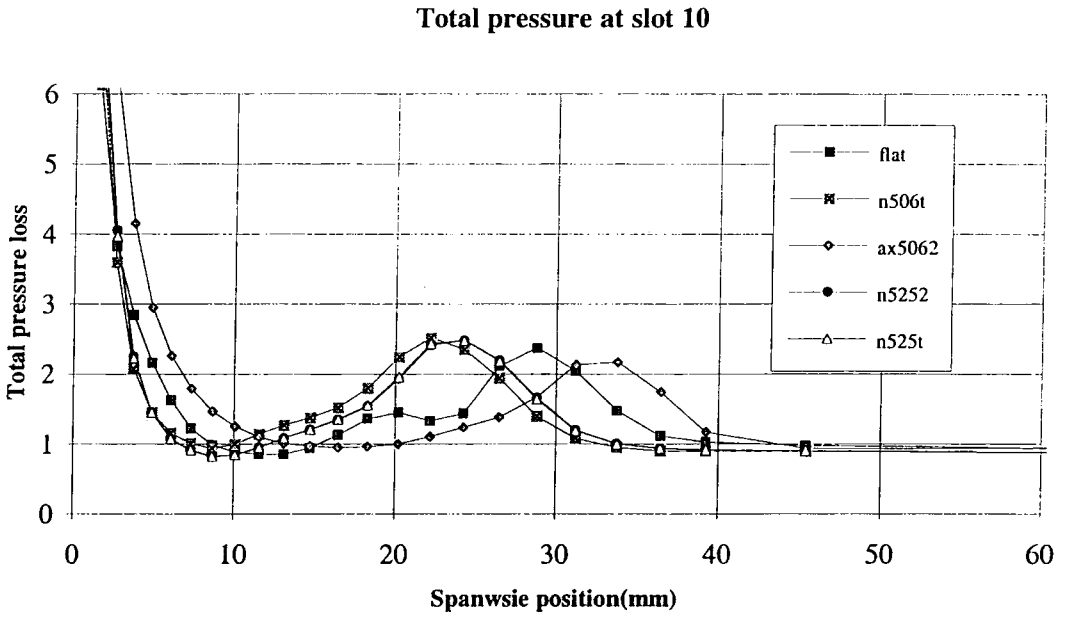

Figure 6.14—The total pressure comparisons for different profiles

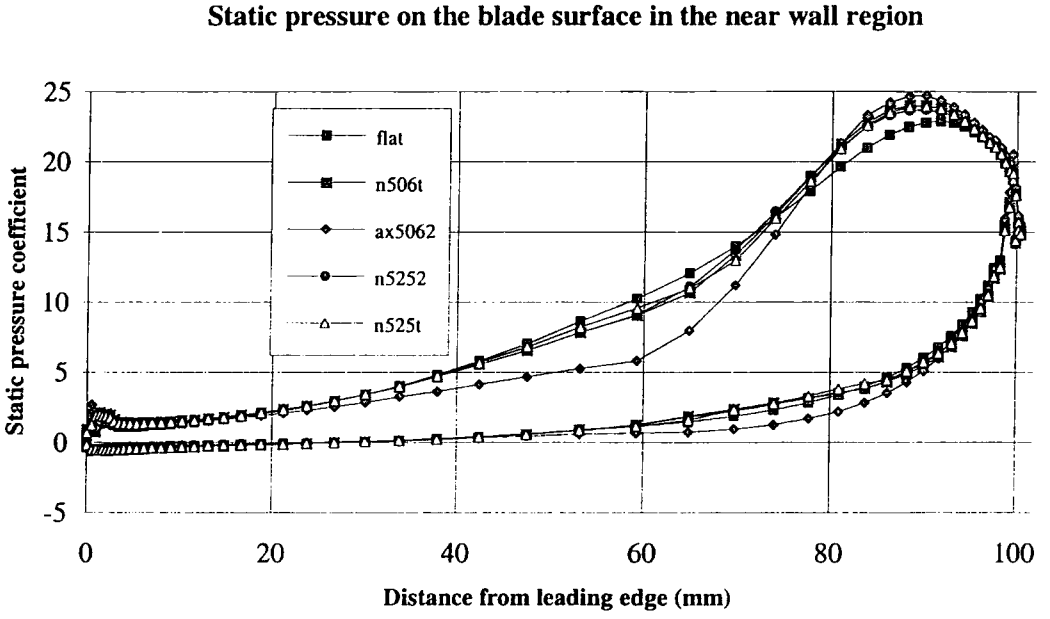

Figure 6.15—The static pressure on the blade surface

a) Total pressure loss contours

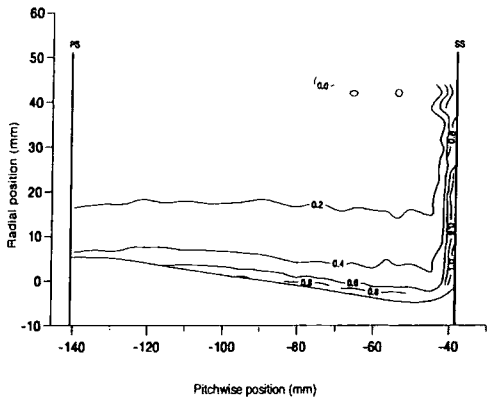

b) Secondary kinetic energy contour (%)

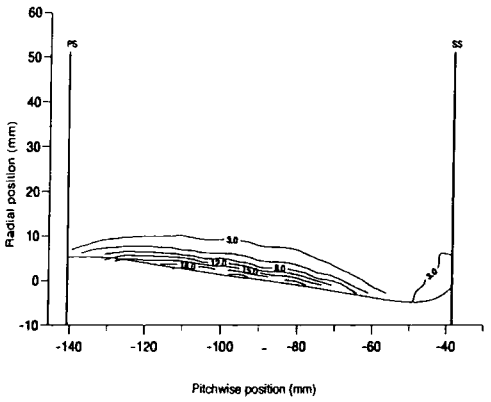

c) Yaw angle contour

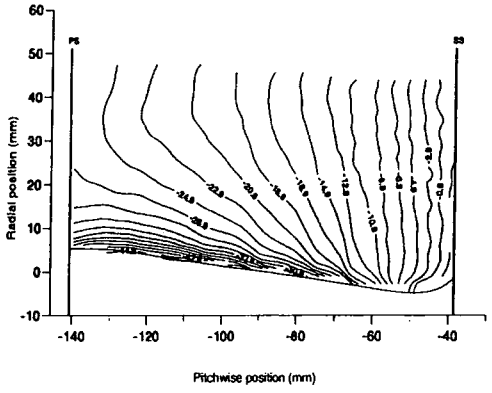

d) Pitch angle contour

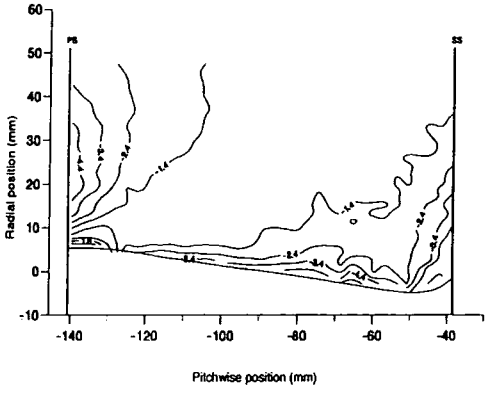

e) Secondary vector plot

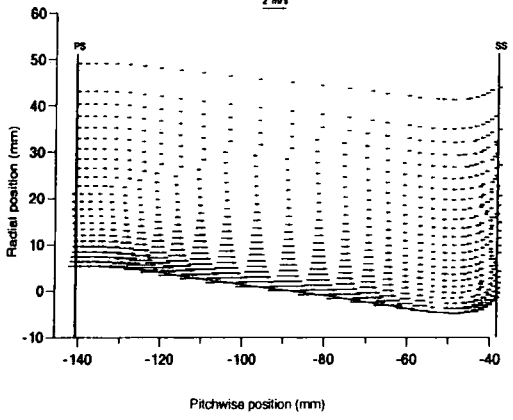

Figure 6.16—The CFD results at slot 4 for the n525t

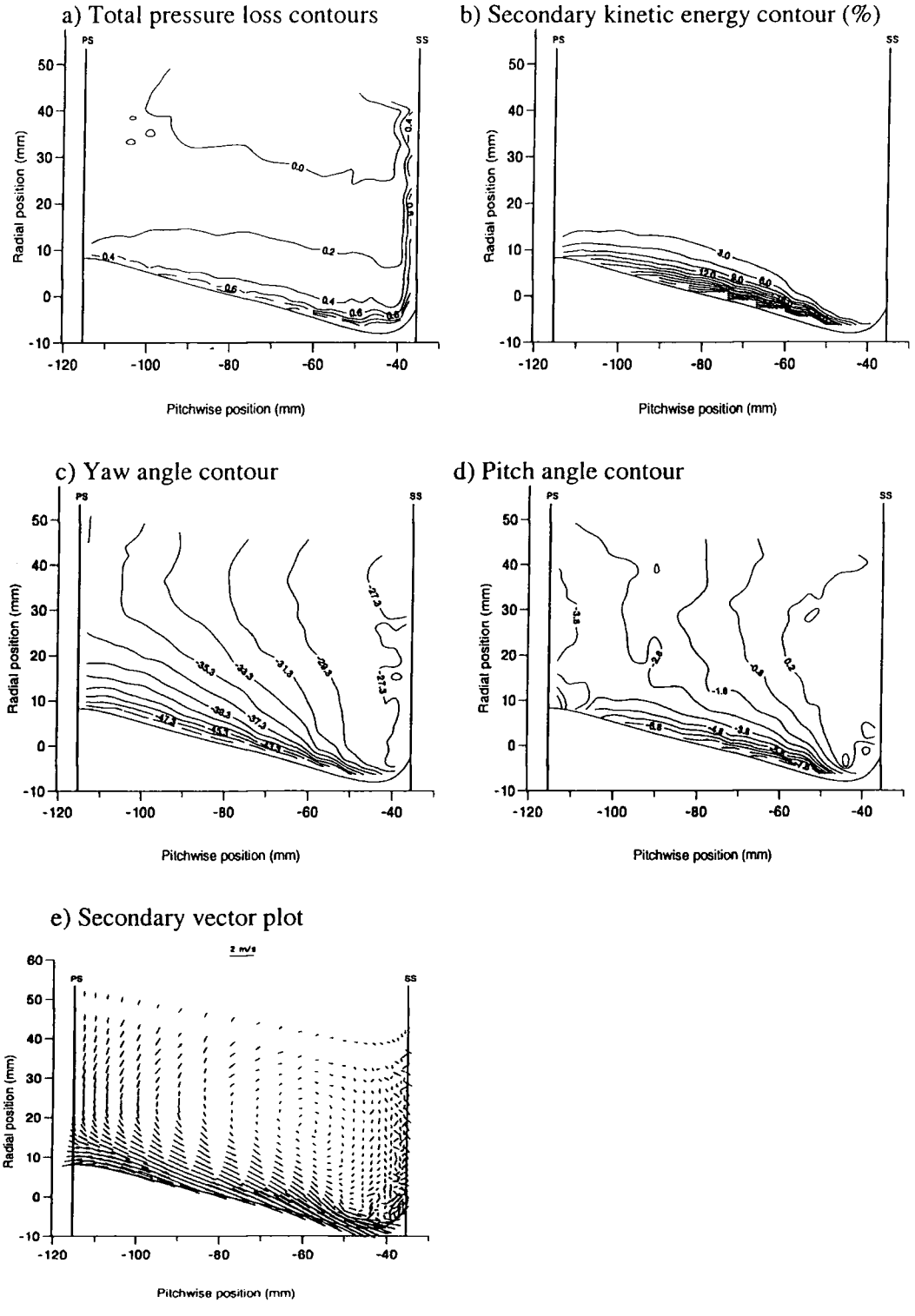

Figure 6.17—The CFD results at slot 5 for the n525t

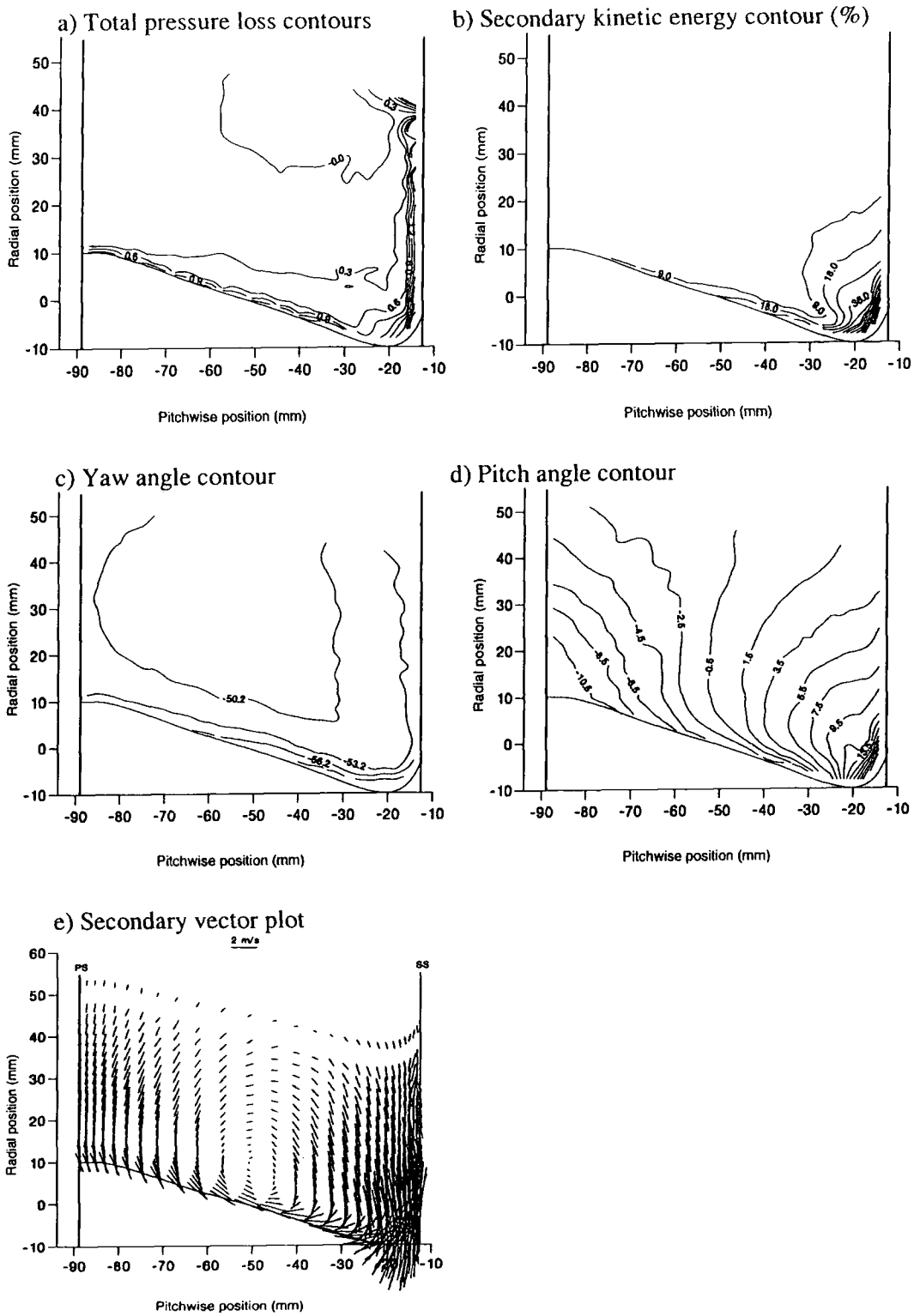

Figure 6.18—The CFD results at slot 6 for the n525t

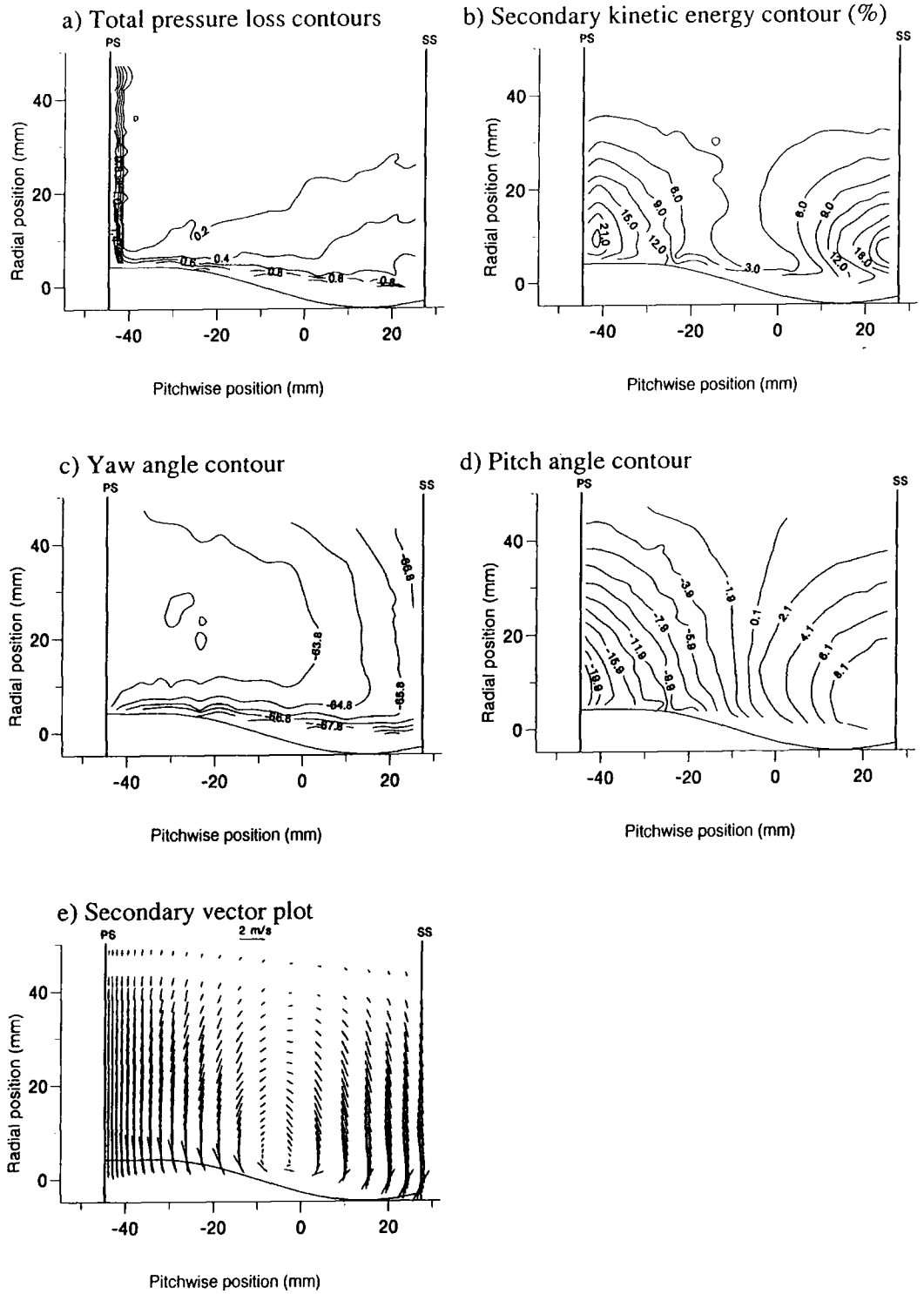

Figure 6.19—The CFD results at slot 7 for the n525t

a) Total pressure loss contours

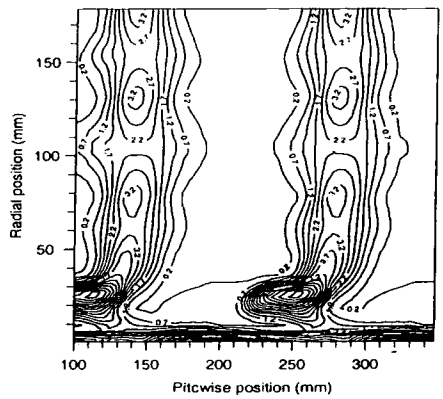

b) Secondary kinetic energy contour (%)

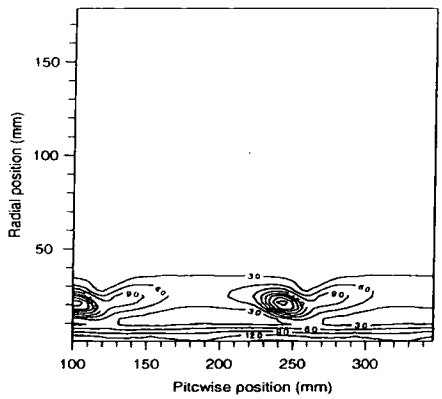

c) Yaw angle contour

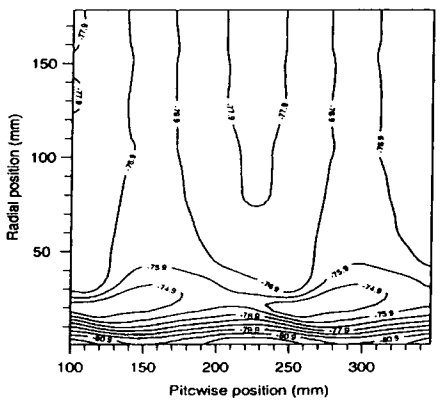

d) Pitch angle contour

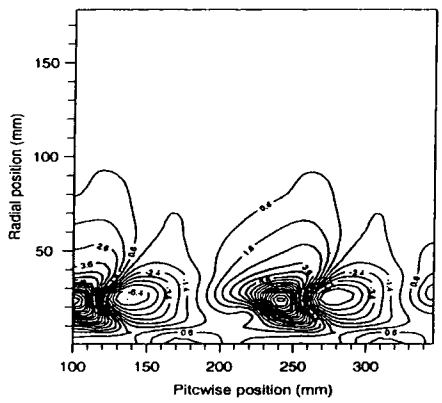

e) Secondary vector plot

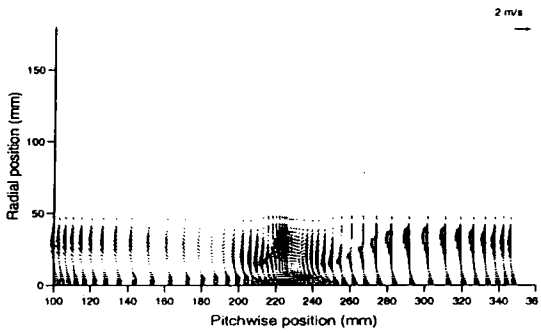

Figure 6.20—The CFD results at slot 10 (half span) for the n525t

a) Total pressure loss contours

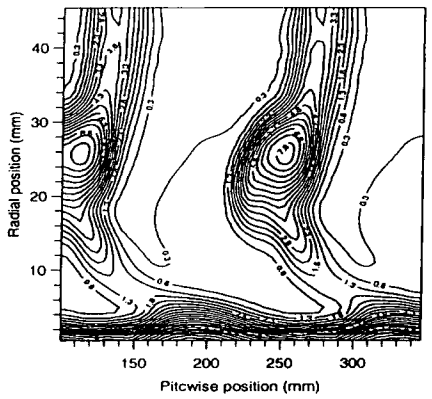

b) Secondary kinetic energy contour (%)

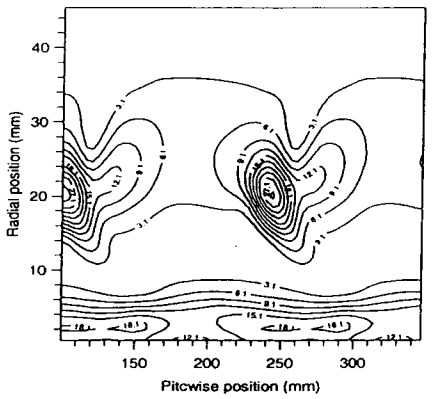

c) Yaw angle contour

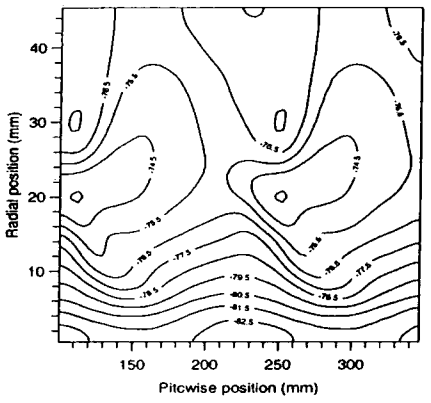

d) Pitch angle contour

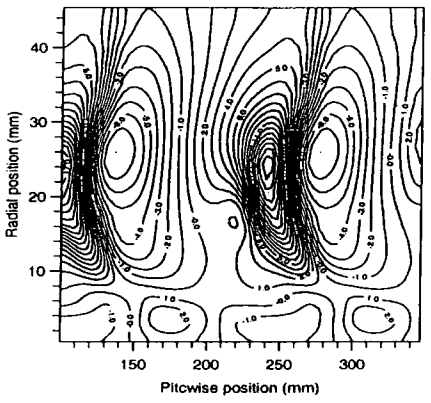

e) Secondary vector plot

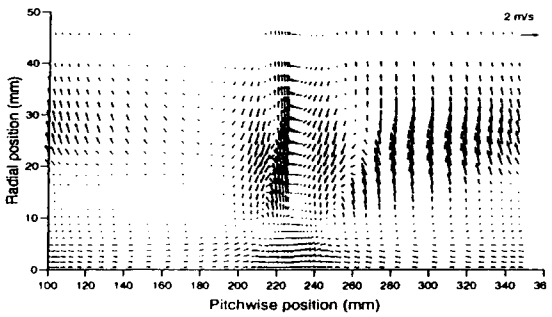

Figure 6.21—The CFD results at slot 10 (near wall region) for the n525t

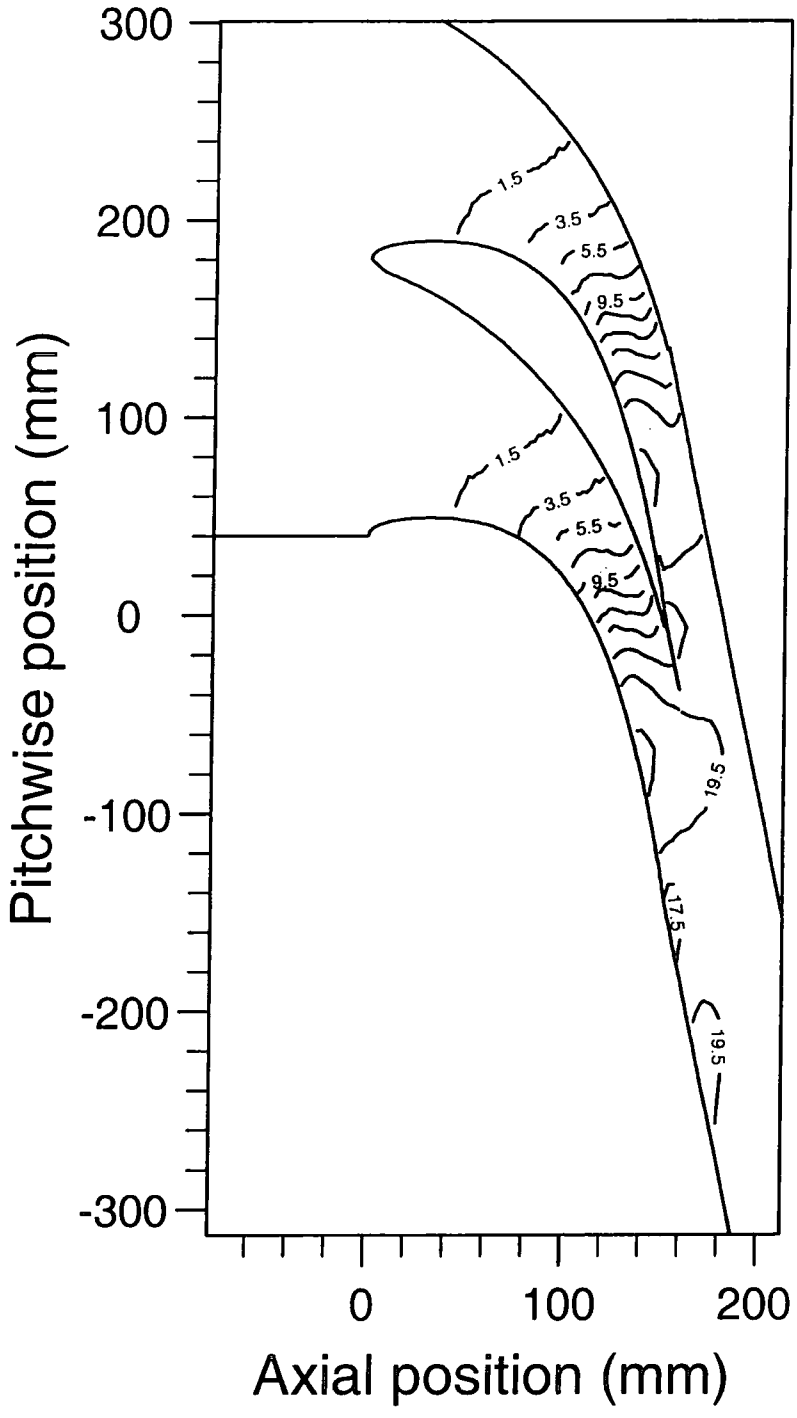

Figure 6.22—Static pressure on the shaped end wall

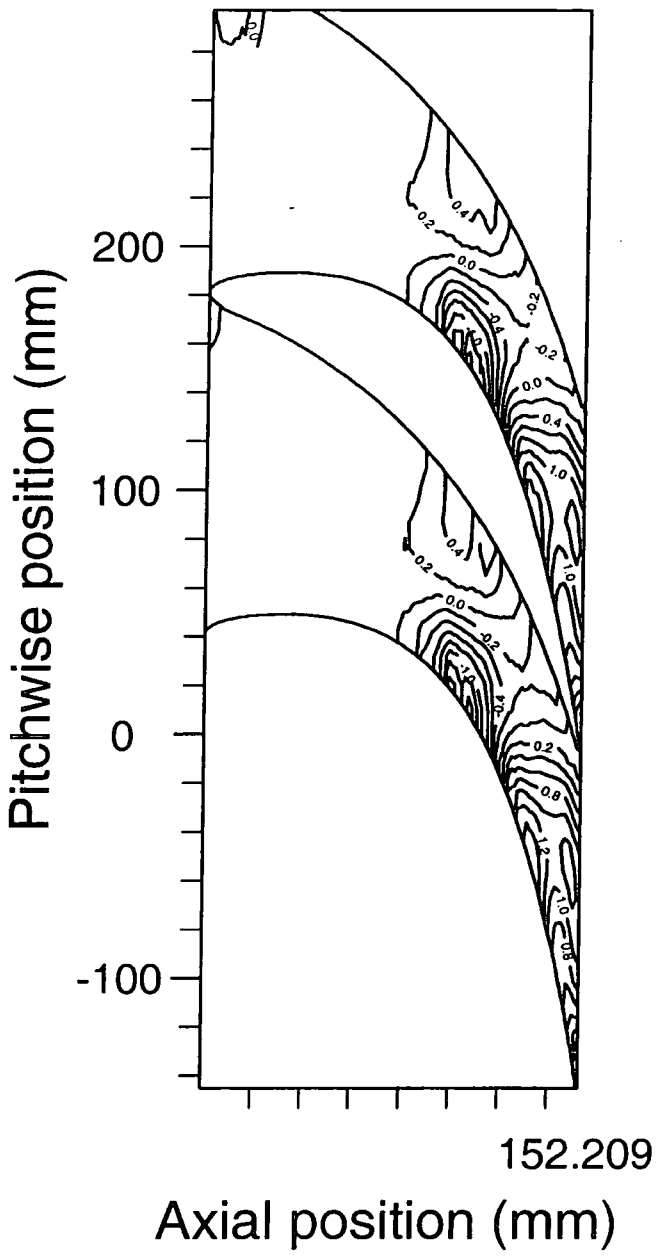

Figure 6.23—Static pressure difference on the end wall as results of shaped end wall

Chapter 7

Experimental Results of Non-axisymmetric End wall

7.1 Introduction

The end wall profile n525t was manufactured. A whole piece of the end wall with three n525t profiles was made using a CNC machine. The detailed flow investigations were done with five hole probes for a number of slots. The results are presented in forms of total pressure losses, secondary kinetic energy, yaw angle, pitch angle contours and secondary vector plot. In order to show the detail near the end wall, half-span contours and vector plot are presented as well. The pitch and area averaged values were calculated for every investigated slot. The comparisons are made with the flat end wall results and the CFD predictions.

7.2 Manufacture of the shaped end wall

According to the in-house design results, an end wall profile was selected to be made. The shaped end wall was made from microcellular modelling board on a base of

polyurethane (NECURON 100). Because of the complicated 3-D profile of the end wall, the only available machine in Durham to manufacture it was a three axis CNC milling machine. The CNC milling machine in the CAM laboratory has been linked to an IBM PC, and software has been written for both the PC and CNC machine to facilitate downloading of ASCII files. The file format for downloading required 4 columns of numbers. The first column was the command code. The next three columns were the spatial co-ordinate x, y and z respectively. The detail of the program which generate the ASCII file may be found in Hartland et al (1996). The tool selections were shown in the table 7.1. The cutters move according to the data files generated by a FORTRAN program. Because the machine moves the cutters in term of the cutter centre, the cutters should move at the distance of their radius parallel to the actual 3-D surface of the end wall. The data of the actual end wall profile was converted to the movement data file for the cutter centre. The perimeter of the shaped end wall was exactly the same as the perspex window. The holes for the blades were manufactured slightly smaller than those on the perspex window. This ensured the shaped end walls fitted closely on the cascade. The shaped end wall surface was then painted with varnish (Melamine Varnish) using three layers. In the end, the surface was smoothed by using P400 sand paper. Static pressure tappings were made on the shaped end wall. The tapping positions are the same as those on the perspex window and were drilled by using the CNC milling machine. Plastic tubing was then inserted in the hole and glued. The inner end of the plastic tube was trimed to make the end wall inner surface smooth.

Table 7.1—Tool selection

Area	3-D surface	Flat surface	Blade profiles	Perimeter of the end wall
Tool	20 mm OD ball end cutter	20 mm OD flat end cutter	4 mm OD flat end cutter	14 mm OD flat end cutter

7.3 The experimental results

The shaped end wall was fitted onto the cascade with the transition trips still kept on the blade surfaces. The traverse grids were kept the same in the pitchwise direction. The last radial grid points of every pitchwise location were varied according to the local end wall profile in such a way that the five hole probe was driven as near to the end wall as it was possible. Then the grid points were expanded to the mid-span at an expanding ratio of 1.2 at every pitch position. Slot traverses have been done by using the five hole probe. The total pressure loss, secondary kinetic energy, yaw angle distribution, pitch angle distribution and the secondary flow vector are plotted. The secondary vector was defined in the same way as shown in Fig. 4.1. The pitch averaged results were obtained by integrating along the traversing grid. For the shaped end wall, inside the blade passage the pitch averaged radial positions were different from those of the flat end wall case. A mapping procedure was done to the pitch averaged results inside the passage. The mapping factor for every slot was obtained by dividing the local traversing span length by 200 mm which is the radial traversing length for the flat end wall traverses. Every pitch averaged radial position was then manipulated by the mapping factor. The static pressure on the shaped end wall and the blade surfaces were measured as well. A flow visualisation on the shaped end wall was also done.

7.3.1 Traverse results for Slot 2

The slot 2 was traversed to investigate the inlet condition. The position of slot 2 is shown in Fig. 3.4. The area plots of the experimental results are not presented here, but the pitch averaged results are shown in Fig. 7.1. Compared to the flat end wall, both the yaw angle and the total pressure loss have not been changed by the shaped end wall. This means the inlet condition for the shaped end wall test was kept the same as the test with the flat end wall.

7.3.2 Traverse results for Slot 3

Slot 3 was located at 3.3% downstream the leading edge as shown in Fig. 3.4. According to the starting position of the shaped end wall profile, the effects of the shaped end wall on the flow field were expected to be seen. The pitch averaged traversing results are presented here. The total pressure distribution has not been changed compared to the flat end wall results as shown in Fig. 7.2. The CFD prediction for the shaped end wall gives slightly more loss near the end wall. But the CFD prediction for the flat end wall in Fig. 5.9 matches very well with the experimental results with flat end wall. This implies that the shaped end wall effect on the total pressure loss took place earlier in the CFD predicted flow than in the experiments. It might also be due to the numerical effect and the different computational grids. In the mid-span the CFD gives slightly higher loss prediction as well. In the experiments, the flow field near the blade surface is very difficult for 5 hole probe to get close enough for investigation. Hence, the total pressure loss near the blade surface was not integrated into the pitch averaged loss distribution. This could explain why the mid-span loss from the CFD is higher than that from the experiments. The yaw angle distribution of the shaped end wall shown in Fig. 7.2 gives a bigger overturning than that of the flat end wall. This indicates the inviscid effect of the shaped end wall on the flow. This effect causes the flow near the end wall running toward the concave part of the shaped end wall. The small underturning of the flat end wall has vanished with the shaped end wall. The CFD results match closely with the experimental results.

7.3.3 Traverse results for Slot 4

The traversing results of slot 4 are presented in the form of pitch averaged results in Fig. 7.3. The total pressure loss distribution of the shaped end wall is the same as that of the flat end wall. The profile of the shaped end wall is still quite small at this slot. It has

not changed the total pressure loss yet. The CFD again gives more loss prediction near the end wall and at the mid-span. The yaw angle distribution with the shaped end wall gives more overturning and less underturning than that with the flat end wall. The CFD gives very good prediction of the yaw angle compared with the experimental results.

7.3.4 Traverse results for Slot 5

The area plots of the results in the near wall region are shown in Fig 7.4. There is a high loss concentration in the concave region near the suction surface. The loss distribution is similar to that with the flat end wall in Fig. 4.10. There is slightly more secondary kinetic energy near the concave region. The yaw angle distribution near the end wall has also been affected by the end wall profile. The overturning was increased but the underturning has been reduced. The secondary vector plot shows a strong cross flow near the mid-pitch position running toward the concave region which is due to the inviscid effect of the shaped end wall.

The pitch averaged total pressure loss of the shaped end wall as shown in Fig. 7.5 still does not show too much difference from the flat end wall case. The CFD gives more loss in the mid-span but good agreement near the end wall. The CFD predicted loss at mid-span still shows a sudden jump which has happened in the flat end wall case as indicated in section 5.4.3. However, the sudden loss increase predicted by the CFD for the shaped end wall is much less than the CFD results for the flat end wall. The reason of this was also explained there. The yaw angle distribution from the experiments shows little underturning but more overturning compared with the yaw angle distribution with the flat end wall. The more overturning was caused by the inviscid effect of the shaped end wall. The CFD gives bigger underturning and overturning which means stronger secondary flow.

7.3.5 Traverse results for Slot 6

The area plots of the experimental results at slot 6 are presented in Fig. 7.6. The total pressure loss contour shows the loss centre is in the concave region of the shaped end wall. The secondary kinetic energy is smaller than that at previous slot. The profile of the shaped end wall has passed the maximum point, which is at about 64% axial chord from the leading edge, and starts to reduce. The inviscid blockage effect is smaller compared to that at slot 5. Therefore the cross flow near the end wall is smaller than that at slot 5 and so is the secondary kinetic energy near the end wall. Compared with the flat end wall results in Fig. 4.12, the high secondary kinetic centre has moved nearer to the suction surface. The amount of secondary kinetic energy is about the same as the flat end wall case. The yaw angle distribution away from the end wall shows nearly no change from the pressure surface to the suction surface. This is consistent with the flat end wall results. The overturning near the end wall is smaller than that of the flat end wall. This indicates a smaller secondary flow near the end wall. The secondary vector plot shows a passage vortex at the mid-pitch position. The secondary flow near the pressure surface has been greatly reduced by the end wall profiling. But near the suction surface, there is a slight increase of secondary flow.

The pitch averaged results are shown in Fig. 7.7. The shaped end wall results show slightly less loss in the near wall region than that of the flat end wall. The CFD results agree with the experimental results quite well until about 10 mm from the end wall. Within this 10 mm, the CFD gives higher loss. The yaw angle distribution shows more underturning and less overturning than that with the flat end wall. The CFD gives more underturning and overturning than that of the experimental results. This indicates that the CFD predicts more secondary flow as at slot 5.

7.3.6 Traverse results for Slot 7

The area plots of the experimental results at slot 7 are shown in Fig. 7.8. The total pressure loss has not changed. The shaped end wall obviously has reduced the loss core movement towards the suction surface which is directly caused by the secondary flow. Therefore, the secondary flow effect has been reduced. There is smaller secondary kinetic energy compared with the flat end wall results as shown in Fig. 4.14. The yaw angle distribution shows bigger underturning than that of the flat end wall but smaller overturning near the end wall. This implies that the convection effect which drives the low energy material towards the suction surface has been reduced. The secondary vector plot shows much smaller secondary vectors near the end wall than the flat end wall case. The centre of the passage vortex is located relatively closer to the end wall.

The pitch averaged results are shown in Fig. 7.9. The total pressure loss distribution is quite different from that of the flat end wall. The shaped end wall results have not shown the boundary layer movement which is shown by the flat end wall results. This boundary layer movement away from the end wall is because of the strong secondary flow effect. With the shaped end wall, the secondary flow is reduced so much that the boundary layer moving away has not happened at this slot. The CFD gives a very similar profile to the experimental results but with bigger values including the blade boundary layer which was not measured in the experiments. The pitch averaged yaw angle distribution shows about the same underturning but far less overturning compared to the flat end wall case. The underturning peak was moved closer to the end wall by the shaped end wall. It is indicated that the shaped end wall has reduced the secondary flow.

7.3.7 Traverse results for Slot 8

The area plots of the experimental results are shown in Fig. 7.10. Because the shaped end wall was tested with trip, the comparisons will be made to those results for the flat

end wall with trip. The end wall profile has become flat at this slot. The total pressure loss centre has moved to the suction corner. In Fig. 4.30, the loss core has already moved onto the suction surface with the flat end wall. The movement of the low energy material with the shaped end wall was much less than that with the flat end wall. The low energy material movement near the end wall is caused by the secondary flow. The less movement means a smaller secondary flow. The secondary kinetic energy area has spread out towards the mid-span. Compared with the flat end wall in Fig. 4.30, the secondary kinetic energy is less concentrated and smaller. The yaw angle distribution shows much less overturning than the flat end wall case. The secondary vectors near the end wall are much smaller. The passage vortex is smaller with its centre located much closer to the end wall than the flat end wall case. At about 20 mm way from the end wall, the underturning secondary vectors are bigger.

The pitch averaged total pressure loss at slot 8 in Fig. 7.11 shows similar profile to that at slot 7. It generally gives less loss than the flat end wall. It has started to show an increase of the boundary layer on the end wall. The CFD predicts a high and sharp loss peak and higher loss in the mid-span. The shaped end wall results show bigger underturning but smaller overturning compared with the flat end wall results. The yaw angle distribution predicted by the CFD agrees very well with the experimental result.

7.3.8 Traverse results for Slot 9

Slot 9 is the first slot down stream of the trailing edge. The traverse plane covers nearly two passages. The area plots of the results are shown in Figs. 7.12 and 7.13. The wakes near the mid-span are more or less the same as those with the flat end wall in Fig. 4.31. In the near wall region, the total pressure loss contour shows less distorted wakes compared to the flat end wall results in Fig. 4.32. The secondary kinetic energy contour shows a big reduction compared with the flat end wall case. This difference is more obvious in the near wall region plot. The yaw angle contour shows smaller underturning near the end wall. In the mid-span region the flow turning angle distribution is about

the same as that with the flat end wall. The pitch angle distribution does not show much difference from that with the flat end wall. The secondary vector plots show an overall reduction of the secondary flow. A small counter vortex very near the end wall can be seen at about 150 mm pitch position. The centre of the passage vortex is staying about 8 mm from the end wall while it stays about 13 mm from the end wall with the flat end wall as shown in Fig 4.32. The secondary flow near the end wall in Fig. 7.12 is smaller which means a weaker convection effect.

The pitch averaged results are shown in Figs. 7.14 together with the CFD results and the flat end wall results. In order to see the details of the end wall region where all the changes took place, only the results within 80 mm from the end wall are shown. The pitch averaged total pressure loss shows less loss in the region of 24 mm to 50 mm and higher loss in the region of 7 mm to 24 mm than that with the flat end wall. The lower loss peak which means less low energy fluid indicates a smaller secondary flow convection. The weaker secondary flow swept less low energy fluid from the near wall region and left higher loss near the end wall. The CFD results show a much bigger loss peak than the experimental results. The pitch averaged yaw angle shows much less overturning than that with the flat end wall. The CFD predicts less turning of the flow and more overturning and underturning which mean more secondary flow.

7.3.9 Traverse results for slot 10

The area plots for slot 10 are shown in Figs. 7.15 and 7.16. The total pressure loss contours show that the wake is less distorted than the flat end wall case in Fig. 4.33. At the near wall region, there is significantly less loss compared to the flat end wall results as shown in Fig. 4.34. The secondary kinetic energy contour shows less secondary kinetic distribution. There is no obvious change in the yaw angle distribution contour plot. The pitch angle distribution shows smaller pitch angles. The secondary vector plots shows a vortex centre at about 7 mm from the end wall. With the flat end wall, the

vortex centre is about 15 mm from the end wall. The secondary flow near the end wall is less than that with the flat end wall.

The pitch averaged results of total pressure loss and yaw angle distribution are shown in Fig. 7.17. In the mid-span, the loss values with different end wall are the same. Near the end wall, the total pressure loss of the shaped end wall is always lower than the total pressure loss of the flat end wall. This proves that a reduced total pressure loss distribution has been achieved by the shaped end wall. The loss peak has been also moved closer to the end wall by the effect of the shaped end wall. The yaw angle distribution shows a vortex closer to the end wall. The underturning and the overturning have both been reduced. This indicates that the secondary flow has been reduced by the shaped end wall.

7.4 Static pressure distribution on the end wall and the blade surfaces

The static pressure on the shaped end wall surface was measured through the tappings on the end wall. As shown in Fig 7.18, the pressure gradient across the passage has been reduced compared to Fig. 4.24. The difference between the shaped end wall and the flat end wall was obtained by subtracting the static pressure reading on the flat end wall from that of the shaped end wall. The results are shown in Fig. 7.19. The negative value on the contours indicates an increase of the pressure. It can be seen that the shaped end wall raised the pressure on the suction surface and reduced the pressure on the pressure surface. It is found that there was a delay between the end wall profile shape and its effect on the static pressure distribution. The static pressure difference between the shaped end wall and the flat end wall from CFD is shown in Fig. 6.23. The CFD results show difference from the experimental results in Fig. 7.19. The CFD predicts a bigger area of pressure reduction near the pressure surface. The amount of pressure increase near the suction surface is inadequate in the CFD results. The static pressure readings on the end wall with the flat end wall and the shaped end wall were

then used to calculate the end wall $\int C_D V^3 dA$ coefficients which is defined as in Equation 2.1 of section 2.2.2. The integration is done over only end-wall area within the blade passage. This means that the V cubed integral will be the same for slot 9 and slot 10. The calculation results are shown in Table 7.2. The shaped end wall has different static pressure on the end wall and larger surface area than the flat end wall. As shown in Table 7.2, the end wall $\int C_D V^3 dA$ coefficient of the shaped end wall is bigger than that of the flat end wall. This indicates that the shaped end wall has increased the surface friction loss. However, the amount of increase is quite small (within the experimental accuracy). This shows that the effect of increased area of end-wall was small.

7.5 Flow visualisation

After the static pressure measurement, the flow visualisation was done on the blade surfaces and the end wall surface. The dye was injected onto the end wall surface through the static pressure tappings. The result is shown in Fig 7.20. Compared with the flow visualisation on the flat end wall shown in Fig 4.26, the flow shows a quite noticeable change. In Fig 4.26, the steak lines from the pressure surface, which have been driven by the cross passage pressure gradient and the main stream flow, have travelled short distances before they meet the suction surface. In Fig 7.20, these distances have been extended. This means there is less cross flow because of the smaller cross passage pressure gradient achieved by applying the shaped end wall.

7.6 Conclusion

The flow field with the shaped end wall has been investigated. The experimental results show the effect of the shaped end wall. The mass averaged total pressure loss for every slot is shown in Fig. 7.21. The mass averaged total pressure loss values at slot 2-8 do not include the boundary layer on the blade surface because of the traverse limitation. It

can be seen that with the shaped end wall the total pressure loss shows similar distribution to that with the flat end wall. The slightly higher loss from slot 3 to slot 7 might be caused by the shaped end wall effect and experimental errors. At slot 8, the area averaged total pressure loss for the flat end wall and the shaped end wall are the same. With the same inlet condition, the results with the shaped end wall give less total pressure loss than the flat end wall with trip at slots 9 and 10. The area averaged secondary kinetic energy for every slot is shown in Fig. 7.22. At slot 2 where the shaped end wall profile has just started, the secondary kinetic energy with the shaped end wall is the same as the flat end wall. The shaped end wall gives higher secondary kinetic energy from slot 3 to slot 6. This is due to the inviscid effect of the shaped end wall which redistributes the flow near the end wall. From slot 7 to slot 10, the shaped end wall has reduced the secondary kinetic energy.

The CFD gives fairly good predictions of the shaped end wall effect. The area averaged results at slot 9 and 10 are also shown in Table 7.2 and 7.3. The secondary kinetic energy shows a reduction of 35% at slot 9 with the shaped end wall. With the inlet boundary conditions not being changed with the shaped end wall, the net secondary loss is reduced by about 21% as shown in Table 7.2 and 7.3.

The friction loss on the end wall surface was calculated by using the static pressure measurements on the end wall surface. The method is shown in equation 2.1. The shaped end wall causes negligible more friction loss than the flat end wall. The CFD gives less friction loss on the end wall for the shaped end wall. However, the difference between the friction loss on the shaped end wall and the flat end wall is rather small. It might be caused by the numerical errors. The mixing out loss is reduced by 1.7% compared with the results with the flat end wall. The secondary kinetic energy is reduced by 23.8% compared with the results of the flat end wall.

Table 7.2—Mass averaged results at slot 9 and 10 based on the inlet dynamic pressure

Slot No	total pressure loss	secondary kinetic energy (×100)	mixed out loss	$C_D\int V^3dA$ coefficient over the end wall
Slot 9 with the flat end wall	0.802	0.602	1.210	0.051
Slot 9 with the shaped end wall	0.763	0.390	1.189	0.055
Slot 10 with the flat end wall	0.944	0.42	1.212	0.051
CFD with the flat end wall at slot 10	1.161	0.98	1.214	0.060
Slot 10 with the shaped end wall	0.903	0.32	1.190	0.055
CFD with the shaped end wall at slot 10	1.088	0.87	1.486	0.056

Table 7.3—Mass averaged results at slot 9 and 10 based on the inlet dynamic pressure

Slot No	Full Span averaged total pressure loss	Mid-span total pressure loss	Gross secondary loss	Net secondary loss
Slot 9 with the flat end wall	0.802	0.570	0.232	0.211
Slot 9 with the shaped end wall	0.763	0.580	0.183	0.162
Slot 10 with the flat end wall	0.944	0.748	0.196	0.175
CFD with the flat end wall at slot 10	1.161	0.980	0.181	0.160
Slot 10 with the shaped end wall	0.903	0.746	0.159	0.138
CFD with the	1.088	0.980	0.108	0.087

Table 7.4—Mass averaged results at slot 9 and 10 based on the exit isentropic dynamic pressure

Slot No	total pressure loss	secondary kinetic energy (×100)	mixed out loss	$C_D\int V^3dA$ coefficient over the end wall
Slot 9 with the flat end wall	0.0376	0.028	0.0567	2.39×10^{-3}
Slot 9 with the shaped end wall	0.0381	0.018	0.0557	2.58×10^{-3}
Slot 10 with the flat end wall	0.0443	0.020	0.0568	2.39×10^{-3}
Slot 10 with the shaped end wall	0.0423	0.015	0.0558	2.58×10^{-3}

Table 7.5—Mass averaged results at slot 9 and 10 based on the exit isentropic dynamic pressure

Slot No	Full Span averaged total pressure loss	Mid-span total pressure loss	Gross secondary loss	Net secondary loss
Slot 9 with the flat end wall	0.0376	0.0267	0.0109	0.0099
Slot 9 with the shaped end wall	0.0381	0.0269	0.0112	0.0111
Slot 10 with the flat end wall	0.0443	0.0351	0.0091	0.0081
CFD with the flat end wall at slot 10	0.0546	0.0460	0.0086	0.0076
Slot 10 with the shaped end wall	0.0423	0.0350	0.0074	0.0064
CFD with the shaped end wall at slot 10	0.0510	0.0460	0.0050	0.0040

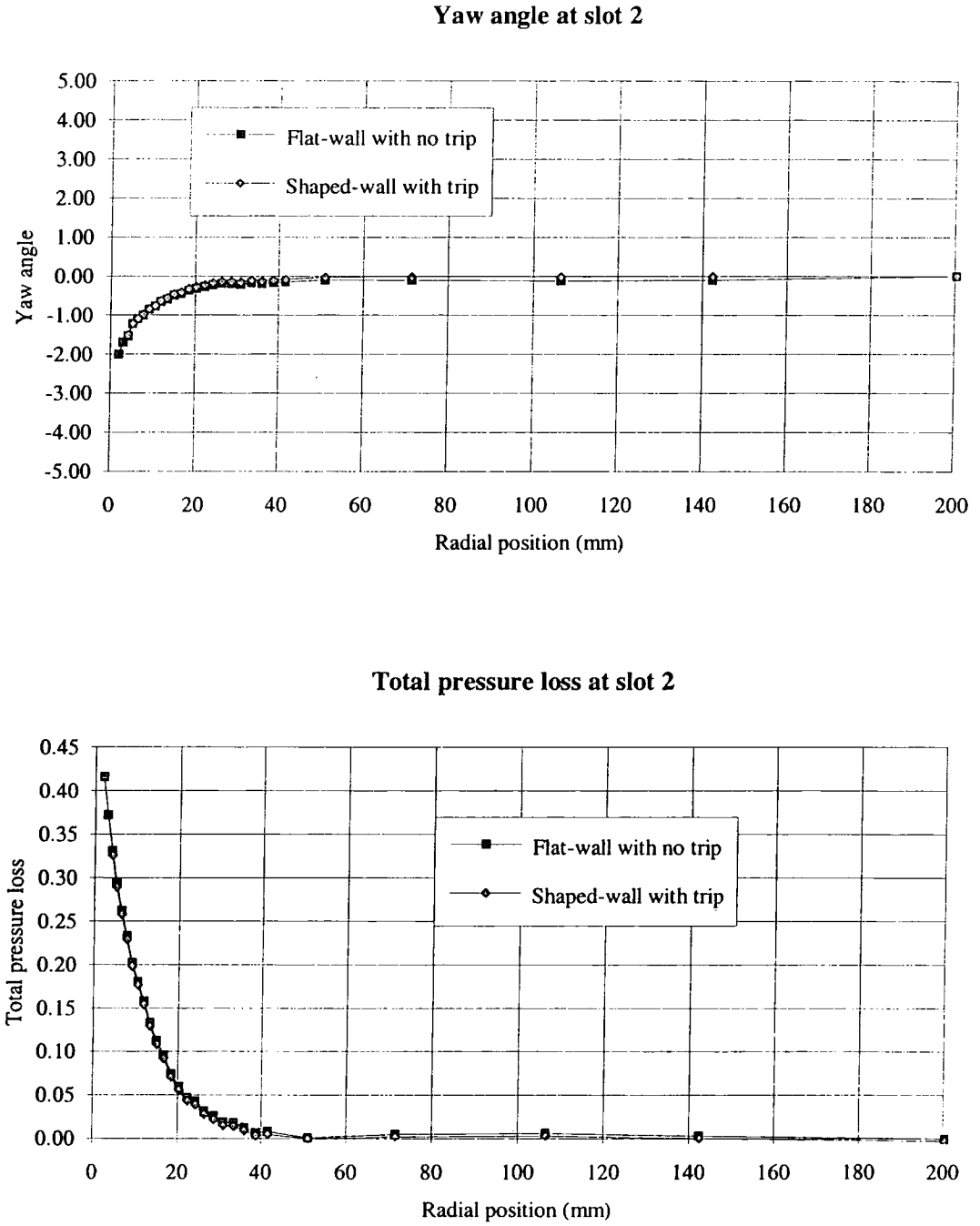

Figure 7.1—Pitch averaged results for Slot 2

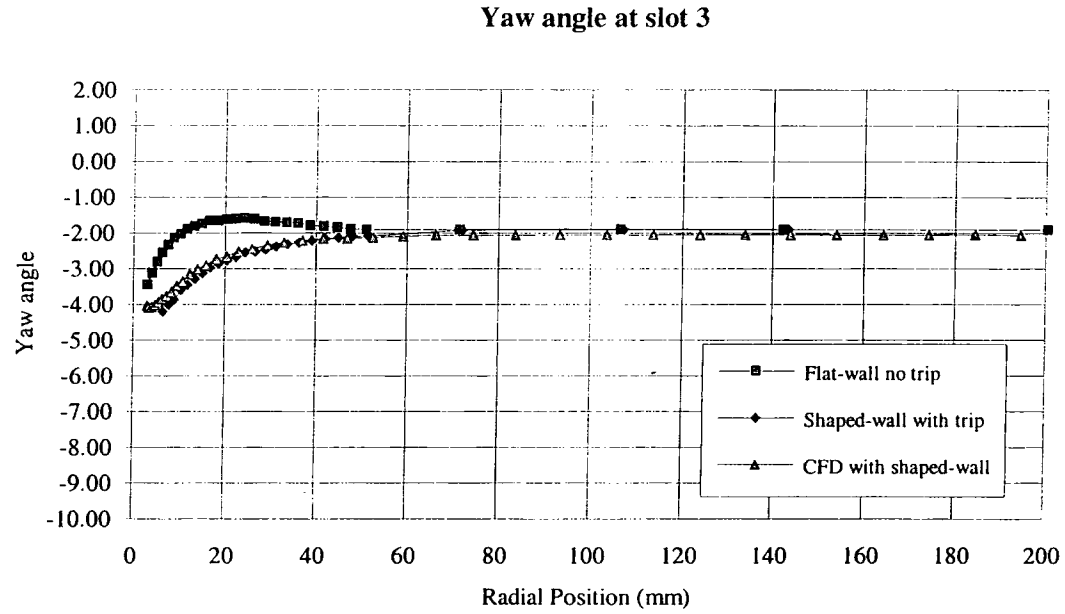

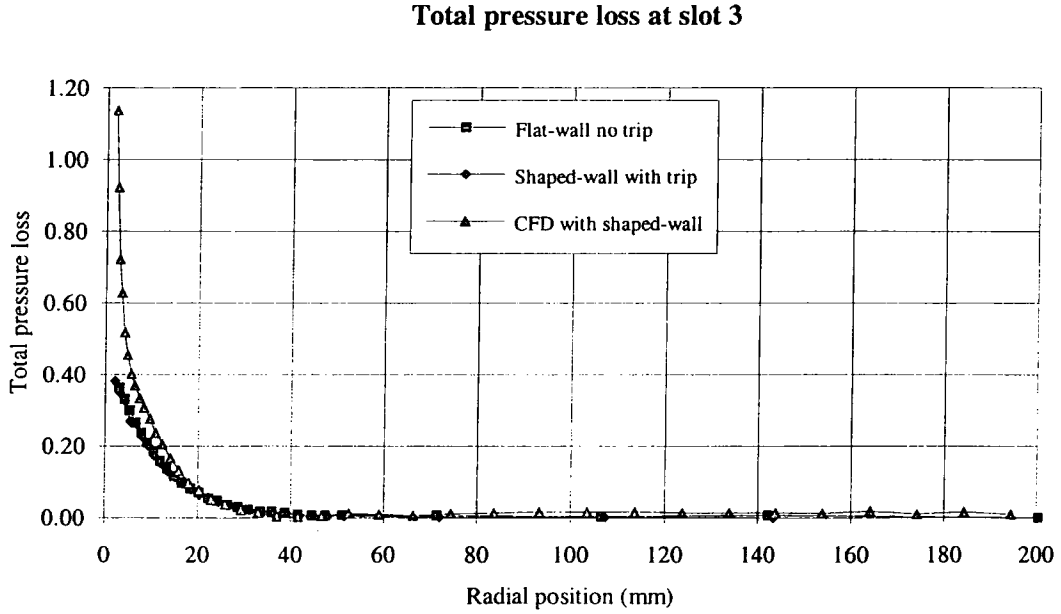

Figure 7.2—Pitch averaged results for Slot 3

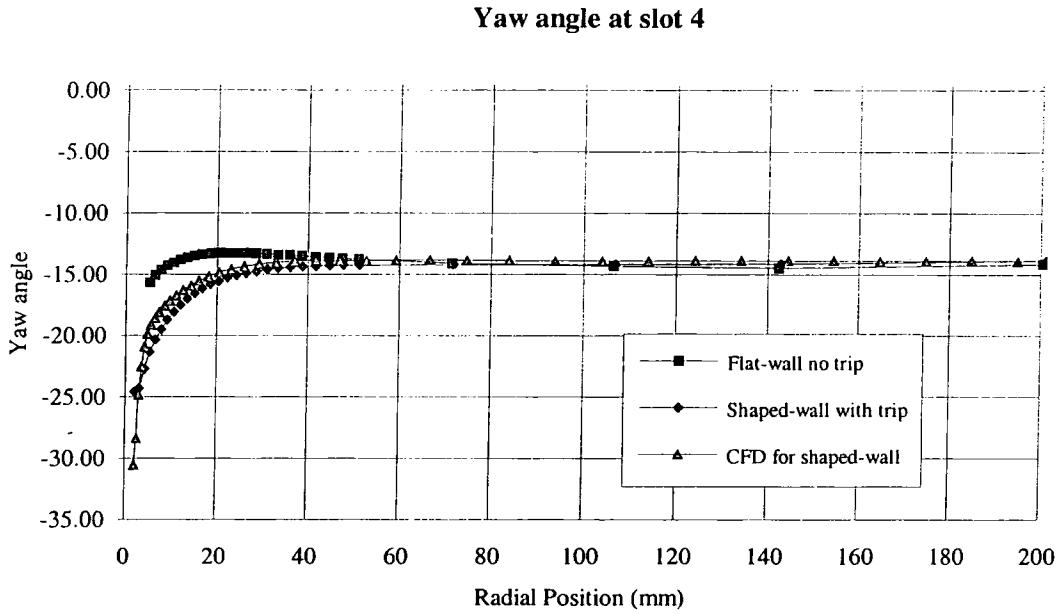

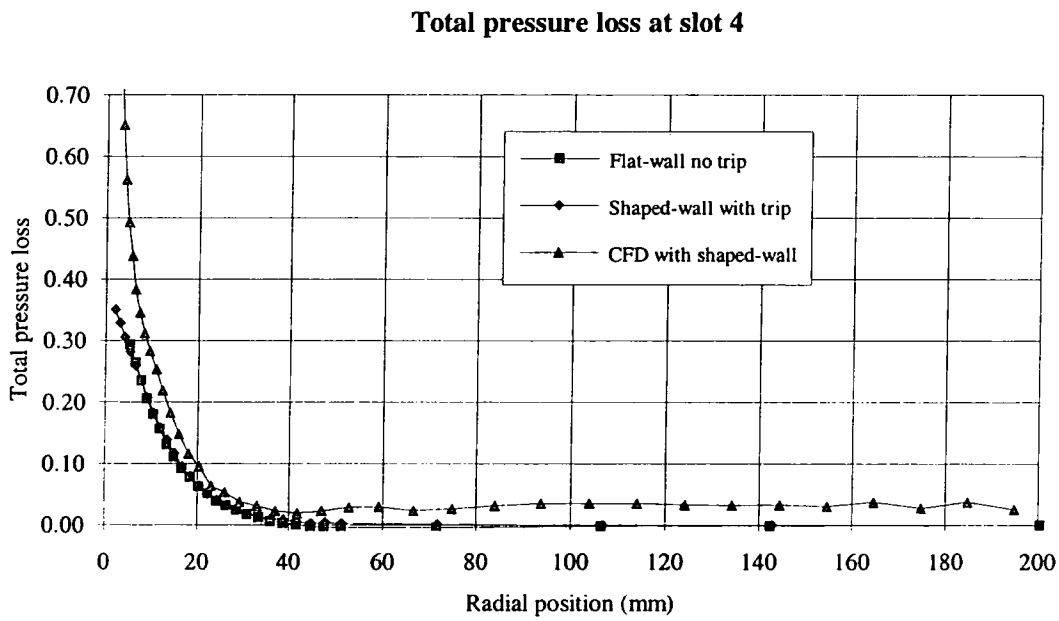

Figure 7.3—Pitch averaged results for Slot 4

a) Total pressure loss contours

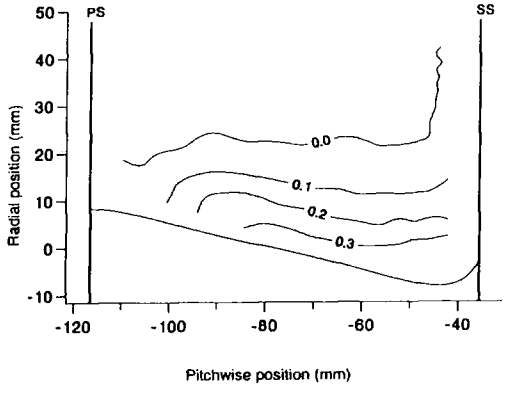

b) Secondary kinetic energy contour (%)

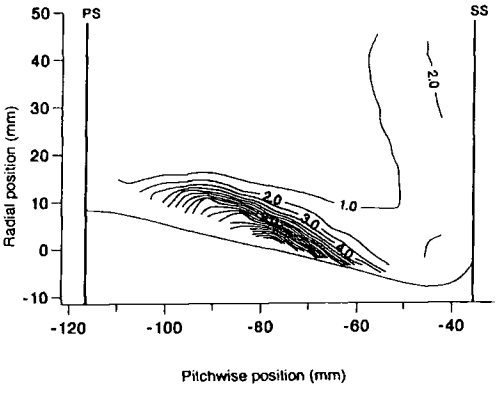

c) Yaw angle contour

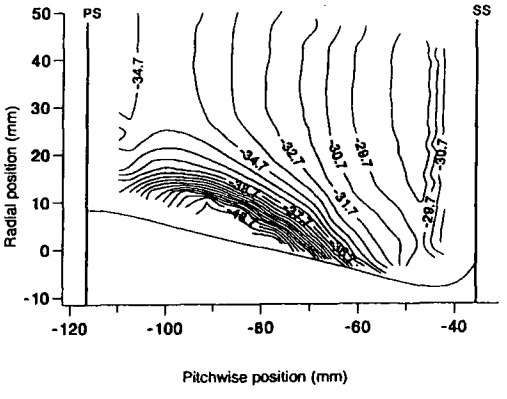

d) Pitch angle contour

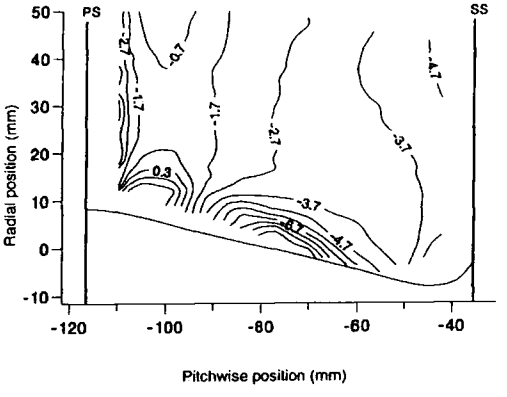

e) Secondary vector plot

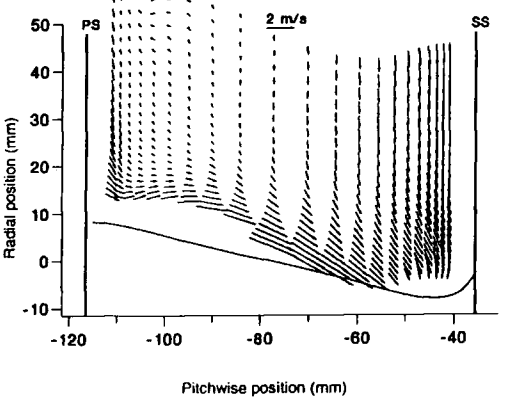

Figure 7.4—Area plot at Slot 5

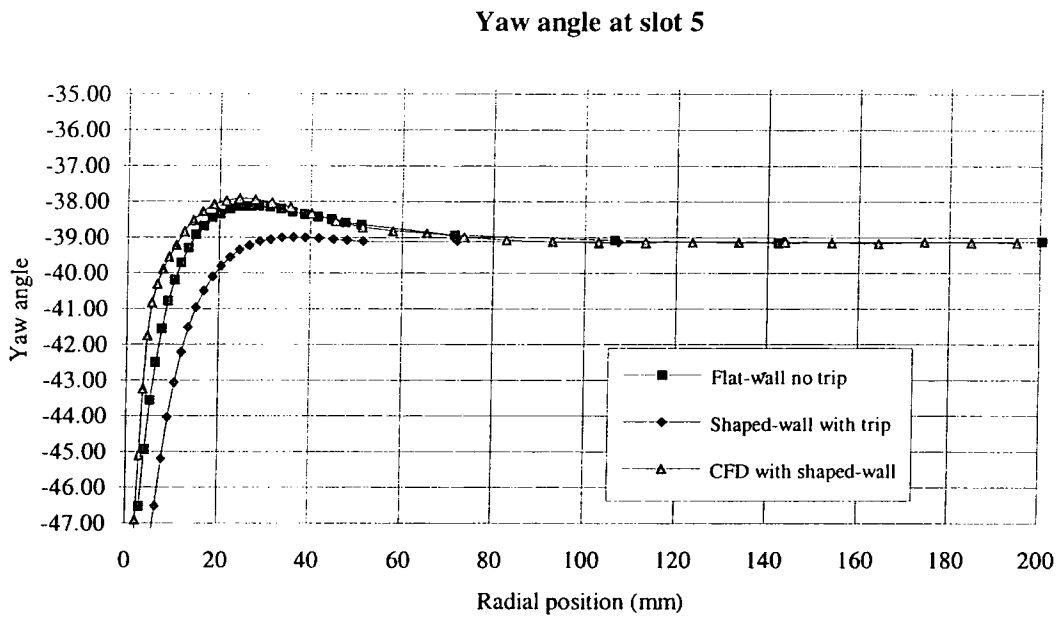

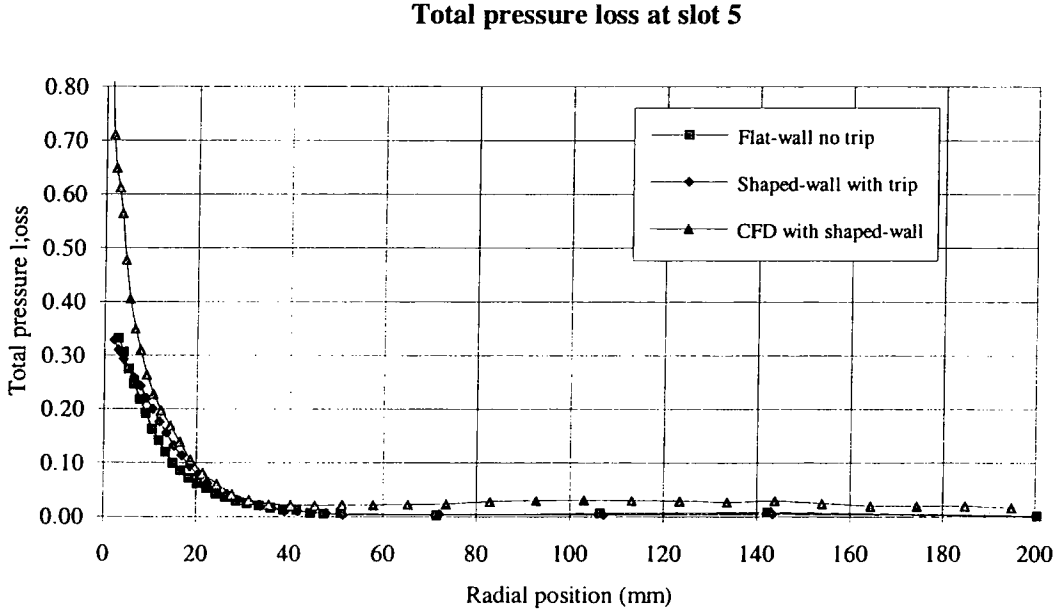

Figure 7.5—Pitch averaged results for Slot 5

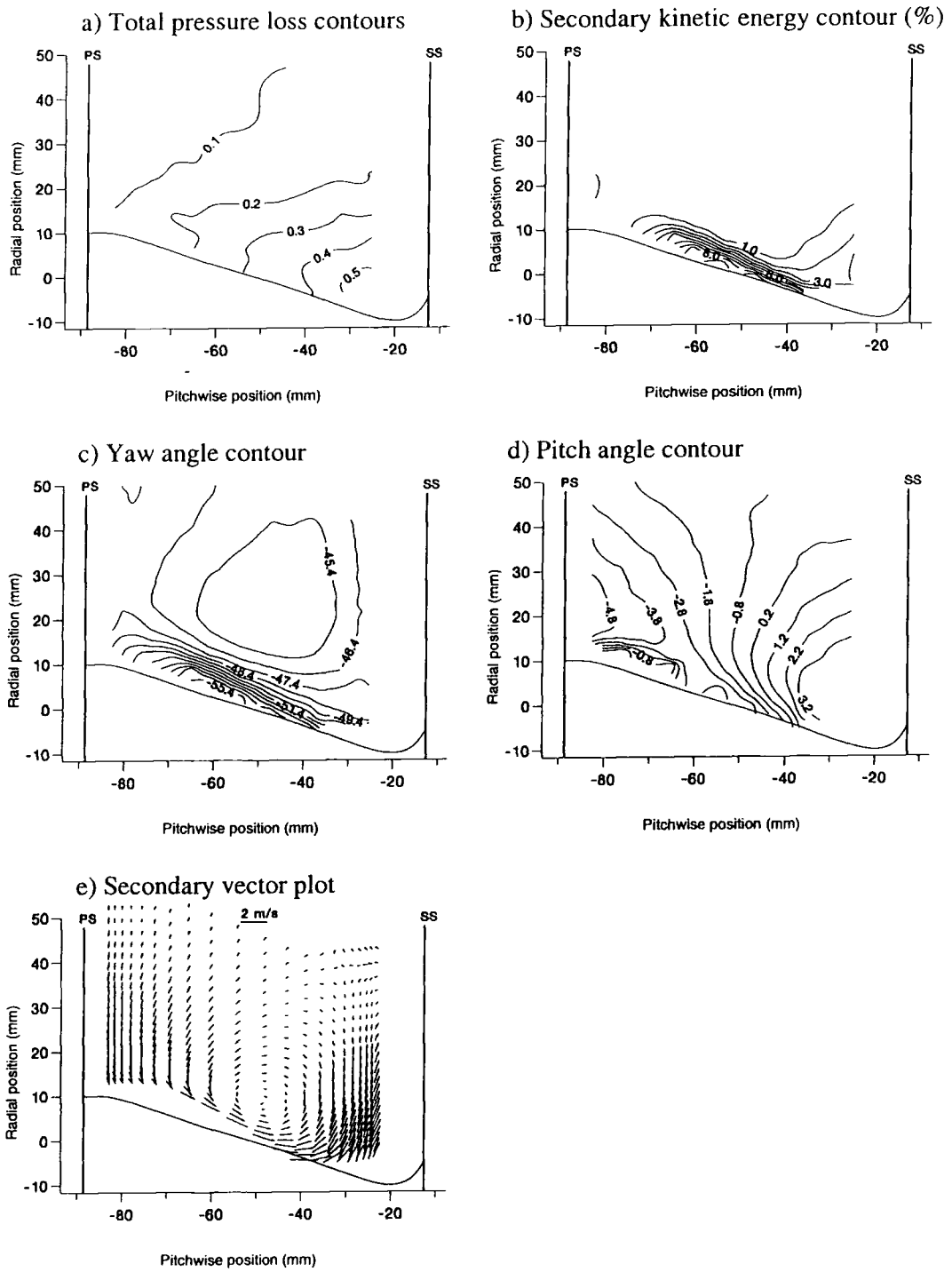

Figure 7.6—Area plot at Slot 6

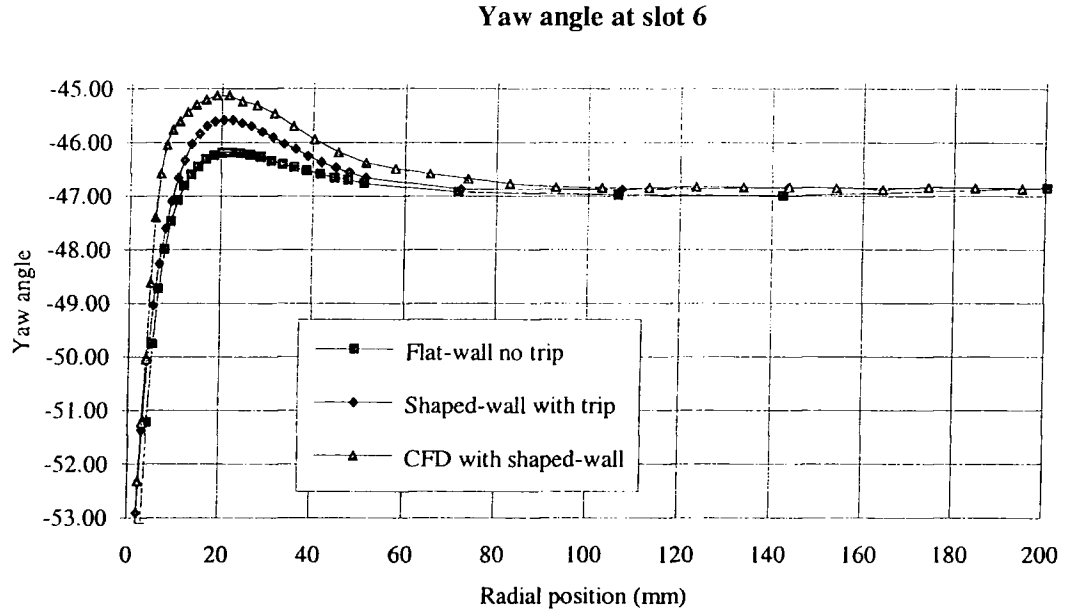

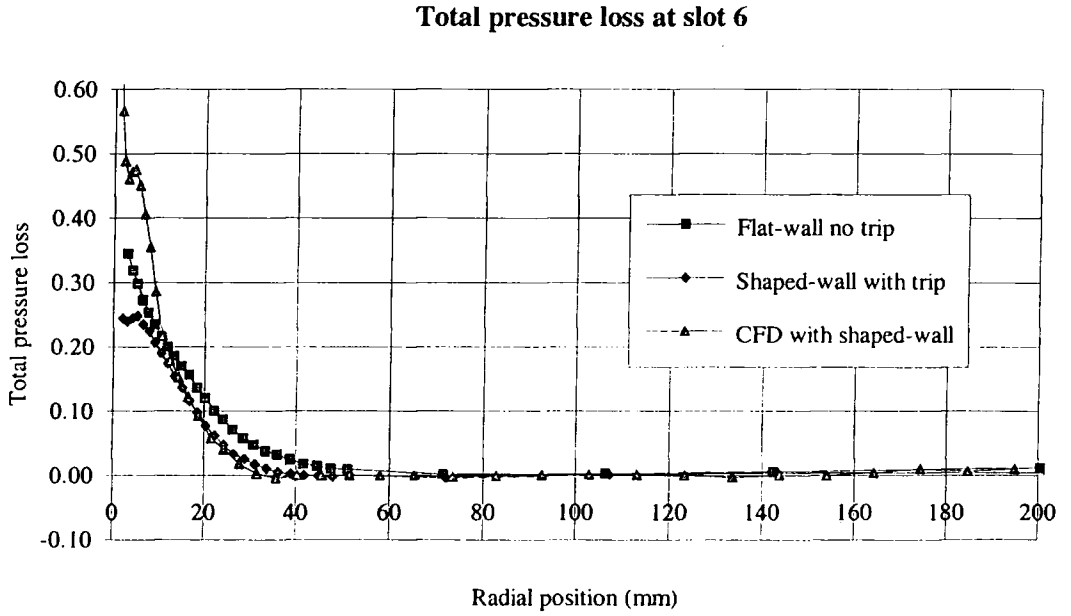

Figure 7.7—Pitch averaged results for Slot 6

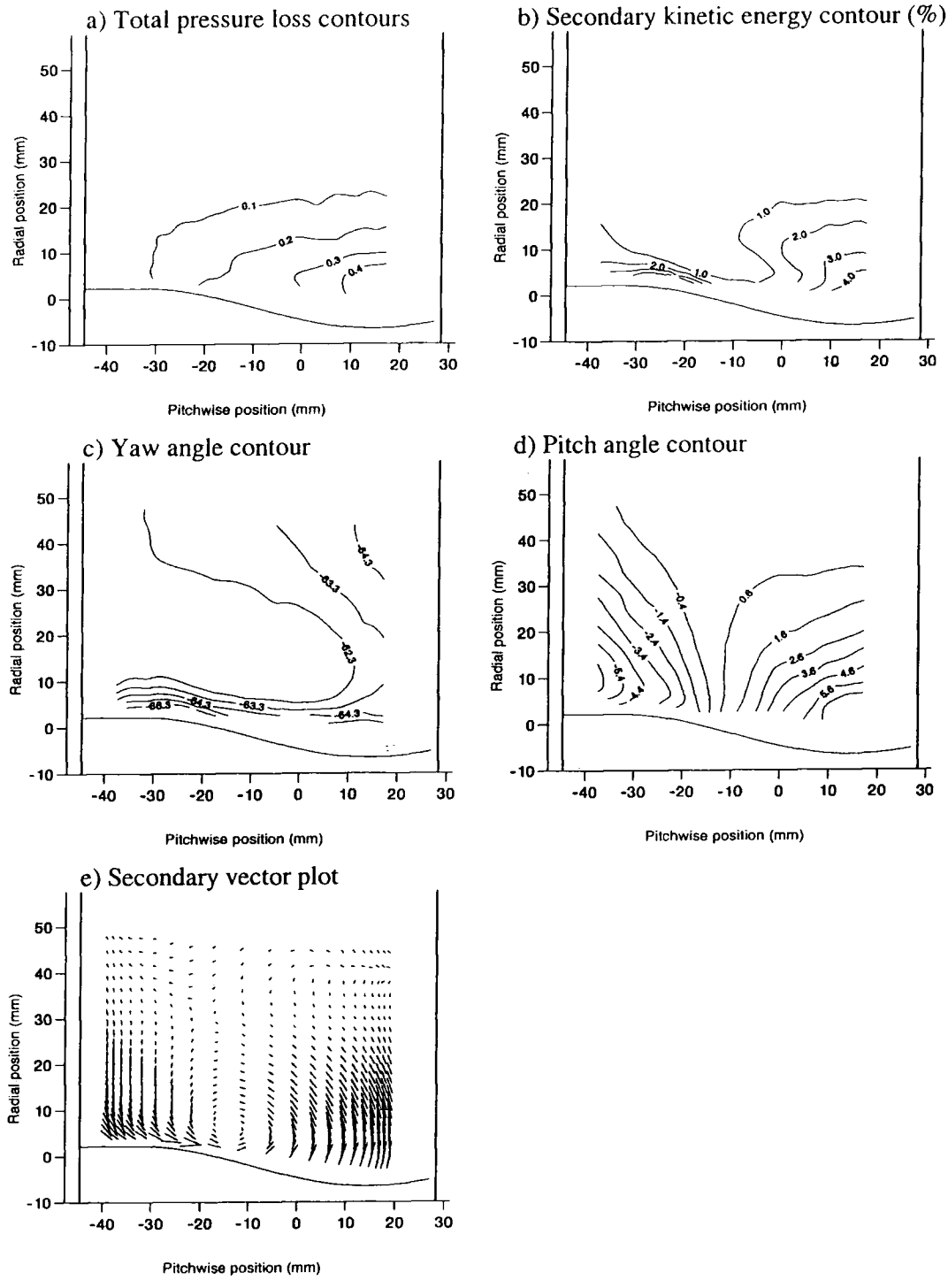

Figure 7.8—Area plot at Slot 7

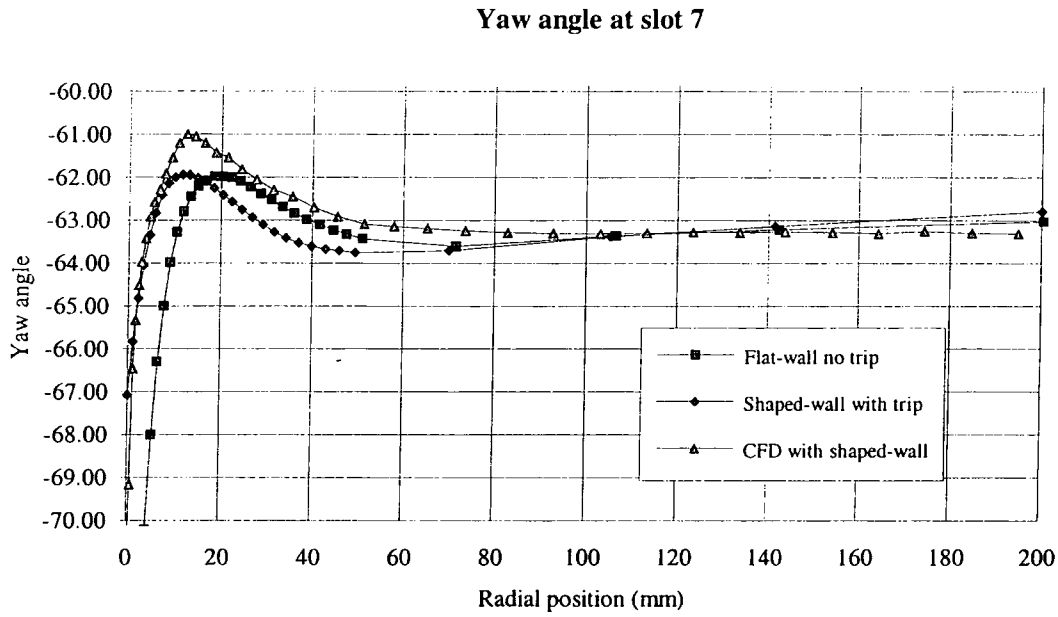

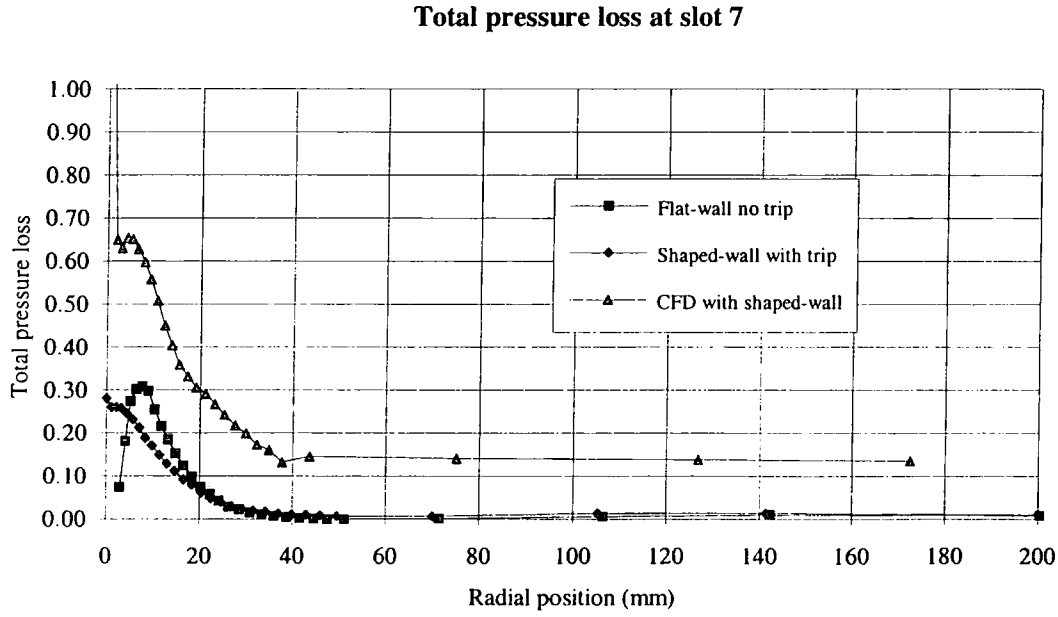

Figure 7.9—Pitch averaged results for Slot 7

a) Total pressure loss contours

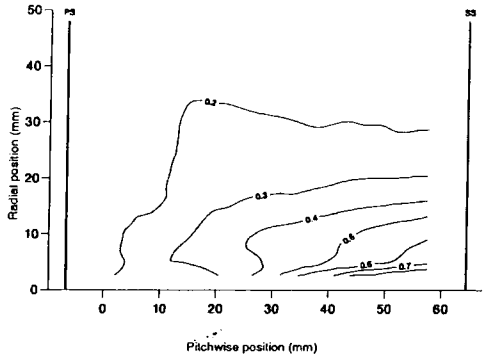

b) Secondary kinetic energy contour (%)

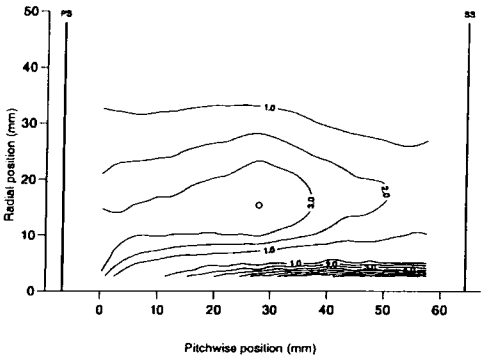

c) Yaw angle contour

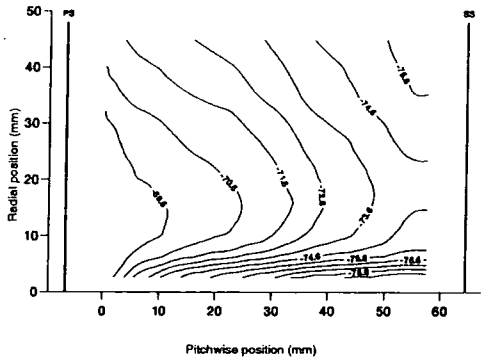

d) Pitch angle contour

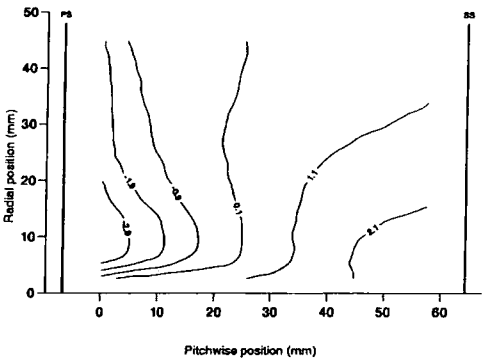

e) Secondary vector plot

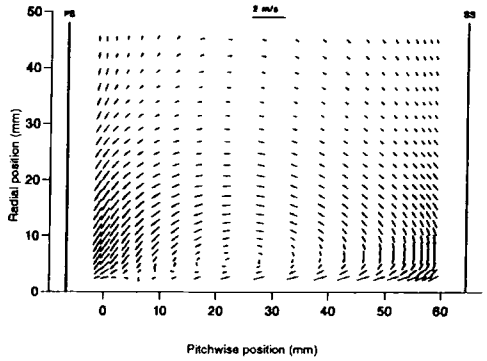

Figure 7.10—Area plot at Slot 8

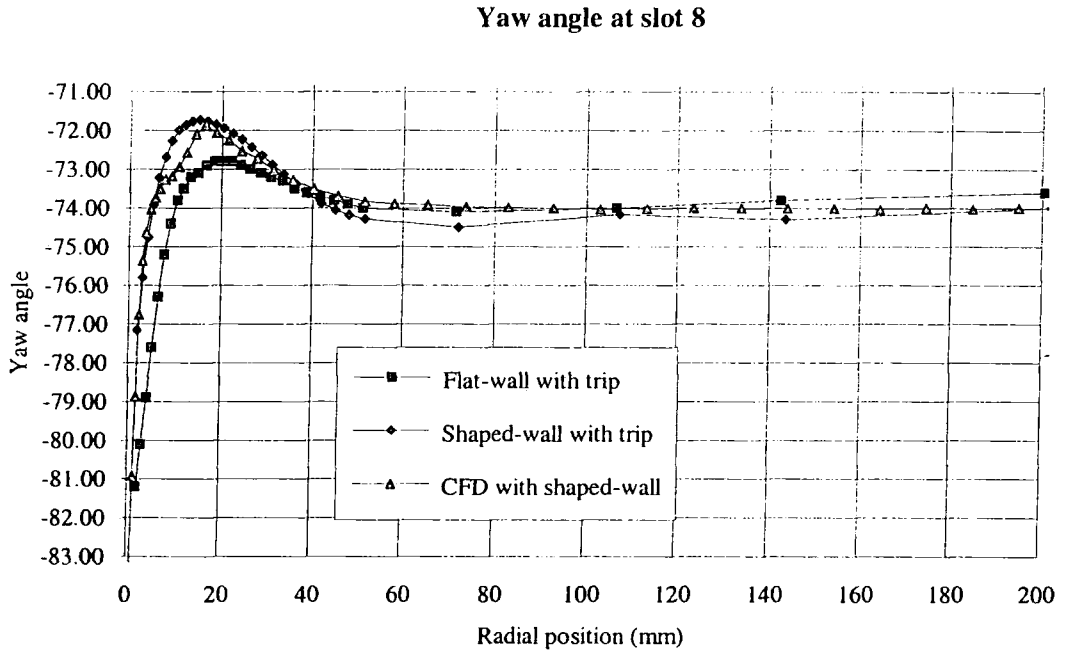

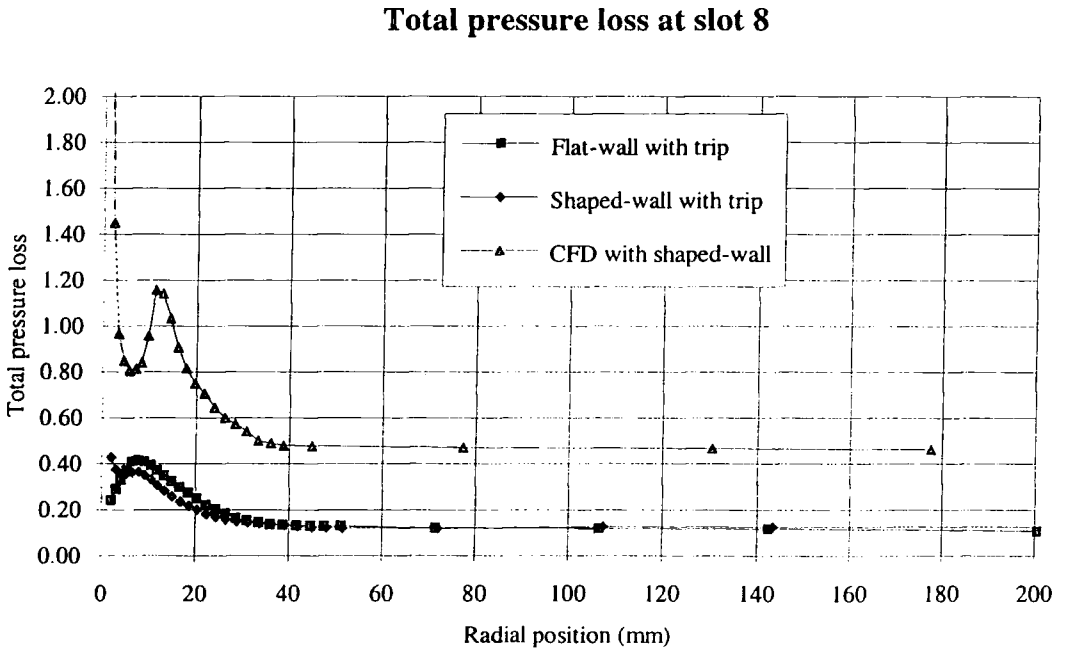

Figure 7.11—Pitch averaged results for Slot 8

a) Total pressure loss contours

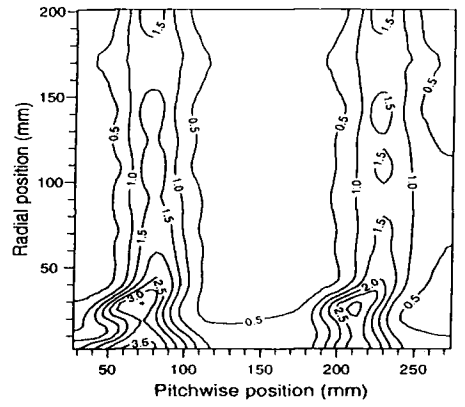

b) Secondary kinetic energy contour (%)

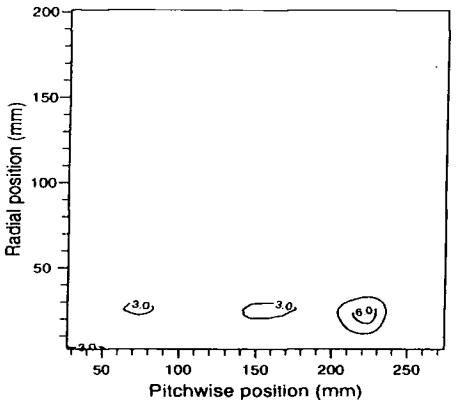

c) Yaw angle contour

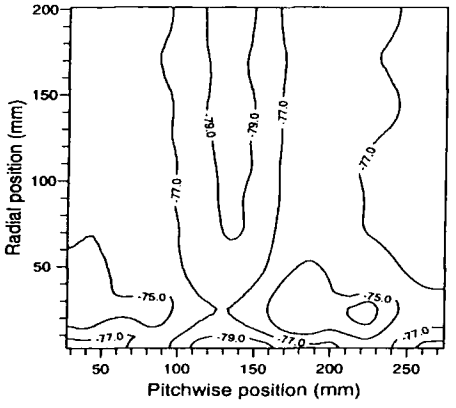

d) Pitch angle contour

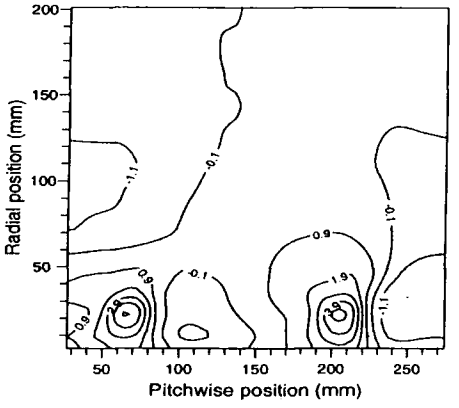

e) Secondary vector plot

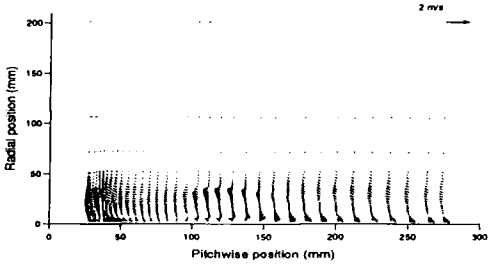

Figure 7.12—Area plot at Slot 9 (half span)

a) Total pressure loss contours

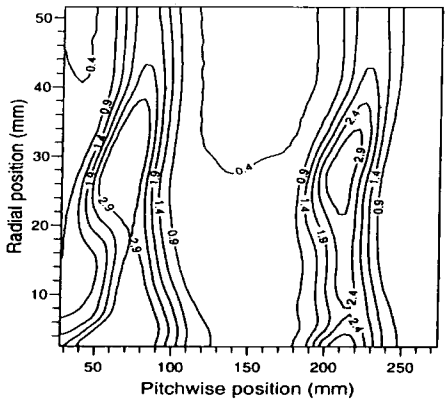

b) Secondary kinetic energy contour (%)

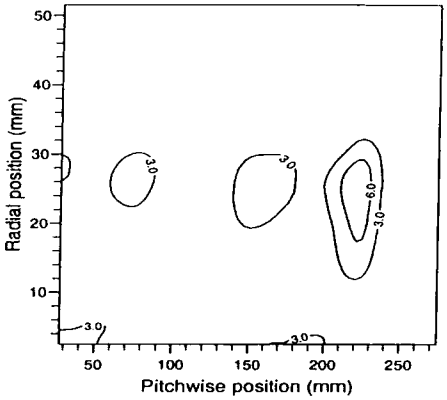

c) Yaw angle contour

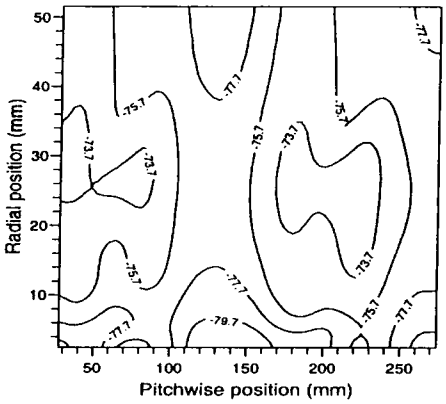

d) Pitch angle contour

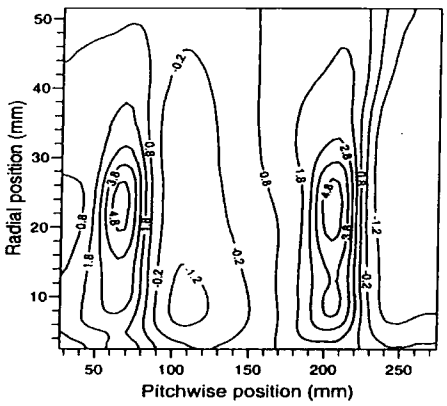

e) Secondary vector plot

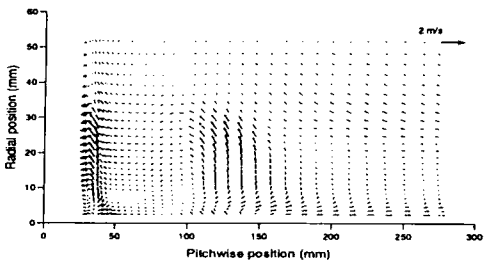

Figure 7.13—Area plot at Slot 9 (near wall region)

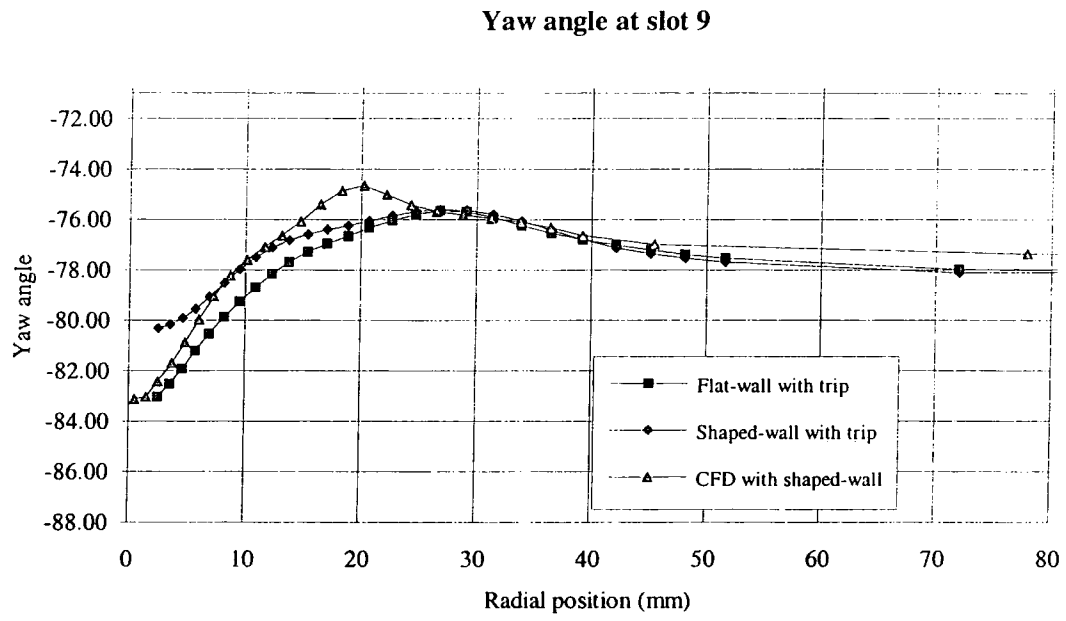

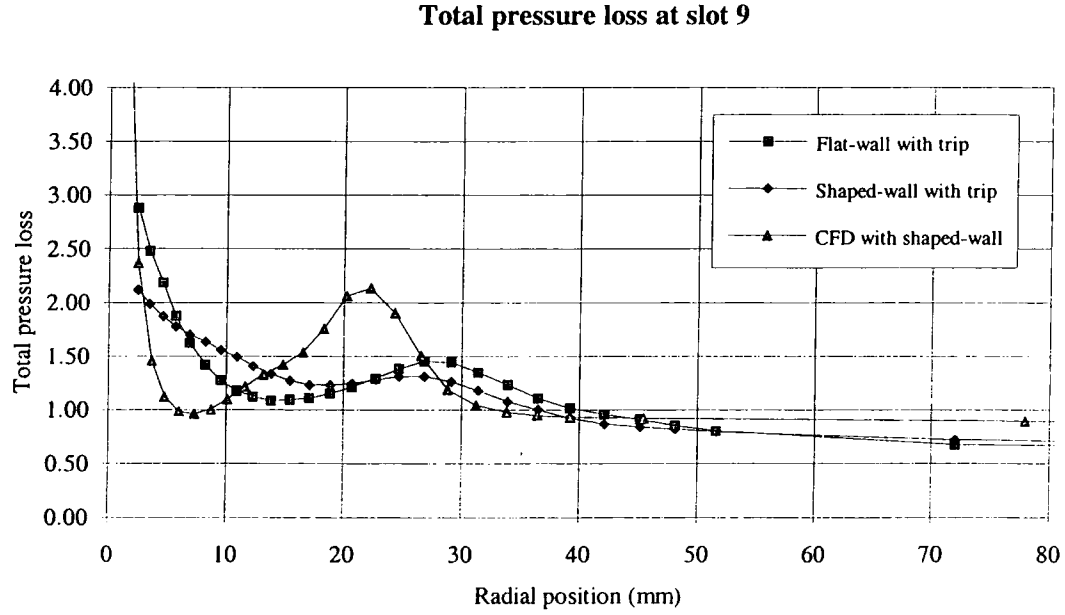

Figure 7.14—Pitch averaged results for Slot 9

a) Total pressure loss contours

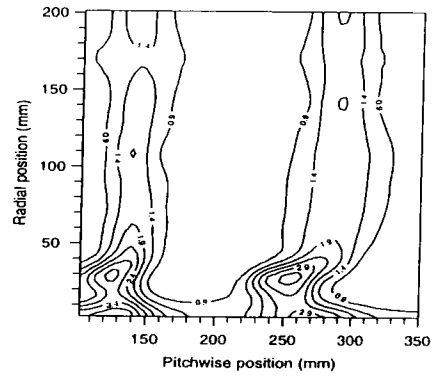

b) Secondary kinetic energy contour (%)

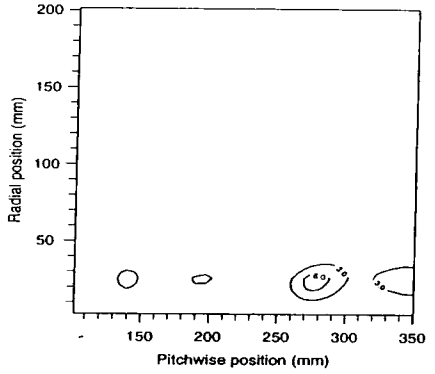

c) Yaw angle contour

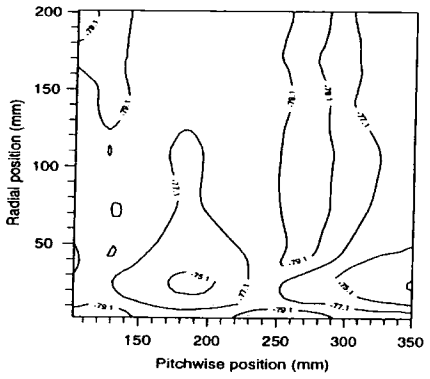

d) Pitch angle contour

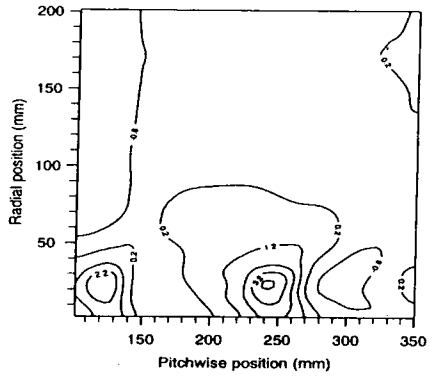

e) Secondary vector plot

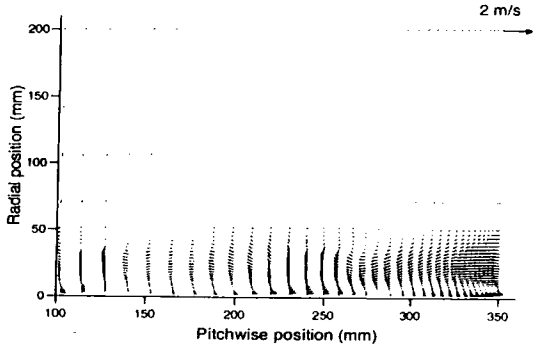

Figure 7.15—Area plot at Slot 10 (half span)

a) Total pressure loss contours

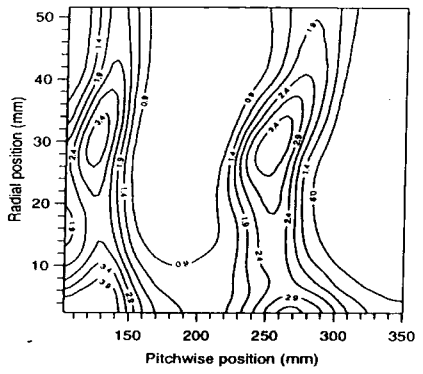

b) Secondary kinetic energy contour (%)

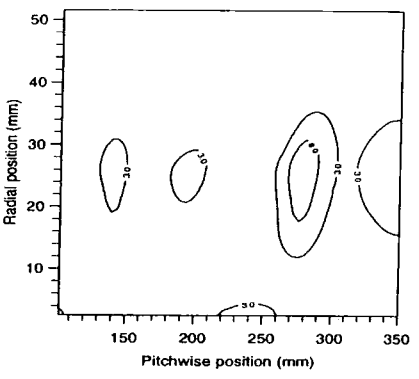

c) Yaw angle contour

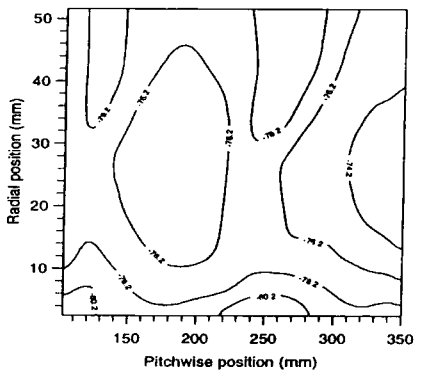

d) Pitch angle contour

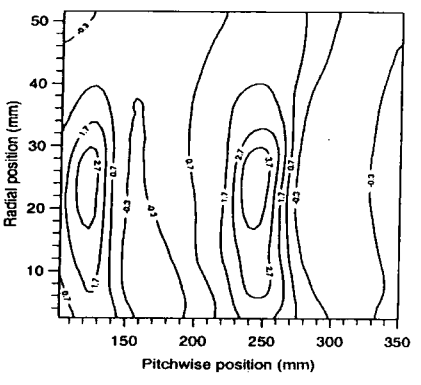

e) Secondary vector plot

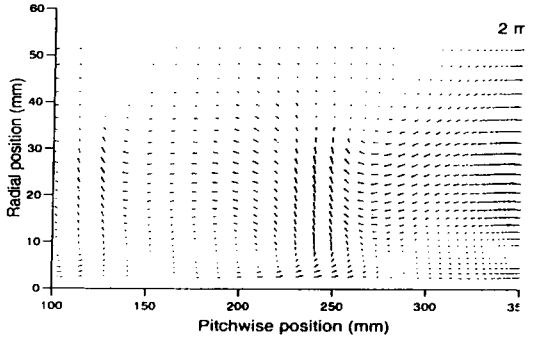

Figure 7.16—Area plot at Slot 10 (near wall region)

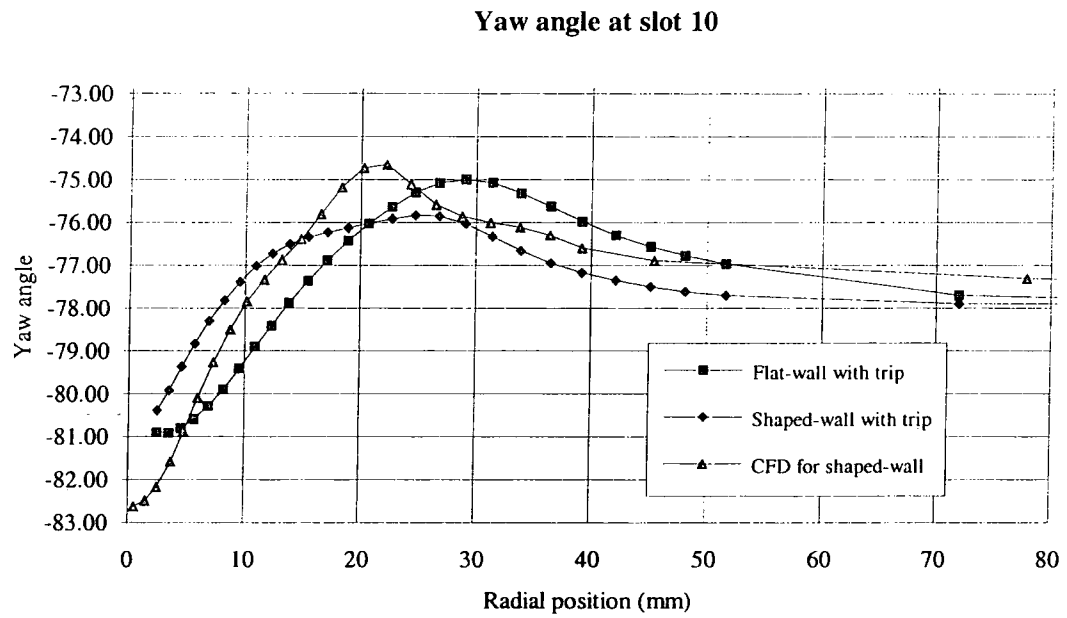

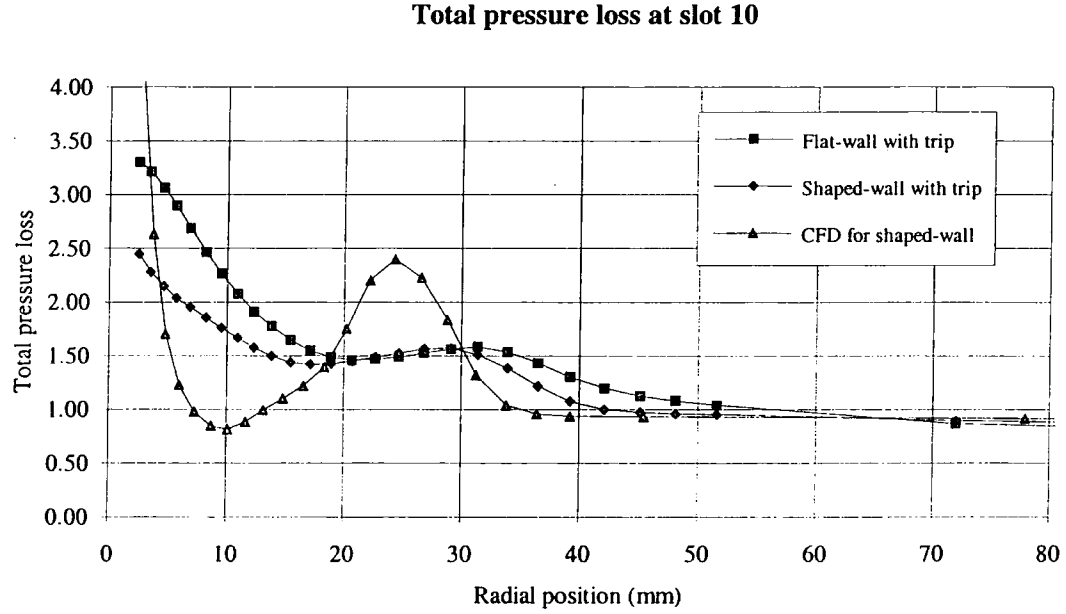

Figure 7.17—Pitch averaged results for Slot 10

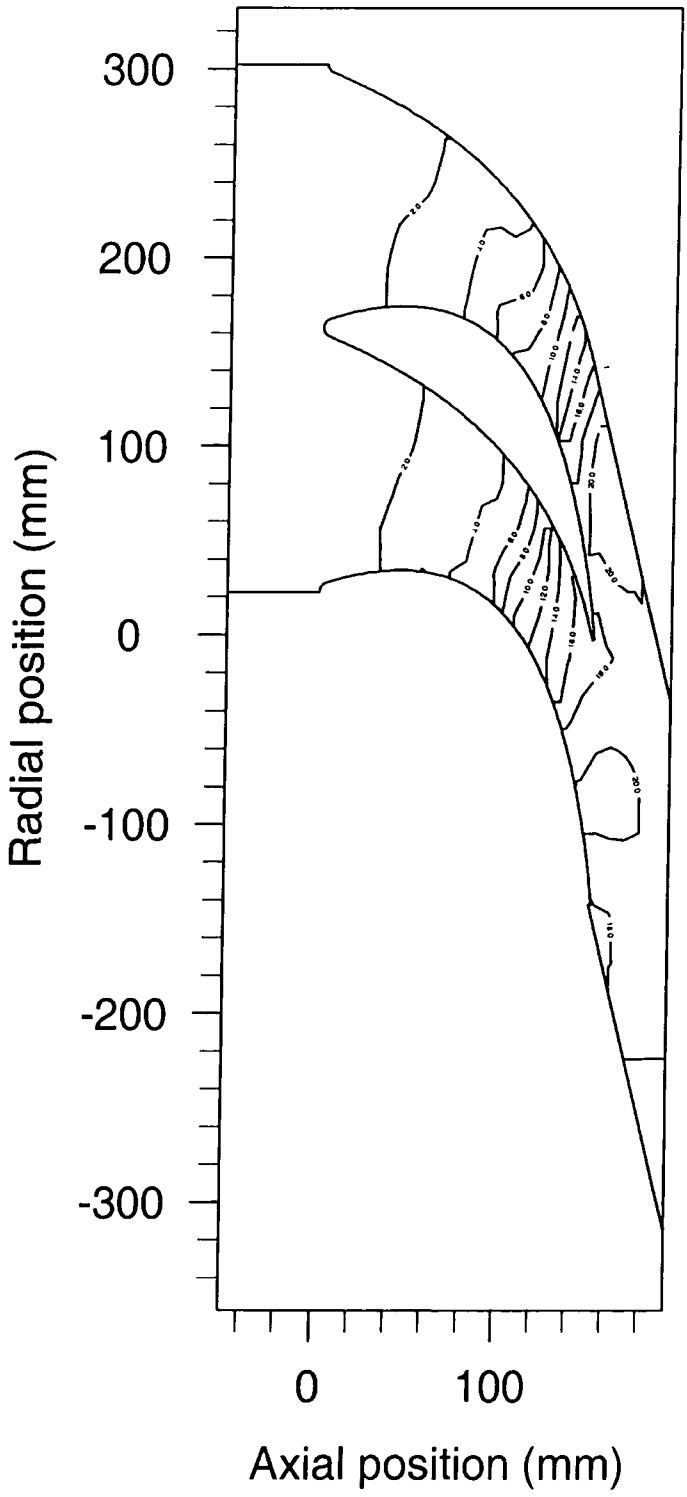

Figure 7.18—Static pressure on the shaped end wall

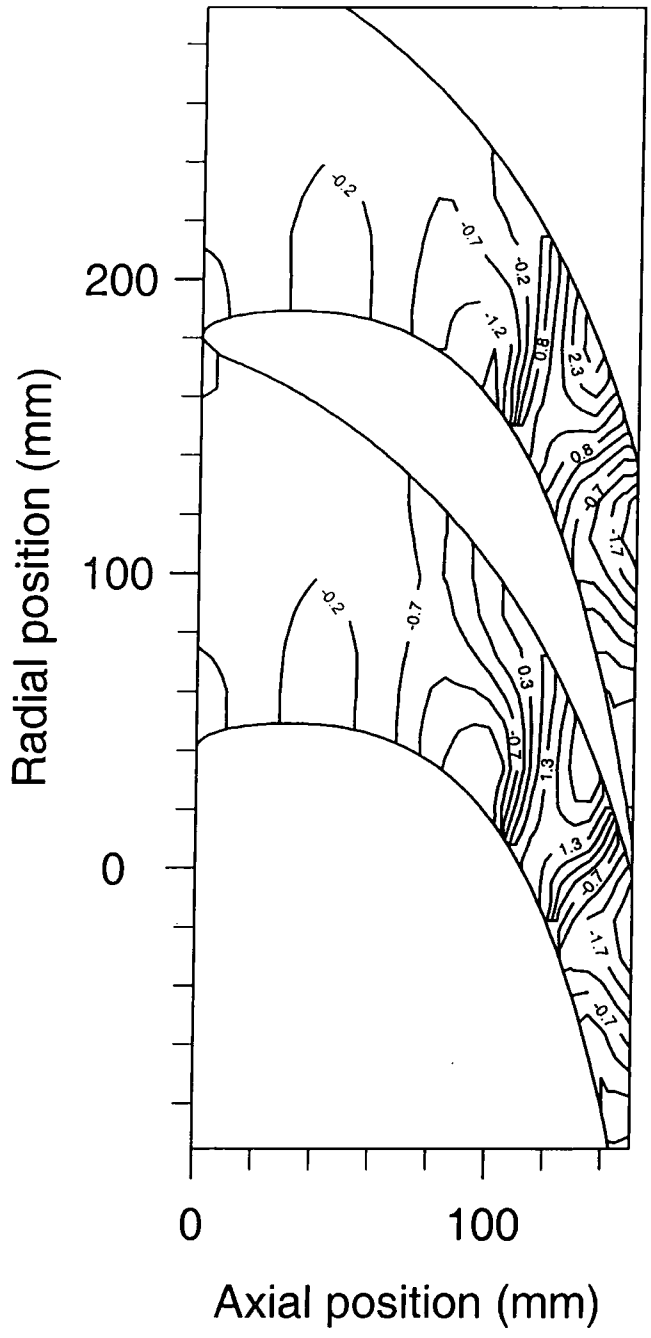

Figure 7.19—Static pressure difference between the flat and shaped end wall on the end wall

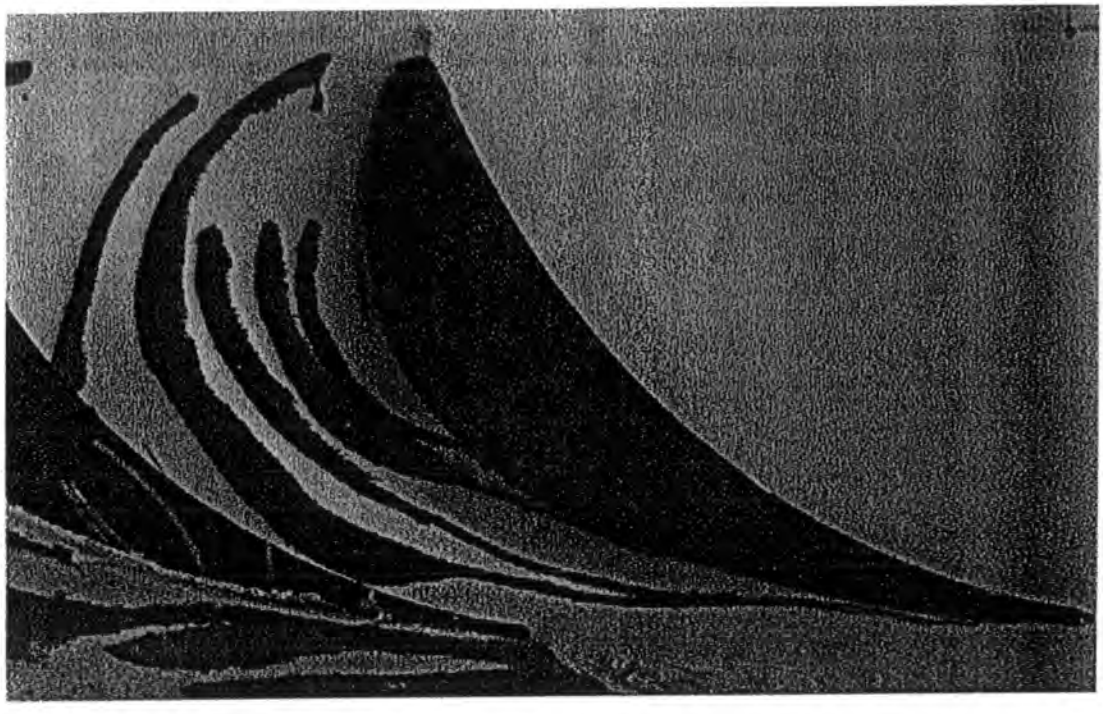

Figure 7.20—Flow visualisation on the shaped end wall surface

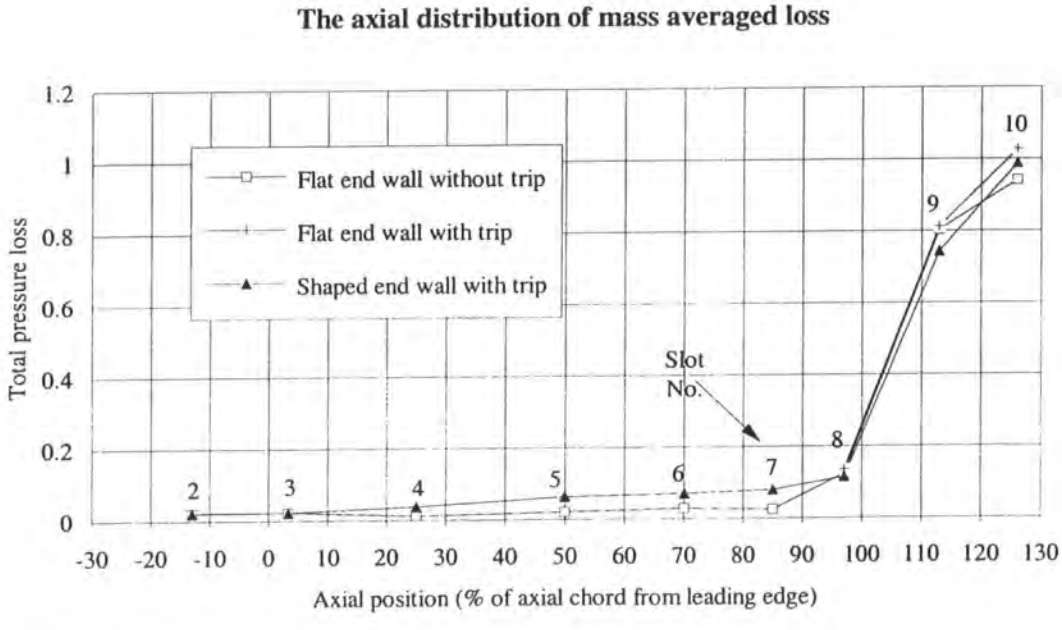

Figure 7.21—The mass averaged total pressure loss for every slot (measurements at slot 2-8 do not include boundary at the blade surface)

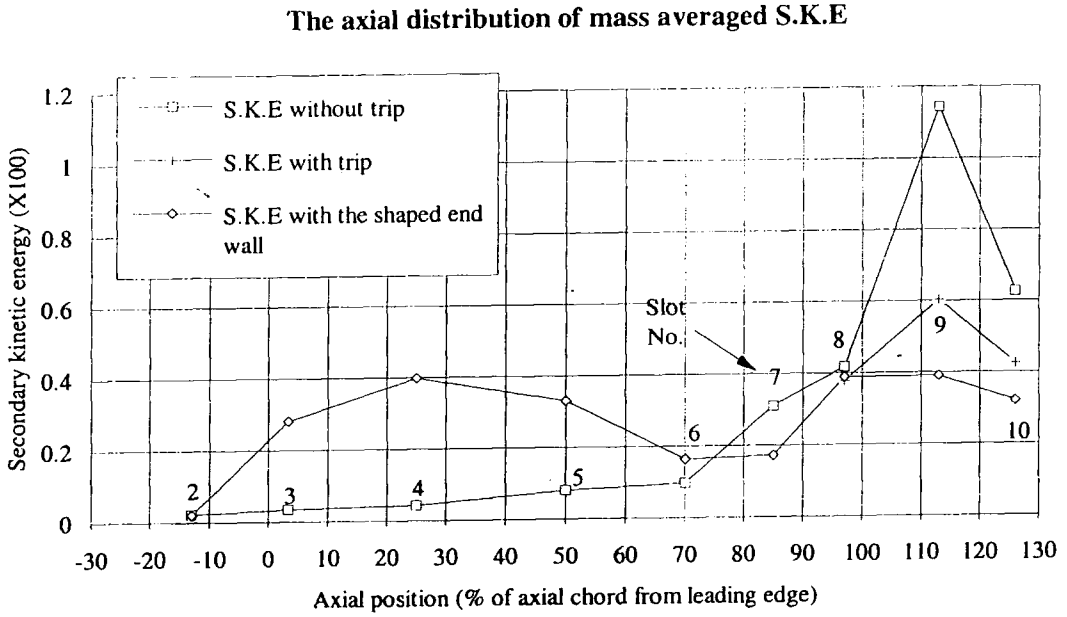

Figure 7.22—The mass averaged secondary kinetic energy for every slot (measurements at slot 2-8 do not include boundary at the blade surface)

Chapter 8 Over View and Discussion

8.1 Introduction

The aim of this work has been to investigate the effect of the shaped end wall on the secondary flow and total pressure loss in a linear cascade. The linear cascade with the nozzle guide vanes of ALSTOM Energy Ltd was designed and built. The blade is a nozzle guide vane with high contraction ratio. The high contraction ratio leads to a very narrow throat area. The blade was designed in such a way that the secondary flow is comparatively small and concentrated in the near end wall region. The pitch to chord ratio of the nozzle guide vane is low compared to the optimum value from Zweifel (1945) as in section 2.3.1. Chosen to reduce secondary flow, the blade may not be idea to see the effect of the end wall profiling but ASLTOM wanted to compare with real machine conditions. The small throat area also increases the difficulty of the experimental secondary flow investigation within the blade passage. The nearest distance to the end wall which probe can get to is relatively big compared to the small secondary flow affected area. But downstream, where the loss needs to be measured, the size of the probe was less of a problem. The data acquisition system including traverse gear, transducer and control software were designed and assembled. Several five hole probes were designed and calibrated for the purpose of investigation. Static pressure tappings were placed on the blade surface and the end wall surface.

8.2 Experiment results with the flat end wall

In order to investigate the shaped end wall effect, the flow field in the linear cascade with the flat end wall was investigated in great detail. Five hole probes were used to investigate the flow field at the 10 slots. Static pressure on the blade surface and the end wall surface was measured through the tappings. Flow visualisation on the blade surfaces and the end wall surface were carried out. Transitional trips were used on the blade suction surfaces to stimulate the transition on the blade surfaces. Then slot 8, 9 and 10 were investigated again by using the five hole probes.

After the cascade was connected to the wind tunnel exit, the inlet flow of the cascade was investigated. The initial results show a bump near the end wall in the inlet velocity distribution as shown in Fig 3.6. This was due to the wide gap between the last turbulence generating bar and the end wall. This wide gap produced a jet flow with high energy and resulted in an uneven velocity profile. A small bar was then fitted at the position of 24 mm from the end wall. It is proved in Fig 3.6 that the velocity profile is greatly improved. So an ideal inlet condition was set up for the experiments.

Slot 2 was investigated by a small head five hole probe. At this slot, the flow is about to meet the leading edge of the blade. In the secondary vector plot, it can be seen that the horse shoe vortex has started to developed. The yaw angle shows an overturning near the end wall. This is because of the shape of the blade and the angle of attack. With a zero attack angle, the pressure surface shape obviously gives more effect and therefore gives a stronger vortex leg near its side. The total pressure loss does not show too much change from the upstream condition apart from the boundary layer growth. Slot 3 is the slot just down stream of the blade leading edge. There is a small vortex near the pressure surface. This is the pressure side leg of the horse shoe vortex. There seems to be another vortex near the suction surface which is not very clear in the secondary vector plot. This probably indicates the existence of the weak suction side leg of the

horse shoe vortex. At slot 4, the pressure side leg of the horse shoe vortex has moved away from the pressure surface because of the pressure gradient across the passage. A strong passage vortex becomes dominant in the blade passage. The yaw angle of the flow is clearly affected by the vortex movement by showing both underturning and overturning near the end wall. At slot 5, the vortex strength has become stronger than before as shown in Fig. 4.10. There is more underturning and overturning in the yaw angle distribution. At slot 6, The low energy fluid near the end wall is being swept out toward the mid-span by the movement of the secondary flow. The secondary flow is stronger than the previous slots. At this slot, the yaw angle at mid-span shows little difference near mid-span between the pressure surface and the suction surface. The reason for this is that the suction surface and the pressure surface are nearly parallel at slot 6. At slot 7, the low energy fluid has been swept out from the suction corner by the stronger secondary movement. The pitch averaged total pressure loss shows a loss peak at about 10 mm away from the end wall. The secondary vector plot shows a very strong secondary flow near the end wall. The yaw angle distribution exhibits underturning and overturning near the end wall. The turning angle at mid-span shows a big increase from slot 6. This is probably the reason for the dramatic increase of the secondary kinetic energy. Slot 8 is the slot just before the trailing edge of the blade. At this slot, the secondary flow has increased sharply from slot 7. Between slot 7 and slot 8, the high velocity of the flow generate a great deal of secondary flow. The vortex centre of the passage vortex has moved nearer to the suction surface due to the pressure gradient between two surfaces. The size of the vortex has also become bigger. The secondary kinetic energy show its maximum value in the suction surface corner. The centre of the total pressure loss contour has been moved onto the suction surface from the end wall. The pitch averaged total pressure loss shows an increase of mid-span loss and a loss peak slightly further away from the end wall. Because of the effect of the vortex movement, the yaw angle distribution shows a big overturning and underturning. Slot 9 is the first slot to be investigated after the trailing edge. At this slot, the wake of the blade trailing edge become a dominant effect at the mid-span position. Near the end

wall, the development of the new boundary layer and the convection effect of the secondary flow push the loss peak further away from the end wall. The counter vortex can be noticed from its effect on the total pressure loss in Fig. 4.19. The vortex centre has moved away from the end wall more. The secondary flow here is much stronger than that within the passage. This is because of the vortex shedding after the trailing edge. At this stage, the dissipation and diffusion are obviously the dominant effects. The secondary flow will become weaker further downstream. At slot 10, the total pressure loss peak has been moved away from the end wall more by the secondary convection effect and the growth of the boundary layer on the end wall. The counter vortex has grown bigger. The secondary velocities are smaller than at the slot 9 but cover a larger area. The secondary kinetic energy is much less than at slot 9. The mixing process diffuses the secondary flow quickly as well as the dissipation process of turbulence flow. From slot 9 and 10, it can be seen that the secondary flow is gradually losing its concentration and strength due to the dissipation and diffusion effect.

Overall, the flow in the linear cascade experiences three stages. In the first stage, the flow approaches the leading edge of the blade and starts forming the horse shoe vortex. The pressure side leg of the horse shoe vortex is the stronger. In the second stage, the flow goes downstream inside the passage. The pressure gradient between the pressure surface and the suction surface makes the secondary flow stronger. The strong convection effect of the secondary flow moves the low energy material away from the end wall. A new boundary layer start to develop on the end wall surface. In the third stage after the trailing edge, the flow experiences the diffusion effect. The secondary flow becomes smaller and smaller further downstream. The size of the vortex becomes larger, while the strength of the vortex declines.

The flow visualisation on the blade surface indicated a flow separation on the suction surface near the trailing edge of the blade in Fig. 4.27. This in fact means that the boundary layer was laminar up to the separation point. In order to simulate the situation

in a real machine, the boundary layer on the blade surface need to be turbulent. For this purpose, the transition trips were put on the blade surface to stimulate the transition. It was shown those transition trips worked. With the transition trip, it was possible that the flow field could be changed in the cascade. Investigations were carried out again at slot 8, 9 and 10. At slot 8, the flow shows slightly more total pressure loss with the trips. The secondary kinetic energy was decreased which means smaller secondary flow with the trips. At slot 9, the total pressure loss was also increased, and the secondary flow reduced massively with the trips. The reason for this large reduction is not clear, but may due to strong spanwise flows in the separation bubble leading to strong shed vorticities as seen in Fig. 4.19. At slot 10, the secondary flow is again smaller than that without the trips. Because of the weaker convection effect from the secondary flow, the loss peak stays closer to the end wall than that without the trip, see Fig. 4.23. In Table 8.1, the secondary kinetic energy is shown for three slots with and without the trips. It can be seen that the turbulent boundary layer on the suction surface gives less secondary flow than that with the laminar boundary layer. The turbulent boundary layer on the blade surface also makes the mixing process of the secondary kinetic energy much slower than the laminar boundary layer. There is a 54% secondary kinetic energy decline from slot 9 to 10 with the laminar boundary layer. There is only 30% secondary kinetic energy decline from slot 9 to 10 with the turbulent boundary layer.

Table 8.1—The effect of the transitional trips on the secondary kinetic energy

(Area averaged value based on inlet)

Slot No.	Slot 8	Slot 9	Slot 10
No trip	0.0042	0.0114	0.0063
With trips	0.0038	0.0060	0.0042

The experimental results are compared with the results of correlations from Dunham, which is Equation 2.3 in section 2.2.3. The gross secondary loss is 0.0091 from

experiments. The secondary loss from the correlation is 0.0080. Apparently, the secondary loss is under-predicted although the result is surprisingly close. As the correlations contain little physics, the credibility of their predictions is in doubt.

8.3 Computational results

The CFD code is a non-orthogonal 3D finite volume code developed within the Aerodynamics group of ALSTOM Energy Ltd. A pressure correction scheme, SIMPLE proposed by Patankar (1980), is used to determine the flow field. It is well known that the fully-collocated grid arrangement creates a numerical decoupling between the collocated velocity and pressure values and results in chequerboard oscillation. The non-linear interpolation scheme proposed by Rhie & Chow (1993) is used to achieve numerical stability within the collocated storage arrangement.

The convective fluxes are approximated with the quadratic QUICKS scheme of Leonard (1979). This scheme is third-order accurate for uniform grids. The unbounded nature of QUICKS scheme prevents its use for turbulence quantities. Several researchers have formulated bounded forms of QUICKS scheme. The code used in this study employs the MUSCLE approach proposed by Lien & Leschziner (1994). The calculations have been started by using the UPWIND scheme to enhance stability and the QUICKS scheme is activated after a number of iterations. The turbulence models involved are K-ε model and its S-Ω modification.

The code was validated against the Durham test case. At first, 2-D calculations for the Durham test case were carried out. In the 2-D calculations, the H type grid was used. Different numerical schemes such as UPWIND, QUICKS, UMIST and MINMOD were tested. The comparisons of the yaw angle and the total pressure loss predictions against the experimental results are shown in table 4.4. The QUICKS & UMIST scheme gives the best loss prediction. However, the yaw angle was not well predicted and the loss is

much higher than the experimental results. This is due to several reasons. The H type grid gives very skewed cell near the trailing edge. The incorrect base pressure prediction from the CFD is another reason. The assumption of turbulent flow everywhere in the CFD might be another source of high loss prediction. In their experiments, the flow on the end wall showed laminar transitional characteristics, Moore & Gregory-Smith (1996). The turbulence models were tested, both the standard k-ε model and S-Ω modification. For the reason explained in the Chapter 5, the S-Ω modification seems to give less loss prediction, but it is still more than the experimental results. From those 2-D calculations, the best numerical scheme and the turbulence model were decided to be QUICKS&UMIST and S-Ω modification. For the static pressure around the blade surface, the 2-D calculation gives reasonable results except for the trailing edge. Near the trailing edge, the CFD gives a sudden jump which means a big pressure drop. Compared with the experimental results, the CFD results are not correct near the trailing edge. This indicates that the CFD code has problem in dealing with the base pressure. This problem will further influences the loss and the exit yaw angle predictions. A 2-D calculation for the nozzle blade cascade was carried out as well. The CFD results were compared with the experimental results at high Reynolds number in Table 4.7. The CFD with the QUICKS&UMIST again gave the best results. The best results are much closer to the experimental results than for the Durham test case. Apart from the fact that at high Reynolds number the boundary layer on the blade surface is fully turbulent which is more suitable for the CFD assumption, it might imply that the code works better with the lower turning blade. Durham blade has a turning of 111 degree but on the other hand the nozzle guide vane from ALSTOM only has about 77 degree turning.

3-D calculations against the Durham test case were completed with the experimental boundary conditions. To check the grid dependence of the code, several cases with different grid sizes were done. The grid with the size of 25×99×50 was proved to be

adequate. The contours of the 3-D calculation results show fairly good agreement with the experimental results. The pitch averaged total pressure loss and the yaw angle distribution from the CFD were compared with the experimental results. The CFD results show a good mid-span yaw angle prediction. Near the end wall, less underturning and more overturning were predicted. The secondary kinetic predicted by the CFD is smaller than that of the experiments. The smaller secondary flow results in less convection effect within the end wall boundary layer and the loss peak stays closer to the end wall. 3-D calculations for the nozzle cascade have been done. The comparisons between the CFD and the experimental results were carried out from slot 2 to slot 10. The CFD gave higher loss and stronger secondary flow. The stronger secondary flow results in the higher loss peak near the end wall.

The CFD gives higher secondary flow for the nozzle cascade but lower secondary flow for the Durham cascade. There are differences between these two cases. The Durham cascade has a much bigger turning angle than the Nozzle cascade. The Nozzle blade has a fully turbulent boundary layer but the Durham blade has a partial turbulent boundary layer. However, these differences seem to be inadequate to explain the different secondary flow predictions from the CFD.

8.4 Shaped end walls design

The idea of the non-axisymmetric end wall profile was to influence the local pressure field. The end wall profile was designed based on the assumption that the end wall static pressure could be locally raised by applying concave curvature to the end wall. Likewise, the static pressure could be lowered by convex curvature. The final profile as shown in Fig. 6.6 is a combination of the shape in the pitchwise and the profile in the axial direction. The CFD code was used to test systematically different profiles with the important parameters at, ct, sp and ss being varied. The final choice was the type "t" profile with at=10 mm and ct=52 mm (code n525t). A value of 10 mm rather than 12

mm was chosen for at as there seemed no advantage with the higher value, and it would be easier to manufacture. The type "t" was chosen for the same reason, and also it would reduce the "wetted area" of the end wall and pressure surface.

A detailed CFD study was made of the flow with the chosen profile. The effect of the end wall is to reduce the pressure difference in the region of the maximum turnning. This could be seen in the static pressure around the blade surface in Fig. 6.21. The contours of the flow field predicted by the CFD were shown from slot 4 to 10. These plots indicate the slower rolling up of the end wall boundary layer and the reduced secondary kinetic energy. The reduced secondary flow may be seen from the pitch averaged results at slot 10, where the loss peak is closer to the end wall having been convected less by the lower secondary flow velocities. The area averaged results of the CFD indicates a total loss reduction of 6.6%.

8.5 The experimental results with the shaped end wall

The shaped end wall n525t was manufactured by the CNC machine. It was put on the cascade instead of the perspex window. Slot traverses have been done from slot 2-10. The static pressure on the blade surface and the end wall surface was also recorded. Slot 2 is the slot just upstream of the leading edge. The traversing results show almost exactly the same total loss and the yaw angle distribution as those with the flat end wall. This confirms the inlet conditions were not changed by the shaped end wall. At slot 3 and 4, the results show little difference from those with the flat end wall. At slot 5, the end wall profile starts showing its inviscid effect on the secondary flow. The yaw angle show less underturning and more overturnning than with the flat end wall. Near the end wall, there is a strong cross passage flow toward the concave part of the end wall. The CFD gives very good prediction in term of the secondary flow vector plot. At slot 6, the passage vortex can be clearly seen rolling up the low material near the end wall. The yaw angle shows higher underturning which reflects the inviscid effect of the shaped end wall. The total pressure loss shows thinner boundary layer near the end wall. At

this stage, the secondary flow is more or less the same as that with the flat end wall. But near the end wall, the secondary flow vector is getting smaller. At slot 7, the secondary kinetic energy is less concentrated and spreads wider in the span wise direction. The secondary flow vector plot also shows less secondary flow near the end wall but stronger secondary velocities upward from the suction corner. The pitch averaged results of the yaw angle distribution show less overturning and underturning near the end wall. The CFD results show more underturning and the overturning which suggest more secondary flow was predicted than that in the experiments. The pitch averaged total loss shows less loss near the end wall. The loss peak has not moved away from the end wall yet, but with the flat end wall, the loss peak is located at about 8 mm away from the end wall. This is the result of less secondary flow which imposes less convection effect. At slot 8, the yaw angle distribution shows a much bigger underturnning and much smaller overtrunning than those with the flat end wall. This is because the profile of the shaped end wall was going back to the flat platform as shown in Fig. 6.6. The decreasing bump near the pressure surface and the rising dip near the suction surface create a strong cross flow from the suction surface to the pressure surface at about 20 mm away from the end wall. Near the end wall, the secondary flow is much smaller than with the flat end wall. At slot 9, there is apparently less secondary flow, the secondary kinetic energy showing a big reduction, and there is less overturning in the yaw angle distribution. Because of the smaller secondary flow, the low energy material that has been moved away from the end wall is less than that with the flat end wall. As a consequence, the loss is slightly higher in the region from 7 mm to 22 mm span wise and lower in the region from 22 mm to 50 mm spanwise than that with the flat end wall. From slot 9 to slot 10, the flow experienced mainly the mixing process. Compared to the flat end wall, the mixing process was slower. The shaped end wall has moved the vortex centre closer to the end wall at slot 10, and the secondary kinetic energy was reduced. The secondary flow reduction is also shown in the pitch averaged yaw angle distribution. Less overturning and underturning can be seen. The shaped end wall reduced the secondary flow and weakened the rolling up of the low energy material

from the end wall. Eventually the shaped end wall resulted in a lower loss of 0.903 compared to 0.944 with the flat end wall. The net secondary loss was reduced by 21% at slot 10. The effect of the shaped end on the static pressure on the blade surface is hardly visible, but on the end wall surface the shaped end wall has reduced the pressure gradient across the passage. It is found that there was a delay between the end wall profile shape and its effect on the static pressure distribution. The flow visualisation also shows different results from that with the flat end wall.

Overall it can be concluded that the shaped end wall has changed the static pressure distribution near the end wall and so it has reduced the secondary flow and total pressure loss.

Chapter 9 Conclusions and Future Work

The experimental and computational results presented in this thesis are concluded in this chapter. Recommendations for the future work are made.

9.1 Experimental work

The flow field with the flat end wall and the shaped end wall was investigated in detail. The secondary flow structures and loss growth for both conditions were understood. The effect of the shaped end wall was drawn from the results and comparisons. Conclusions from the experimental work are presented below.

9.1.1 Experimental results with the flat end wall

(1). It was found that the turbulence generation grid has a great effect on the inlet boundary condition. In order to achieve the ideal boundary inlet condition, a small bar was inserted in the gap between the turbulence grid and the end wall. This small bar is proved to be essential to achieve a uniform inlet boundary condition. This suggests that the turbulence generation bar can be used to vary inlet total pressure distribution. In real turbines, the inlet total pressure varies along the spanwise direction. By modifying the turbulence generation bars, a particular inlet total pressure distribution from a real machine may be obtained in the linear cascade.

(2). The cobra five hole probe has proved to be a good measurement tool. The probe should be always calibrated at a high dynamic head. The large velocity range from the inlet to exit did not affect the probe's accuracy, so that the calibration results from high dynamic head can be used at low dynamic head. But it is difficult for it to approach the wall very closely. The closest distance between the wall and the probe head should not be less than 5 mm. It was more difficult for the probe to investigate the shaped end wall. It is suggested that a pitot-static probe might be used to investigate the flow near the end wall. The small head five hole probe was used to investigate the flow field at slot 2. Because of the short stem, the pitch angle obtained shows a slightly larger error than that of the cobra probe. But for the upstream slot 2 where the flow does not show too much pitch variation, the results from the small head probe are as good as that with the cobra probe.

(3). The flow field was investigated from the inlet to the exit for the flat end wall. The secondary flow and the total loss developments are understood. The pressure side leg of the horseshoe vortex could be seen clearly at slot 2 and slot 3. On the other hand, the suction side leg is too small to be seen. The pressure side leg of the horseshoe vortex grows into a big passage vortex, which becomes a dominant vortex from slot 4 onwards. There is quite a small counter vortex which could be seen at slot 9 near the end wall. The secondary flow continues growing from the leading edge to the trailing edge of the passage. Downstream of the trailing edge, the secondary flow starts being dissipated. The total pressure development from slot 2 to slot 10 shows the growth, lift off and regeneration of the boundary layer on the end wall. The total pressure loss core movement is related to the secondary flow.

(4). The flow visualisation shows separation bubbles on the suction surface of the blade. Transition trips were put on to stimulate the turbulent transition, and then the separation bubbles were eliminated. The transition trip made the boundary layer turbulent and thus more dissipation of the secondary flow was resulted. The separation bubbles, which

seem to generate more secondary flow, were eliminated. Therefore the secondary flow is smaller than without the trip.

(5). The static pressure on the blade surface does not vary much at different spanwsie positions.

9.1.2 Experimental results with the shaped end wall

The flow field with the shaped end wall was investigated. The inlet conditions were kept the same as those were with the flat end wall. The effect of the shaped end wall on the flow was obtained by comparing the results with the flat end wall results.

(1). The shaped end wall has changed the static pressure distribution on the end wall. It has increased the pressure near the suction surface of the blade and decreased the pressure near the pressure surface. The pressure gradient has been reduced by the shaped end wall in most of the area. There is a delay between the end wall shape and the corresponding pressure change.

(2). The secondary flow was reduced by the shaped end wall. The smaller pressure gradient reduced the driving force of the generation of the secondary flow. At slot 10, there is about 24% secondary kinetic energy reduction.

(3). The total pressure loss was reduced by the shaped end wall. At slot 10, about 4.3% loss reduction was achieved. The mixed out loss is reduced as well.

9.2 Computational work

The 3-D viscous code from ALSTOM was modified to work with the shaped end wall. It was validated against the Durham test case and the nozzle cascade.

9.2.1 Validation of the code

(1). By using different turbulence models, the S-Ω modification of the k-ε model turned out to be the best turbulence model, although the k-ε model was found more stable than its S-Ω modification.

(2). The UMIST and QUICKS scheme are higher order schemes but with less stability. The UPWIND scheme is quite stable but with bigger numerical error. The UPWIND scheme was used at first in the calculation for 400 iteration. Then the UMIST and QUICKS schemes were used for momentum and scalar equations. This is proved to be an efficient method to run the code.

(3). The CFD results generally give more loss. The yaw angle of the CFD is smaller than the reality. The CFD static pressure distribution on the blade surface shows that the base pressure is incorrect.

(4). The secondary flow prediction for the Durham test case is smaller than the experimental results. But on the other hand, for the nozzle cascade it gave a higher secondary flow. The CFD code assumes the boundary layer all turbulent in the calculation. In the Durham test case, the boundary layer on the blade surface is partially turbulent. The actual secondary flow dissipation rate is smaller than with a fully turbulent boundary layer. So at slot 10, the CFD gives smaller secondary flow. For the nozzle cascade, the boundary layer on the blade surface is turbulent. The dissipation rate of the secondary flow is apparently higher than the CFD prediction.

(5). The computational grid is H type grid. The grid cells near the trailing edge are too skewed and this in fact affects the flow exit angle prediction. It is suggested that the multi-block grid could solve the problem.

9.2.2 The shaped end wall design by using the code

After the validation, the code was used to test different end wall profiles. The total pressure loss and secondary kinetic energy were compared with the flat end wall case.

(1). The CFD code is capable of dealing with the complex end wall shape.

(2). The effect of the shaped end wall on the vortex development was accurately predicted. The CFD gave more secondary flow and a stronger upward flow in the suction corner. At slot 10, the upward flow is much stronger than that from the experimental results.

(3). The general change in pattern is correctly predicted by the CFD. However, the static pressure prediction on the end wall shows less change than that from the experimental results.

The CFD method is proved to give the correct flow field with the shaped end wall. The effect of the shape end wall is predicted well by the code. Even if the absolute values, especially of loss, predicted by the CFD are not very accurate, it generally gives the correct trend. The CFD method is feasible to be used to design the shaped end wall.

9.3 Future work

After the conclusions of the work in this thesis, the work, which might be developed in the future, is suggested here.

(1). The blades in the cascade might need to be replaced by better made blades. This means the blades that are made in such a way that the blades are exactly the same without twist in the spanwise direction.

(2). The scale of the cascade should be made bigger. The present cascade has a too small throat area between the blades. This makes it very difficult to traverse the slot 8, which is near the throat. The probe probably has affected the flow field because of its relative big stem diameter (10 mm) compared with the throat (32.94 mm). A smaller probe will be also able to resolve the problem. A bigger pitch to chord ratio near the optimum as calculated from Zweifel (1945) in section 2.3.1 might be applied. This might make the end wall profiling effect bigger than it is in the present cascade.

(3). Smaller five hole probes might be made in the future to allow closer investigations near the blade and end wall surface. Pitot-static and three hole probes might be used to investigate the flow detail near the end wall. The loss development and the effect of the shaped end wall could be measured more accurately.

(4). The inlet turbulence intensity might be measured by a hot-wire manometer. This hopefully will help to predict the inlet boundary condition more accurately and reduce the over-prediction of the loss by the CFD.

(5). There was only one shape end wall tested because of time. It is suggested that more end wall profiles should be tested to get more understanding of the shaped end wall effect.

(6). The shaped end wall was only tested in the linear cascade. The effect of it on the real machine which has more complicated flow field needs to be investigated. It is suggested that the shaped end wall should be tested in a model turbine. This will make

it possible to determine the potential benefit of the more uniform flow on the next row of the blades.

Appendix

1 Area Traverse Plots

1.1 Total Pressure Loss Coefficient

$$C_{pol} = \frac{Po_u - Po_l}{\frac{1}{2}\rho v_u^{\,2}}$$

1.2 Static Pressure Coefficient

$$C_{pl} = \frac{P_u - P_l}{\frac{1}{2}\rho v_u^{\,2}}$$

2 Pitch/Mass Averaged Curves

2.1 Total Pressure Loss Coefficient

$$\overline{C}_{pol} = \frac{\int v_x C_{pol} dy}{\int v_x dy}$$

2.2 Secondary Kinetic Energy

$$\overline{C}_{skel} = \frac{\int v_x \left(v_y^{\,2} + v_z^{\,2}\right) dy}{v_u^{\,2} \int v_x dy} \times 100$$

2.3 Yaw angle

$$\overline{\alpha}_y = \arctan \frac{\int v_x v_y dy \bullet s}{\left(\int v_x dy\right)^2} = \arctan \frac{\overline{v}_y}{v_x}$$

3 Area/Mass Averaged Values

3.1 Total Pressure Loss Coefficient

$$C_{po} = \frac{\iint v_x C_{pol} dydz \bullet \rho}{\dot{m}_{cas}} = \overline{\overline{C}}_{pol}$$

3.2 Secondary Kinetic Energy

$$C_{ske} = \frac{\iint v_x \left(v_y^{\,2} + v_z^{\,2}\right) dydz \bullet \rho}{\dot{m}_{cas} \bullet v_u^{\,2}} = \overline{\overline{C}}_{skel}$$

3.3 Exit Angle

$$\alpha_e = \arctan \frac{\iint v_x v_y dydz \bullet \rho^2 \bullet h \bullet s}{\dot{m}_{cas}^{\,2}}$$

$$= \arctan \frac{\overline{\overline{v}}_y}{\overline{\overline{v}}_x}$$

$$= \overline{\overline{\alpha}}_y$$

References

Ainley, D. G., and Mathieson, G. C. R., 1952. "A Method of Performance Estimation for Axial Flow Turbines", NGTE Report R111.

ALSTOM Technical Report AGR 307, 1992.

Atkins, M. J., 1987. "Secondary Losses and End-Wall Profiling in a Turbine Cascade," International Conference on Turbomachinery Efficiency Prediction and Improvement 1-3 September 1987 Paper no. C255/87 pages 29-42

Bains, W.P.Peterson, E.G., 1950. " An Investigation of Flow Through Screen", Trans. ASME, J. Eng. Power, 102, pp 88-97.

Biesinger, T. E., and Gregory-Smith, D. G., 1993. "Reduction in Secondary Flows and Losses in a Turbine Cascade by Upstream Boundary Blowing," ASME May 24-27, 1993. Paper No.93-GT-114.

Belik, L., 1975. "Secondary Losses in Turbine Blade Cascade With Low Aspect Ratios and Large Deflection," Proc. 6th conf. on Steam Turbines of Large Power Output, Plzen, Czechoslovakia, Sept. 1975.

Boletis E, 1985. 'Effect of Tip Endwall Contouring on the Three Dimensional Flow-Field in an Annular Turbine Nozzle Guide Vane: Part 1 – Experimental Investigation', Journal of Engineering for Gas Turbines and Power Vol. 107, pp983-990.

Carter, A.D.S., 1948, "Three-Dimensioanl Floe Theories for Axial Compressors and Turbines", Proc. ImechE, Vol. 159.

Came, P. M., and Marsh, H., 1974. "Secondary Flow in Cascades: Two Simple Derivations for The Components of Vorticity", Journal Mechanical Engineering Science, 1974.

Chen, L. D., and Dixon, S. L., 1985. "Growth of Secondary Flow Losses Downstream of a Turbine Blade Cascade", ASME Paper No. 85-GT-35.

Craig, H. R. M., and Cox, A., 1970. "Performance Estimation of Axial Flow Turbines", Proc. ImechE, 185, 407-424.

Denton, J. D., 1982. "An Improved Time Marching Methods for Turbomachinery Flow Calculation", ASME paper 82-GT-239. 1982.

Denton J.D., 1993. 'Loss Mechanisms in Turbomachines', IGTI Scholar Lecture, J. Turbomachinery, Vol. 115, pp 621-656.

Dejc, M. E., and Trojanovskij, B. M., 1973. "Untersunchung Und Berechnung Axialer Turbinenstufen", Berlin, VEB Verlag Technik, 1973.

Deich, M. E., and Zaryankin, A. E., et al, 1960. "Method of Increasing The Efficiency of Turbine Stages", Teploenergetica No. 2, Feb 1960, pp. 18-24. Translation in AEI Translation No. 2816.

Dominy, R.G., 1992. "An Investigation of Factors influencing the Calibration of 5-Hole Probes for 3-D Flow Measurements", ASME, 92-GT-216.

Dunham, J., 1969. "A Review of Cascade Data on Secondary Losses in Turbines", Journal Mechanical Engineering Science, July, 1969.

Erich, F. F., 1955. "Secondary Flows in Cascades of Twisted Blades", J. Aeron. Sciences, Vol. 22, 1955.

Ewen J S, Huber F W, Mitchell J P, 1973. 'Investigation of the Aerodynamic Performance of Small Axial Turbines', Journal of Engineering Power, pp.326-332.

Fillipov, G.A, Van Chzhun-Tsi, 1964. "The Effect of Flow Twisting on the Characteristics of Guide Rows", Teploenergetika, 11, 5, pp54-57.

Gregory-Smith D.G., 1995. 'ERCOFTAC Seminar and Workshop on 3D Turbomachinery Flow Prediction, ERCOFTAC Bulletin', 18-22.

Gregory-Smith, D. G., and Cleak, J. G. E., 1990. "Secondary Flows Measurements in a Turbine Cascade with High Inlet Turbulence", ASME paper No. 90-GT-20.

Gregory-Smith, D. G., and Walsh, J. A., 1989. "Inlet Skew and the Growth of Secondary Losses and Vorticity in a Turbine Cascade," ASME 89-GT-65.

Gregory-Smith, D. G., and Graves, C. P., 1983. "Secondary Flows and Losses in a Turbine Cascade," Viscous Effects in Turbomachines, AGARD CP 351, 1983.

Griepentroc, H., 1969. "Prediction des Perfomance des Grilles D'aubes Transsoniques a Haute Deflexion et Faible Allongement", VKI TN 59.

Haller, B. R., 1997. "Secondary and Tip-clearance Flows in Axial Turbines," Von Karman Institute Lecture Series 1997-01.

Harrison, S., 1990. "The Influence Blade Lean on Turbine Losses," ASME paper No. 90-GT-55.

Hartland J.C., Gregory-Smith D.G., 1996. "Progress Report 2 of Non-axisymmetric Endwall Profiling in a Turbine Rotor Blade". Durham Technical Report.

Hartland J.C., Gregory-Smith D.G., Rose M.G., 1998. "Non-axisymmetric Endwall Profiling in a Turbine Rotor Blade". ASME Paper No. 98-GT-525.

Hawthorne, W. R., 1951. "Secondary Circulation in Fluid Flow," Proc. Roy. Soc., Vol. A206, 1951, pp. 374-397.

Hirsch, C., and Denton, J. D., 1981. "Throughflow Calculations in Axial Flow Turbomachines", AGARD AR-175, 1981.

Ho, Y.-H., and B. Lakshminarayana. "Computational Modeling of Three-Dimensional Endwall Flow Through a Turbine Rotor Cascade With Strong Secondary Flows", ASME 94-GT-136.

Jones, W.P. and Launder, B.E., 1972. "The Prediction of Laminarisation with a Two-Equation Model of Turbulence", Int. J. Heat and mass transfer, Vol. 15, pp. 301-314.

Kato, M, and Launder, B.E., 1993. "The Modelling of Turbulent Flow around Stationary and Vibrating Square Cylinders", Proc. 9th Symp. turbulent shear flows., Kyoto, pp. 10-14.

Kawai, T., Shinoki, S. and Adachi, T., 1989. "Secondary Flow Control and Loss Reduction in a Turbine Cascade Using Endwall Fences", JSME International Journal, Series II, Vol 32, No. 3, pp 375-387.

Lakshminarayana, B., and Horlock, J. H., "Secondary Flow and Losses in Cascade and Axial Flow Turbomachines", Int. J. Mech. Sci., 5(1963) 287

Langston, L. S., Nice, M. L. and Hooper, R. M., 1977. "Three Dimensional Flow With a Turbine Blade Passage," ASME Journal of Engineering for Power, Vol. 99, No. 1, Jan. 1977, pp. 21-28.

Lauder, B.E., and Spalding, D.B., 1974, "The Numerical Computation of Turbulent Flows", Methods in Applied Mechanics and Engineering. Prog. Energy Comb. Sci., 4:221-270, 1978.

Leonard, B.P., 1979. 'A Stable and Accurate Convective Modelling Procedure Based on Quadratic Upstream Interpolation', Comp. Mech. Appl. Mech. Eng., Vol 19, p59.

Lien, F.S and Leschziner, M.A. (1994). 'Multi-grid Acceleration for Turbulent Flow with a Non-Orthogonal, Collocated Scheme', Comp. Mech. Appl. Mech. Eng., Vol 118, p351

Marchal, P., and Sieverding, C. H., 1977. "Secondary Flows Within Turbomachinery Bladings," Secondary Flows in Turbomachines, AGARD CP 214,1977.

Moore H., Gregory-Smith D.G., 1996. 'Transition Effects on Secondary Flow in a Turbine Cascade', ASME Paper No. 96-GT-100.

Moore H, 1995. "Experiments In A Turbine Cascade For The Validation Of Turbulence And Transition Models", Ph.D thesis, Durham University

Morris, A. W. H., and Hoare, R. G., 1975. "Secondary Losses Measurements in a Cascade of Turbine Blades with Meridional Wall Profiling", ASME paper 75-WA/GT-13, 1975.

Norris, L.H. and Reynolds, W.C., 1975. 'Turbulent Channel Flow with a Moving Wavy Boundary', Rep. FM-10, Dept. of Mech. Engrg., Stanford University

Patankar, Suhas. V., 1980. "Numerical Heat Transfer and Fluid Mechanics", Hemisphere Publishing Co.

Roach, P.E., 1986. "The Generation of Nearly Isotropic Turbulence by means of Grids", Int. J. Heat and Fluid Flow, 8, pp 88-91, 1986.

Prümper, H., 1972. "Methoden zur Verminderung der Sejundarverluste in Axialen Turbinenstufen", ZFW, Bd 20, Heft ½.

Prümper, H., 1975, "Application of Boundary Layer Fences in Turbomachinery", AGARD-AG-164, Paper II-3.

Rhie, C.M and Chow, W.L. (1993), "Numerical Study of the Turbulent Flow past an Airfoil with Trailing Edge Separation", AIAA Journal., p125

Rose, M.G., (1994). "Non-axisymmetric Endwall Profiling in the HP NGV's of an Axial Flow Gas Turbine." ASME Paper No. 94-GT-249

Sieverding, C. H., 1975. "Reduction of Secondary Losses in Turbines", von Karman Institute for Fluid Dynamics, Lecture Series 72, 1975.

Sieverding, C. H., 1984. "Recent Progress in the Understanding of Basic Aspects of Secondary Flows in Turbine Blade Passages", ASME. Paper No. 84-GT-78.

Sieverding, C. H., and Van Den Bpsch, P., 1983. "The Use of Coloured Smoke to Visualize Secondary Flows in a Turbine-Blade Cascade", Journal of Fluid Mechanics, Vol. 134, Sept. 1983, pp. 85-89.

Singh, G., Walker, P.J., and Haller, B.R., 1995. "Development of Three-Dimensional Stage Viscous Time Marching Method for Optimisation of Short Height Stages", 1st European Conference on "Turbomachinery Fluid Dynamic and Thermodynamic Aspects" Erlangen, March 1995.

Squire, H.B., and Winter, K.G., "The Secondary Flow in a Cascade of Aerofoils in a Non-uniform Stream", J aeronaut. Sci., 18(4), (1951) 271

Treaster A.L., Yocum A.M., 1979. 'The Calibration and Application of Five-hole Probes', *ISA Transactions*, Vol. 18, No. 3, pp 23-34

Walraevens R.E., Gallus H.E., 1995. "Stator -Rotor-Stator Interaction in an Axial Flow Turbine and its Influence on Loss Mechanisms", AGARD-CP-571 Paper No.39

White F. M., 1991. "Viscous Fluid Flow", Second Edition, McGraw-Hill, Inc.

Willis, G. D., and Truelove, A. H., "Some Practical Aspects of Cascade Testing at High Reynolds Number", GEC technical papers.

Zweifel, O. (1945), "The Spacing of TurbomachineryBlading especially with Large Angular Section", Brown Boveri Review, December, pp. 436-444.